

Acoustic emission as on-line tool for non-destructive inspection of welding

Dries De Ruyck, Hannes Polijn

Student numbers: 01500150, 01508860

Supervisors: Prof. dr. ir. Wim De Waele, Dr. ir. Koen Faes (BIL)

Counsellor: Ir. Irene Kwee (Belgisch Instituut voor Lastechniek)

Master's dissertation submitted in order to obtain the academic degree of
Master of Science in de industriële wetenschappen: elektromechanica

Academic year 2018-2019

Acoustic emission as on-line tool for non-destructive inspection of welding

Dries De Ruyck, Hannes Polijn

Student numbers: 01500150, 01508860

Supervisor: Prof. dr. ir. Wim De Waele, Dr. ir. Koen Faes (BIL)

Counsellors: Ir. Irene Kwee (Belgisch Instituut voor Lastechniek)

Master's dissertation submitted in order to obtain the academic degree of
Master of Science in de industriële wetenschappen: elektromechanica

Academic year 2018-2019

De auteurs geven de toelating deze masterproef voor raadpleging beschikbaar te stellen en delen ervan te kopiëren voor persoonlijk gebruik. Elk ander gebruik valt onder de beperkingen van het auteursrecht, in het bijzonder met betrekking tot de verplichte bronvermelding bij het gebruiken of aanhalen van teksten of resultaten uit deze masterproef.

The authors give permission to make this master dissertation available for consultation and to copy parts of it for personal use. In case of any other use, the copyright terms have to be respected, in particular with regard to the obligation to state expressly the source when quoting results from this master dissertation.

Ghent, June 2019

Preface

In this preface we would like to thank the people that supported and guided us during the academic year in which we handled this master dissertation.

First of all our gratitude goes out to dr. ir. Koen Faes and ir. Irene Kwee of the Belgian Welding Institute for granting us the opportunity to work on one of their projects. They were happy to make time for guiding and supporting us throughout the year, it was a pleasure working with them.

We would also like to thank prof. dr. ir. Stijn Hertelé and especially prof. dr. ir. Wim De Waele for sticking op to our subject and making time to evaluate us during the year based on interim presentations.

Furthermore we would like to thank Sam Demeester, ing. Benny Droesbeke and ing. Jurgen Feyaerts of the Belgian Welding Institute for guiding us through the welding machine setup and for making time so we could investigate arc welds made with a robot. All employees were very kind and helped us with a smile.

We are grateful to the Belgian Welding Institute in overall for providing us the needed materials and tools.

Last but not least I would like to thank my fellow student and friend with whom I was able to realise this work.

Both authors declare agreement with the content of this master dissertation.

Hannes Polijn and Dries De Ruyck, June 2019

Acoustic emission as a tool for non-destructive inspection of welds

By Dries De Ruyck and Hannes Polijn

Master thesis submitted in order to obtain the academic degree of
Master of Science in Electromechanical Engineering

Faculty of Engineering and Architecture

Academic year 2018 – 2019

Supervisors: prof. dr. ir. Wim De Waele, dr. ir. Koen Faes

Department of Electrical Energy, Metals, Mechanical Constructions & Systems
Chair: prof. dr. ir. Luc Dupré

Abstract

The use of acoustic emission (AE) monitoring to determine the welding quality is a non-destructive investigation method that is constantly being researched and further developed. In this master dissertation the use of AE monitoring on friction stir spot welding and arc welding is investigated. Friction stir spot welding is a technique for joining lightweight aluminium and magnesium alloy sheets in the overlap configuration by means of frictional heat and mechanical work. The technique has a high potential for the modern industry.

The main objective of this master dissertation is to investigate and develop a non-destructive quality check for EN AW-6082-T6 friction spot weld by using AE. Quality standards are found in previous work [1][3] based on destructive testing. The influence of several welding parameters on the AE result was investigated and a standard setup with a minimum of background noise was developed. To get a better understanding of the AE technique, a second welding technique namely MIG/MAG robotic welding was investigated. This master dissertation contains a literature study and continues with its own experimental program.

Keywords: acoustic emission, friction stir spot welding, EN AW-6082-T6, weld quality inspection

Acoustic emission as on-line tool for non-destructive inspection of friction stir spot welds

Dries De Ruyck, Hannes Polijn

Supervisors: Prof. dr. ir. Wim De Waele, Dr. ir. Koen Faes

Abstract: Acoustic emission (AE) monitoring is a non-destructive testing method to determine the weld quality, that is constantly being investigated and further developed. In this work, it is applied on friction stir spot welding of the aluminium alloy EN AW-6082-T6. This welding method enables to weld different aluminium alloys, and also the non-weldable aluminium alloys such as materials from the 2000 and 7000 series. It is a solid-state welding process, meaning that welding takes place at temperatures below the melting point. Especially the aerospace and transport industry show great interest in this welding method, because high-strength lightweight materials can be welded. The AE evaluation method was used together with lap shear testing, metallographic examination and temperature measurements.

Keywords: acoustic emission, refill friction stir spot welding, EN AW-6082-T6, weld quality inspection

I. INTRODUCTION

The weld quality can be investigated by using AE monitoring. This is a non-destructive method that records the sounds produced by the material during the weld cycle. This method is not to be confused with ultrasonic (US) examination, where sound waves are sent through a material in order to locate cracks based on the recurring signal.

This investigation method will be applied on refill friction stir spot welding (RFSSpW), a welding technique which has a promising future in the aerospace and automotive industry. However, like in all processes, some defects can appear when inappropriate welding parameters are used, which can negatively affect the weld strength. The intention of this research is to determine the presence of a weld defect based on AE. By using this non-destructive inspection technique, low-quality welds with defects are distinguished from good welds. Previous work [1] focused on the evaluation of the weldability of high-strength aluminium alloys using RFSSpW, while this work focuses on the use of AE monitoring on the same welding process.

II. FRICTION STIR SPOT WELDING

A. Process description

The RFSSpW process produces a single welded spot, while the material is temporarily in a plastic state. The metallurgical bond is realised using the heat of friction generated by a three-component welding tool. The joint is realised between two overlapping aluminium sheets, fixed on a welding table. The components of the tool are shown in figure 1. This illustrates the complete weld cycle which consists of four stages. The clamping ring fixes the two overlapping aluminium sheets by applying a force in the axial direction. The frictional heat is

created by the rotation of the pin and sleeve which plasticise the material in order to create a metallurgical bond.

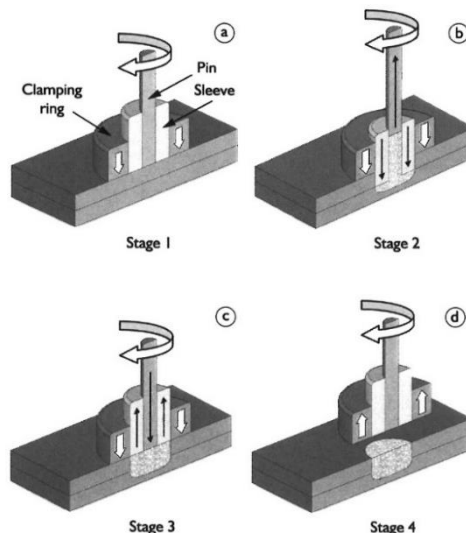


Figure 1: Refill friction stir spot welding [2].

In stage 1 (figure 1a), the three-component tool is lowered until it makes contact with the sheets to be welded. While lowering, the pin and sleeve start to accelerate in order to reach the desired rotation speed. Once the clamping ring exerts the predefined clamping force in order to prevent movement of the aluminium sheets during welding, the sleeve is lowered and pushed into the sheets at the predefined rotation speed (stage 2: figure 1b). At the same time, the pin is retracted to create a cavity underneath the pin. The material underneath the sleeve is plasticised due to the frictional heat and is pushed into the created cavity. This event is called ‘plunging’. At stage 3 (figure 1c), the pin and sleeve return to their initial position, forcing the plasticised material to refill the keyhole. The welding zone is called ‘the weld nugget’. In the last stage (stage 4: figure 1d), the tool starts to decelerate and is withdrawn from the joint, leaving a flat surface with minimum material loss.

B. Welding parameters

The duration of previous describes phases depend on the used welding process parameters. The most important welding parameters are the rotation speed (RS), plunge depth (PD), plunge time (PT), dwell time (DT) and retraction time (RT). Based on the PD and the PT, the plunge rate (PR) can be calculated, which is the speed of the sleeve plunging into the material. Analogue to this, the PD and RT determine the retraction rate (RR). The PT, DT and RT together determine the joining time (JT) which is the total time for the creation of the joint. A visualisation of these parameters plotted as a function

of time (ms) is shown in figure 2. The position of the sleeve and pin (mm) is illustrated by the purple and dark blue curve respectively. The orange curve stands for the rotation speed (rpm).

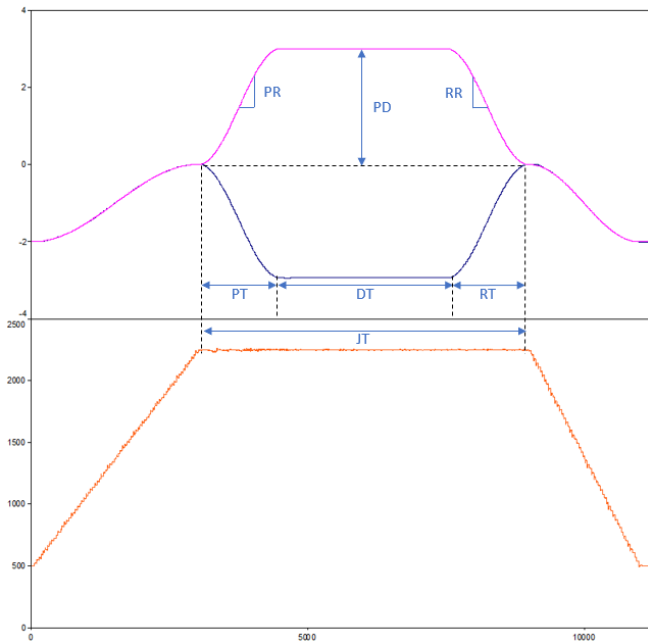


Figure 2: The welding parameters.

C. Weld quality

The mechanical and microstructural properties of a refill friction spot weld is investigated based on metallographic examination. The weld quality is determined by the presence of certain geometrical zones and features that occur in the weld nugget.

Figure 3 shows a typical cross-section of a refill friction stir spot weld. Four different zones can be distinguished, that appear in every weld: the stir zone (SZ), thermo-mechanically affected zone (TMAZ), heat affected zone (HAZ) and the base material (BM).



Figure 3: Cross-section of a friction stir spot weld with the associated zones [2].

The SZ contains the material that effectively has been mixed by the pin and sleeve and is characterised by finer grains due to dynamic recrystallisation [3]. The TMAZ is a zone with larger recrystallised distorted grains in comparison to the SZ. The grain structure is highly elongated because of the mechanical action exerted by the welding tool [4]. The material in the HAZ only experiences a thermal weld cycle, inducing more coarse grains compared to the BM [5]. Also, the heat causes the grains to grow. The grain size variations in the different weld zones are visible in figure 4. Associated with the grain size, a variable

hardness appears along the cross-section of a refill friction spot weld. The geometrical zones and hardness are further discussed in the master dissertation.

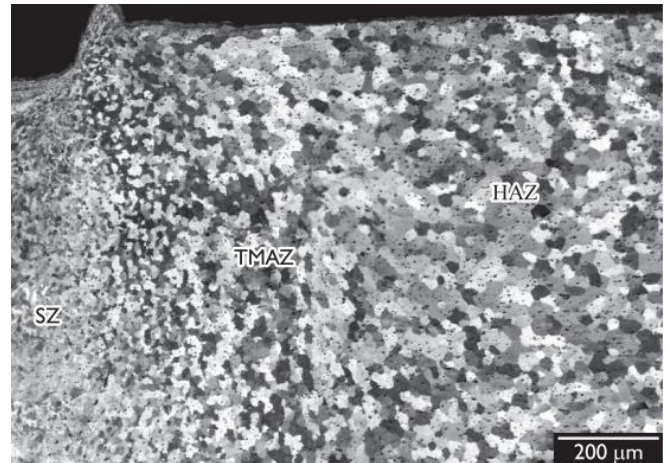


Figure 4: Grain size variations in the different welding zones [3].

III. ACOUSTIC EMISSION MONITORING

A. AE basics

An AE monitoring detection system measures the emissions produced by a workpiece subjected to a welding process, performs data processing and looks for features which might indicate a weld defect [6]. Two different types of AE signals in the time domain can be distinguished: the continuous and the burst emissions. The continuous emissions have a low amplitude and quickly repeating waves, while burst emissions have incidental eruptions, which is characterised by a large amount of energy and a large amplitude. The difference is illustrated in figure 5.

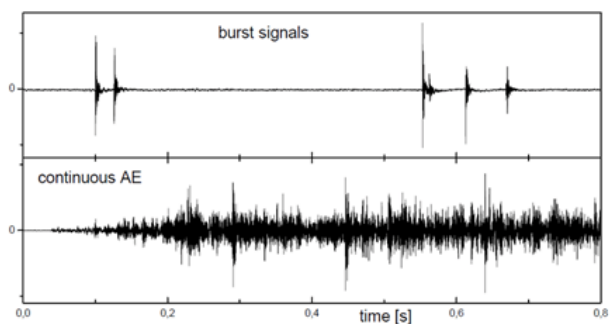


Figure 5: Bursts signals (top) and continuous AE (bottom) [7].

Burst signals exceeding the threshold contain the most information. The following information can be extracted from the measured signals:

- **Amplitude:** largest deviation from the equilibrium position.
- **Risetime:** time for a pulse to rise between 10 and 90% of a specified maximum value.
- **Counts:** number of times that the chosen threshold is exceeded by the AE signal.
- **MARSE** (Measured Area Rectified Signal Envelope): measurement of the area under the envelope of the rectified linear voltage time signal

from the sensor [8]. It contains the energy of the bursts.

- **Duration:** time between the first and last exceedance of the chosen threshold.

These are visually represented in figure 6.

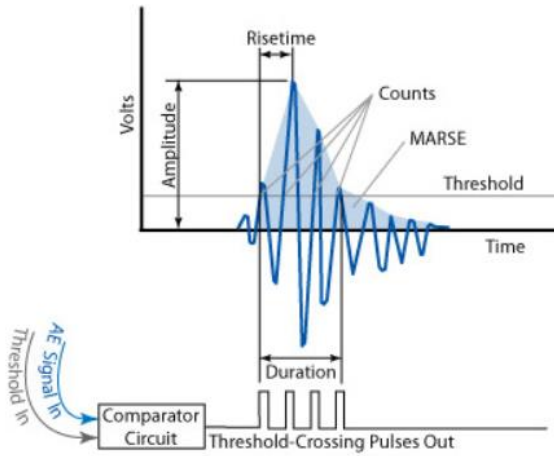


Figure 6: Burst information in an AE signal [9].

B. Equipment

In order to detect the acoustic signals emitted by the formation of a weld defect, a sensor or transducer is used. Subsequently, the signal passes through a pre-amplifier, filter amplifier and is finally detected by a signal conditioner and event detector. Once all these stages are passed, the signal is processed by specific software. A principle sketch of an AE monitoring system is shown in figure 7.

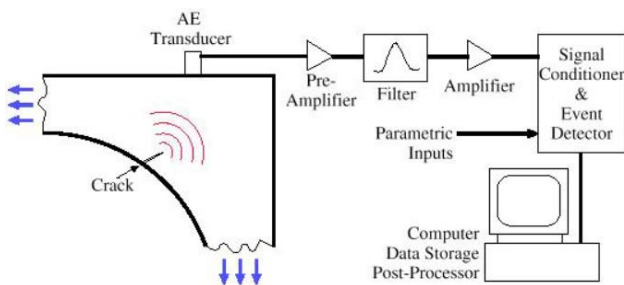


Figure 7: Measuring system for recording AE signals [6].

For a more detailed discussion about the measuring system, the master dissertation is referred to.

IV. EXPERIMENTAL STUDY

A. Intention

The goal of this investigation was to find a good AE configuration which filters out contaminations. Contaminations appear due to background noise and mechanical movements of the welding machine. Signals of previous tests, made with another AE configuration contained these kind of contaminations, as they showed a lot of variations between the wavestreams. In order to be able to compare the relevant signals emitted during welding and to draw conclusions about the weld quality, the contaminations have to be filtered out.

B. Materials and equipment

The experiments were performed using a commercial refill friction spot welding equipment RPS 100 (Harms & Wende, Germany). Four welds with identical welding parameters were made using the EN AW-6082-T6 aluminium alloy with a thickness of 2 mm. The chemical composition and mechanical properties of EN AW-6082-T6 is given in table 1 and 2 respectively.

Table 1: Chemical composition of the EN AW-6082-T6 alloy (wt%) [10].

Si	Fe	Cu	Mn	Mg	Cr	Zn	Ti
0.7 - 1.3	≤ 0.5	≤ 0.1	0.4 - 1.0	0.6 - 1.2	≤ 0.25	≤ 0.2	≤ 0.1

Table 2: Mechanical properties of the EN AW-6082-T6 alloy [10].

Yield strength (MPa)	UTS (MPS)	Elongation (%)	Hardness (HRB)	Density (g/cm ³)	Melting point (°C)
143	300	11	117	2.70	555

Destructive lap shear testing was performed according to EN ISO 14273 on a tensile testing machine; Instron model 8801. A displacement rate of 10 mm/min was applied.

Metallographic research was performed on the cross-sections, using an Olympus MX51 optical microscope.

For recording the AE signals, a W50D-sensor was used. The sensor was placed at the welding table, on which the aluminium sheets were fixed.

C. Welding parameters

The used welding parameters for creating the welds are given in table 3.

Table 3: Used welding parameters.

RS (rpm)	PD (mm)	DT (s)	PT (s)	RT (s)	Hold time (s)
2250	2.2	3	1.5	1.5	2

D. AE configuration

The used AE configuration is given in table 4.

Table 4: Used AE configuration.

Sample rate (MSPS)	Frequency range (kHz)	Resonance frequency (kHz)	Threshold (dB)
2	400 - 800	500	50

V. RESULTS

A. Acoustic emission evaluation

The recorded wavestreams are shown in figure 8. They are expressed in amplitude (dB) over time (μ s). The signals are clean with a lot of similarities.

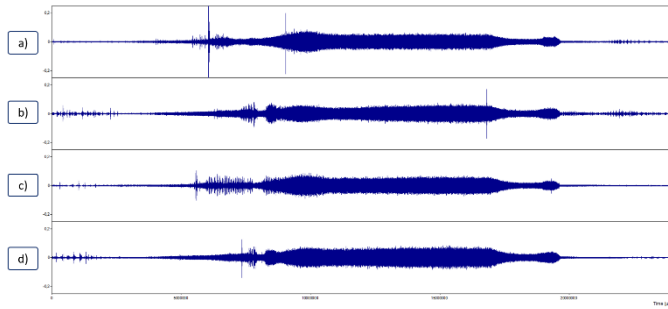


Figure 8: Recorded wavestreams for refill friction spot welds (R19).

Based on the waveforms, one could say the welds are exactly the same. In order to investigate the relevance of the AE configuration, cross-sections of the welds were made and investigated. If these results also show the same phenomenons and do not deviate too much, a conclusion can be made regarding the AE configuration.

The cross-sections are illustrated in figure 9.

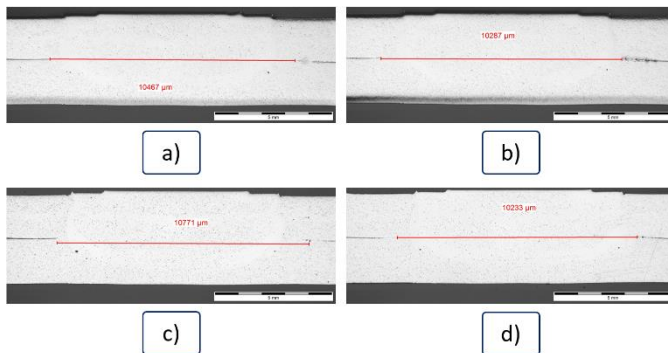


Figure 9: Metallographic research of the cross-sections.

Also the cross-sections show an unambiguously result: no welding defects appear, and the bonding ligament varies little. Even though tis AE configuration shows promising results, more research is required to further confirm this.

VI. CONCLUSION

It became clear that AE monitoring of a welding process is a very complex task. Deducing concrete conclusions at the start of the investigation about the weld quality for refill friction spot welding was difficult due to the presence of contaminations. During the last investigations, a standard configuration which filters out most of the noise showed promising results. Nevertheless, this configuration still has to be investigated further in order to examine the detection capabilities for all possible weld defects.

ACKNOWLEDGEMENTS

This work is a part of a master dissertation at Ghent University in cooperation with the Belgian Welding Institute (2019).

REFERENCES

- [1] J. Vercauteren, “*Experimental investigation of the weldability of high strength aluminium alloys using friction spot welding*”, master dissertation at Ghent University, 2017.
- [2] ‘Friction spot welding | www.bil-ibs.be’. [Online]. Available: <http://www.bil-ibs.be/en/friction-spot-welding>

- [3] B. Parra, V. T. Saccon, N. G. de Alcântara, T. Rosendo, J. F. dos Santos, “*An investigation on friction spot welding in AA6181-T4 alloy*”, 2011.
- [4] G. Bussu, P. E. Irving, “*The role of residual stress and heat affected zone properties on fatigue crack propagation in friction stir welded 2024-T351 aluminium joints*”, *International Journal of Fatigue* 25 (2003) 70-88, 2002.
- [5] Z. Shen, X. Yang, S. Yang, Z. Zhang, Y. Yin, “*Microstructure and mechanical properties of friction spot welded 6061-T4 aluminum alloy*”, *Materials and Design* 54 (2014) 766-778, 2013.
- [6] P. A. Fleming, “*Monitoring and control in friction stir welding*”, 2009.
- [7] H. J. Schoorlemmer, “*Akoestische emissie analyse tijdens lassen*”, 1983.
- [8] Unknown, “*Nondestructive Testing Encyclopedia – Acoustic Emission*”, [Online]. Available: <https://www.ndt.net/article/az/ae/marse.htm>. [Accessed: 18-Apr-2019].
- [9] W. J. P. Vink, “*Niet-destructief onderzoek (editie 2)*”, 2000.
- [10] S. Missori and A. Sili, “*Mechanical behavior of 6082-T6 aluminium alloy welds*”, Vol. 18 (1), 2000.

Akoestische emissie voor online en niet-destructieve inspectie van wrijvingspuntlassen

Dries De Ruyck, Hannes Polijn

Begeleiders: Prof. dr. ir. Wim De Waele, Dr. ir. Koen Faes

Abstract: Het monitoren van akoestische emissie (AE) is een niet-destructieve testmethode om de laskwaliteit te bepalen en wordt voortdurend onderzocht en verder ontwikkeld. In dit werk wordt het toegepast op wrijvingspuntlassen van de EN AW-6082-T6 aluminiumlegering. Deze lasmethode maakt het mogelijk verschillende aluminiumlegeringen te lassen zoals ook de niet-lasbare aluminiumlegeringen uit series 2000 en 7000. Het volledige proces gebeurt in vaste toestand, wat betekent dat het lassen gebeurt op temperaturen lager dan de smelttemperatuur. Vooral de luchtvaart- en transportindustrie zijn geïnteresseerd in deze lastechniek omdat enorm sterke, lichte materialen gelast kunnen worden. De AE evaluatie methode werd gebruikt samen met trektesten, metallografisch onderzoek en temperatuurmetingen.

Kernwoorden: akoestische emissie, wrijvingspuntlassen, EN AW-6082-T6, laskwaliteit inspectie

I. INLEIDING

De laskwaliteit kan bepaald worden door het gebruik van AE controle. Het is een niet-destructieve onderzoeksmethode dat de geproduceerde geluiden van een materiaal gedurende een lascyclus kan opnemen. Deze methode is niet te verwarren met ultrasoon (US) onderzoek, waar geluiden door het materiaal gestuurd worden en defecten opgespoord kunnen worden op basis van het ontvangen signaal.

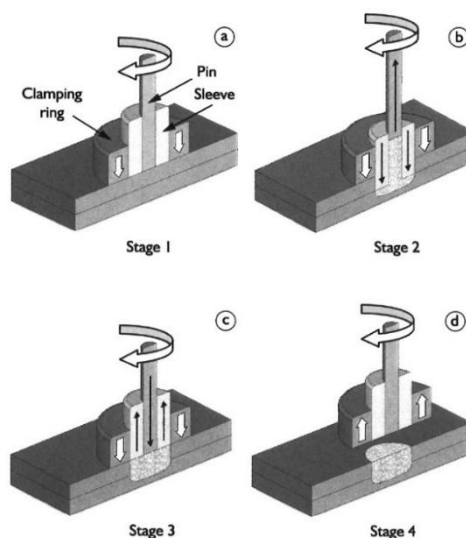
Deze onderzoeksmethode zal toegepast worden op wrijvingspuntlassen, een lastechniek met een veelbelovende toekomst in de luchtvaart- en automobiellindustrie. Echter, zoals in andere lasprocessen komen er ook bij deze lasmethode defecten voor wanneer er ongeschikte lasparameters gebruikt worden. Deze defecten hebben een negatieve invloed op de lassterkte en worden best vermeden. De bedoeling van dit onderzoek is met behulp van AE de aanwezigheid van deze defecten te kunnen bepalen. Door gebruik te maken van deze niet-destructieve inspectietechniek, worden lassen met een lage kwaliteit onderscheiden met lassen met een goede kwaliteit. Vorig werk [1] richtte zich op de evaluatie van de lasbaarheid van sterke aluminiumlegeringen met wrijvingspuntlassen, terwijl dit werk zich focust op het gebruik van AE voor hetzelfde lasproces.

II. WRIJVINGSPUNTLASSEN

A. Procesbeschrijving

Het wrijvingspuntlasproces produceert één puntlas terwijl het materiaal zich tijdelijk in plastische toestand bevindt. De metallurgische verbinding komt tot stand door gebruik te maken van wrijvingswarmte, gegenereerd door een driedelig lasgereedschap. De verbinding wordt gerealiseerd tussen twee overlappende aluminiumplaten, gefixeerd op een lastafel. De componenten van het lasgereedschap wordt weergegeven in

figuur 1. Het illustreert de volledige lascyclus welke uit vier stappen bestaat. De klemring fixeert de twee overlappende plaatsjes door kracht in axiale richting uit te voeren. De wrijvingswarmte wordt gegenereerd door rotatie van de pin en huls die het materiaal plastificeren zodanig dat er een metallurgische verbinding tot stand komt.



Figuur 1: Het wrijvingspuntlasproces [2].

In stap 1 (figuur 1a), zakt het driedelig gereedschap tot het contact maakt met het te lassen materiaal. Terwijl het gereedschap zakt, versnellen de pin en de huls tot een vooraf ingestelde rotatiesnelheid. Van zodra de klemring de nodige klemkracht, nodig om beweging van de platen te voorkomen, bereikt heeft, zakt de huls met een bepaalde rotatiesnelheid in het materiaal (stap 2: figuur 1b). Op hetzelfde moment wordt de pin teruggetrokken zodanig dat er onder de pin een caviteit ontstaat. Het materiaal dat zich onder de huls bevindt is plastisch vanwege de wrijvingswarmte en wordt in de caviteit geduwd. Deze gebeurtenis heet 'plunging'. Bij stap 3 (figuur 1c) keren de pin en huls terug naar hun oorspronkelijke positie wat ervoor zorgt dat het plastische materiaal het gecreëerde gat terug opvult. De cilindervormige verbinding die dan tot stand gekomen is wordt de 'weld nugget' genoemd. In de laatste stap (stap 4: figuur 1 d) vertraagt het gereedschap en wordt het teruggetrokken van de verbinding. Het laat een plat oppervlak achter met een minimum aan materiaalverlies.

B. Lasparameters

Het eerder besproken lasproces is afhankelijk van de gebruikte lasparameters. De meest belangrijke zijn de rotatiesnelheid (RS), plunge diepte (PD), plunge tijd (PT),

‘dwell’ tijd (DT) en intrektijd (RT). Op basis van de PD en de PT kan de plungesnelheid berekend worden. De plungesnelheid is de snelheid waarmee de huls in het materiaal duikt. Analoog bepalen de PD en RT de intreksnelheid (RR). De PT, DT en RT bepalen samen de verbindingstijd (JT) welke de tijd is waarin de verbinding tot stand komt. Een visualisatie van deze parameters, uitgezet over de tijd (ms) is te zien in figuur 2. De positie van de pin en huls (mm) worden respectievelijk voorgesteld door de donkerblauwe en roze curve. De oranje curve stelt de rotatiesnelheid (rpm) voor.

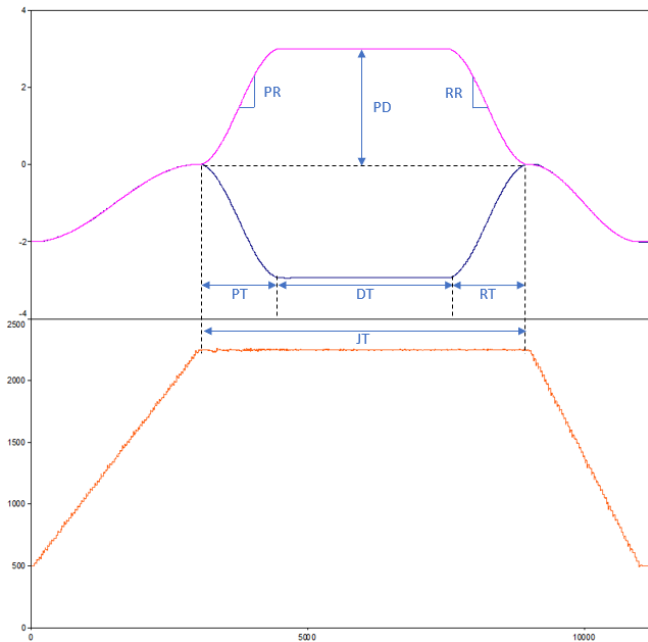
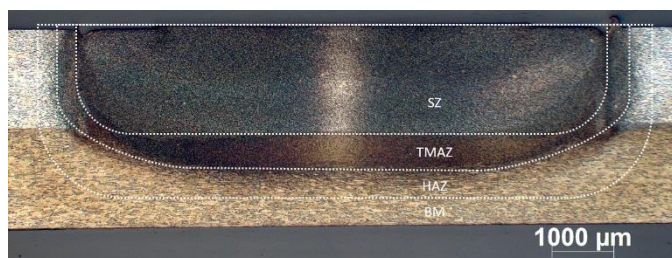


Figure 2: De lasparameters.

C. Laskwaliteit

De mechanische en microstructurele eigenschappen van een wrijvingspuntlas is geanalyseerd op basis van een metallografisch onderzoek. De laskwaliteit wordt bepaald door de aanwezigheid van bepaalde geometrische zones en kenmerken die in de ‘weld nugget’ voorkomen.

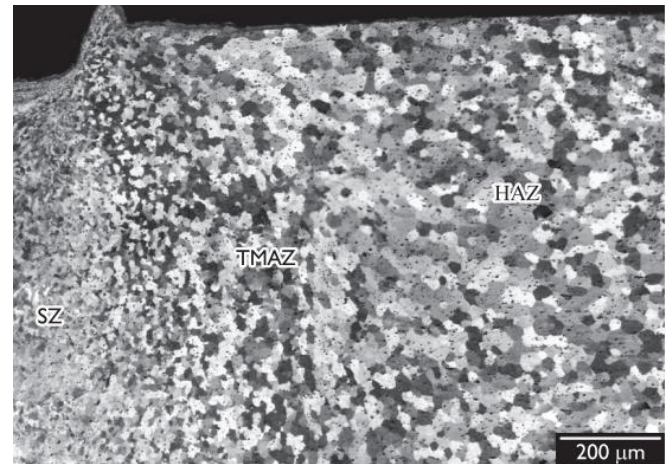
Figuur 3 geeft een typische dwarsdoorsnede van de puntlas weer. Vier verschillende zones, welke in elke las voorkomen, kunnen onderscheiden worden: de mengzone (SZ), thermo-mechanisch beïnvloede zone (TMAZ), hitte beïnvloede zone (HAZ) en het basismateriaal (BM).



Figuur 3: Dwarsdoorsnede van een puntlas met de geassocieerde zones [2].

De SZ bevat het materiaal dat effectief vermengd geweest is door de pin en de huls en wordt gekenmerkt door kleine korrelgroottes vanwege dynamische rekristallisatie [3]. De TMAZ is een zone met grotere gekristalliseerde korrels in

vergelijking met de SZ. De korrelstructuur is uitgerekt vanwege de mechanische bewegingen van het lasgereedschap [4]. Het materiaal in de HAZ ondervindt enkel een thermische lascyclus waardoor er meer grovere korrels voorkomen dan in het BM [5]. Ook de optredende warmte zorgt ervoor dat de korrels groeien. De korrelgroottevariëaties voor elke laszone is zichtbaar in figuur 4. Geassocieerd met de korrelgrootte zal er een variabele hardheid in de dwarsdoorsnede van de wrijvingslas voorkomen. De geometrische zones en hardheidsvariëaties worden verder besproken in het eindwerk.



Figuur 4: Korrelgrootte variaties volgens de verschillende laszones [3].

III. AKOESTISCHE EMISSIE

A. De basis

Een AE-detectiesysteem meet de emissie van een werkstuk dat onderhevig is aan het lasproces, voert dataverwerking uit en zoekt naar kenmerken die op een lasdefect kunnen duiden [6]. Twee verschillende types van AE signalen in het tijdsdomein kunnen onderscheiden worden: het continue emissie en de burst-emissie. De continue emissie heeft een lage amplitude met snel veranderende golven, terwijl de burst-emissie vooral uit signalen met een grote amplitude bestaat. De burst-emissie is gekenmerkt door een grote hoeveelheid energie. Het verschil tussen beiden is weergegeven in figuur 5.

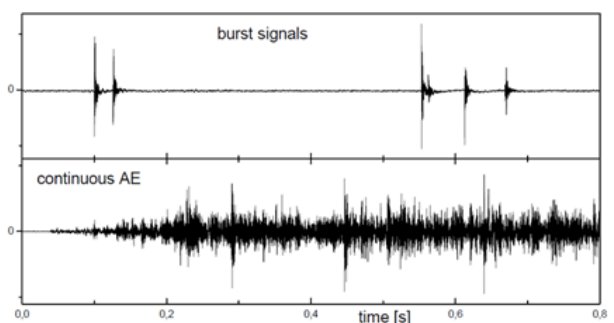
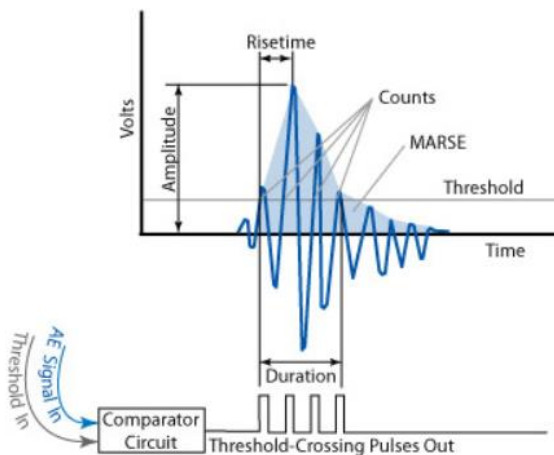


Figure 5: Burst-signalen (bovenaan) en continue AE (onderaan) [7].

Burst -signalen die de vooraf ingestelde drempel (threshold) overschrijden bevatten de meeste informatie. Volgende informatie kan uit het signaal gehaald worden:

- **Amplitude:** grootste afwijking van de evenwichtspositie.
- **Risetime:** Stijgtijd, de tijd waarin een puls stijgt tussen 10 en 90% van een gespecificeerde waarde.
- **Counts:** aantal keer dat de gekozen drempel overschreden wordt door het AE signaal.
- **MARSE** (Measured Area Rectified Signal Envelope): grootte van het oppervlak onder de omhulling van het gelijkrichte lineaire spannings-tijdsignaal van de sensor [8]. Het bevat de energie van het AE signaal.
- **Duration:** tijd tussen de eerste en de laatste overschrijding van de gekozen drempel.

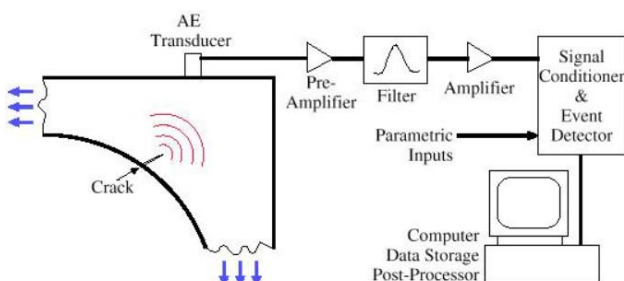
Bovenstaande termen worden voorgesteld in figuur 6.



Figuur 6: Informatie uit het AE signaal [9].

B. Uitrusting

Om de akoestische emissie, geëmitteerd door de vorming van een lasdefect, te kunnen detecteren wordt er een sensor gebruikt. Achtereenvolgens gaat het signaal door een voorversterker, filterversterker en wordt uiteindelijk gedetecteerd door een signaalconditioner en gebeurtenisdetector. Eens al deze fasen doorlopen zijn, wordt het signaal verwerkt door een specifieke software. Een principeschets van een AE-meetsysteem wordt weergegeven in figuur 7.



Figuur 7: Meetsysteem om AE signalen mee op te nemen [6].

Voor een meer gedetailleerde beschrijving van het meetsysteem wordt er naar het eindwerk verwezen.

IV. EXPERIMENTELE UITVOERING

A. Het doel

De bedoeling van dit onderzoek was om een goede AE configuratie te vinden welke de vervuilingen van het signaal eruit filtert. Vervuilingen komen voor vanwege achtergrondgeluiden en mechanische bewegingen van het lasapparaat. Signalen van vorige testen, gemaakt met een andere AE configuratie bevatten deze vervuilingen waardoor er veel variaties in het signaal voorkwamen. Om de relevante signalen, geëmitteerd tijdens het lassen, met elkaar te kunnen vergelijken en conclusies te kunnen trekken moeten deze vervuilingen bijgevolg uit het signaal gefilterd worden.

B. Materiaal en gereedschap

De experimenten werden uitgevoerd met een commerciële wrijvingspuntlasmachine RPS 100 (Harms & Wende, Duitsland). Vier puntlassen met identieke lasparameters werden gemaakt op het EN AW-6082-T6 aluminiumlegering met een dikte van 2 mm. De chemische samenstelling en mechanische eigenschappen van het materiaal is gegeven in tabel 1 en 2 respectievelijk.

Tabel 1: Chemische samenstelling van de EN AW-6082-T6 legering (wt%) [10].

Si	Fe	Cu	Mn	Mg	Cr	Zn	Ti
0.7 - 1.3	≤ 0.5	≤ 0.1	0.4 - 1.0	0.6 - 1.2	≤ 0.25	≤ 0.2	≤ 0.1

Tabel 2: Mechanische eigenschappen van de EN AW-6082-T6 legering [10].

Reksterkte (MPa)	UTS (MPS)	Rek (%)	Hardheid (HRB)	Dichtheid (g/cm ³)	smeltpunt (°C)
143	300	11	117	2.70	555

Destructieve trekproeven werden uitgevoerd volgens EN ISO 14273 op een trektoestel; Instron model 8801. Een treksnelheid van 10 mm/min werd toegepast.

Metallografisch onderzoek werd uitgevoerd op de dwarsdoorsnede van de puntlas door gebruik te maken van een Olympus MX51 optische microscoop.

Om de AE signalen op te nemen werd een W50D-sensor gebruikt. De sensor werd op de lastafel geplaatst waar de aluminium platen op gefixeerd lagen.

C. Lasparameters

De lasparameters die gebruikt werden om de puntlassen te maken worden weergegeven in tabel 3.

Tabel 3: Gebruikte lasparameters.

RS (rpm)	PD (mm)	DT (s)	PT (s)	RT (s)	Hold time (s)
2250	2.2	3	1.5	1.5	2

D. AE configuratie

De gebruikte AE configuratie wordt weergegeven in tabel 4.

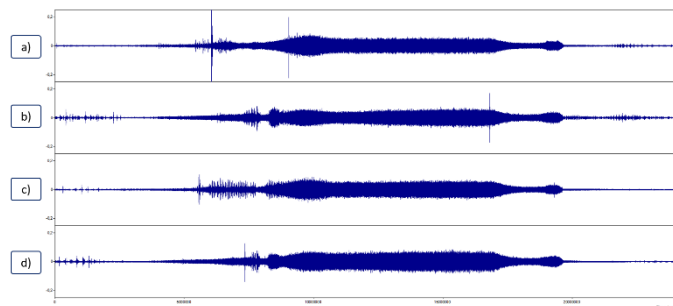
Tabel 4: Gebruikte AE configuratie.

Sample snelheid (MSPS)	Frequentie-bereik (kHz)	Resonantie-frequentie (kHz)	Drempel (dB)
2	400 - 800	500	50

V. RESULTATEN

A. Evaluatie van de akoestische emissie

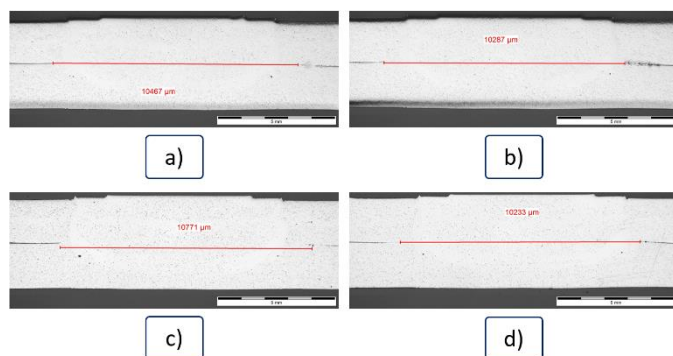
De opgenomen geluidsgolven zijn zichtbaar in figuur 8. De signalen zijn zuiver en bevatten veel gelijkenissen. Ze zijn uitgedrukt in amplitude (dB) over tijd (μ s).



Figuur 8: Opgenomen geluidsgolven voor de puntlassen van R19.

Op basis van de geluidsgolven kan men stellen dat de lassen zo goed als exact hetzelfde zijn. Om de relevantie van de AE configuratie te kunnen onderzoeken, worden de dwarsdoorsnedes van de puntlassen ook onderzocht. Wanneer ook deze dezelfde verschijnselen vertonen en niet teveel afwijken kan er een besluit genomen worden betreft de AE configuratie.

De dwarsdoorsnedes worden geïllustreerd in figuur 9.



Figuur 9: Metallografisch onderzoek van de dwarsdoorsnedes.

Ook de dwarsdoorsnedes tonen een éénduidig resultaat: geen lasdefecten komen voor en de lengte van de lasverbinding varieert slechts enkele μ m. Zelfs al toont deze AE configuratie veelbelovende resultaten, toch zal er meer onderzoek nodig zijn om dit verder te bevestigen.

VI. CONCLUSIE

Het werd duidelijk dat AE controle van een lasproces een complexe taak is. Concrete besluiten trekken over de laskwaliteit was moeilijk aangezien er bij de start van het onderzoek veel vervuilingen aanwezig waren. Gedurende de laatste onderzoeken werd er een goede AE configuratie

opgesteld die de meeste vervuilingen weg filtert en veelbelovende resultaten gaf. Desalniettemin moet deze AE configuratie verder onderzocht worden om detectiemogelijkheden voor alle lasdefecten te analyseren.

ERKENNINGEN

Dit werk is deel van een master thesis aan Universiteit Gent in samenwerking met het Belgisch instituut voor lastechniek (2019).

REFERENTIES

- [1] J. Vercauteren, "Experimental investigation of the weldability of high strength aluminium alloys using friction spot welding", masterproef aan Universiteit Gent, 2017.
- [2] 'Friction spot welding | www.bil-ibs.be'. [Online]. Beschikbaar: <http://www.bil-ibs.be/en/friction-spot-welding>
- [3] B. Parra, V. T. Saccon, N. G. de Alcântara, T. Rosendo, J. F. dos Santos, "An investigation on friction spot welding in AA6181-T4 alloy", 2011.
- [4] G. Bussu, P. E. Irving, "The role of residual stress and heat affected zone properties on fatigue crack propagation in friction stir welded 2024-T351 aluminium joints", International Journal of Fatigue 25 (2003) 70-88, 2002.
- [5] Z. Shen, X. Yang, S. Yang, Z. Zhang, Y. Yin, "Microstructure and mechanical properties of friction spot welded 6061-T4 aluminum alloy", Materials and Design 54 (2014) 766-778, 2013.
- [6] P. A. Fleming, "Monitoring and control in friction stir welding", 2009.
- [7] H. J. Schoorlemmer, "Akoestische emissie analyse tijdens lassen", 1983.
- [8] Onbekend, "Nondestructive Testing Encyclopedia – Acoustic Emission", [Online]. Beschikbaar: <https://www.ndt.net/article/az/ae/marse.htm>. [Geraadpleegd op: 18-Apr-2019].
- [9] W. J. P. Vink, "Niet-destructief onderzoek (edition 2)", 2000.
- [10] S. Missori and A. Sili, "Mechanical behavior of 6082-T6 aluminium alloy welds", Vol. 18 (1), 2000.

Content

- CONTENT..... XI**
- LIST WITH FIGURES..... XIII**
- LIST WITH TABLES XVII**
- LIST OF ABBREVIATIONS..... XIX**
- INTRODUCTION..... 1**
- 1. USED WELDING PROCESSES 2**
 - 1.1 REFILL FRICTION STIR SPOT WELDING..... 2**
 - 1.1.1 *Mechanical joining and resistance spot welding: disadvantages* 2
 - 1.1.2 *RFSSpW: advantages*..... 3
 - 1.1.3 *Process*..... 3
 - 1.1.4 *Welding tool*..... 4
 - 1.1.5 *Welding parameters*..... 6
 - 1.2 ARC WELDING..... 7**
 - 1.2.1 *Introduction*..... 7
 - 1.2.2 *MIG/MAG process: general principles*..... 7
 - 1.2.3 *Welding parameters*..... 8
 - 1.2.4 *Different modes*..... 9
 - 1.2.5 *Equipment* 9
- 2. WELD QUALITY 11**
 - 2.1 REFILL FRICTION STIR SPOT WELDING..... 11**
 - 2.1.1 *Introduction*..... 11
 - 2.1.2 *Geometrical zones and features*..... 11
 - 2.1.3 *Hardness evaluation*..... 13
 - 2.1.4 *Weld defects and features*..... 14
 - 2.1.5 *Overview of mechanical properties* 19
 - 2.2 ARC WELDING..... 22**
 - 2.2.1 *Welding errors*..... 22
- 3. ACOUSTIC EMISSION..... 25**
 - 3.1 INTRODUCTION AND OBJECTIVES..... 25**
 - 3.2 GENERAL PRINCIPLES 26**
 - 3.3 DISADVANTAGES OF AE 32**
 - 3.4 FACTORS AFFECTING AE 33**
 - 3.5 AE EQUIPMENT..... 35**
 - 3.6 AE APPLIED TO DIFFERENT WELDING APPLICATIONS: STATE-OF-THE-ART 40**
- 4 SETUP 44**
 - 4.1 REFILL FRICTION STIR SPOT WELDING..... 44**
 - 4.2 ARC WELDING..... 45**
 - 4.3 ACOUSTIC EMISSION 46**
- 5 EVALUATION METHODS OF THE TEST SERIES 49**
 - 5.1 LAP SHEAR STRENGTHS..... 49**
 - 5.2 METALLOGRAPHIC EXAMINATION 50**
 - 5.3 TEMPERATURE MEASUREMENTS 51**
 - 5.4 ACOUSTIC EMISSION EXAMINATION METHODS..... 53**

5.4.1	Wavestream data.....	53
5.4.2	Hit driven data.....	57
6	ANALYSIS OF THE ACOUSTIC EMISSION RESULTS	63
6.1	TEST SERIES R1 – RFSSPW	64
6.2	TEST SERIES R2 – RFSSPW	65
6.3	TEST SERIES R3 – RFSSPW	67
6.4	TEST SERIES R4 – RFSSPW	69
6.5	TEST SERIES R5 – RFSSPW	70
6.6	TEST SERIES R6 – RFSSPW	78
6.7	TEST SERIES R7 – R10 – RFSSPW	82
6.8	TEST SERIES R11 – RFSSPW	84
6.9	TEST SERIES R12 AND R13 – RFSSPW	88
6.10	TEST SERIES R14 – RFSSPW	89
6.11	TEST SERIES R15 – ARC WELDING	91
6.12	TEST SERIES R16 – ARC WELDING	95
6.13	TEST SERIES R17 AND R18 – RFSSPW	98
6.14	TEST SERIES R19 AND R20 – RFSSPW	102
6.15	TEST SERIES R21 – ARC WELDING	107
6.16	TEST SERIES R22 AND R23 – ARC WELDING	111
6.17	TEST SERIES R24, R25 AND R26 – ARC WELDING	114
6.18	TEST SERIES R27 – ARC WELDING	117
6.19	TEST SERIES R28 – RFSSPW	117
6.20	GENERAL CONCLUSION	119
7	FURTHER INVESTIGATION	120
7.1	RFSSPW	120
7.2	MIG/MAG ROBOT WELDING	121
8	CONCLUSION	122
	REFERENCES	123
	APPENDIX A: DATASHEET WD SENSOR.....	130
	APPENDIX B: DATASHEET R50D SENSOR	131
	APPENDIX C: DATASHEET 2/4/6 PREAMPLIFIER	132
	APPENDIX D: DATASHEET AE2A/AE5A WIDE BANDWIDTH AMPLIFIER	133

List with figures

FIGURE 1: THE FRICTION STIR SPOT WELDING PROCESS IN 4 STAGES [3].	3
FIGURE 2: CROSS SECTION OF THE WELD SURFACE OF A WELD NUGGET WITH IRREGULARITIES [9].	4
FIGURE 3: GAP LOADING BETWEEN CONCENTRIC TOOL COMPONENTS [3].	5
FIGURE 4: USED CLEANING PROGRAM.	5
FIGURE 5: THE WEAR PROBLEM WITH GAP LOADING BETWEEN THE TOOL COMPONENTS [9].	5
FIGURE 6: OVERVIEW OF THE WELDING PARAMETERS.	6
FIGURE 7: SCHEMATIC ILLUSTRATION OF GAS METAL ARC WELDING (GMAW) PROCESS [11].	7
FIGURE 8: CURRENT RANGE ACCORDING TO THE WELD WIRE DIAMETER [16].	8
FIGURE 9: BASIC EQUIPMENT FOR GMAW [17].	9
FIGURE 10: USED WELDING TOOL TO PRODUCE THE WELDS WHICH ARE INVESTIGATED IN THIS SECTION [18].	11
FIGURE 11: CROSS-SECTION OF A FRICTION SPOT WELD WITH ASSOCIATED ZONES [20].	12
FIGURE 12: GRAIN SIZE VARIATIONS ACCORDING TO THE DIFFERENT ZONES [18].	12
FIGURE 13: GEOMETRICAL ZONES ALONG WITH THEIR HARDNESS [18].	13
FIGURE 14: MAGNIFIED VIEW OF THE SZ WITH FOLLOWING WELDING CONDITIONS: RS = 1500 RPM, DT = 3s [21].	14
FIGURE 15: THE WELD DEFECTS [18].	14
FIGURE 16: HOOKING IN THE SZ (RS = 2100 RPM, DT = 2s, PD = 1.9 MM) [23].	15
FIGURE 17: POSSIBLE HOOKING CREATION DURING THE TRANSITION FROM STAGE 2 TO STAGE 3 [23].	15
FIGURE 18: HOOKING IN THE TMAZ (RS = 2100 RPMS, DT = 4s, PD = 2.3 M) [23].	16
FIGURE 19: THE DIFFERENCE BETWEEN A HIGH (A) AND LOW (B) STRENGTH WELD ACCORDING TO THEIR BBL VALUES [26].	16
FIGURE 20: INDICATION OF THE CIRCUMFERENTIAL CRACK SITES THAT MIGHT OCCUR DURING A TENSILE SHEAR STRENGTH TEST [18].	17
FIGURE 21: FRACTURE MODE IN SHEAR TENSILE TESTS: A) THROUGH WELD WITH CIRCUMFERENTIAL CRACK; B) PLUG PULL-OUT WITH NUGGET TEARING; C) PLUG PULL-OUT WITH BACK PLUG VARIATIONS ON UPPER AND LOWER (D) SHEET; E) COMPLETE FAILURE [18].	17
FIGURE 22: INDICATION OF THE PLACES WHERE INCOMPLETE REFILL AND VOIDS MIGHT OCCUR DUE TO THE SLEEVE PLUNGING PATH [18].	18
FIGURE 23: DETAILED VIEW OF THE VOIDS (LEFT) AND THE INCOMPLETE REFILL (RIGHT) APPEARING AT THE CONTOUR OF THE WELD NUGGET [18].	18
FIGURE 24: POROSITY AS WELDING DEFECT [57].	22
FIGURE 25: SLAG INCLUSIONS AS WELDING DEFECT [58].	23
FIGURE 26: BINDING FAILURES AS A WELDING DEFECT [56].	23
FIGURE 27: DIFFERENT SORTS OF CRACKS IN A WELD AS A WELDING DEFECT [56].	23
FIGURE 28: SPATTERS AS A WELDING DEFECT [61].	24
FIGURE 29: BURSTS SIGNALS (TOP) AND CONTINUOUS AE (BOTTOM). [64]	26
FIGURE 30: BURST INFORMATION IN AN AE SIGNAL [65].	27
FIGURE 31: AE CUMULATIVE COUNT AND TENSILE STRENGTH [70].	29
FIGURE 32: DFT SPLIT. [77]	31
FIGURE 33: GROUP VELOCITY (M/S) VS TEMPERATURE (°C) [85].	34
FIGURE 34: THE AE MEASURING CHAIN [68].	35
FIGURE 35: SENSOR STRUCTURE [87].	36
FIGURE 36: AE LASER TECHNIQUE [87].	37
FIGURE 37: MOST USED CONNECTOR (BNC) [88].	39
FIGURE 38: MOST USED CABLE (RG-58) [89].	39
FIGURE 39: Z-FORCE DURING FSSPW OF 5052-H32 ALUMINIUM ALLOYS AS A FUNCTION OF TIME (TOP) AND AE AMPLITUDE DURING FSSPW OF 5052-H32 ALUMINIUM ALLOYS AS A FUNCTION OF TIME [91].	41
FIGURE 40: PEAK AMPLITUDE AND RMS DISTRIBUTION FOR GOOD AND BAD WELDING JOINTS WITH DEFECTS [92].	42
FIGURE 41: KURTOSIS DISTRIBUTION FOR GOOD AND BAD WELDING JOINTS OVER ACOUSTIC EMISSION RMS [92].	42
FIGURE 42: FFT SPECTRUM FOR WELDING JOINTS WITH A DEFECT [92].	43
FIGURE 43: FFT SPECTRUM FOR A GOOD WELDING JOINT [92].	43
FIGURE 44: USED REFILL FRICTION STIR SPOT WELDING MACHINE [4].	44
FIGURE 45: WELDING TABLE WITH TWO FITTINGS.	44

FIGURE 46: USED ROBOT TO CREATE THE ARC WELDS DISCUSSED IN THIS INVESTIGATION.....	45
FIGURE 47: SETUP FOR THE ARC WELDING.	45
FIGURE 48: PLACEMENT OF THE SENSOR.....	46
FIGURE 49: PREAMPLIFIER OF MISTRAS WHICH WAS USED IN THIS INVESTIGATION [3].....	47
FIGURE 50: DIMENSIONS OF THE TENSILE TEST SAMPLES ACCORDING TO EN ISO 14273.	49
FIGURE 51: PRINCIPLE OF A TENSILE TEST [1].	49
FIGURE 52: NON-ETCHED CROSS-SECTION (TOP) AND AREA PERCENTAGE OF IMPERFECTIONS (BOTTOM) [97].....	50
FIGURE 53: METALLOGRAPHIC EVALUATION OF ARC WELDS (WELD SW-ROB-R16-1.3).....	50
FIGURE 54: SEEBECK-EFFECT USED IN A THERMOCOUPLE [99].	51
FIGURE 55: SOLDERED THERMOCOUPLES ON THE CLAMPING RING.	51
FIGURE 56: TYPICAL CURVE OF THE MEASURED TEMPERATURE (WELD NR. SW-68-R17-1.1).	52
FIGURE 57: VISUALISATION OF THE AE SIGNAL IN COMBINATION WITH THE WELDING PARAMETERS (WELD NR. SW-68-R5-1.9). ...	53
FIGURE 58: WAVESTREAM CURVE: AMPLITUDE (V) VS TIME (μ S) (ABOVE) AND FFT CURVE: AMPLITUDE (V^2_{RMS}) VS FREQUENCY (MHZ) (BELOW) (WELD NR. SW-68-R5-1.3).	54
FIGURE 59: DIVISION IN PHASES BASED ON THE WELDING PARAMETERS (TEST SERIES: SW-68-R5).	55
FIGURE 60: DIVISION OF THE WAVESTREAM.	55
FIGURE 61: WAVESTREAM OF PHASE 2 (ABOVE) AND ITS CORRESPONDING FFT (BELOW) (WELD NR. SW-68-R5- 1.3).....	56
FIGURE 62: WAVESTREAM OF PHASE 3 (ABOVE) AND ITS CORRESPONDING FFT (BELOW) (WELD NR. SW-68-R5- 1.3).....	56
FIGURE 63: WAVESTREAM OF PHASE 4 (ABOVE) AND ITS CORRESPONDING FFT (BELOW) (WELD NR. SW-68-R5- 1.3).....	56
FIGURE 64: ASL/TIME FOR A MAG WELD (NR. SW-R22-1.5).	57
FIGURE 65: ASL/TIME FOR A REFILL FRICTION STIR SPOT WELD (NR. SW-68-R28-1.4).	57
FIGURE 66: CUMULATIVE ASL/TIME FOR A MAG WELD (NR. SW-R22- 1.5).	58
FIGURE 67: CUMULATIVE ALS/TIME FOR A REFILL FRICTION STIR SPOT WELD (NR. SW-68-R28-1.4).	58
FIGURE 68: DURATION/AMPLITUDE FOR A MAG WELD (NR. SW-R22- 1.5).	58
FIGURE 69: DURATION/AMPLITUDE FOR A REFILL FRICTION STIR SPOT WELD (NR. SW-68-R28-1.4).	58
FIGURE 70: AMPLITUDE/TIME FOR A MAG WELD (NR. SW-R22-1.5).	59
FIGURE 71: AMPLITUDE/TIME FOR A REFILL FRICTION STIR SPOT WELD (NR. SW-68-R28-1.4).	59
FIGURE 72: FREQUENCY CENTROID/TIME FOR A MAG WELD (NR. SW-R22-1.5).	59
FIGURE 73: FREQUENCY CENTROID/TIME FOR A REFILL FRICTION STIR SPOT WELD (NR. SW-68-R25-1.4).	60
FIGURE 74: COUNTS/TIME FOR A MAG WELD (NR. SW-R22-1.5).....	60
FIGURE 75: COUNTS/TIME FOR A REFILL FRICTION STIR SPOT WELD (NR. SW-68-R28-1.4).	60
FIGURE 76: ABSOLUTE ENERGY/TIME FOR A MAG WELD (NR. SW-R22- 1.5).	61
FIGURE 77: ABSOLUTE ENERGY/TIME FOR A REFILL FRICTION STIR SPOT WELD (NR. SW-68-R28- 1.4).	61
FIGURE 78: RISETIME/TIME FOR A MAG WELD (NR. SW-R22-1.5).	61
FIGURE 79: RISETIME/TIME FOR A REFILL FRICTION STIR SPOT WELD (NR. SW-68-R28-1.4).....	61
FIGURE 80: ENERGY/COUNTS FOR A MAG WELD (NR. SW-R21-1.3).	62
FIGURE 81: ABSOLUTE ENERGY/RISE TIME FOR A MAG WELD (NR. SW-R21-1.3).	62
FIGURE 82: WAVEFORM AND EVOLUTION OF THE WELDING PARAMETERS OVER TIME (WELD NR. SW-68-R1-1.2).....	65
FIGURE 83: AMPLITUDE (V) VS TIME (μ S) FOR THE COMPLETE WAVEFORM (A); WAVEFORM PHASE 1 (B); WAVEFORM PHASE 2 (C); WAVEFORM PHASE 3 (D); WAVEFORM PHASE 4 (E); WAVEFORM PHASE 5 (F) (WELD NR. SW-68-R2-1.5).....	66
FIGURE 84: AMPLITUDE (V^2_{RMS}) VS FREQUENCY (MHZ) OF THE COMPLETE FFT CURVE (A); FFT CURVE PHASE 1 (B); FFT CURVE PHASE 2 (C); FFT CURVE PHASE 3 (D); FFT CURVE PHASE 4 (E); FFT CURVE PHASE 5 (F) (WELD NR. SW-68-R2-1.5).....	66
FIGURE 85: WAVEFORMS OF THE COMPLETE PROCESS IN THE TIME DOMAIN (WELD NRS. SW-68-R3-1.1 TO SW-68-R3-1.5).....	68
FIGURE 86: TEMPERATURES FOR WELD NRS. SW-68-R3-1.1 AND SW-68-R3-1.10.	68
FIGURE 87: PIN FORCE (N) VERSUS TIME (MS) FOR WELD NRS. SW-68-R3-1.1 TO SW-68-R3-1.5.	69
FIGURE 88: CURRENT REQUIRED FOR PIN ROTATION (MA) VS TIME (MS) FOR WELD NRS. SW-68-R3-1.1 TO SW-68-R3-1.5.	69
FIGURE 89: WAVEFORM COMPARISON OF WELD NRS. SW-68-R3-1.3 AND SW-68-R4-1.3.	70
FIGURE 90: CONTROL CHART OF THE LAP SHEAR STRENGTHS IN TEST SERIES R5.	72
FIGURE 91: WAVEFORM: AMPLITUDE (V) OVER TIME (μ S) (TOP) AND FFT CURVE: AMPLITUDE (V^2_{RMS}) OVER FREQUENCY (MHZ) (BOTTOM) OF WELD NR. SW-68-R5-1.3.	72
FIGURE 92: WAVEFORM: AMPLITUDE (V) OVER TIME (μ S) (TOP) AND FFT CURVE: AMPLITUDE (V^2_{RMS}) OVER FREQUENCY (MHZ) (BOTTOM) OF WELD NR. SW-68-R5-1.10.	73

FIGURE 93: WAVEFORM: AMPLITUDE (V) OVER TIME (μs) (TOP) AND FFT CURVE: AMPLITUDE (V^2_{RMS}) OVER FREQUENCY (MHZ) (BOTTOM) OF WELD NR. SW-68-R5-1.8.	73
FIGURE 94: PLUNGE TIME PHASE (PHASE 2) OF WELD NR. SW-68-R5-1.3: WAVEFORM (TOP) AND FFT CURVE (BOTTOM).....	74
FIGURE 95: PLUNGE TIME PHASE (PHASE 2) OF WELD NR. SW-68-R5-1.10: WAVEFORM (TOP) AND FFT CURVE (BOTTOM).....	74
FIGURE 96: ASL/TIME-ANALYSIS OF WELD NR. SW-68-R5-1.1 (A) AND SW-68-R5-1.2 (B).	75
FIGURE 97: DURATION/AMPLITUDE-ANALYSIS OF WELD NRS. SW-68-R5-1.1 (A), SW-68-R5-1.2 (B), SW-68-R5-1.3 (C).	75
FIGURE 98: FREQUENCY CENTROID/TIME ANALYSIS FOR WELD NRS. SW-68-R5-1.1 (263,86 °C) (A), SW-68-R5-1.2 (271,57 °C) (B), SW-68-R5-1.3 (281,81 °C) (C).	76
FIGURE 99: CUMULATIVE COUNTS/TIME-ANALYSIS FOR WELD NR. SW-68-R5-1.1 (A), SW-68-R5-1.2 (B), SW-68-R5-1.3 (C).	77
FIGURE 100: ENERGY/TIME-ANALYSIS FOR WELD NR. SW-68-R5-1.1 (A), SW-68-R5-1.3 (B), SW-68-R5-1.5 (C).	77
FIGURE 101: CONTROL CHART OF THE LAP SHEAR STRENGTHS IN TEST SERIES R6.	79
FIGURE 102: WAVEFORM: AMPLITUDE (V) OVER TIME (μs) (TOP) AND FFT CURVE: AMPLITUDE (V^2_{RMS}) OVER FREQUENCY (MHZ) (BOTTOM) OF WELD NR. SW-68-R6-1.9.	79
FIGURE 103: WAVEFORM: AMPLITUDE (V) OVER TIME (μs) (TOP) AND FFT CURVE: AMPLITUDE (V^2_{RMS}) OVER FREQUENCY (MHZ) (BOTTOM) OF WELD NR. SW-68-R6-1.5.	80
FIGURE 104: ASL/TIME-ANALYSIS OF WELD NRS. SW-68-R6-1.3 (A) AND SW-68-R6-1.6 (B).	80
FIGURE 105: DURATION/AMPLITUDE-ANALYSIS OF WELDS SW-68-R6-1.3 (A) AND SW-68-R6-1.6 (B).	81
FIGURE 106: FREQUENCY CENTROID/TIME-ANALYSIS OF WELD NRS. SW-68-R6-1.3 (A) AND SW-68-R6-1.6 (B).	81
FIGURE 107: CUMULATIVE COUNTS/TIME-ANALYSIS OF WELD NRS. SW-68-R6-1.3 (A) AND SW-68-R6-1.6 (B).	82
FIGURE 108: CUMULATIVE ABSOLUTE ENERGY/TIME-ANALYSIS OF WELD NR. SW-68-R6-1.3 (A) AND SW-68-R6-1.6 (B).	82
FIGURE 109: CONTROL CHARTS FOR SERIES R7 - R10.	84
FIGURE 110: TEST SAMPLES OF TEST SERIES R11.	85
FIGURE 111: WAVEFORM OF WELD NRS. SW-68-R11-1.3 (A), SW-68-R11-1.4 (B), SW-68-R11-1.5 (C), SW-68-R11-1.6 (D).	86
FIGURE 112: ASL/TIME-REPRESENTATION OF WELD NRS. SW-68-R11-1.3 (A), SW-68-R11-1.4 (B), SW-68-R11-1.5 (C), SW-68-R11-1.6 (D).	87
FIGURE 113: DURATION/AMPLITUDE-REPRESENTATION OF WELD NRS. SW-68-R11-1.3 (A), SW-68-R11-1.4 (B), SW-68-R11-1.5 (C).	87
FIGURE 114: RISE/TIME-REPRESENTATION OF WELD NR. SW-68-R11-1.3 (A), WELDS SW-68-R11-1.4 (B), WELDS SW-68-R11-1.5 (C), WELDS SW-68-R11-1.6 (D).	87
FIGURE 115: FREQUENCY CENTROID/TIME-REPRESENTATION OF WELD NRS. SW-68-R11-1.3 (A), SW-68-R11-1.4 (B), SW-68-R11-1.5 (C), SW-68-R11-1.6 (D).	88
FIGURE 116: WAVEFORMS OF WELD NRS. SW-68-R12-1.1 (A), SW-68-R12-1.2 (B), SW-68-R12-1.3 (C), SW-68-R12-1.4 (D).	89
FIGURE 117: RESULTS OF SERIES R14: TAPPING THE WELDING TABLE 3 TIMES (A), CLAPPING HANDS 6 TIMES (B) AND BACKGROUND NOISE (C).	90
FIGURE 118: VISUAL INSPECTION OF THE WELDS IN TEST SERIES R15.	91
FIGURE 119: WAVEFORM-ANALYSIS OF WELD NRS. SW-ROB-R15-1.1 (A) AND SW-ROB-R15-1.6 (B).	92
FIGURE 120: DURATION/TIME-ANALYSIS OF WELD NRS. SW-ROB-R15-1.1 (A) AND SW-ROB-R15-1.6 (B).	93
FIGURE 121: DURATION/AMPLITUDE-ANALYSIS OF WELD NR. SW-ROB-R15-1.2.	93
FIGURE 122: FREQUENCY CENTROID/TIME-REPRESENTATION OF WELD NRS. SW-ROB-R15-1.1 (A), SW-ROB-R15-1.2 (B) AND SW-ROB-R15-1.6 (C).	93
FIGURE 123: ASL/TIME-REPRESENTATION OF WELD NRS. SW-ROB-R15-1.1 (A), SW-ROB-R15-1.2 (B) AND SW-ROB-R15-1.6 (C).	94
FIGURE 124: CUMULATIVE ABSOLUTE ENERGY/TIME-REPRESENTATION OF WELD NRS. SW-ROB-R15-1.1 (A), SW-ROB-R15-1.2 (B) AND SW-ROB-R15-1.6 (C).	94
FIGURE 125: VISUAL INSPECTION OF THE WELDS IN TEST SERIES R16.	96
FIGURE 126: WAVEFORM EVALUATION OF WELD NRS. SW-ROB-R16-1.2 (A) AND SW-ROB-R16-1.8 (B).	96
FIGURE 127: CROSS-SECTIONS OF THE WELDS WITH SHIELDING GAS SUPPLY: SW-ROB-R16-1.1 (A), SW-ROB-R16-1.2 (B) AND SW-ROB-R16-1.3 (C).	97
FIGURE 128: CROSS-SECTIONS OF A WELD WITH SHIELDING GAS SUPPLY: SW-ROB-R16-1.4 (A) AND WITHOUT SHIELDING GAS SUPPLY: SW-ROB-R16-1.7 (B).	97
FIGURE 129: CUMULATIVE ABSOLUTE ENERGY/TIME OF THE WELDS IN SERIES R16.	98

FIGURE 130: WAVEFORM-ANALYSIS OF TEST SERIES R17.	99
FIGURE 131: ASL/TIME-REPRESENTATION OF WELD NRS. SW-68-R17-1.1 (A), SW-68-R17-1.2 (B), SW-68-R17-1.3 (C), SW-68-R17-1.4 (D).	99
FIGURE 132: DURATION/AMPLITUDE-REPRESENTATION OF WELD NRS. SW-68-R17-1.1 (A), SW-68-R17-1.2 (B), SW-68-R17-1.3 (C), SW-68-R17-1.4 (D).	100
FIGURE 133: FREQUENCY CENTROID/TIME-ANALYSIS OF WELD NR. SW-68-R17-1.1 (A), SW-68-R17-1.2 (B), SW-68-R17-1.3 (C), SW-68-R17-1.4 (D).	100
FIGURE 134: CUMULATIVE ABSOLUTE ENERGY/TIME-ANALYSIS OF WELDS SW-68-R17-1.1 (A), SW-68-R17-1.2 (B), SW-68-R17-1.3 (C), SW-68-R17-1.4 (D).	101
FIGURE 135: CUMULATIVE COUNTS/TIME-ANALYSIS OF WELDS SW-68-R17-1.1 (A), SW-68-R17-1.2 (B), SW-68-R17-1.3 (C), SW-68-R17-1.4 (D).	101
FIGURE 136: WAVEFORM-ANALYSIS OF TEST SERIES R19.	103
FIGURE 137: WAVEFORM-ANALYSIS OF TEST SERIES R20.	103
FIGURE 138: METALLOGRAPHIC RESEARCH OF WELD NRS. SW-68-R19-1.1 (A), SW-68-R19-1.2 (B), SW-68-R19-1.3 (C), SW-68-R19-1.4 (D).	104
FIGURE 139: METALLOGRAPHIC RESEARCH OF WELD NRS. SW-68-R20-1.1 (A), SW-68-R20-1.2 (B), SW-68-R20-1.3 (C), SW-68-R20-1.4 (D).	104
FIGURE 140: ASL/TIME-ANALYSIS OF WELD NRS. SW-68-R19-1.1 (A), SW-68-R19-1.2 (B), SW-68-R20-1.1 (C), SW-68-R20-1.2 (D).	105
FIGURE 141: DURATION/AMPLITUDE-ANALYSIS OF WELD NRS. SW-68-R19-1.1 (A), SW-68-R19-1.2 (B), SW-68-R20-1.1 (C), SW-68-R20-1.2 (D).	105
FIGURE 142: FREQUENCY CENTROID/TIME-ANALYSIS OF WELDS SW-68-R19-1.1 (A), SW-68-R19-1.2 (B), SW-68-R20-1.1 (C), SW-68-R20-1.2 (D).	105
FIGURE 143: CUMULATIVE ABSOLUTE ENERGY/TIME-ANALYSIS OF WELD NRS. SW-68-R19-1.1 (A), SW-68-R19-1.2 (B), SW-68-R20-1.1 (C), SW-68-R20-1.2 (D).	106
FIGURE 144: CUMULATIVE COUNTS/TIME-ANALYSIS OF WELD NR. SW-68-R19-1.1 (A), SW-68-R19-1.2 (B), SW-68-R20-1.1 (C), SW-68-R20-1.2 (D).	106
FIGURE 145: VISUAL INSPECTION OF THE ARC WELDS IN SERIES R21.	108
FIGURE 146: WAVEFORM EVALUATION OF THE WELDS IN TEST SERIES R21 (WELD NRS. SW-COB-R21-1.3 AND SW-COB-R21-1.4).	108
FIGURE 147: METALLOGRAPHIC EVALUATION OF WELD NRS SW-COB-R21-1.3 (A) AND SW-COB-R21-1.4 (B).	109
FIGURE 148: FREQUENCY CENTROID/TIME-ANALYSIS OF WELD NRS. SW-COB-R21-1.3 (A) AND SW-COB-R21-1.4 (B).	109
FIGURE 149: CUMULATIVE ASL/TIME-ANALYSIS OF WELD NRS. SW-COB-R21-1.1 (A), SW-COB-R21-1.2 (B), SW-COB-R21-1.3 (C), SW-COB-R21-1.4 (D).	110
FIGURE 150: CUMULATIVE ABSOLUTE ENERGY/TIME OF WELDS SW-COB-R21-1.3 (A) AND SW-COB-R21-1.4 (B).	110
FIGURE 151: VISUAL INSPECTION OF THE GOOD QUALITY ARC WELDS IN TEST SERIES R22.	111
FIGURE 152: VISUAL INSPECTION OF THE BAD QUALITY ARC WELDS IN TEST SERIES R23.	112
FIGURE 153: WAVEFORM EVALUATION OF WELD NRS. SW-COB-R22-1.1 (A) AND SW-COB-R22-1.2 (B), SW-COB-R23-1.1 (C) AND SW-COB-R23-1.2 (D).	112
FIGURE 154: CUMULATIVE ASL/TIME-ANALYSIS OF WELDS SW-COB-R22-1.1 (A) AND SW-COB-R23-1.1 (B).	113
FIGURE 155: FREQUENCY CENTROID/TIME-ANALYSIS OF WELD NRS. SW-COB-R22-1.1 (A) AND SW-COB-R23-1.1 (B).	113
FIGURE 156: CUMULATIVE ABSOLUTE ENERGY-ANALYSIS OF THE WELDS IN TEST SERIES R22 AND R23.	114
FIGURE 157: WAVEFORM EVALUATION OF WELD NRS. SW-ROB-R24-1.2 (A), SW-ROB-R25-R1.2 (B) AND SW-ROB-R26-1.2 (C).	116
FIGURE 158: CUMULATIVE ABSOLUTE ENERGY OF THE WELDS IN TEST SERIES R24, R25 AND R26.	116
FIGURE 159: WAVEFORM-ANALYSIS OF TEST SERIES R28.	118

List with tables

TABLE 1: MECHANICAL PROPERTIES OF AL ALLOYS WITH THE RFSSPW PROCESS.	19
TABLE 2: AE CHANNEL SETUP CONFIGURATION.	63
TABLE 3: PREAMP CONFIGURATION.	63
TABLE 4: SENSORS, FILTERS AND WAVEFORMS CONFIGURATION.	63
TABLE 5: WAVEFORM STREAMING CONFIGURATION.	64
TABLE 6: DATA SETS AND PARAMETRIC CONFIGURATION.	64
TABLE 7: WELDING PARAMETERS OF TEST SERIES R1.	64
TABLE 8: OTHER PARAMETERS OF TEST SERIES R1.	64
TABLE 9: AE CONFIGURATION OF TEST SERIES R1.	64
TABLE 10: WELDING PARAMETERS OF TEST SERIES R2.	65
TABLE 11: OTHER PARAMETERS OF TEST SERIES R2.	65
TABLE 12: AE CONFIGURATION OF SERIES R2.	65
TABLE 13: WELDING PARAMETERS OF TEST SERIES R3.	67
TABLE 14: OTHER PARAMETERS OF TEST SERIES R3.	67
TABLE 15: AE CONFIGURATION OF TEST SERIES R3.	67
TABLE 16: WELDING PARAMETERS OF TEST SERIES R4.	69
TABLE 17: OTHER PARAMETERS OF TEST SERIES R4.	69
TABLE 18: AE CONFIGURATION OF TEST SERIES R4.	69
TABLE 19: WELDING PARAMETERS OF TEST SERIES R5.	70
TABLE 20: OTHER PARAMETERS OF TEST SERIES R5.	70
TABLE 21: AE CONFIGURATION OF TEST SERIES R5.	71
TABLE 22: LAP SHEAR STRENGTH RESULTS FOR TEST SERIES R5.	71
TABLE 23: WELDING PARAMETERS OF TEST SERIES R6.	78
TABLE 24: OTHER PARAMETERS OF TEST SERIES R6.	78
TABLE 25: AE CONFIGURATION OF TEST SERIES R6.	78
TABLE 26: LAP SHEAR STRENGTH RESULTS FOR TEST SERIES R6.	78
TABLE 27: WELDING PARAMETERS OF TEST SERIES R7 – R10.	82
TABLE 28: OTHER PARAMETERS OF TEST SERIES R7 - R10.	83
TABLE 29: AE CONFIGURATION OF TEST SERIES R7 - R10.	83
TABLE 30: INDUCED WELD DEFECTS FOR TEST SERIES R7 - R10.	83
TABLE 31: LAP SHEAR STRENGTH RESULTS FOR TEST SERIES R7 - R10.	83
TABLE 32: WELDING PARAMETERS OF TEST SERIES R11.	84
TABLE 33: OTHER PARAMETERS OF TEST SERIES R11.	84
TABLE 34: AE CONFIGURATION OF TEST SERIES R11.	84
TABLE 35: SELECTED PD FOR EVERY WELD IN TEST SERIES R11.	85
TABLE 36: WELDING PARAMETERS OF TEST SERIES R12 AND R13.	88
TABLE 37: OTHER PARAMETERS OF TEST SERIES R12 AND R13.	88
TABLE 38: AE CONFIGURATION OF TEST SERIES R12 AND R13.	88
TABLE 39: WELDING PARAMETERS OF TEST SERIES R14.	89
TABLE 40: OTHER PARAMETERS OF TEST SERIES R14.	90
TABLE 41: AE CONFIGURATION OF TEST SERIES R14.	90
TABLE 42: ARC WELDING PARAMETERS OF TEST SERIES R15.	91
TABLE 43: OTHER PARAMETERS OF TEST SERIES R15.	91
TABLE 44: AE CONFIGURATION OF TEST SERIES R15.	91
TABLE 45: ARC WELDING PARAMETERS OF TEST SERIES R16.	95
TABLE 46: OTHER PARAMETERS OF TEST SERIES R16.	95
TABLE 47: AE CONFIGURATION OF TEST SERIES R16.	95
TABLE 48: WELDING PARAMETERS OF TEST SERIES R17 AND R18.	98
TABLE 49: OTHER PARAMETERS OF TEST SERIES R17 AND R18.	98
TABLE 50: AE CONFIGURATION OF TEST SERIES R17 AND R18.	98

TABLE 51: WELDING PARAMETERS OF TEST SERIES R19 AND R20.	102
TABLE 52: OTHER PARAMETERS OF TEST SERIES R19 AND R20.	102
TABLE 53: AE CONFIGURATION OF TEST SERIES R19 AND R20.	102
TABLE 54: ARC WELDING PARAMETERS OF TEST SERIES R21.	107
TABLE 55: OTHER PARAMETERS OF TEST SERIES R21.	107
TABLE 56: AE CONFIGURATION OF TEST SERIES R21.	107
TABLE 57: ARC WELDING PARAMETERS OF TEST SERIES R22 AND R23.	111
TABLE 58: OTHER PARAMETERS OF TEST SERIES R22 AND R23.	111
TABLE 59: AE CONFIGURATION OF TEST SERIES R22 AND R23.	111
TABLE 60: ARC WELDING PARAMETERS OF TEST SERIES R24, R25 AND R26.	114
TABLE 61: OTHER PARAMETERS OF TEST SERIES R24, R25 AND R26.	114
TABLE 62: AE CONFIGURATION OF TEST SERIES R24, R25 AND R26.	115
TABLE 63: WELDING PARAMETERS OF TEST SERIES R28.	117
TABLE 64: OTHER PARAMETERS OF TEST SERIES R28.	117
TABLE 65: AE CONFIGURATION OF TEST SERIES R28.	117
TABLE 66: RECAP OF ALL RELEVANT CONFIGURATIONS AND DATA OUTPUTS ACCORDING TO EACH WELDING PROCESS.	119

List of abbreviations

A	Ampere
AC	Alternating current
AE	Acoustic emission
Al	Aluminium
AM	Additive material
ASL	Average signal level
ASL	Average signal level
cm	Centimeter
DC	Direct current
DFT	Discrete fourier transformation
DT	Dwell time
EMI	Electromagnetic interference
FFT	Fast fourier transformation
FSSW, FSSpW	Friction stir spot welding
FSW	Friction stir welding
GMAW	Gas metal arc welding
HAZ	Heat affected zone
HT	Hold time
JT	Joining time
LBU	Laser based ultrasonic
MAG	Metal active gas
MARSE	Measured area under the rectified signal envelope
Mg	Magnese
MIG	Metal inert gas
MSPS	Mega samples per second
PD	Plunge depth
PT	Plunge time
RDC	Ring down counting
RFSSpW	Refill friction stir spot welding
RMS	Root mean square
RS	Rotational speed
RSW	Resistance spot welding
RT	Retraction time
SFFT	Short-time fast fourier transformation
Si	Silicon
SNR	Signal to noise ratio
SZ	Stir zone
TIG	Tungsten inert gas
TMAZ	Thermo-mechanically affected zone
UTS	Ultimate tensile strength
V	Voltage
WN	Weld nugget
WT	Wavelet transform

Introduction

In this work, the quality of a weld is investigated by making use of acoustic emission (AE) during a welding process. The AE investigation is a non-destructive method that records the sounds produced by the material itself. This method is not to be confused with ultrasonic (US) examinations. In ultrasonic research, sound waves are sent through a material while in acoustic emission research, the audible sounds released by the material due to a high load are recorded. The advantage of AE is that the data is real-time and thereby dynamic phenomena can be detected because the welding process causes the material to send the AE-signals [2].

The AE research will be executed on two different welding types: refill friction stir spot welding (RFSSpW), and arc welding with a robot. These processes are discussed in Chapter 1. The RFSSpW process will be dealt with for the most part.

The intention of the AE research is to determine the weld quality based on the AE signals. The weld quality is determined by the presence of certain defects, which will be further discussed in Chapter 2.

Chapter 3 contains more information about the acoustic emission process. The general principles, advantages and disadvantages, influencing factors and equipment are being discussed.

In Chapter 6, the acoustic emission results from different test series are analysed. The test series were made with a setup, described in Chapter 4. Furthermore, the results were analysed based on different evaluation methods such as the lap shear strengths of the welds and metallographic research. More about these examination methods is discussed in Chapter 5.

Chapter 7 describes the occurred problems which were encountered while investigating. It shortly discusses what could be investigated in future work, based on the results in this master dissertation.

Lastly, conclusions about the conducted investigation are drawn in Chapter 8.

1. Used welding processes

1.1 Refill friction stir spot welding

Refill friction stir spot welding (RFSSpW) is a solid-state welding technique derived from friction stir welding (FSW) and is suitable for joining aluminium and magnesium alloys. The technique is used for joining strong and lightweight parts in aerospace, automotive, shipbuilding and train applications by the need for fuels saving, safety and performance increasement. The process can replace mechanical joining or resistance spot welding (RSW), which are used today and discussed in the following paragraphs of this chapter. The friction stir spot welding process will lead to various benefits, such as the ability to weld light-weight materials and the appearance of relatively low temperatures [1] [3].

Nowadays, a lot of steel is used in the automotive industry because of its wide range of desirable properties, ease of processing, availability and recyclability. It would be a big step forward to replace steel by aluminium, as it has the advantages of a lower density than steel and a much higher corrosion resistance [4]. The problem of replacing aluminium is the need and development of new joining methods for these materials and the optimal application of the methods.

In this chapter, the RFSSpW process and its parameters will be described in detail.

1.1.1 Mechanical joining and resistance spot welding: disadvantages

Using mechanical fastening to join lightweight materials has a weight penalty by the additionally used material. Another disadvantage of mechanical fastening is the requirement for sealants and the potential corrosion problems. The difficulty of automation will cause economical disadvantages. Using fusion-based techniques for joining aluminium, such as resistance spot welding, will cause problems associated to material melting and low weldability for some alloys [5].

Aluminium components are usually welded by manual arc welding techniques, like MIG or TIG. However, aluminium shows a comparatively lower weldability than steel due to various reasons: a high affinity of aluminium towards atmospheric gases, a high thermal expansion coefficient, a high thermal and electrical conductivity, etc.. These characteristics make them sensitive to defect formation during welding (e.g. porosities, inclusions, solidification cracking, described in chapter 3). Besides this, some of the higher-strength aluminium alloys, like material from the 2000 or 7000 series, are not weldable at all using conventional welding technologies.

The disadvantages of manual welding techniques are that they are generally recognised as labour-intensive and thus costly operations. It requires relatively high-skilled welders and the joint quality is highly dependent on the skills of the welder. Moreover, components are likely to show an unacceptable amount of distortion which requires a significant amount of post-weld finishing operations and rework.

Resistance spot welding is one of the most commonly employed automated joining method for steel sheets. Its principle benefits are high speed and low cost operation, plus the ability to weld a wide range of joint configurations with the same gun.

However, there are still plenty of problems when spot welding aluminium alloys. The main barrier to the adoption of resistance spot welding for aluminium is the short life of the welding electrodes and the associated reduction of weld quality when the electrodes degrade. Frequent milling, dressing and changing of the electrodes interrupts production and increases the operating costs.

The relatively higher electrical conductivity of aluminium requires a significantly higher energy to obtain a weld. Critical porosities and other imperfections occur nearly unpredictable within the welding zone. Welding spatter pollutes both the welds and the welding cells, necessitating costly post-weld machining and clean-up work [6].

1.1.2 RFSSpW: advantages

Considering these problems, the importance of developing the RFSSpW technique becomes clear. RFSSpW has the following advantages compared to conventional resistance spot welding and the processes mentioned above [7]:

- Mechanised and repeatable process
- Ability to weld the 'non-weldable' aluminium alloys such as materials from the 2000 and 7000 series
- Excellent mechanical weld properties
- Low distortion and shrinkage, due to solid-state nature of the welding process
- Welding in any position
- High efficiency process with very low energy consumption
- No shielding gas required,
- Operator health & safety benefits: no welding fumes, metal spatter, UV radiation or loud sounds
- A RFSSpW joint can be repaired by the same process or just be welded twice (important for the quality assurance).

Summarising, this new spot welding technique provides interesting opportunities for solving the current problems of conventional joining processes (e.g. resistance spot welding).

In order to fully develop this technique, a non-destructive testing method is required. In this master dissertation the goal is to find a way to decide with certainty that a friction spot weld has a good quality and can be used in production.

1.1.3 Process

The RFSSpW process will produce a single spot while the material remains solid. The metallurgical bond is realized by the heat created due to friction and by plastic work. The joint will be realised between two overlapping aluminium plates. The whole process is executed by a tool with three main components, which can be seen in Figure 1. The clamping ring will clamp the two overlapping aluminium plates by applying pressure in the axial direction. The pin and the sleeve rotate to create frictional heat and to push the softened material into the plates to form a metallurgical bond. The whole process consists of 4 stages, which can be seen in Figure 1 [8][1][3].

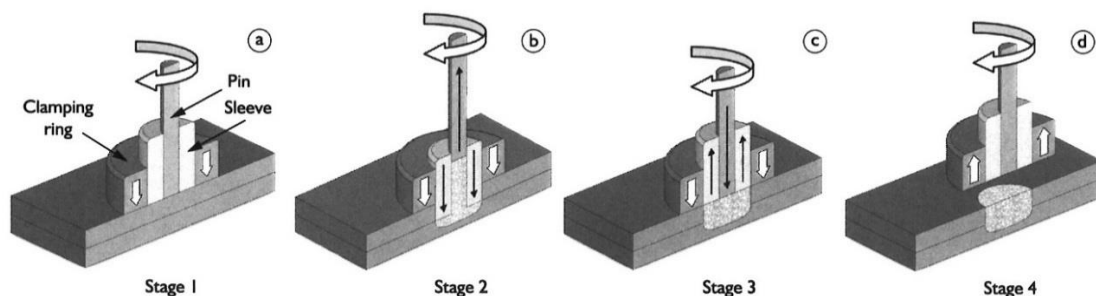


Figure 1: The friction stir spot welding process in 4 stages [3].

At the second stage, the sleeve is lowered and pushed into the sheets at the predefined rotation speed. At the same time, the pin is retracted to create a cavity. The material underneath the sleeve is plasticised and pushed into the created cavity. The movement of the sleeve and pin continues until the sleeve reaches the set plunge depth. This action is called 'plunging'.

During the third stage, the pin and sleeve return to their initial position forcing the displaced material to completely refill the keyhole (Figure 1c). Finally, at the fourth stage, the tool rotation is stopped and the tool is withdrawn from the joint leaving a flat surface with minimum material loss (Figure 1d) [1][3].

In these four stages there are some important process parameters which are the rotational speed (RS), the axial load, the plunge depth (PD), the welding time (WT) as well as the pin and sleeve position. These parameters will be discussed in detail in a further section.

1.1.4 Welding tool

As the welding tool, or welding head, is the most important component of the friction spot welding machine it will be further described in this section. As was already clear, it consists of three components: the clamping ring, the sleeve and the pin. During the welding process, the pin and sleeve are in close contact with the workpiece material. They experience high axial forces, torques and thermal cycles which means that they are subjected to wear [3]. The result of this wear might be irregularities on the surface of the welding nugget. Examples of these irregularities are illustrated in Figure 2.

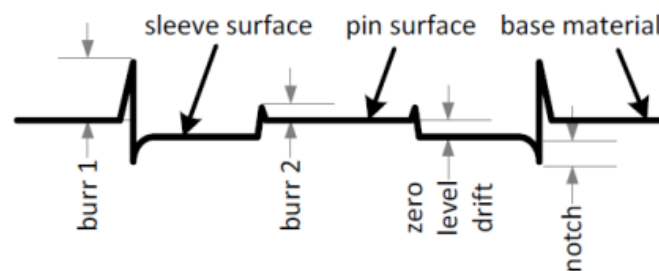


Figure 2: Cross section of the weld surface of a weld nugget with irregularities [9].

Firstly, the zero-level drift between the pin surface and the sleeve surface is a result of the fact that the bottom surfaces are not in plane when idle. It is suggested that also the adhesion forces between the tool and the workpiece have an influence on this zero-level drift.

Secondly, the notch at the sleeve-clamping ring interface is a result of a reduced inner sleeve length due to the wear. There can be concluded that the bottom of the sleeve is worn out at the internal diameter of the sleeve component.

As a third irregularity, the appearance of the burrs are dependent of the tolerance between the pin and sleeve and between the sleeve and clamping ring as they are concentric within narrow tolerances. It is possible that the material remains in these small ring-shaped gaps. During welding, these gaps are continuously filled with plasticized base material of the workpiece which requires a higher torque in order to rotate the tool component at the required RS [9]. At stage three, when the sleeve goes up and the pin pushes the material back into the keyhole, it might be possible that little material still is present in the tolerance gaps, resulting in two ring-shaped burrs. Burrs 1 and 2 are visible in Figure 2, and have equal diameters as respectively the pin and sleeve. In literature, the continuously filled gap is referred to as the gap loading. Figure 3 illustrates this phenomenon with exaggerated gap dimensions for illustrative purposes [3].

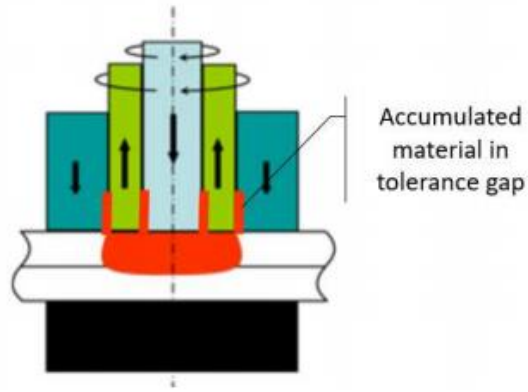


Figure 3: Gap loading between concentric tool components [3].

Due to the appearance of the base material in these tolerance gaps, it is necessary to frequently clean the tool in order to avoid too high overload currents and temperatures, motor shutdowns and sleeve failure [10]. In the test series described in this master dissertation, the tool was cleaned every two welds. Program 197 was used, a visualisation of the pin and sleeve movement along with the RS is visible in Figure 4.

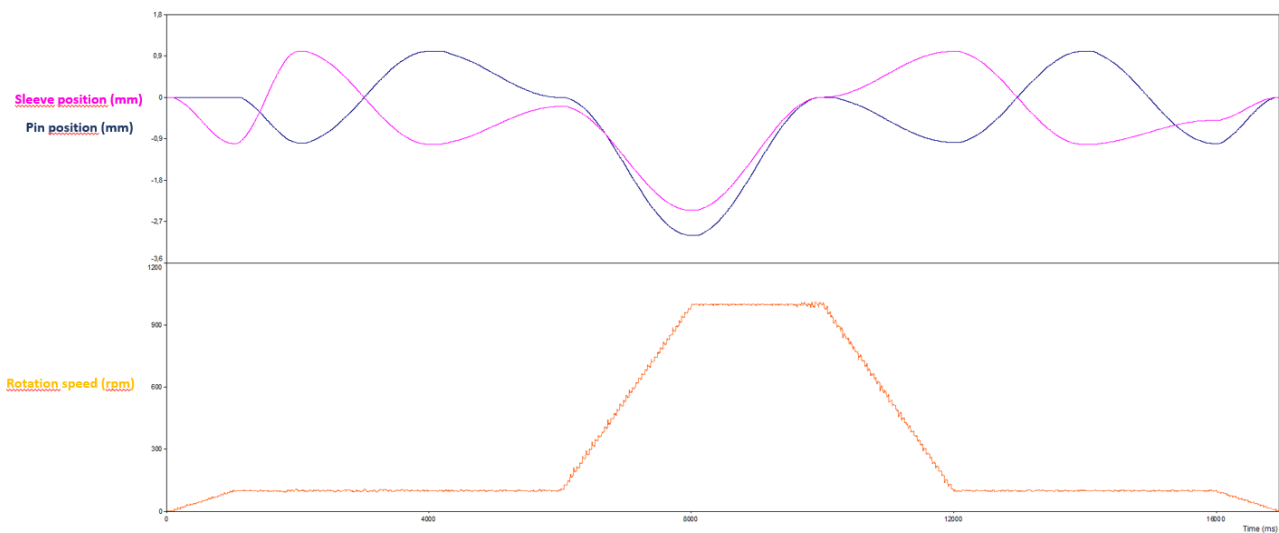


Figure 4: Used cleaning program.

To summarize the temperature, torque and gap loading are all factors who have their influence on the tool wear. This cycle of increasing tool wear is illustrated in Figure 5.



Figure 5: The wear problem with gap loading between the tool components [9].

One positive aspect related to tool wear is that no dependency with lap shear strengths can be found [9]. The increased tool wear along with the increased temperature might even improve the metallurgical bonding between the aluminium sheets. This independency is a major advantage for industrial applications [3].

1.1.5 Welding parameters

The FSSW process has a lot of adjustable parameters. In this paragraph, the most important ones will be explained.

At the first stage, the clamping force of the clamping ring can be chosen. This force has to be high enough to clamp the plates, during the weld cycle. It has to be prevented that the force is too high, because this can causes damage of the plates. At the beginning of phase 1, the rotation speed is equal to 500 rpm. After initiation of the weld cycle, the rotation speed of the pin and sleeve is increased to maximum rotational speed (RS) which is used during the second and third stage [1][3][8].

At the second stage, the pin and sleeve are rotating using the set rotational speed. The sleeve is lowered until it reached the predefined PD. The time of lowering the sleeve into the material is called the plunge time (PT) and is also adjustable. The plunge time influences the rate of plastic deformation [1][3]. The plunge rate (PR) is the speed of lowering the sleeve and is related to both the PD and PT.

At the third stage, the pin and sleeve are still rotating at the set rotational speed. The duration of this stage is called the dwell time (DT), and is also a parameter that can be adjusted. The time of retraction of the tool is called the retraction time (RT), which also has an influence on the rate of plastic deformation. The retraction rate (RR) is the speed of lifting the sleeve back up to its original position and is related to both the PD and RT.

The three different time parameters (PT, DT, RT) determine the total joining time (JT), which has an influence on the total heat input [1][3]. An overview of all these parameters is given in Figure 6.

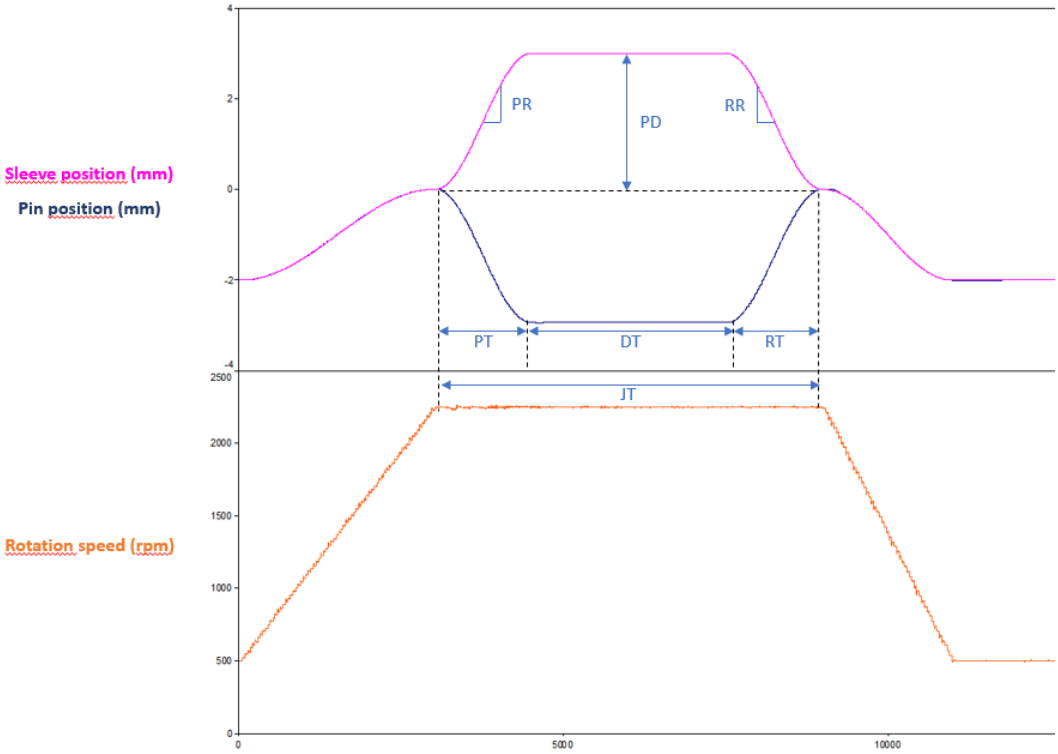


Figure 6: Overview of the welding parameters.

1.2 Arc welding

1.2.1 Introduction

The arc welding process is used to join two metals by heat, which is created by electricity between two electrodes, in order to melt the metals along with the welding wire. The welding wire then forms a bonding together with the molten metals when the material is cooled down. The name of the process comes from the fact that an electric arc (due to the current) is created between the metal to be welded and the welding wire. The current is powered by a welding power supply. This all is presented in Figure 7.

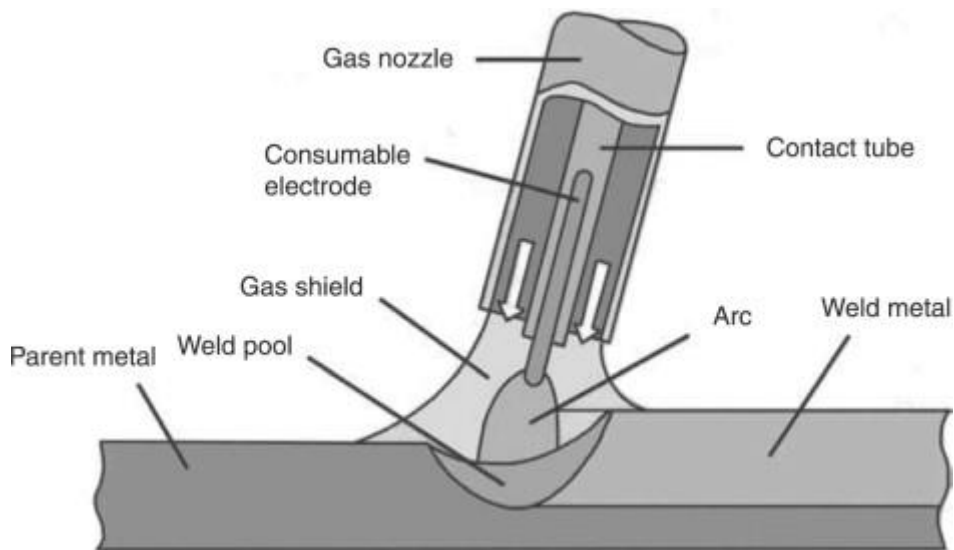


Figure 7: Schematic illustration of gas metal arc welding (GMAW) process [11].

This process can be executed manually, semi-automated or fully automated. Nowadays, it still is one of the most important processes to create assembled structures [12]. As there are many different types of arc welding, this work only focuses on the metal inert gas and metal active gas (MIG/MAG) type, because this was used to create the welds who are described in further test series.

1.2.2 MIG/MAG process: general principles

MIG/MAG processes are subtypes of the gas metal arc welding (GMAW) process. This technique was developed in the 1940s, in order to achieve a shorter welding time. However, shorter welding times lead to an extra cost of inert gas. Later on, this was solved by using semi-inert gasses which reduced the cost. Nowadays the GMAW process is mostly used in the industry [13].

The MIG/MAG processes make use of a shielding gas, which is released through the welding gun between the electrodes, in order to avoid contamination due to air. At the start of the process, when the current has to flow from the first electrode to the other, an electric arc is created. The gas that is present between these electrodes excites more easily than the air that was originally, making it easier for the arc to be formed and maintained during the welding process. As the welding process progresses, the welding zone is constantly fed with the welding material [14].

The process that was used in this work is a semi-automatic welding process one with a robotic arm, where different welding parameters could be set and adjusted. The parameters will be discussed in a following section. The power supply that was used provided a constant DC voltage, and the shielding gas is composed out of 18 % CO₂ and 82 % Ar.

1.2.3 Welding parameters

The set of welding parameters are very important as they will directly affect the quality of the weld, the penetration of the arc and the bead geometry. In this paragraph, the different parameters are discussed. They are not completely independent and should be determined after the workpiece material is chosen.

First of all, there is the current expressed in Ampère. The value of this current is determined by the thickness of the workpiece material. A guideline says that every 0,001 inch (or 0,00254 cm) requires 1 A [15]. The current is directly related to the deposition rate, the weld bead size and shape, and the penetration. Some parameters are related; for example, the current is interdependent with the wire speed. They both have to be increased in order to increase the deposition rate and the wire melt-off.

The thickness and size of the feeding wire is also a factor that depends on the value of the current. There are different diameters that require a minimum and maximum current range. An example is given in Figure 8.

Typical Welding Parameters of Mild Steel & Low Alloy SMAW (Electrodes)				
Diameter of Rod		Voltage (V)	Amperage (A)	
Inches	Millimeters		Flat	Vertical & Overhead
3/32	2.4	21 – 25	65 – 80	65 – 75
1/8	3.2	21 – 25	90 – 110	80 – 95
5/32	4.0	21 – 26	135 – 160	120 – 140
3/16	4.8	22 – 26	160 – 210	140 – 160

Figure 8: Current range according to the weld wire diameter [16].

Along with the standard solid welding wires, there is also a different kind, namely the tubular welding wires. They have an internal core filled with granular powder or flux. This powder, or flux, provides a better arc stability and a deeper penetration. There is also less risk for defects when this type of wire is used [14].

Secondly, there is the welding voltage which is directly related to the arc length. This parameter is very important because the arc length has to be under control. A too long arc length disturbs the gas shielding, whereas a too short arc length may extinguish at the expense of the weld quality. When increasing the voltage, the bead will become flatter and the penetration will increase until an optimum value is reached. Too high voltages will cause spatters, porosity appearances and cracks. Too low voltages also may cause porosities [15].

The travel speed of the arc is controlled by the robot and is therefore continuous. The effects are similar to the voltage effects. An optimum of penetration at a certain value of travel speed will be obtained. Too slow travel speeds cause poor fusion, lower penetration, porosity, slag inclusions and an uneven bead [15]. On the other hand, faster travel speeds lead to less penetration and spatters. The travel speed is selected based on the workpiece material.

Furthermore, the size of the electrode will affect the weld bead and penetration. It also has an effect on the travel speed, as a larger electrode generally requires a higher minimum current for the same characteristics [15].

The type of shielding gas depends on the steel material and its conditions, and has to be chosen carefully. Two main types of gases exist: inert gas and active gas. Examples of inert gases are argon,

helium and argon-helium mixtures, while active gases include carbon dioxide, argon/oxygen or argon/carbon dioxide mixtures [14].

The electrode extension or stick-out is defined by the length of the filler wire between the end of the contact tip and the end of the electrode [15]. It is the part of the wire that conducts the current. When the extension is too long, the resistance of the wire will increase and therefore the temperature of the electrode will rise [15]. It seems very logical that this parameter has to be carefully monitored in order to achieve a good arc length.

At last, there is the position of the wire electrode relative to the weld which affects the bead shape and penetration. The position of the wire electrodes depends on two parameters, namely two angles which are called the 'work' and 'travel' angles [15].

1.2.4 Different modes

In order to transfer the weld metal from the electrode to the work, there are four possible modes:

1. Short circuiting transfer
2. Globular transfer
3. Spray transfer
4. Pulsed spray transfer

The modes are determined by the welding current, electrode size, electrode composition, electrode stick-out and the shielding gas [15]. As these welding types were not used to create the welds cited in this work, they will not be further discussed.

1.2.5 Equipment

The basic equipment for the GMAW process is indicated with numbers in Figure 9. The numbers will be further explained in following text. The welds that were created for the AE research were produced with a robot which also contains these parts.

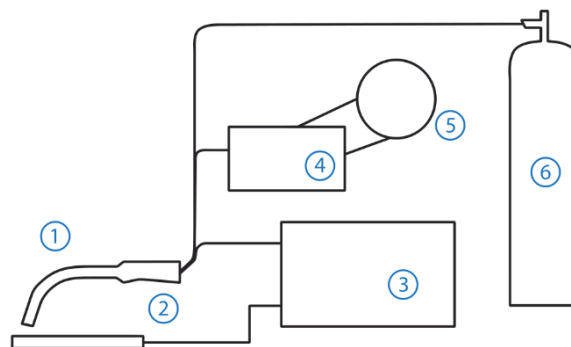


Figure 9: Basic equipment for GMAW [17].

Number 1 is called a welding gun with a wire feed unit. The gun has a contact tip made out of copper in order to transmit the electricity from one electrode to the other. At the end of the gun, it is connected to two cables. One cable provides the power supply to create a current and the other one supplies the gas. A gas nozzle in the front takes care of the gas flow, whereas an electrode at the end makes sure that an arc is formed. As an option, a water cooling system could be fitted into the gun, but normally the gun is air-cooled [13]. However, when an air-cooled gun is used, the current is limited to a value of 300 A. In order to reach higher current values, the gun has to be water-cooled [14]. Furthermore, there is a wire feed system to supply a metallic alloy wire as an electrode. The kind of

alloy and the selected size are dependent on the steel material and its condition. The weld quality is directly related to the choice of the electrode, which needs to be carefully determined [13].

Number 2 represents the welded workpiece. It is notable that this workpiece has to be connected to the power supply (number 3) with a clamp, in order to obtain a circuit in which the current can flow.

Number 3 is the power supply who provides a constant voltage. Mostly a direct current (DC) is used in welding applications, because it provides the maximum heat input and penetration into the workpiece [14]. Another benefit of the use of a DC power source is the high stability. The arc will naturally stabilize if it is powered at a constant voltage and generated in a wire which is fed at a constant rate [14]. Another kind of power source uses pulsed current, which are not regulated by the amount of voltage, but by the train of pulses of the current. Since this type is not used to create the welds in this work, it is not further discussed.

Number 4 and 5 show the wire feed unit and the motor respectively. In the wire feeder, the wire is pushed into the welding gun with this motor. By regulating the motor, the wire feed rate value can be adjusted [14].

Number 6 indicates the shielding gas supply cylinder. It is a tank which stores the shielding gas, used in the welding process. The gas protects the weld against atmospheric gasses which can lead to metal defects.

2. Weld quality

2.1 Refill friction stir spot welding

2.1.1 Introduction

In this part of the chapter, the mechanical and microstructural properties of a refill friction stir spot weld will be discussed based on metallographic investigation. It will be demonstrated that some geometrical zones and features occur in the welding nugget. Along with these phenomena's, the hardness of the different zones in the weld will be investigated as well.

This will be illustrated using the results of the welding trials with a the aluminium alloy AA6181-T4, with a thickness of 1,7 mm [18]. Different parameters were investigated in order to produce high quality welds, in terms of microstructure and mechanical performance. The metallographic investigation was performed with optical microscopy, while the mechanical properties were evaluated using tensile testing. The lap shear tensile strength was on average equal to 6,8 kN. The geometric zones and features played an important role for the fracture mechanism and therefore the mechanical performance [18].

The toolset that was used consisted of three components: a 18 mm diameter clamping ring, a 9 mm diameter threaded sleeve and a 5,2 mm diameter grooved pin. More details are shown in Figure 10.

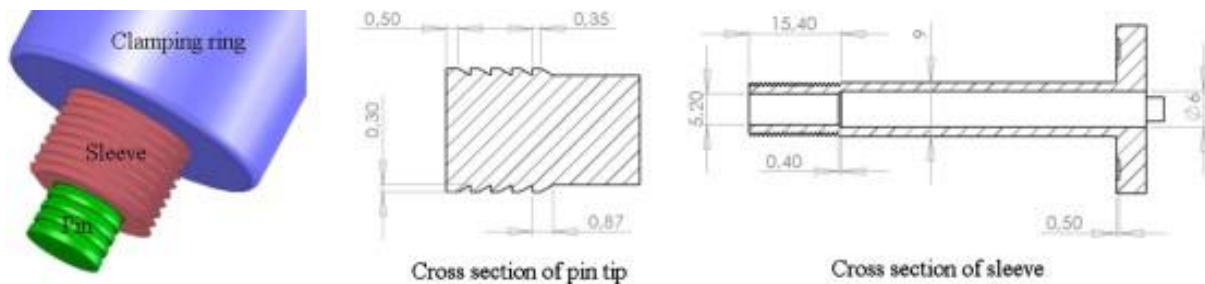


Figure 10: Used welding tool to produce the welds which are investigated in this section [18].

2.1.2 Geometrical zones and features

The friction stir spot welds are obtained by frictional heat that is released when the welding tool is rotating in the material. The material becomes plastic due to this heat, which causes a local microstructural change of the aluminium alloy. The heat generation depends on the tool rotation speed (RS) and plunge depth (PD). In general, a higher RS and PD results in more heat generation which contributes to more recrystallization and larger grains [19]. The cooling rate that occur after welding is directly influencing the grain size and thereby also to the hardness. In general, hardness is the resistance to local plastic deformation of a material and is higher when the cooling rate is higher (quenching) and when the grain size is smaller. The weld hardness will be further discussed in the next section.

Figure 11 shows a cross section of a friction stir spot weld. Four different zones can be distinguished who typically appear in every weld: the stir zone (SZ), the thermo-mechanically affected zone (TMAZ), the heat affected zone (HAZ) and the base material (BM).

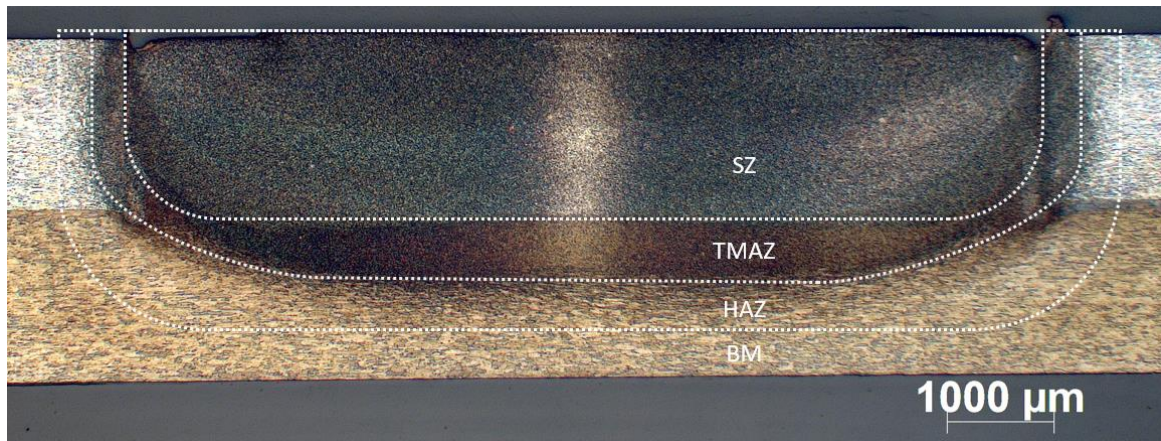


Figure 11: Cross-section of a friction spot weld with associated zones [20].

The SZ contains the material that effectively has been mixed by the pin and sleeve and is characterised by finer grains due to dynamic recrystallization caused by the high strain rate during the plunging stage and the thermal cycle imposed by the process [18]. These grains are visible in more detailed in Figure 12, left. It is clear that the grain size increases further away from the SZ.

The TMAZ is characterized by the larger recrystallized distorted grains in comparison to the SZ. The combination of a moderate strain rate and a moderate temperature are responsible for the microstructural changes in this zone. When zooming in on the TMAZ, elongated grains pointing upwards are revealed near the SZ. The TMAZ is visible in Figure 12, between the SZ and the HAZ [18].

The material in the HAZ only experiences the thermal weld cycle, inducing more coarse grains compared to the BM [21]. Due to the heat, the grains start to grow and get bigger. In this case, the grain size of the material in the HAZ has a value of 22 μm, while the grain size of the BM is only 17 μm [21].

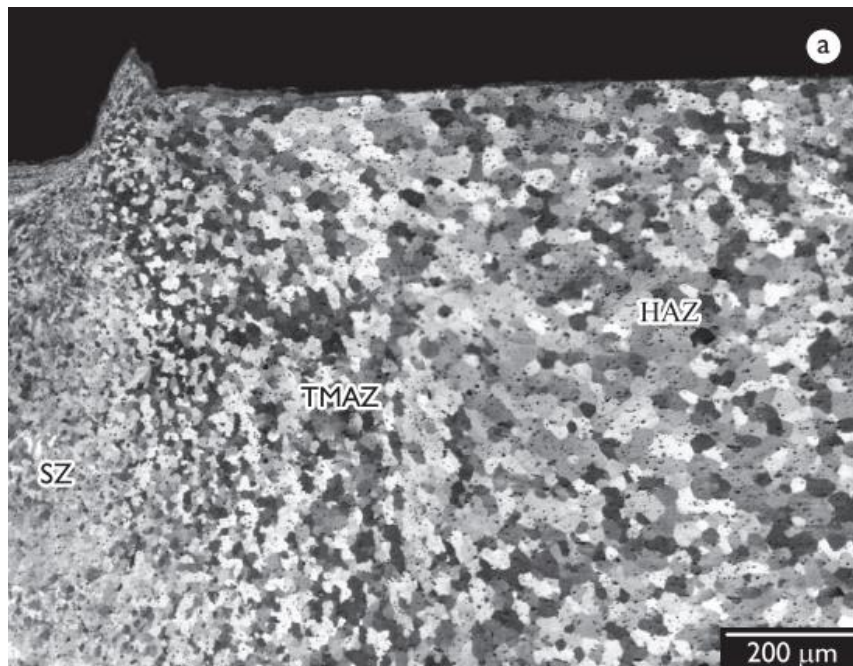


Figure 12: Grain size variations according to the different zones [18].

2.1.3 Hardness evaluation

Figure 13 shows a cross section of a weld, welded with a RS of 2900 rpm and a dwell time (DT) of 3 seconds. The hardness is also given and was measured through the different zones in the middle of the upper aluminium sheet. The hardness changes in the different microstructural zones and is dependent on associated grain size.

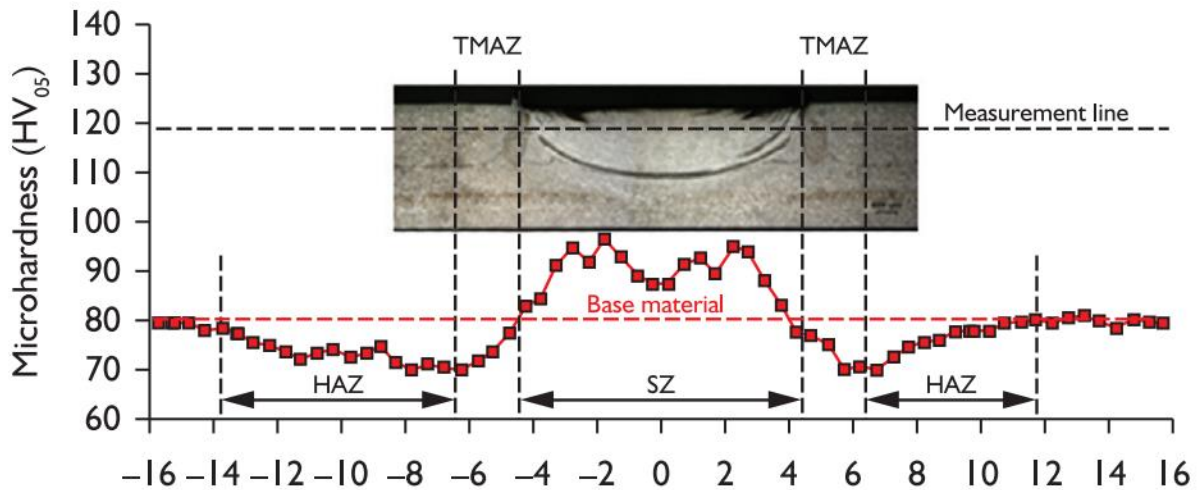


Figure 13: Geometrical zones along with their hardness [18].

As visible in Figure 13, the base material has an average hardness of 80 HV. This value can vary depending on the temper treatment of the base material (indicated by the T-factor in the specified material). In this case, the used material was AA6181-T4. T4 indicates that the material is solution heat treated, and naturally aged to a substantially stable condition.

The hardness starts to decrease in the HAZ to a minimum value of 70 HV in the transition to the TMAZ. The hardness loss at the transition is mainly associated to the microstructural changes of the BM. Although the temperature in the HAZ is relatively low, it is high enough for grain nucleation and grain grow. A bigger grain size results in a reduction of the hardness.

Next to the HAZ, the TMAZ is located, where the hardness starts to rise again, because of the coarsening of the material. This phenomenon has shown to be predominant for the hardness increase, due to the thermal cycle in this zone. The deformation level might also have a little influence on the strain hardening, although not enough to suppress the softening coming from the precipitate coarsening.

In the SZ, the hardness continues to increase to a maximum value of approximately 100 HV. The increase in the SZ is due to recrystallization of a very fine grain structure [22]. During RFSSpW, the process can eliminate some or all of the cold work effects. Also coarsening and even solubilisation might occur on the strengthening particles [18].

A dip in the hardness in the middle of the weld nugget is visible. This phenomenon appears due to small variations of the grain size in the width and thickness direction in the SZ. Visually, this can be seen in Figure 14. In general, the grains at the outer side (regions C, D and E in Figure 14) are much finer than those in the centre, because they are located on the path of the plunging pin into the upper sheet. It can be attributed to the high-strain rate in the periphery of the pin due to the plunge speed (a high linear velocity). Another factor that might also be the cause of this dip is that the material located at the top surface of the upper sheet (region E in Figure 14, right beneath the pin) is stirred for

a slightly longer time than the material at the bottom of the upper sheet. This means that the original material at the top surface has a smaller grain size in the SZ [21].

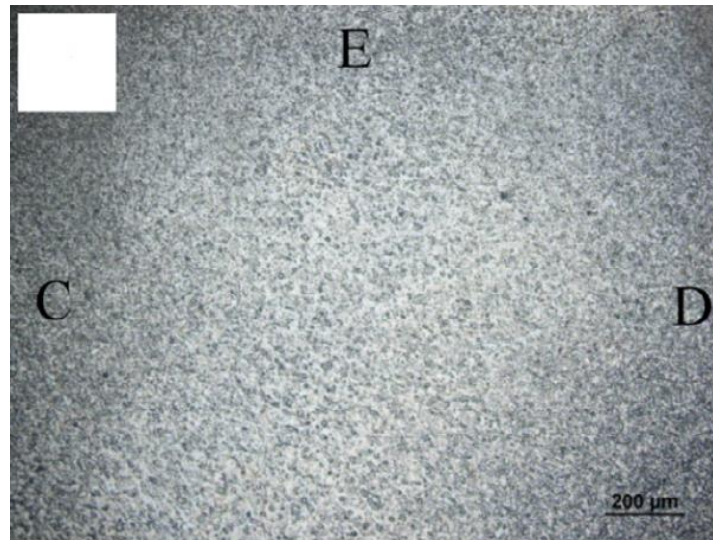


Figure 14: Magnified view of the SZ with following welding conditions: RS = 1500 rpm, DT = 3s [21].

2.1.4 Weld defects and features

Defects that occur in the welding nugget are best avoided since they can cause a low lap shear strength or low-quality welds. These defects are the result of non-optimised process parameters. Figure 15 gives an overview of the different weld defects that might occur.

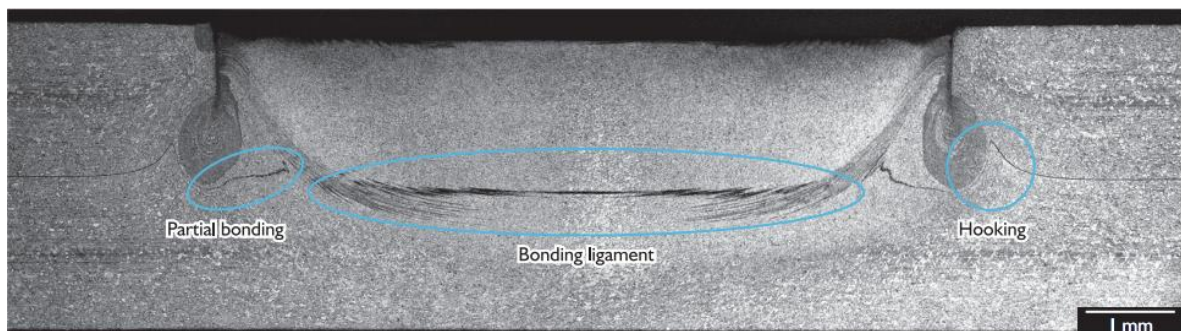


Figure 15: The weld defects [18].

As shown in Figure 15, the appearance of the black lines indicate some geometrical features in the weld: partial bonding, the bonding ligament and hooking. At the sides, two vertical lines are also visible; this indicates the sleeve path. Sometimes voids can appear at that location due to lack of mixing, but also due to an incomplete refill. In the following sections, each type of defect is being discussed and illustrated by means of an Olympus MPG3 light optical microscope [18].

Hooking

As can be seen in Figure 15, hooking is the interlocking of the upper and lower sheet. It is defined as a partially metallurgical bonding area, a transition zone between the completely bonded areas and the non-bonded ones [23]. It is formed as a result of the upward bending of the local sheet interface due to the tool penetration into the bottom sheet [24]. When lap shear tests are performed, the presence of hooking results in stress concentrations. Because of this, hooking works as a crack nucleation site, similar as partial bonding (explained in a next section). The sharpness of the hooks are related to the crack nucleation. When the hook is too sharp, it causes a crack that easily nucleates and grows in the

upper sheet, even under small loads. Micrographic analysis indicated that the duration of the dwell time is directly related to the sharpness of the hooks. In general, a longer dwell time means a greater sharpness due to the high level of plasticity of the lower sheet caused by the intense energy input provided by longer welding times. This assessment explains in some cases the deterioration of the mechanical strength when the welding time is increased [18]. However, this does not mean that an increase of the dwell time results in a decrease of the lap shear strength, as other parameters also have influences. When the hooking phenomenon is absent in the weld, an increase of the dwell time might be the cause of a better bond and thus an increase of the lap shear strength.

Cao et al [23]. indicated that there are two different types of hooking, related to the plunge depth. The hook imperfections and their locations are different. The two hooking types are visible in Figure 16 and Figure 18.

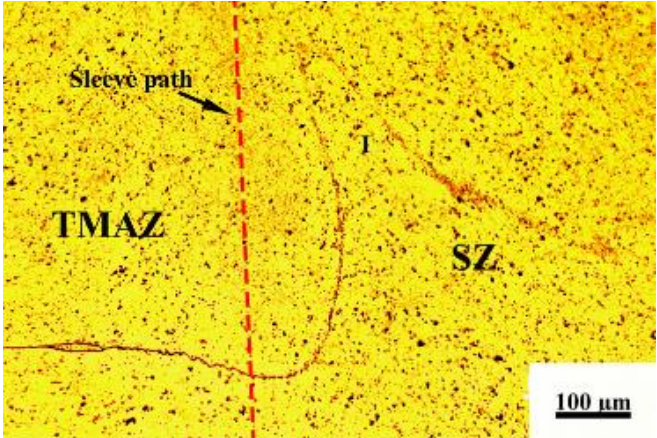


Figure 16: Hooking in the SZ (RS = 2100 rpm, DT = 2s, PD = 1.9 mm) [23].

The first type of hooking is located in the SZ of the weld. The plunge depth that was used was smaller than the thickness of the upper sheet (1,9 mm and 2 mm respectively) which caused only stirring in the upper sheet and no penetration in the bottom sheet. While the formation mechanism of its geometry is still unclear, many believe that it is a consequence of the pin pushing the extruded material back into the created keyhole in the third stage of the welding process [3]. This theory seems logical when looking at Figure 17.

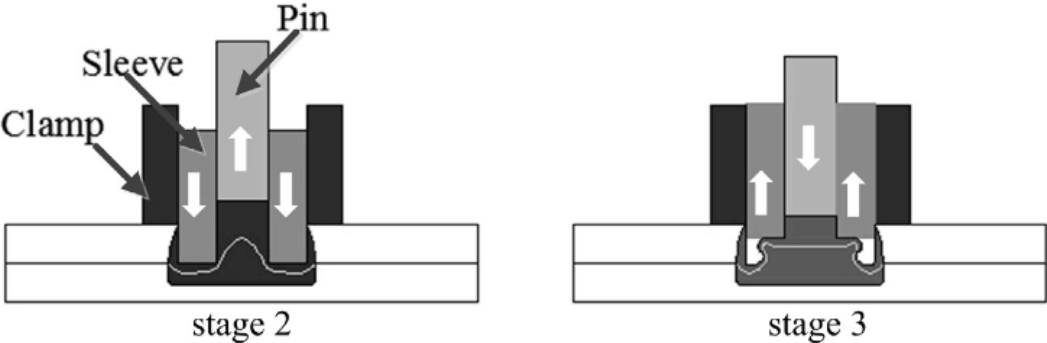


Figure 17: Possible hooking creation during the transition from stage 2 to stage 3 [23].

The second type of hooking appears when the plunge depth is increased to a value that is bigger than the thickness of the upper sheet. It only appears on the outside of the SZ, in the TMAZ, visible in Figure 18. This type of hooking is the same as the one indicated in Figure 15 and has an upside down V-shape. As mentioned before, this phenomenon is the result of the upward bending of the interface due to the

tool penetration into the lower sheet [24]. The hook defect influences the hook height, as can be seen in Figure 18. This is the distance between the top of the hook and the original sheet interface [3]. The hook height that occurs in a weld is believed to be controlled by two factors: the amount of plasticised material related to the rotational speed and plunge depth, and the upward material flow related to the retraction speed. It is generally known that an increase of the hook height results in a decrease in the tensile shear strength [23].

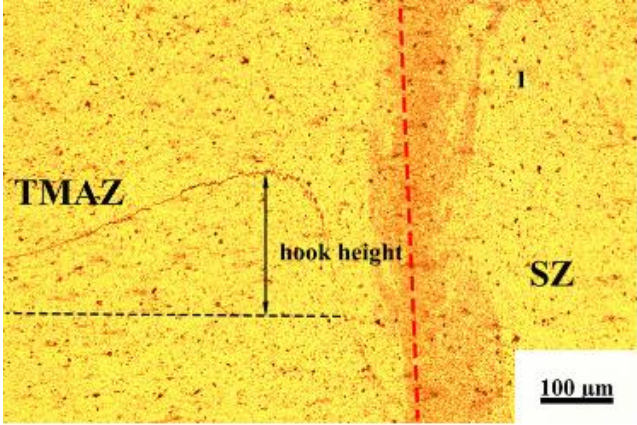


Figure 18: Hooking in the TMAZ (RS = 2100 rpms, DT = 4s, PD = 2.3 m) [23].

Bonding ligament

Different from the other defects that are being discussed, the bonding ligament is the area of good adhesion between the upper and lower sheet material and is thus no defect [25]. It is visible in both Figure 15 and Figure 19 as a black line, lying underneath the SZ as it forms the base of the welding nugget. As visible in Figure 19, the width of this bonding ligament is expressed in the bonding ligament length (BLL). This value is directly related to the lap shear strength because a greater value of the BLL means a greater value for the lap shear strength. A high-quality, strong weld consists of a long, flat bonding ligament and a big BLL value with the absence of defects. Tier et al. [26] indicated that a longer, flatter and stronger bonding ligament can be obtained by lowering the rotational speeds, while high rotation speeds result in a more upwards curved bonding ligament where the BLL is smaller due to the inadequate bonding (IB) [3]. The difference is indicated in Figure 19 underneath.

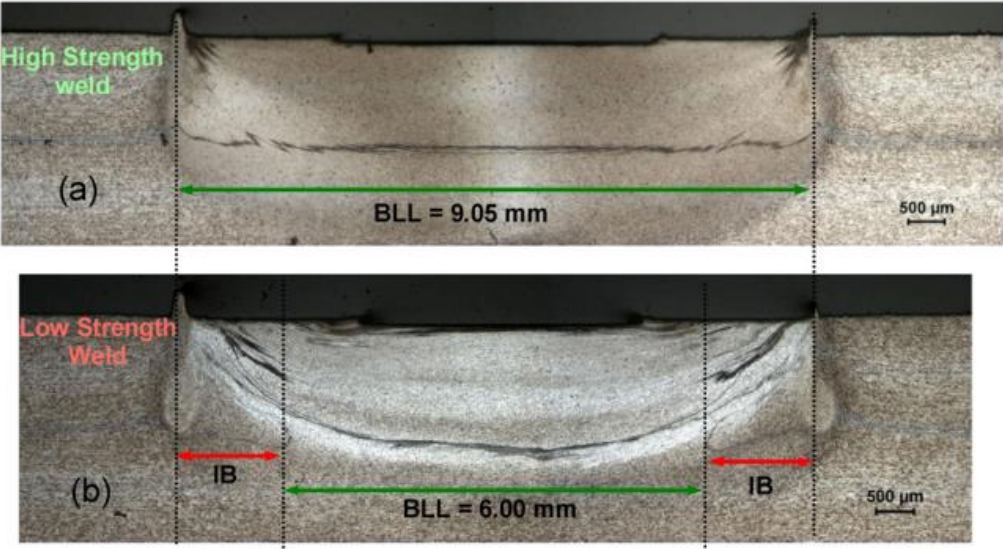


Figure 19: The difference between a high (a) and low (b) strength weld according to their BLL values [26].

Partial bonding

The partial bonding defect mostly influences the fracture modes during tensile shear testing. All the fracture modes are associated to the same fracture initiation mechanism, where partial bonding plays an important role [18]. It is the area where the upper and lower material sheet meet and form a weaker bond. It is also a transition area between the hooking zone and the bonding ligament and is the result of a lack of mixing and incomplete refill [25]. When forces are applied at the sheets during lap shear testing, circumferential crack sites may nucleate at both the lower and upper sheet. In that case, the stir zone is the only connection between the upper and lower sheets and thus the only effective shear area. This principle is visible in Figure 20, experimental examples are visible in Figure 21.

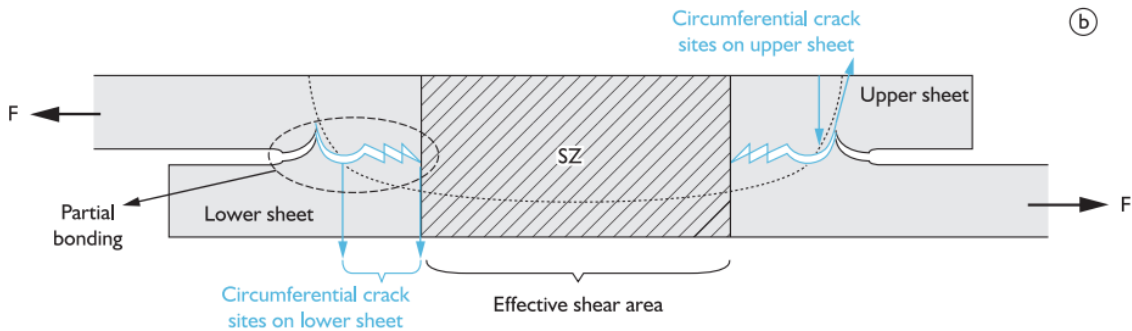


Figure 20: Indication of the circumferential crack sites that might occur during a tensile shear strength test [18].

The further separation (tearing) leads to an annular crack that surrounds the SZ. It depends on the properties of the other zones (TMAZ, HAZ) how big this annular crack can grow through the bonding ligament. The effective shear area of the joint becomes smaller because of this annular crack [18]. Figure 21 shows an overview of the different fracture modes that might occur.

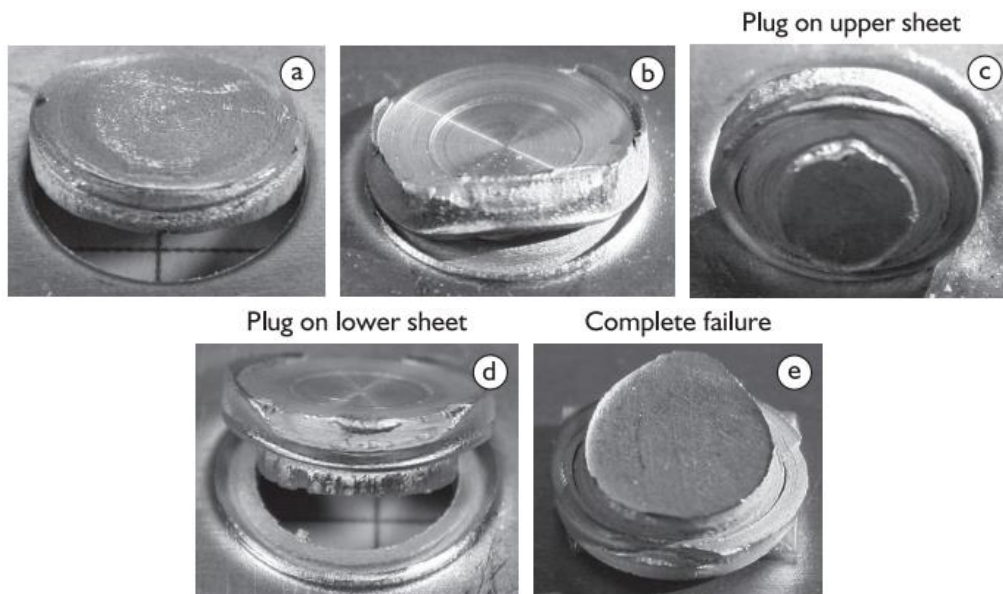


Figure 21: Fracture mode in shear tensile tests: a) Through weld with circumferential crack; b) Plug pull-out with nugget tearing; c) Plug pull-out with back plug variations on upper and lower (d) sheet; e) Complete failure [18].

Incomplete refill and voids

The last kind of weld defects that might occur are voids and incomplete refill defects. Both of these defects are located at the sleeve plunge path, where the sleeve penetrates in the sheets during stage 2. The location of these defects is shown in Figure 22.

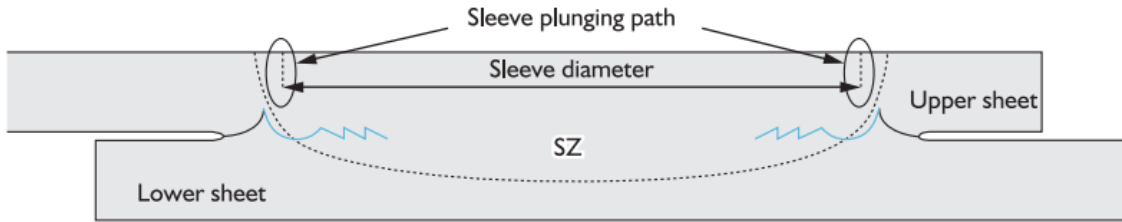


Figure 22: Indication of the places where incomplete refill and voids might occur due to the sleeve plunging path [18].

The voids are areas where no mixed material is present and are the result of an insufficient material flow, a lack of mixing or thermal shrinkage [21].

The incomplete refill defect is also due to the insufficient material flow. It is directly related to the retraction speed of the sleeve in stage 3 (see Figure 17). When the retraction speed of the sleeve is too high, the extruded material located at the pin has not enough time to fill the created keyhole again, and an incomplete refill is formed. Both the voids and incomplete refill defects are visible in Figure 23.

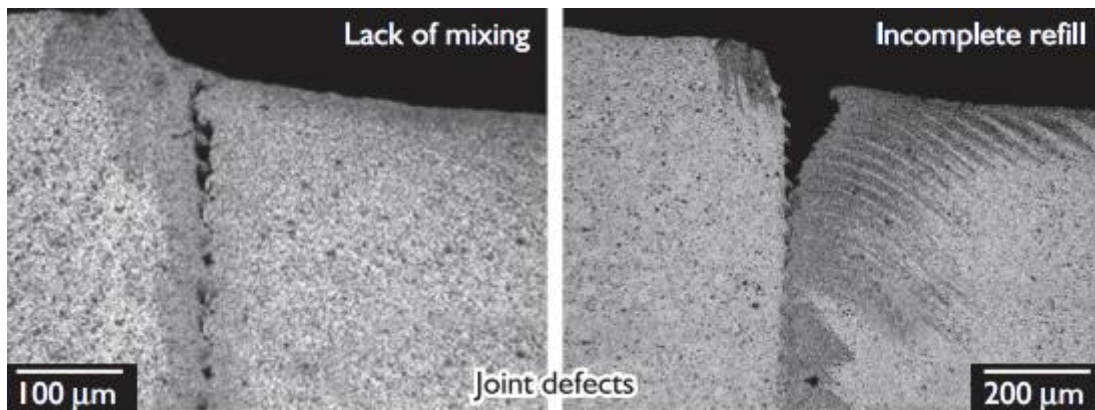


Figure 23: Detailed view of the voids (left) and the incomplete refill (right) appearing at the contour of the weld nugget [18].

As other defects, these defects are also best avoided since there might be a corrosion risk in those areas. Because corrosion affects the material, this results in a weld that becomes increasingly weaker as the corrosion increases.

2.1.5 Overview of mechanical properties

An overview of different Al alloys based on articles out of the literature is given in Table 1 beneath. This table is continued on a previous work of J. Vercauteren (2016) [3].

Table 1: Mechanical properties of Al alloys with the RFSSpW process.

Materials	Thickness (mm)	Overlap (mm x mm)	Lap shear strength (kN)	BM hardness (HV)	Maximum hardness reduction (- %)	UTS (MPa)	Shear load requirements minimum; average (kN per spot weld) [47]	Reference
2xxx								
EN AW-2024-T3 (Alclad)	2	46x46	7,5 - 10,68	110	16	359 - 510	4,560 ; 5,715	[27]
EN AW-2024-T3 (Alclad)	2	60x35	6,8 - 10,2	190	16	359 - 510	4,560 ; 5,715	[28]
EN AW-2024-T3 (Alclad)	2	46x60	9	100 - 120	16	359 - 510	4,560 ; 5,715	[29]
EN AW-2024-T3 (Alclad)	2	60x46	6,44 - 10,68	115 - 145	16	359 - 510	4,560 ; 5,715	[27]
EN AW-2024-T3	2	46x60	8,0 - 10,0	/	/	359 - 510	2,980 ; 4,635	[30]
EN AW-2024-T3	1,6	38x45	7,0 - 8,0	/	/	359 - 510	2,980 ; 4,635	[10]
EN AW-2024-T3	1,6	/	3,97 - 8,68	/	/	483	2,980 ; 4,635	[31]
EN AW-2024-T3	2	25x25	4,8 - 10,1	88 - 130	/	486	2,980 ; 4,635	[32]
EN AW-2024-T3	2	/	9,7 - 10,7	128 - 148	/	486	2,980 ; 4,635	[33]
EN AW-2024-T3	2	/	6,3 - 10,3	/	/	425	2,980 ; 4,635	[30]
EN AW-2024-T351	2	60x35	6,3 - 10,3	130 - 213	/	420	/	[23]
EN AW-2024-T4 (Alclad)	1,5 / 2,0	50x60	9,36	140	10	359 - 445	2,725 ; 3,307	[34]
EN AW-2024-T4 (Alclad)	1,2 / 2,0	50x50	/	130 - 158	10	359 - 445	2,725 ; 3,307	[35]
EN AW-2024-T4 (Alclad)	1,5 / 2	50x60	5,25 - 9,2	123 - 142	10	359 - 445	2,725 ; 3,307	[36]
EN AW-2024-T8	3,2	35x60	14,7	150	23	450	9,430 ; 11,785	[28]
EN AW-2198-T8	3,2	60x35	10,97 - 14,73	112 - 134	/	/	/	[37]
EN AW-2198-T8	2	/	4,5 - 9,8	110 - 139	/	/	/	[38]
EN AW-2198-T8	1,6	35x46	4,9 - 10,7	/	/	/	/	[5]

5xxx								
EN AW-5042-O	1,5	50x60	4,5 - 6,3	/	/	240 - 350	2,503 - 3,135	[26]
EN AW-5042	1,6	25,4x25,4	7,3 - 9,34	/	/	411	/	[39]
6xxx								
EN AW-6061-T6	2	25x25	7,4 - 8,6	115	10	233 - 257	3,805 ; 4,760	[23]
EN AW-6061-T4	1,7	46x46	6,8	80	12,5	200	2,675 ; 3,390	[25]
EN AW-6061-T4	/	/	6,0 - 7,0	/	12,5	200	2,675 ; 3,390	[40]
EN AW-6061-T4	1,7	/	6,5	/	12,5	200	2,675 ; 3,390	[25]
EN AW-6061-T4	2	40x40	5,2 - 7,1	42 - 62	12,5	198,9	2,675 ; 3,390	[21]
EN AW-6061-T6	2	25x25	6,7 - 7,5	72,5 - 81	35	280 - 340	3,805 ; 4,760	[41]
EN AW-6061-T6	2	25x25	7,4 - 9	60 - 95	35	280 - 340	3,805 ; 4,760	[23]
EN AW-6061-T6	2	25x25	8,6 - 9,8	65 - 92	35	280 - 340	3,805 ; 4,760	[42]
EN AW-6082-T6	2	35x45	10,5	107	35	280 - 340	3,805 ; 4,760	[1]
EN AW-6181-T4	1,7	60x46	5,2 - 7	68 - 98	/	/	/	[18]
7xxx								
EN AW-7B04-T74 (Alclad)	1,9	30x30	7 - 11,9	165 - 175	18	498	4,115 ; 5,160	[38]
EN AW-7B04-T74 (Alclad)	1,9	30x30	6,5 - 11,5	130 - 183	18	498	4,155 ; 5,160	[43]
EN AW-7475-T761	1,6	38x45	7,00 - 8,00	/	/	455 - 503	2,980 ; 3,635	[10]
EN AW-7475-T761	1,6	35x45	5,38	150	16	455 - 503	2,980 ; 3,635	[1]
EN AW-7075-T6 (Alclad)	0,8	25x25	4,00 - 4,75	165 - 180	23	434 - 580	1,115 ; 1,445	[44]
EN AW-7075-T6 (Alclad)	0,8	25x25	3,4 - 5,2	135 - 160	23	434 - 580	/	[44]
EN AW-7075-T6	1,6 / 0,8	30x30	6,3 - 7,7	/	/	540	/	[45]
EN AW-7075-T6	1,6 / 0,8	30x30	5,3 - 7,8	/	/	482,6	/	[46]
EN AW-7075-T6	1,6 / 0,8	30x20	5,6 - 7,6	/	/	482,6	/	[47]
EN AW-7075-T6	1,6	35x45	/	180	22	434 - 580	2,980 ; 3,635	[1]
EN AW-7075-T6	2	40x40	7,03	140 - 150	17	434 - 580	4,560 ; 5,715	[48]
EN AW-7075-T6	2	40x40	3,5 - 7	125 - 150	/	453,4	/	[48]
EN AW-7075-T6	2	50x50	/	120 - 153	/	453,4	/	[48]
EN AW-7075	0,8	/	3,6 - 4,7	130 - 160	/	/	/	[49]

EN AW-7075-T76	2	45x45	5,25 - 9,2	125 - 170	/	/	/	[50]
EN AW-7475-T761	2	60x35	9,3 - 12,3	116 - 200	/	/	/	[37]
Dissimilar								
EN AW-7475-T761/ EN AW-2024-T3	1,6	38x45	8,00 - 10,00	/	/	455 - 503 / 359 - 510	2,980 ; 3,635	[10]
EN AW-6061-T6 / EN AW-2024-T3	0,635 / 0,508	30x30	2,2 - 2,5	60 - 75 / 130 - 142	/	/	/	[51]
EN AW-2024-T3 / EN AW-7075-T6	5	35x50	6,0 - 25,0	98 - 141	/	477 / 464	/	[52]
EN AW-6022-T4 / EN AW-7075-T6	0,9 / 2	25x25	1 - 4	60 - 140	/	/	/	[53]
EN AW-6063 / EN AW-5083	2	40x40	5,8 - 8	/	/	/	/	[54]

2.2 Arc welding

2.2.1 Welding errors

Like other welding techniques, some faults may occur during the MIG/MAG welding process. The objective of this experimental research is to reveal these faults by means of AE. The most common welding defects and their possible causes will be discussed in the following paragraphs.

Porosity

Porosity is a contamination of the weld, caused by gas that is trapped within the weld, as illustrated in Figure 24. This occurs when the shielding gas cannot reach the entire weld pool and the atmospheric gas affects the weld. The defect can be recognized by spherical holes within the weld. Porosities can occur in the cases listed up below [55][56].

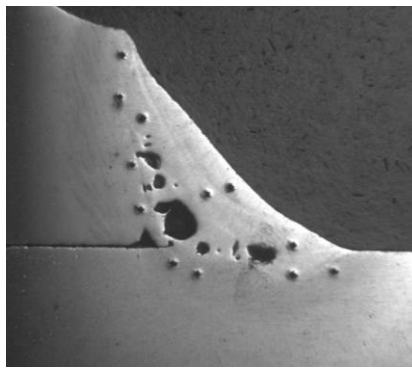


Figure 24: Porosity as welding defect [57].

- Wire, gas or moisture on the workpiece
- Insufficient gas flow
- Excessive gas (turbulence)
- Gas nozzle is filled with spatters, dirty diffuser
- The wire sticks out too much
- Gas leakage
- Excessive arc voltage
- Work piece is too hot

The welds in this experimental work will contain these porosities, since welding experiments were performed, during which the shielding gas was turned off at the start of the MAG process. These results will be further described in Chapter 6.

Slag inclusions

Slag inclusions can be considered as elongated lines along the weld in a radiograph. Slag is the remaining flux that is solidified and is therefore a by-product of shielded metal arc welding. Sometimes the slag is embedded in the metal, as shown in Figure 25.

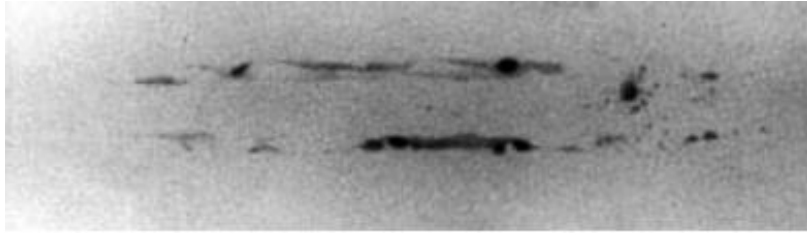


Figure 25: Slag inclusions as welding defect [58].

The most common possible cases in which slag inclusions are observed are listed up below [56][58][59].

- Wire speed too slow or too high
- Welding pushing (pulling with slag wires)

Binding failures

Binding failures occur when both materials are not accurately welded and the metal pre-solidifies, which leads to a non-filled gap within the molten metal [60]. This defect is visible in Figure 26.

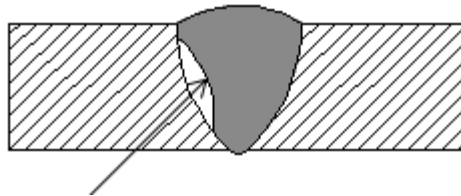


Figure 26: Binding failures as a welding defect [56].

Binding failure can occur in the following cases [56]:

- Arc voltage too high / too low
- Too fast / too slow travel speed
- Low current
- Incorrect torch angle

Cracks

There are many different types of cracks, as illustrated in Figure 27.

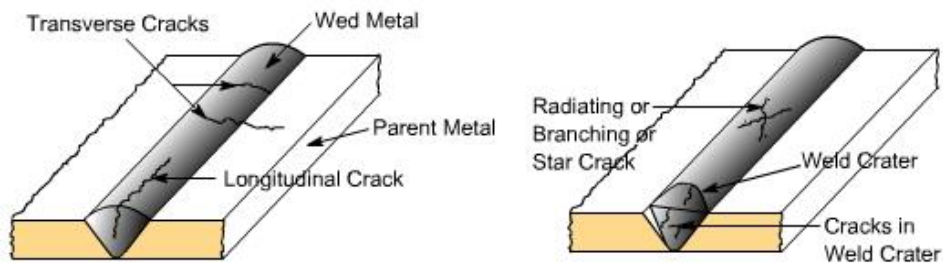


Figure 27: Different sorts of cracks in a weld as a welding defect [56].

Cracks can occur in the following cases, as listed below [56].

- Improper welding technique (for example, when the heat input is too high)
- Incorrect filler metal
- Insufficient ferrite in stainless steel

Weld spatters

Weld spatters are droplets of molten metal that are splashed around the welding line during the process (see Figure 28).



Figure 28: Spatters as a welding defect [61].

Following cases can lead to the appearance of spatters [56]:

- Insufficient arc voltage
- Too much wire speed
- Bad current carrying capacity (worn out contact-tip)
- Too low inductance
- Incorrect torch angle
- Sticking out of the wire is too long

3. Acoustic emission

3.1 Introduction and objectives

Nowadays acoustic emission (AE) is widely used for many different applications, ranging from monitoring welding processes to controlling the strength of bridges during their lifespan. By using AE as an in-line quality control system, it is possible to listen to the sounds emitted by materials during the investigated process. The main goal of AE is to surveil industrial processes or structures in a non-destructive way. It will therefore contribute to a higher productivity, lower cost and greater reliability of the produced components. It will be checking and controlling the strength of different applications during or after the process. This will result in a reduction in re-work and an increase of the quality.

The AE technique is based on the detection and conversion of high-frequency waves into electrical signals. When a metal is stressed, for example during plastic deformation, fracture or other local instabilities, low-level sounds are emitted [62]. The energy for these sounds originates from the stored elastic energy in the object or from externally performed work. The generated voltage waves can be longitudinal, transverse or surface waves. The waves will cause a displacement at the surface that can be measured with a sensor [63]. In order to accurately distinguish the signals originating from the AE source, external sounds should be excluded. This can be done for example by looking into the frequency domain, since the sound waves of the material have relatively high frequencies [62][64].

AE is currently being used for the surveillance of industrial processes or structures, as listed below:

Crack detection

Using AE-monitoring, it is possible to reveal crack initiation and crack growth in metal objects [65]. For example, crack monitoring is used for landing gears of planes to prevent a break down. With this technique the gears can be updated at the right time.

Vessel inspection

To check a spherical storage vessel before and during its use, a water pressure test is performed. During the entire testing period, spherical tanks can only be investigated from inside. This means the entire surface of the inside sphere cannot be checked. Without the use of AE, it is necessary to dispose the water after remediation to allow the technicians to go inside the tank [66]. The testing can also be done by AE to detect and locate propagations in hard conditions for people to enter. AE will add more safety to the testing method, lower the costs and lower the period that the vessel is unavailable [66].

Leak detection

The flow in a leakage is normally turbulent. The fluctuating pressure field that is generated by the turbulence will generate a specific AE signal. This signal is transmitted through the fluid or the pipe walls and can be detected with a sensor on the pipes [67].

Pulp and Paper industry

In the industry AE is used to test the paper structures when a mechanical loading is applied. It will help with the development of new paper fibers to understand the physical and mechanical properties.

Welding processes

Welding industries are faced with the need to monitor weld quality and system integrity more frequently, in order to guarantee the structural functionality of the products. Hence, weld quality is becoming increasingly important as customer expectations increase. A primary concern is to detect weld defects fast, reliable and cost-effectively. Current destructive and non-destructive techniques are

time-consuming and expensive and are not always appropriate for assessing the weld quality. AE as an in-line quality control system allows to overcome the current limitations of the conventional characterization techniques.

The main objective of this work is to examine the acoustic emission technique applied to two innovative welding processes, namely the refill friction stir spot welding process and Metal Inert Gas (MIG) welding using a robot. Hereto, the following sub-objectives are identified:

- To investigate the reproducibility of the AE signals.
- To determine the appropriate AE settings.
- To recognize weld errors on base of AE results.
- To develop a non-destructive weld quality monitoring system based on AE.

AE could eliminate or considerably reduce the post-production selective inspection, reduce the number of destructive tests and increase the reliability of the assembly process. In chapter 1, the general principles of the AE techniques will be discussed. The following chapter deals with the state-of-the-art literature of AE. Chapter 3 concerns the equipment necessary to measure the AE signals. In the last chapter, the known AE results and evaluation methods for different welding methods will be discussed.

3.2 General principles

In this section, different ways of analysing the AE output will be discussed. First, the AE basics are explained, afterwards various methods to extract information out of the AE signal are presented and at last the different transformations to look into the frequency domain are discussed.

3.2.1 AE basics

In general, an AE detection system monitors the emissions of a workpiece, performs a certain amount of processing and looks for features which might indicate a failure [68]. AE signals in the time domain can be distinguished into two types, namely continuous emission and burst emission. Continuous emission has a low amplitude and quickly repeating waves. This type of emission can be compared to determining the root mean square (RMS). Burst emission consists of an incidental eruption which is displayed as a large amount of energy and a large amplitude. The two types of emission can be seen in Figure 29. The eruptions in burst emission are bursts or hits [62][64].

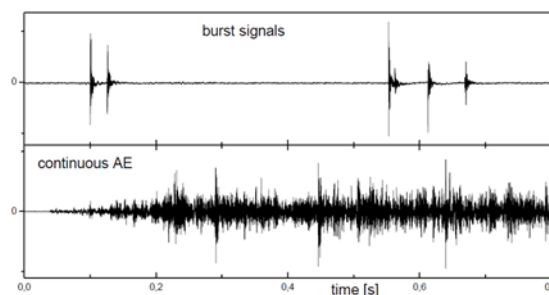


Figure 29: Bursts signals (top) and continuous AE (bottom). [64]

The characteristics listed below can be extracted from of a burst or hit. They are visually represented in Figure 30:

- Amplitude: largest deviation from the equilibrium position.
- Risetime: the time for a pulse to rise between 10% and 90% of a specified high value.

- Counts: the number of times that the chosen threshold is exceeded by the signal.
- MARSE (Measured Area Rectified Signal Envelope): a measurement of the area under the envelope of the rectified linear voltage time signal from the sensor [69]. This contains the energy of the burst.
- Duration: the time between the first and the last exceedance of the chosen threshold.

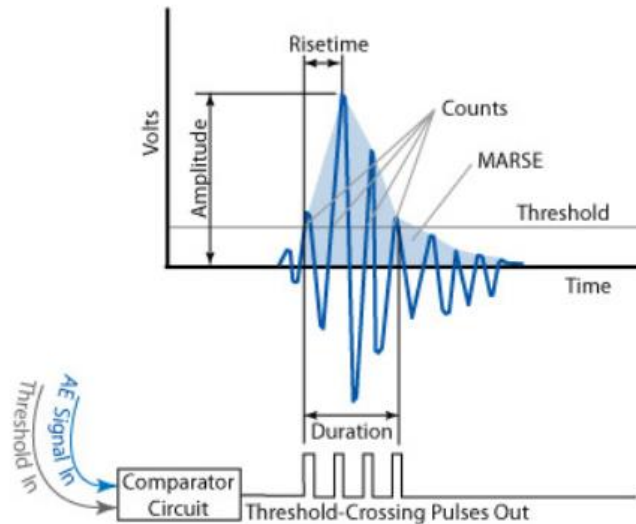


Figure 30: Burst information in an AE signal [65].

Based on the entire wavestream of the AE signals, the following information can be derived:

- Abundancy: the top voltage signal reached by the AE waveform.
- Fourier-transformation.
- Root mean square: the measure of the area under the envelope of the rectified linear voltage time signal [70]. This provides a measure of the amount of energy of the complete process.

The goal of the AE analysis is to detect, locate and discriminate the burst in the AE signals, which can then be coupled to a defect in the weld quality. In the next paragraphs, these techniques will be discussed along with the convenient ways to extract information from the AE signal.

Detection

A burst is detected if a chosen threshold is exceeded. Ringdowncounting (RDC) can be used to compare the bursts by looking at the amplitude. The amount of RDC is equal to how many times in a row the threshold is exceeded. The number of RDC can be considered as a representation of the amount of energy of a burst. The AE-signals of a burst can be added up (cumulative) or can be determined per time unit to represent the intensity. The term ringdowncounts can also be abbreviated to counts [64][63].

Location

In order to specify the location of an AE source, it is necessary to position multiple sensors. The difference in arrival time allows to locate the source if the location of the sensors is exactly known. The time at which a chosen threshold is exceeded for the first time is considered as the time of arrival. Using this technique, electrical interfering noises will have the same arrival time and can thus be neglected. Sometimes this technique is used to filter out the electrical interfering noises instead of locating the burst or fault [64]. However, this technique is very difficult and hence- only a few working applications known in literature.

Discrimination

Discrimination in time: The point of time at which the AE signal occurs can provide much information. Specific kinds of faults will occur at specific points of time, and therefore using this method, some of the fault can be eliminated. An application of this method is hot cracking. This kind of fault can only occur while the process is transferring heat and not after the process has finished. Setting out the AE in time is the most used way to investigate AE. When using the discrimination in time method it is important to have a well-known trigger, in order to set to have a perfect zero point of the time axis.

Discrimination in space: In order to use the discrimination in space method, the source first has to be located. If the location of the source is known, the decision for accepting the source can be made [64]. Accepting the signal means that the location of the source can affect the weld, otherwise the signal will be neglected. For example, locating the source of AE during the welding process, prevents that the AE signals are caused by the welding equipment and not by the transformations within the welded object.

Discrimination by amplitude: Another method is to organize the bursts into amplitude ranges. The amplitude of the burst will be similar if the same type of fault occurs. Using this method, the known amplitudes such as the vibrations of a machine head can be neglected.

By looking at the maximum amplitude, it is possible to derive a much better formula for the energy than RDC. This energy can be compared to the energy of this burst in another signal [64]. The formula which is used to calculate the energy is given below:

$$Energy = A_{max}^2 \cdot t$$

With:

$$A_{max}^2 = \text{maximum value for the amplitude}$$
$$t = \text{duration}$$

Using an analysing program such as the NOESIS software [71], it is possible to plot the amplitude of a hit (burst) on the X-axis and its duration on the Y-axis, for all the hits of the complete signal. Using this representation, it is easy to filter out the hits with a small duration and a high amplitude, since these hits can possibly represent cracks. This method can also be used as a filtering method, since electromagnetic interference signals have a high amplitude and a relatively long duration [64].

Discrimination by risetime: The risetime is the time between 10% and 90% of the maximum amplitude. It is known that electromagnetic noise has a very small risetime. By discriminating the small risetimes, it is possible to filter out the electromagnetic noise [64]. This can also be performed using special analysing programs which plot the risetime over time or amplitude.

AE cumulative counts

This technique represents the cumulative counts for all the bursts and sets them out over time. This representation provides insight into the “activity” in the material. For example, Yoon quoted by S. Senthilkumar [70] produced a strategy to perform in-procedure continuous weld quality assessment by using AE for disparate contact welding. He found out that ongoing quality assessment of a weld was conceivable by acoustic emanation (AE) procedure. It implies that an in-procedure ongoing quality observing can be improved by taking into account the quantity of acoustic emanation occasions. The outcome of the research of Yoon can be seen in Figure 31.

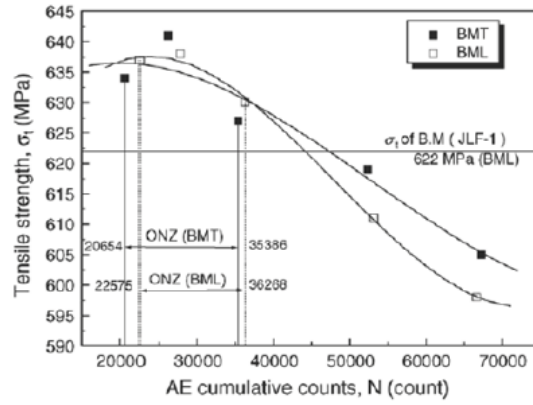


Figure 31: AE cumulative count and tensile strength [70].

Frequency domain

The AE-signal can be processed into the frequency domain, based on spectral analysis by means of the discrete Fourier transformation (DFT), which is the primary tool of digital acoustic signal processing. The DFT can be calculated using the fast Fourier transformation (FFT).

Other techniques include the short FFT (SFFT) or wavelets techniques. The SFFT can analyse a small part of the AE-signals and is therefore more precise. The wavelets techniques only allow a rough representation of the frequency spectrum, and hence they are only used for pattern recognition.

The goal of converting the AE signal into the frequency domain is to correlate the frequency of the signal directly to various interactions that occur during a process. Three different ways to process the AE-signal will be discussed in detail below.

DFT: The DFT is a technique to convert a sequence of complex numbers into a new sequence of complex numbers. The discrete method is used because of the sampling into discrete points of the signal. The discrete method is only slightly different from the continuous method [72].

The discrete formula is shown below:

$$X_k = \sum_{n=0}^{N-1} x_n \cdot e^{-\frac{j2\pi kt}{N}}$$

With:

n = lower limit of number samples

N = upper limit of number sample

X_k = the x - th frequency

$\frac{k}{N}$ = frequency

t = time

Now $\frac{2\pi kn}{N}$ is replaced by b_n and by expanding the summation the result is shown below.

$$X_k = x_0 e^{-b_0 j} + x_1 e^{-b_1 j} + \dots + x_n e^{-b_{N-1} j}$$

With:

X_k = the k^{th} frequency bin

x_n = the n^{th} sample value

By now using the identity of Euler's formula, it is possible to lose the complex exponential of the previous formula [11]. Euler's formula and the rewritten formula are respectively given below.

$$e^{jx} = \cos x + j \sin x$$

$$X_k = x_0[\cos(-b_0) + j\sin(-b_0)] + \dots$$

Afterwards by summing up, the formula is written as a complex number:

$$X_k = A_k + B_k j$$

With:

$A_k = \text{coordinate on the real axis}$

$B_k = \text{coordinate on the imaginay axis}$

With this representation it is possible to easily calculate the magnitude (Mag) and the phase (Θ) [72].

$$Mag = \sqrt{A_k^2 + B_k^2}$$

$$\theta = \tan^{-1} \frac{B_k}{A_k}$$

With the magnitude and phase respectively corresponding to the amplitude and the amount of shifting of the sinusoid at that frequency bin [11].

The DFT requires large sums over all elements which makes a large matrix. These are complex operations which The Cooley-Tukey Algorithm can give a solution to which will be described further [73].

FFT: A FFT is an algorithm that computes the DFT. Every algorithm that can compute the DFT is called a FFT. By using a FFT, the DFT is solved into approximately $\Theta(n \log(n))$ time, instead of $\Theta(n^2)$ time, where n is equal to the amount of samples. There are several FFT algorithms: the Cooley-Tukey Algorithm, in which the FFT is used to convert the time domain of the signal into the frequency domain, the SFFT and wavelets transforms [74].

Cooley-Tukey algorithm: The Cooley-Tukey algorithm is used as a FFT algorithm and is considered as the most common FFT. It was developed in 1965 by J.W. Cooley and J.W. Tukey and can be considered as a relatively modern technique. This invention of the technique was a turning point in digital signal processing and numerical analysis. The first FFT technique was the Gauss technique, invented by Carl Friedrich Gauss in 1805. Later on, Cooley and Tukey independently rediscovered and popularized it 160 years later [73]. It was a similar algorithm to this modern algorithm which will not be further discussed in this work.

Now the case of an algorithm when N is a power of 2 is discussed. Cooley and Tukey used the divide and conquer method and focused on the choice of N . They mathematically proved how special advantage is gained when choosing N to be a power of two, $N = 2^m$ wherewith $m \geq 0$ [75].

This method uses recursion which means that the matrix to perform the FFT on, is split into two parts. Namely one with the even indices and one with the odd indices. The array is split over and over again until a manageable array size is obtained to perform a DFT on. Also a similar re-ordering can be done by using a bit reversal scheme [76].

The most common implementation of the Cooley-Tukey method is known as a radix-2 decimation-in-time (DIT). First the DFT of a sequence is divided into the even and uneven elements [77].

$$X_k = \sum_{n=0}^{\frac{N}{2}-1} x(2n) \cdot e^{-\frac{j2\pi k(2n)}{N}} + \sum_{n=0}^{\frac{N}{2}-1} x(2n+1) \cdot e^{-\frac{j2\pi k(2n+1)}{N}}$$

By factoring out $e^{-j\frac{2\pi k}{N}}$ in the second term, the following formula is obtained:

$$X_k = \sum_{n=0}^{\frac{N}{2}-1} x(2n) \cdot e^{-\frac{j2\pi k(2n)}{N}} + e^{-j\frac{2\pi k}{N}} \sum_{n=0}^{\frac{N}{2}-1} x(2n+1) \cdot e^{-\frac{j2\pi k(2n)}{N}}$$

Thereafter the sum of even and uneven terms can be written as:

$$X_k = X_{even}(n) + e^{-j\frac{2\pi k}{N}} X_{odd}(n)$$

This shows how the number of calculations can be lowered to half of the original calculations [77]. The method of re-expressing the DFT can be used multiple times. The block diagram in Figure 32 illustrates how an N point DFT can be split into two N/2 point DFTs in order to handle the even and odd values of a length 8 sequence [77].

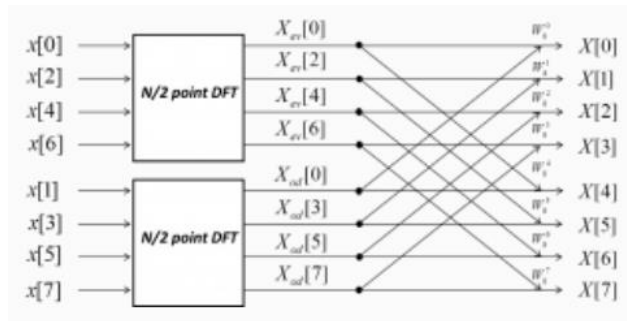


Figure 32: DFT split. [77]

SFFT: The short-time fast Fourier transform is also called the Gabor transform. It is developed to correct shortages of the FFT. The transform method only processes a small section of the signal at a time, which is called windowing. The idea of the SFFT is obtain the frequencies by the use of DFT and also get to know at which points in time these individual frequencies occur.

The technique extracts small pieces with length L (window size) from the signal and looks at the DFT of every signal piece. The formula is shown below, where the DFT starts at point $n = m$ and proceeds for L points, where k is equal to the DFT-index [78].

$$X[m, k] = \sum_{n=0}^{L-1} x[m+n] e^{-j\frac{2\pi nk}{L}}$$

Now it is possible to select the window at the time of a burst and to look at the frequencies of the burst at a specific time. This representation can be considered as a compromise between the time and frequency views, as it provides information about both. A downside is the fact that the window has the same size for all frequencies [78].

Wavelet transformation (WT): The FFT provides precise frequency information, whereas the WT presents information about the band frequency in the time domain and its energy. This method is not

the same as bandpass filtering, since in bandpass filtering the bandpass is constant. WT uses different bandwidths: wavelets at a high frequency are of short duration, whereas wavelets at low frequency have a relatively good frequency resolution [79]. The use of this method fits the analysis of complex signals, because these areas of abrupt changes are the most interesting areas. They are generally the symptoms for the defects or other events that are interesting to investigate. This technique is not explained in this dissertation because it was not used.

The power spectrum: The power spectrum is also referred to as the power spectral density. It describes the distribution of power into frequency components, composing a time series signal [80]. The power spectrum $S(\omega)$ is the discrete time Fourier transformation of the correlation sequence $r[k]$ of the process with:

$$S(\omega) = \sum_{k=-\infty}^{\infty} r[k]e^{-jk\omega}$$

$$r[k] = \frac{1}{2\pi} \int_{-\pi}^{\pi} S(\omega)e^{jk\omega} d\omega$$

The power spectral density integral P_{ab} is taken between ω_a and ω_b as shown below:

$$P_{ab} = \frac{1}{2\pi} \int_{\omega_a}^{\omega_b} S(\omega)d\omega$$

This result will show the average contribution to the total power due to components of the random process between ω_a and ω_b . This is the area under the $S(\omega)$ curve between these two points. The unit of $S(\omega)$ is power/radian. If power/Hz is required, the amplitude has to be scaled. The total power is presented by:

$$r[0] = \frac{1}{2\pi} \int_{-\pi}^{\pi} S(\omega)d\omega = E\{x^2[n]\}$$

The power spectrum is used in AE analysis to compare the different results. It provides insight into the energy of a process and where a specific event happens.

Pattern recognition: Pattern recognition is the automated recognition of patterns and regularities in data [81]. Using this technique in combination with the previous explained transformations, it is possible to recognize the specific outcomes of defect and interesting events in the AE waveform. The combination of these techniques will be the final goal of AE monitoring.

3.3 Disadvantages of AE

AE has a lot of advantages but some disadvantages must be kept in mind. Some disadvantages are listed below:

- Only dynamic errors can be found, noise has to be omitted to detect the error [64].
- The shape of the error cannot be determined, only the size can be determined. To determine the orientation of the error, many sensors must be placed and analysed at the same time, which this is a difficult process [64].
- It is important to know the characteristics of the AE sources and interference sources. With this knowledge the difference between errors and sources of interference can be found. Otherwise incorrect conclusions will be made [64].

3.4 Factors affecting AE

Different AE sources have different AE characteristics. Furthermore, the AE signal is influenced by the welding method, the material, the geometry of the object and the temperature. The next paragraphs will explain these conditions in detail [64].

3.4.1 Characteristics of the different AE sources

In this paragraph the known errors and their characteristics will be discussed. The welding methods discussed in the following paragraphs lead to melting of the material. However, this information can be useful to compare with the results of solid state welding techniques as well.

Cracks

If cracks arise or grow, an AE signal is produced. It is known that in case the amplitude and frequency of the burst will be high and its shape differs from the shape of the burst of a mechanical source. The burst will be small and high, which means that the energy will be quickly emitted. By using RDC, the length of the crack can be determined. The crack can be recognized by the fast increase of the counts, which is illustrated by the cumulative representation over time. By using discrimination in time, the difference can be made between hot cracking while welding and cold cracking after the welding process [64].

Movement of dislocations

A dislocation or Taylor's dislocation is a crystallographic defect or irregularity within a crystal structure. The presence of these dislocations strongly influences the material properties [82]. The movement of these dislocations can be observed as a continuous emission increase of a few mV [63]. The best way to see this increase is by looking at the averaged signal level (ASL), set over the time.

Crack of brittle inclusions

Inclusions of metal, powder or slag change the structure of the weld. The weld is less dense at the location of an inclusion, and therefore there is a risk of crack initiation. Inclusions are welding faults that decrease the mechanical strength of the weld [83]. A crack of brittle inclusions can be recognized by a burst or continuous emission of a few tens of μV [63].

3.4.2 Material choice

The choice of material will strongly affect the shape of the AE. A higher amplitude is expected when working with materials with strong, brittle, coarse grain, anisotropy and inhomogeneous properties [64]. Also the kind of material can influence the creation of micro cracks and inhomogeneous deformation. Phase conversion can occur in certain materials. These conversions will produce an AE signal as mentioned before. Heat conduction coefficient will also influence the AE: a material with a low coefficient will produce a delayed and spread signal [64].

3.4.3 Attenuation

The intensity of an AE signal is larger at the source than at the place where the sensor is positioned, which is due to attenuation or damping. The damping of a signal has three main causes, namely geometric spreading, material damping and wave scattering [64][84].

The geometric spreading is rather easy. As an AE signal spreads from its source in a plate-like material, its amplitude weakens by 30% every time it doubles its distance from the source. In three-dimensional

structures, the signal weakens in the order of 50% [84]. This phenomena can be explained by the conservation of energy.

Secondly the damping of the material plays an important role. If the wave propagates throughout the material, the elastic and kinetic energy is converted into heat and the wave loses energy. The damping of the AE amplitude will be different for each material, frequency and type of wave. It is known that the damping will be higher for higher frequencies. The damping is expressed in dB/m [84].

The last main cause is the scattering of waves. The waves are reflected by discontinuities. These discontinuities are not always boundaries of structures, but also twin boundaries, non-metallic inclusions and grain boundaries in the material can reflect the waves [84].

When materials with low attenuations are being measured, the amount of background noise will be much higher. To detect AE hits in these materials, it is therefore recommended to detect them at high frequencies [84].

3.4.4 Temperatures

The temperature will affect the AE amplitude in many different ways. First of all, the amplitude seems to decrease when working at a higher temperature. However, other research works claim that the AE signal should have a higher intensity because of the easy movement of dislocations. This is something in literature about which different publishers do not have the same opinion [85]. Secondly, large differences in temperature can cause deformations which results into the production of AE signals. At last, large variations in temperature can cause phase deformation, which produce AE signals with a high amplitude and affect the waveforms that pass through it [64].

The temperature is important for the sensor, since each sensor has a maximum working temperature. It is possible to position the sensor further away from the heat source, however in this case the attenuation of the AE will be higher. The use of high temperature sensors can offer a solution, but these sensors have a smaller sensitivity.

M. J. G. N. Boon [85] investigated the effect of temperature on the AE signal. They performed their tests on aluminium 2024-T3 sheets with a thickness of 2,1 mm. They emitted a wave group velocities of a Hanning window signal at 150 and 300 kHz from one sensor and recorded at another sensor different temperatures in the range of -40 °C and 70 °C [85]. Analytical curves are derived from the methodology presented by Dodson and Inman used by M. J. G. N. Boon [85]. These results can be seen in Figure 33.

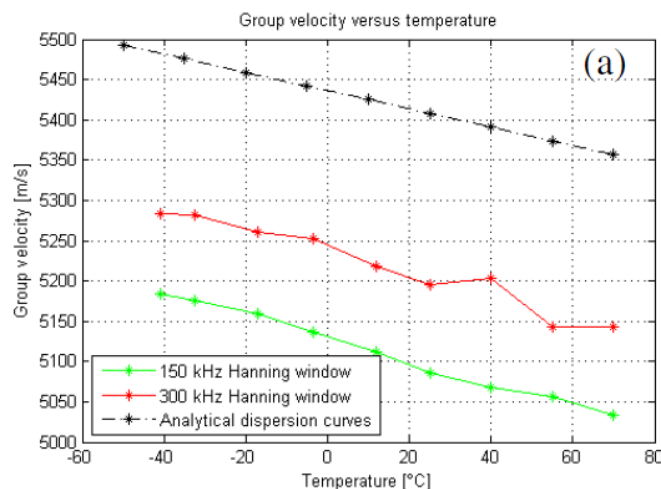


Figure 33: Group velocity (m/s) vs temperature (°C) [85].

3.4.5 AE parameters

Sampling rate

A FFT does not resolve a continuous spectrum into to the frequency spectrum, but uses and returns a discrete spectrum. This means that the number of frequency lines are finite. The sample frequency (f_s) is the amount of samples (N) divided by the acquisition time. This gives the formula [86]:

$$f_s = \frac{N}{T}$$

The frequency resolution (df) can be given by the following formula. The frequency resolution is only determined by the acquisition time [86].

$$df = \frac{1}{T} = \frac{f_s}{N}$$

The sampling rate of a time waveform determines the maximum resolvable frequency. According to the Shannon Sampling Theorem, the maximum resolvable frequency must be half the sampling frequency [86]. The formula to calculate the maximum resolvable frequency (f_{max}) is given below.

$$f_{max} = f_{Nyquist} = \frac{f_s}{2}$$

With:

$$f_{Nyquist} = \text{Nyquist frequency}$$

$$f_s = \text{sampling frequency}$$

By determining the Nyquist frequency, the baseband can be determined, knowing that the minimum resolvable frequency is 0. The number of the spectral lines will be half the number of samples [86].

3.5 AE equipment

This chapter discusses the necessary equipment to record the AE signals. The different parts of the measuring system will be discussed in detail. The measuring chain equipment parts can be seen in Figure 34.

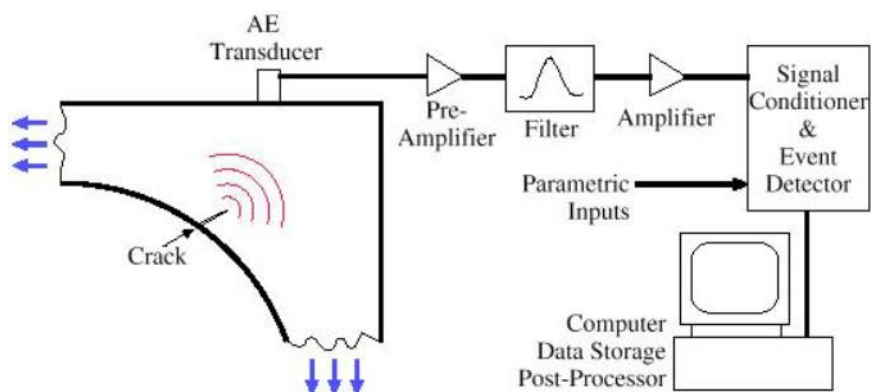


Figure 34: The AE measuring chain [68].

3.5.1 Sensors

The sensor positioned on the object will transform the AE-pulse into an electrical signal. Piezoelectric sensors are mostly used, which can reach up to 1000 V/mm displacement of the surface. Underneath,

the sensor has a clay base to protect it against the heat at the surface of the object. The maximum operating temperature of the sensor is one of the most important properties when selecting a sensor [63].

The AE sensor consists of several parts. The basis is a piezoelectric ceramic element with electrodes at each side. The first electrode is connected to the electric ground, whereas the second electrode is connected to a signal lead. The function of the damping material is to minimize reflections towards the piezoelectric element and the damping of signals around the resonance frequency. To minimize the electromagnetic interference a case is fitted. Sometimes an internal preamplifier is fitted into the sensor, which are called integral sensors [87]. The structure of a typical sensor can be seen in Figure 35.

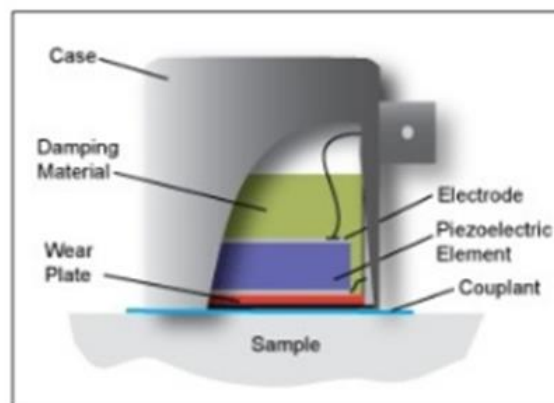


Figure 35: Sensor structure [87].

The piezoelectric element has two principal dimensions: the thickness and the diameter. The element thickness controls the frequencies at which the sensor has the highest electrical output [87], which is called the sensitivity. The diameter of the element affects the area over which the sensor averages the surface motion [87]. The resonance frequency is affected by the piezoelectric and elastic constants of the piezo element.

The effect of temperature of the sensor can be explained by the Curie temperature. At this temperature, the piezoelectric ceramics change permanently and this results into a loss of piezoelectricity. This is why the working temperature of sensors is limited [87].

When working with a fluctuating temperature, sensors can also have disadvantages. The piezoelectric ceramics have multiple domains where the electric polarization is at one specific direction. When the temperature changes, many of these domains can flip. When a domain flips a spurious electric signal can be emitted, which will change the AE result and leads to a false event. This is why sensors should be allowed to reach a thermal equilibrium before the data is taken at different temperatures. The best sensors for fluctuating temperatures are single crystal piezoelectric quartz sensors [87].

The popularity of these types of transductions system is partly due to the fact that AE sensors can be designed to sense a portion of the whole frequency spectrum by changing the piezoelectric dimensions [87].

There are 3 main types of these sensors: resonant sensors, wide band sensors and capacitive sensors. The resonant sensors prefer one or more frequencies of oscillation. This makes them interesting to make a trade-off between detection range and noise environment. Moreover, they have a low fidelity because the output is not similar to the motion of the original wave. They are more sensitive and less expensive than wide band sensors [87].

The second type is a wide band sensor. These are used when a high fidelity AE response is required or where a frequency analysis needs to be performed. This type provides more AE information than the resonant sensors [87].

The third type of sensor is a capacitive sensor. This is basically a position measurement device. The two surface are conductive with a capacitance that exists between them. If the distance between these conductive surfaces changes, the capacitance will also change. The output of these sensors is a flat frequency response. They are mostly used in laboratories [87].

Other properties to check before selecting a sensor are the operating frequency range, since this has to fit the range of interest of the research and the peak sensitivity. The peak sensitivity is expressed in dB.

To position the sensor at a certain location, couplants are used between the object surface and the sensor. The most widely used couplant is silicone rubber.

Nowadays it is possible to measure the vibrations at the surface with a laser called laser based ultrasonic (LBU). This technique has the advantage of measuring the clean signal, where a piezoelectric sensor contains a piezo crystal that still vibrates after the surface signal. A disadvantage of this technique is the fact that most lasers require a reflective surface. The technique is developed to detect flaws in materials. This is performed by one laser which generates ultrasonic waves and another laser that detects the surface motion [87]. This is shown in Figure 36 below.

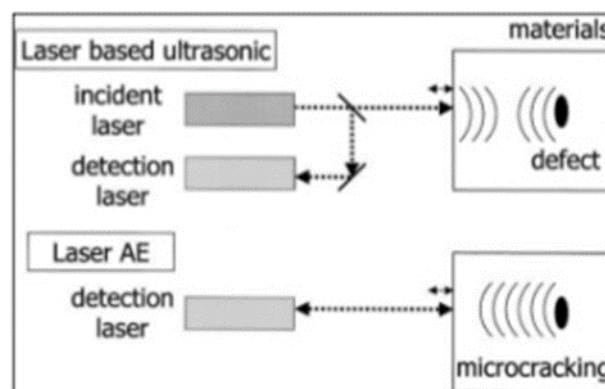


Figure 36: AE laser technique [87].

Location of the sensor

The sensor is connected to the material that needs to be measured using a couplant. This couplant needs to provide a good acoustic path between them. Moreover it needs to be a fluid, since fluids will not transmit shear waves and need to have chemical compatibility. Finally, the couplant needs to fully cover the surface, but not corrode it [87].

The method of mounting the sensor will affect the performance of the sensor, in terms of sensitivity and frequency band. This mounting can be done by compression from a mechanical force or by bonding with an adhesive that acts as couplant [87]. After mounting, it is necessary to obtain a verification of the sensor sensitivity. This can be done by a so-called pencil test. The pencil test is simply breaking a pencil point near the sensor 3 times in a row. If the amplitudes of the waveforms are higher than 90 dB and do not differ more than 4 dB from one another, the sensor is correctly working.

3.5.2 Amplifiers

Preamplifier

The pre-amplifier is a part of the signal conditioning and has the function to amplify the input signal. Pre-amplification of the input signal is required so that the electromagnetic noise picked up by the long cable will have less effect and that the signal will have less loss for long lengths of cable. This pre-amplifier needs to stay at room temperature to avoid disturb noise. Sometimes frequency filters can be integrated into the preamplifier. The most AE preamplifiers are linear according to following formula [87]:

$$\text{Output (voltage)} = \text{Input (voltage)} \cdot \text{Gain}$$

Amplifier

The amplifier brings the signal to a suitable level for the measurement. The total amplification is mostly situated between 40 dB and 80 dB. Some of the amplifiers have an operator-controlled test variable. The input resistance of the amplifier is chosen to optimize the SNR (signal-to-noise ratio). Because of the electrical noise. The level of noise can be reduced by the temperature of the resistor, but practically this will not always work [87] [64].

3.5.3 Filters

Mechanical vibrations of machines, pumps or motors reduce the measuring area, therefore filtering is needed. The filtering has to be performed as close as possible to the sensor. The filter is mostly fitted into the preamplifier and has an accepting range between 100 kHz and 1 MHz. 100 kHz is the lower limit for measuring cracks and filtering out low-frequency mechanical-noise. 1MHz is the lower limit for electromagnetic noise and is sufficiently high to measure the AE signals [64][63].

The frequency filters exist in high pass, low pass and band pass types.

3.5.4 AE processor

The processor receives signals from the AE sensors through the amplifiers and filters as well as signals from external sensors, which might be following the process parameters, external conditions or control inputs. The output of the processor is be the detected activity. In a further stage when the AE-signals are well known, the output can be a comparison between the AE, the external conditions and the control inputs. The goal is an automated quality check.

3.5.5 Coaxial cables and connectors

The function of the cables is transmitting the signal from the source to the data acquisition and to connect all the points electrically. For almost all the AE applications a coaxial cable is used because of its good electrical shielding. The most chosen connector is the BNC type shown in Figure 37, while the most used cable type is shown in Figure 38.



Figure 37: Most used connector (BNC) [88].



Figure 38: Most used cable (RG-58) [89].

3.6 AE applied to different welding applications: state-of-the-art

In the following paragraphs, an overview will be given about the AE information of different welding applications as found in literature. Friction stir welding (FSW), friction stir spot welding (FSSW) and Metal Inert Gas welding (MIG) are discussed. Since AE applied for resistance welding is well known, an overview of resistance welding will not be given.

3.6.1 AE on FSW

Three different papers on AE on FSW are given. At the end a global conclusion on the situation is given.

The applicability of AE technique is studied in the analysis of FSW joints. A model is made to correlate the AE signals with process parameters or other influences. From the studies of OH Sae-Kyoo et. al, it was confirmed through initial energy effects, that AE techniques could reliably be applied to in-process strength monitoring of any type of friction welding [90]. They were able to correlate the cumulative AE counts during welding to the joints strengths of welds with a 95 % confidence [90].

There can be concluded that AE is a fast, reliable, accurate and cost effective method of structural monitoring to detect crack growth in real time. It was found out that the impact of different parameters on the weld quality of FSW welds is already investigated and known. Now it is time to link them with AE events to avoid destructive test methods. At the end an experimental examination and quantitative analysis for the effects of initial energy on AE relating to weld strength is proposed as a new approach which attempts finally to develop an on-line quality monitoring system design for friction welded joints using AE techniques [90].

In another paper the feasibility of acoustic monitoring for FSW of three austenitic stainless steels is investigated. It was found out that the three alloys had different acoustic signatures versus time when the welding parameters were slightly changed. Furthermore a clear link between the appearing bursts and the torque was found for all of the three materials. At last the different acoustic emissions from the different alloys are explained by differences in the acoustic, thermo-physical and thermo-mechanical properties between the alloys [8].

In a third paper, AE of a FSW process is analysed in order to investigate the possibility of applying the AE technique as a monitoring system for FSW. There is especially focused on WT techniques decompose the AE signal. They found out that the wavelet transformations of the AE signal provide plots of frequency spectra vs time. The plots can be used to recognize AE features. The defects can have a specific range of frequencies. By looking at the energy variation a more detailed indication of the gap-induced defects compared to the total energy variation can be found [78].

Conclusion on RFSSpW

There has been a lot of research for AE on FSW. It is multiple times confirmed that AE can be used to control the weld quality but until now only theorems are found. There is proved that the kind of material will affect the results and WT are proposed. A lot of new research has to be done on this subject to create a perfect working AE monitoring system.

3.6.2 AE on RFSSpW

RFSSpW is a relative new technology. Only 1 published paper on AE monitoring could be found, which will be discussed in the next paragraph.

In this paper the Z-axis force and the AE amplitude were compared for a FSSW process on 5XXX material. It was found out that the change of AE signal is more appropriate than that of the Z-axis force for the evaluation of the quality of the welds. It is suggested to use AE signal as an extra parameter to monitor the FSSW process in addition to the commonly modern parameters.

The results found by Yong-Wook Lee, Md. Abu Mowazzem Hossain, Sung-Tae Hong, Young-Jin Yum, and Kyu-Yeol Park [91] can be seen in Figure 39.

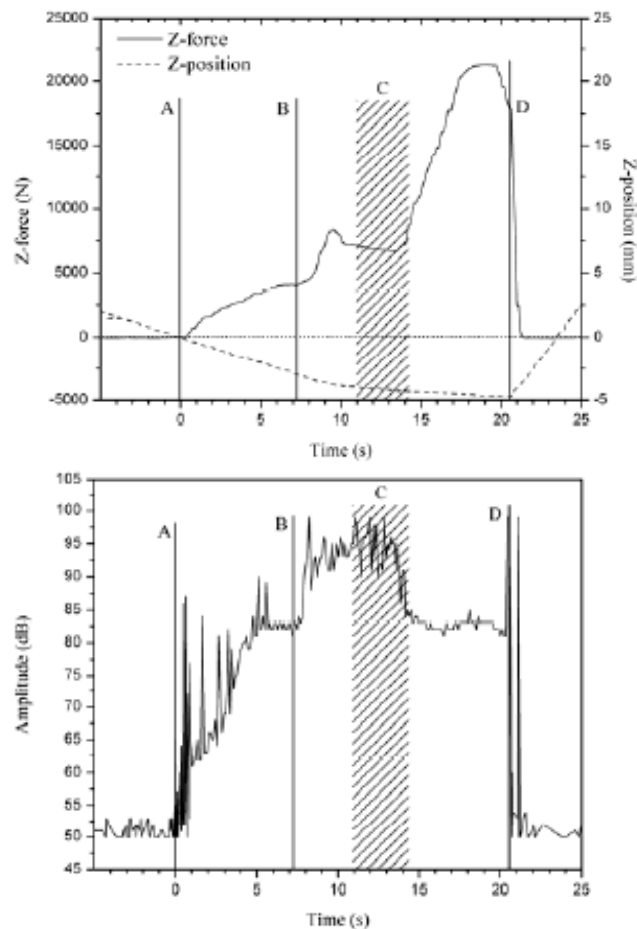


Figure 39: Z-force during FSSpW of 5052-H32 aluminium alloys as a function of time (top) and AE amplitude during FSSpW of 5052-H32 aluminium alloys as a function of time [91].

Conclusion on FSSpW

The AE monitoring of FSSW is a new technique. There are few papers published on this subject that only reveal that the use of AE on this technique could be possible.

3.6.3 AE on MIG/MAG welding

In this this paragraph, different papers on AE MIG/MAG welding monitoring and their results are listed up. This is an older technique with more known information today.

In a first paper AE emission of low carbon, a high strength and low –alloy steel weldments was investigated. Errors were induced in the welding technique to promote cracking. The AE emission was measured for both the in-process and in-cooling time phases. They found out that the source of a large quantity of emission generated by welding or its duration is not directly related to cracking. But there is a relationship between the AE results and cracking. A conclusion was that high-stressed welds produced more emissions than low-stressed ones on a per-electrode-deposited basis [29].

In the second paper, the potential of AE technology to detect welding defects on steel is investigated. There was worked with two pieces of mild steel who were welded together in the middle part. To compare the AE, good quality welds were made and welds with induced errors were made. Welds with defects exhibited higher activities of AE. They have a higher AE peak amplitude. The kurtosis of the welds with defects is also higher. Their results can be seen in Figure 40 and Figure 41 [92].

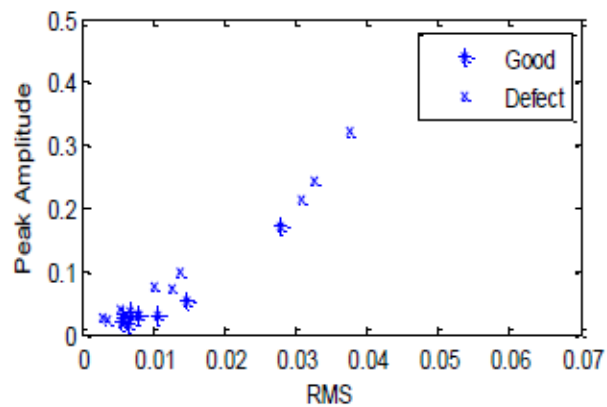


Figure 40: Peak amplitude and RMS distribution for good and bad welding joints with defects [92].

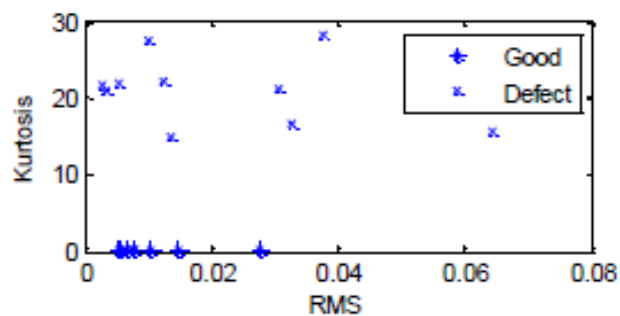


Figure 41: Kurtosis distribution for good and bad welding joints over acoustic emission RMS [92].

Welds with defects exhibited more frequency components compared to the good quality welds. This can be seen in Figure 42 and Figure 43 [92].

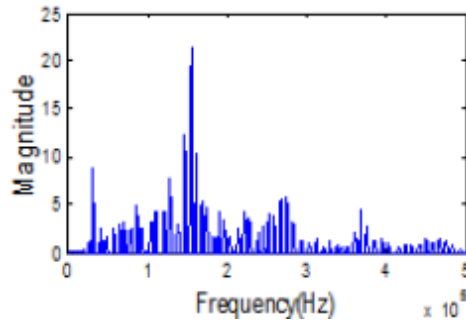


Figure 42: FFT spectrum for welding joints with a defect [92].

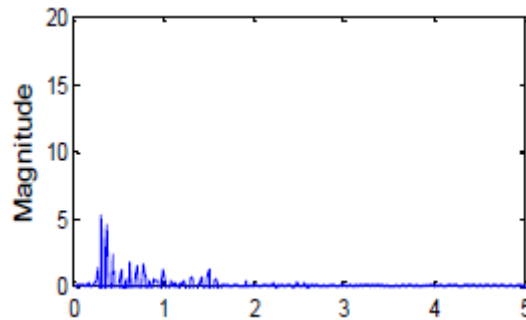


Figure 43: FFT spectrum for a good welding joint [92].

In the third paper AE measurements were done during submerged-arc welding. The goal is to check the capability of AE to detect crack growth. Different welding parameters were used to be compared on AE base. The cracks were produced by putting copper powder into the molten pool. It is possible to detect macroscopic hot cracks in real time by looking at the total of events over the time. With the use of multiple sensors it is possible to linear locate the crack [93].

In the last paper a welding process is carried out using AE. Defects were created: pores, hot and cold cracks, lack of fusion, penetration and slag inclusions. They propose a combination of the hits characteristics: Energy, number of oscillations (Counts), time of hit rising (Rise Time). By looking at the rise time different types of noise can be filtered and the Energy vs rise time representation has a good potential for detection of hot cracks [94].

Conclusions for MIG/MAG welding

MIG has multiple AE based control techniques who are used today. The analysis is done by looking at many different parameters and outcomes. There is still a lot to discover about AE on MIG welding.

4 Setup

4.1 Refill friction stir spot welding

The friction spot welds described in the test series were performed using a commercial refill friction spot welding equipment RPS 100 (Harms & Wende, Germany) and is illustrated in Figure 44 below.



Figure 44: Used refill friction stir spot welding machine [4].

The aluminium samples were clamped to a welding table with two fittings and an extra pincers in order to avoid movement while welding. This setup is visible in Figure 45.

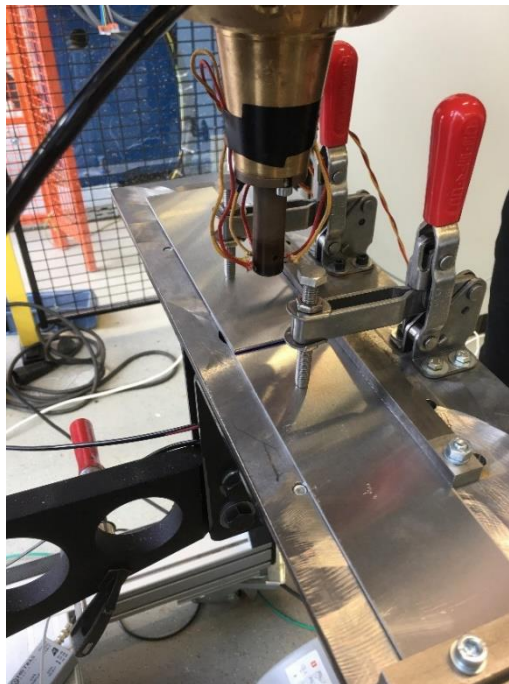


Figure 45: Welding table with two fittings.

4.2 Arc welding

In this section, the setup which was used to create the arc welds will be described. The used welding robot will shortly be discussed along with the selected welding parameters.

Welding robot

The welding robot in this experimental work is a KUKA robot (type KR 15/2). KUKA is an international automation company with their headquarter located in Germany [95]. The robot is visible in Figure 46.



Figure 46: Used robot to create the arc welds discussed in this investigation.

The robot was used to weld onto a steel plate that was placed on a working table, as visible in Figure 46. The sensor for recording the AE signals was clamped at the corner in order to avoid high temperatures at the sensor location. This is shown in Figure 47 and Figure 48.



Figure 47: Setup for the arc welding.

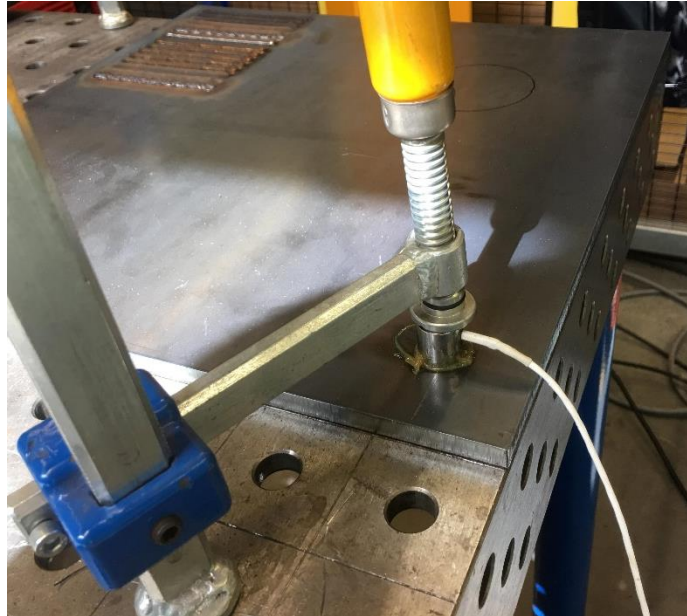


Figure 48: Placement of the sensor.

Selected welding parameters

A quick overview of the welding parameters for the weld tests is listed below:

- **Type of welding:** GMAW - MAG
- **Cooling:** liquid
- **Wire type:** solid
- **Power supply:** constant DC voltage
- **Gas supply:** 18 % CO₂ and 82 % Argon

4.3 Acoustic emission

In this paragraph, the setup that was used to record the AE signals is discussed. The different parts in the measuring system are visible in Figure 34 and will be described in detail hereafter.

As illustrated in Figure 34, a sensor (AE transducer) is used in order to detect the acoustic signals, emitted by the formation of a crack. Subsequently, the signal passes through a pre-amplifier, a filter, an amplifier and is finally detected by a signal conditioner and event detector. Once all these stages are passed, the signal is processed by a specific software.

Sensors

The sensor, or AE transducer in Figure 34, will transform the AE-pulse into an electrical signal. The AE signals in this experimental work which are described in Chapter 6 were recorded with two different types of sensors: the first type is a WD sensor with a resonance frequency of 450 kHz, and the second type a R50D sensor with a resonance frequency of 500 kHz. In first instance, the WD sensor was used, but at a later stage the R50D sensor was employed because of its slightly higher resonance frequency which could possibly eliminate the mechanical interference signals.

The specifications of the WD sensor (manufacturer: Mistras) can be found in the product data sheet in appendix A. This type has a high bandwidth and is therefore suitable to be used for frequency analysis. The optimal operating frequency response range is between 100 – 900 kHz (see appendix A). This sensor was used for the majority of the experiments by refill friction stir spot welding and for some experiments by MAG welding.

More details concerning the R50D (manufacturer: Mistras) can also be found in the product data sheet in appendix B. This type is a differential sensor, which is made to isolate the sensing terminals electrically from the cavity. These characteristics make the sensor suitable for applications with high electrical background noises. The frequency response range normally lies around 100 – 700 kHz. In this work, a digital filter configuration is used which ranges from 400 to 800 kHz. The difference in the upper limit makes sure that all the signals are obtained, measured by the sensor. This sensor was used for the last trials of experiments by refill friction stir spot welding and the majority of the experiments by MAG welding.

Location of the sensor

The location of the sensor was changed in order to investigate the influence of the location. It is generally known that the closer the sensor is placed to the welding location, a more accurate signal is obtained. The larger the distance between the welding location and the sensor, more higher frequent signals are lost. At a first stage, the sensor was placed on the support arm of the welding equipment. This meant that the signals had to travel a long way to the sensor, which resulted into attenuation and losing crucial information along the way. At a later stage, the sensor was clamped onto the working table on which the workpieces to be welded were located. In this way, the distance between the sensor and the weld making was reduced. At the last stage, the sensor was positioned on the workpieces itself, in order to minimize the path that the signals have to travel, resulting in a more accurate signal.

For the experiments made by MIG/MAG welding, the sensor was positioned in the furthest corner of the plate, at a secure distance of the arc welding process because the maximum working temperature of the sensor is 177 °C. During this process, higher temperatures are obtained because the material must be melted. Therefore, the presence of temperatures near the sensor which would be larger than 177 °C, would cause irrevocable damage to the sensor.

Preamplifier

A 2/4/6 switchable gain single ended and differential preamplifier (manufacturer: Mistras) was used and is shown in Figure 49. The switch between 2/4/6 means that gain ranges of 20, 40 and 60 dB is selectable. In this experimental work, the gain was fixed at 40 dB. It can operate with either single-ended or differential sensors. Plug-in filters provide the flexibility to optimize sensor selectivity and noise rejection. These filters are supplied in the low pass, high pass and band pass configurations, and offer constant insertion loss for easy filter swapping without the need for recalibration. Auto sensor tests allow the sensor to characterize its own condition, as well as send out a simulated AE wave that other sensors and AE channels can detect [96]. The datasheet can be found in appendix C.



Figure 49: Preamplifier of Mistras which was used in this investigation [96].

Amplifier and filters

In the equipment, an AE2A/AE5A wide bandwidth AE amplifier is fitted in. The datasheet can be found in appendix D for further specifications. It is a small, high-performance AE system that amplifies and filters an incoming AE signal either directly from an AE sensor or from an external pre-amplifier. The resulting high-frequency AE analog signal output can be connected to a variety of external monitoring and data acquisition instruments (see appendix D).

Coaxial cables and connectors

BNC connector types and coaxial cables are used in order to connect the different parts of the equipment.

External trigger

In order to match the start of the welding process, indicated by the increase of the rotational speed, with the start of the wavestream recording, the AE measuring system makes use of an external trigger. To this end, a pressure switch (type TTL switch) is used to trigger the signal.

When the clamping ring touches the surface of the upper sheet and subsequently the rotational speed increases, a pressure is built up. This is detected by a pressure switch, and hence the voltage increases from 0 to 5 V. At this moment, a triggering signal is sent to the AE measurements system, which starts recording the wavestream.

5 Evaluation methods of the test series

In the next chapter, the test series that were executed will be discussed. These test series consist of both friction spot welds and arc welds, during which AE monitoring was performed. Every time a new aspect in the investigation had to be examined, a new test series was initiated, so conclusions could be made by comparing the two test series. This chapter describes which characterization methods were performed on the welds.

5.1 Lap shear strengths

In first instance, the friction spot welds were characterized for their lap shear strengths. When a test series was made, a tensile test according to EN ISO 14273 (see Figure 50) was applied to the welds, in order to know their lap shear strengths. The principle of a tensile test is given in Figure 51.

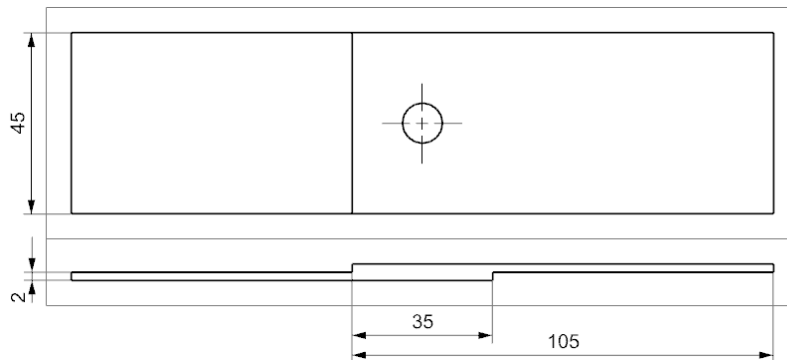


Figure 50: Dimensions of the tensile test samples according to EN ISO 14273.

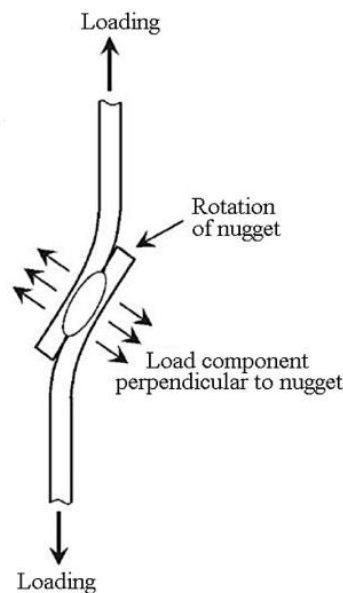


Figure 51: Principle of a tensile test [1].

Different fracture modes were observed, of which a more detailed description is found in section 2.1.4. Based on the values of the lap shear strength, control charts were constructed and the welds which exhibited the most differences in tensile strength were investigated in terms of their AE signals. Sometimes there were differences of 1 kN, while the same welding parameters were applied. The goal was to investigate whether or not these differences in tensile strength could be observed in the AE signal. If successful, a prediction of the tensile strength could be made, based on the AE signal.

5.2 Metallographic examination

At another stage in the investigation, it was more important of being able to predict whether or not a certain weld defect occurred inside the weld. Test series were made in which these weld defects were induced, in order to possibly relate these defects to the AE signals. The appearance of these weld defects and metallographic examples are described in Chapter 2. In order to perform a metallographic examination, a few steps need to be performed: cutting, embedding, polishing and etching.

Metallographic cross-sections were made by cutting the weld in half, through the center of the weld nugget. The samples were thereafter placed into a specimen mounting cup where they were embedded in an epoxy. As was used in previous work [3], a mixture of CaldoFix resin and hardener was applied. The process of embedding takes one day at room temperature. After curing the epoxy traces from the cross-section surface were removed, after which several polishing steps were applied in order to remove all micro-scratches. As a last step, the cross-sections were etched using Keller's reagent, to reveal the details of the microstructure. The duration of this step is variable as this is very important for the variety in grain sizes [3]. After the metallographic preparations, the cross-sections were examined using an Olympus MX51 optical microscope.

Furthermore, there is a technology to investigate the area percentage of imperfections compared to the overall area in order to determine the weld quality. Only the areas with a minimum value of 0,002 mm² are considered as a defect, in order to distinguish small porosities of the base material from the welding defects [3]. An example is given in Figure 52. However the area percentage technology is not used in this work, it will not be further discussed.

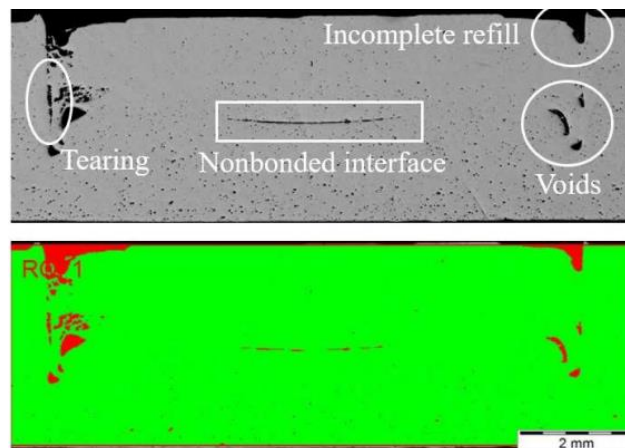


Figure 52: Non-etched cross-section (top) and area percentage of imperfections (bottom) [97].

Next to the metallographic evaluation of the refill friction stir spot welds, also the cross-sections of the arc welds are investigated. A detailed view of the additive material (AM) bonding with the base material (BM) is shown in Figure 53.

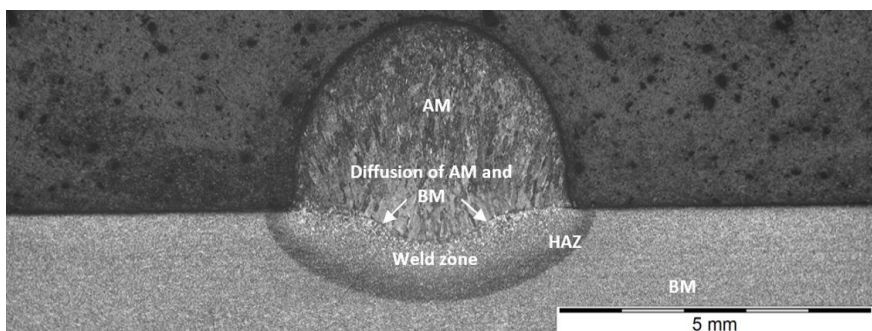


Figure 53: Metallographic evaluation of arc welds (weld SW-ROB-R16-1.3).

5.3 Temperature measurements

In order to investigate the influence of the temperature on the weld quality and the attendant acoustic emission, thermocouples were used. A thermocouple is a kind of temperature sensor based on the Seebeck-effect, visible in Figure 54. It consists of two wires of different metal alloys who are connected. When there is a difference in temperature between the attachments, a potential difference is created. The size of the potential difference depends on the difference in temperature and the used materials. This potential difference is measured and thereafter converted into a temperature measurement [98].

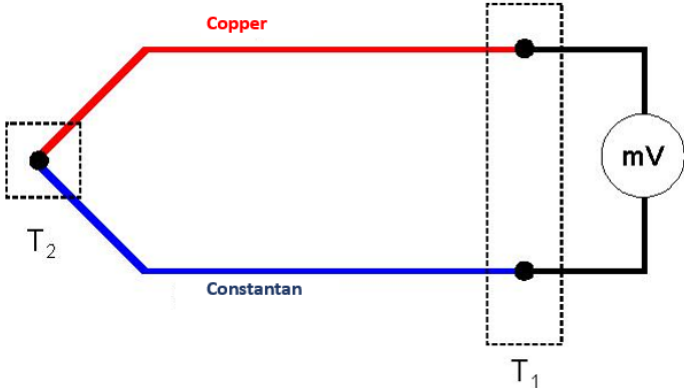


Figure 54: Seebeck-effect used in a thermocouple [99].

Since the aluminium samples need to be replaced each time a weld is created, it would be labour-intensive to place the attachments on the samples. Therefore the thermocouples are soldered on the clamping ring in order to measure the temperature as close as possible to the welding nugget. The used setup is visible in Figure 55.

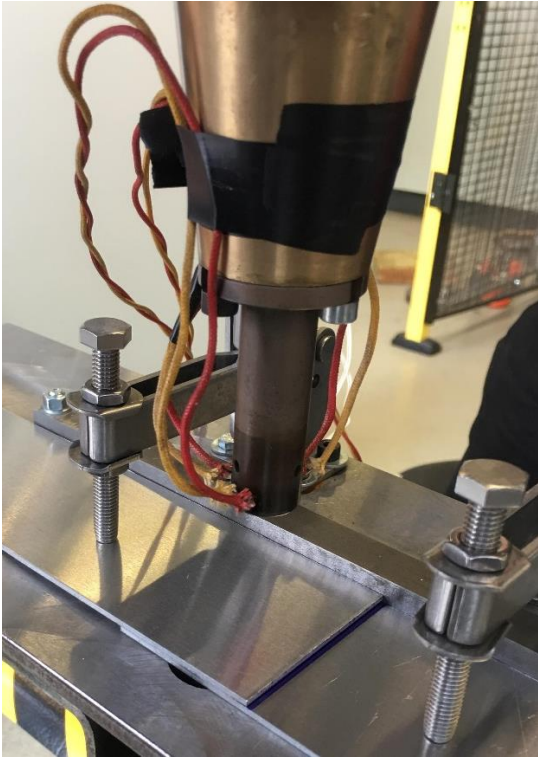


Figure 55: Soldered thermocouples on the clamping ring.

At first, the data received from the thermocouples were processed in a LabVIEW program. After this, a more accurate software program was used, named PicoLog 6. This program was more user-friendly because the received data was directly used to plot a graph without any further analysis needed.

Three thermocouples were used to make sure that the received data was relevant and realistic. The three temperature measurements could be compared with each other in order to spot incorrect values. However, the temperature measurements vary a little bit due to the different positions of the thermocouples.

A typical curve of the measured temperature is shown in Figure 56.

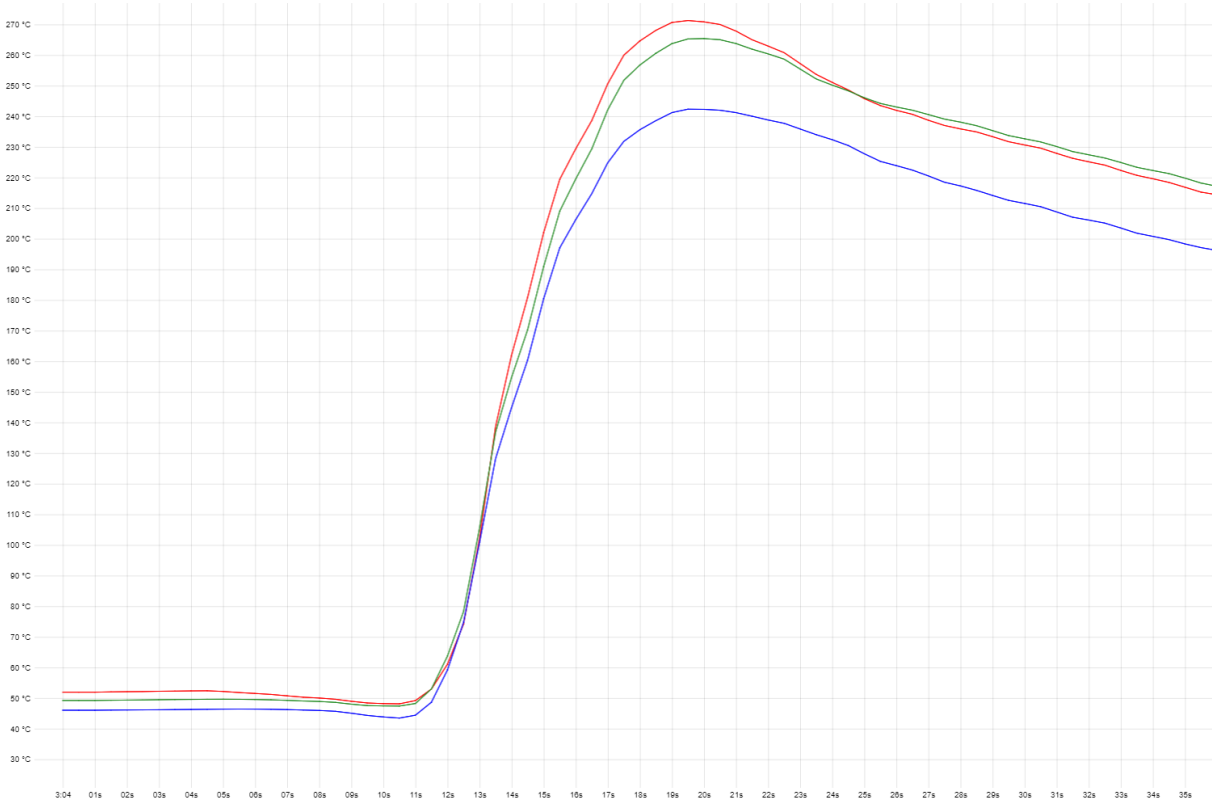


Figure 56: Typical curve of the measured temperature (Weld nr. SW-68-R17-1.1).

5.4 Acoustic emission examination methods

For the acquisition of the AE data, the software program AEwin is used [100]. It is a Windows-based program for real-time simultaneous Acoustic Emission feature and waveform processing, display, fast storage and replay.

For the analysis of the AE signals, two software programs are used: Flexpro and Noesis. FlexPro is an analysis software from Weisang used for data analysis and presentation [101]. The program was used to visualize the wavestream, which is the voltage signal that is recorded during welding. Moreover, the program allows to perform a fast Fourier transformation (FFT) on the wavestream. Noesis is a Windows-based software program for advanced acoustic emission data analysis, pattern recognition and neural networks [71]. This program is used to visualize and process the hit driven data derived from the wavestream signal. The following paragraphs describe the different output data for each program.

5.4.1 Wavestream data

The wavestream is the amplitude (V) vs time (μs) signal that is recorded during welding, using the AEwin program. At the same time the welding parameters of the welding machine, such as the mechanical movements, rotational speed and currents are recorded using the mScope program. In order to relate the wavestream signal to the different stages during the welding process, the two different data sets had to be plotted on top of each other. The FlexPro (student version 6.0) software was able to do this which was the reason of usage.

The wavestream data (format: wfs files) were exported to .txt files using Noesis, whereas the welding parameter data were logged as csv files. Both files could be imported into the Flexpro program. Once imported, these signals were displayed in columns with datapoints in different rows. By merging the columns of the welding parameters and the AE signals, a graph could be composed that allowed to relate the different welding phases to a specific part of the wavestream, as illustrated in Figure 57.

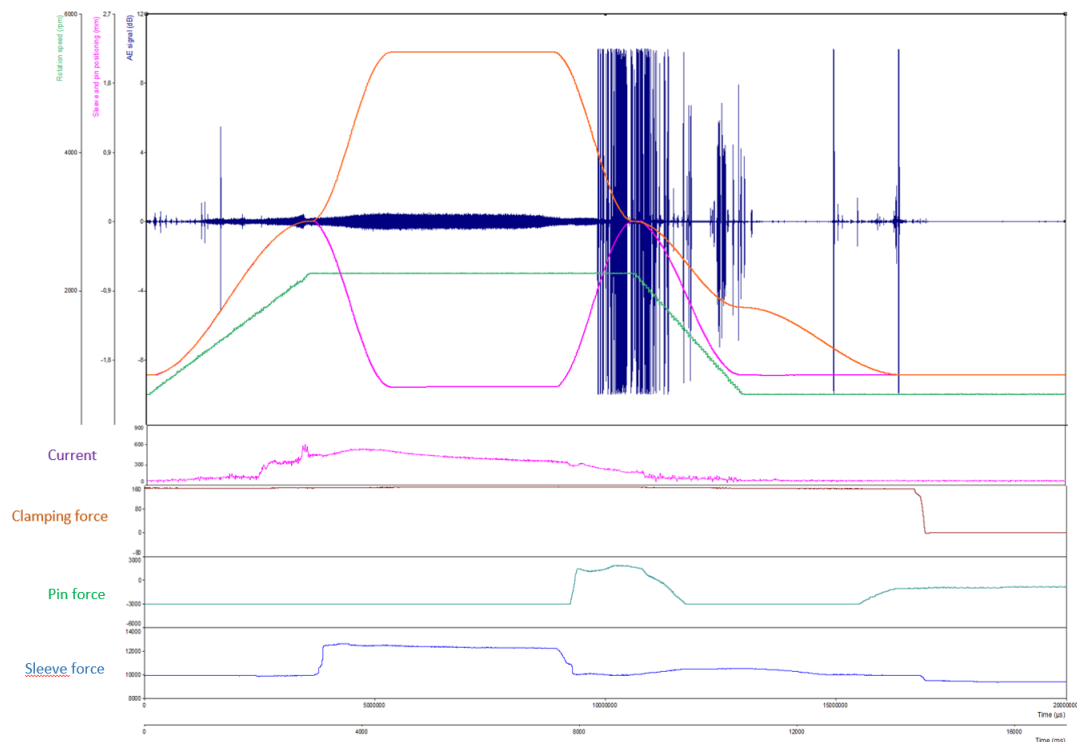


Figure 57: Visualisation of the AE signal in combination with the welding parameters (weld nr. SW-68-R5-1.9).

The first chart represents the wavestream signal (Amplitude in V vs time in μs), sleeve and pin positioning (mm) and the rotational speed (rpm) in dark blue, orange, purple and green, respectively. The wavestream in the time domain is expressed in microseconds (μs), because one million samples (sampling rate = 1 MSPS) were recorded in one second, while the other curves are expressed in milliseconds (ms).

Below this chart, there are 4 other curves with different Y-axes. These curves display the measured current, needed for the actuator to let the spindle rotate and the forces. The currents are normally expressed in Ampère and the clamping force in kN, but due to the transition from MScope to FlexPro, these values are also transformed. Because of this, there is no certainty to determine the correct unit. However, the mathematical ratio between these values is retained.

The next step was to examine the wavestream by performing manipulations on it. A fast fourier transformation (FFT) on the wavestream seemed the best method to investigate the signal in the frequency spectrum. More explanation is given in the next paragraph.

Fast Fourier Transformation (FFT)

A FFT was applied on the wavestream signal in order to investigate it in the frequency domain. The intention was to identify peaks at certain frequencies and relate them to mechanical movements or events that happened within the weld in order to determine the weld quality. A visualisation of the wavestream signal and its FFT curve is given in Figure 58.

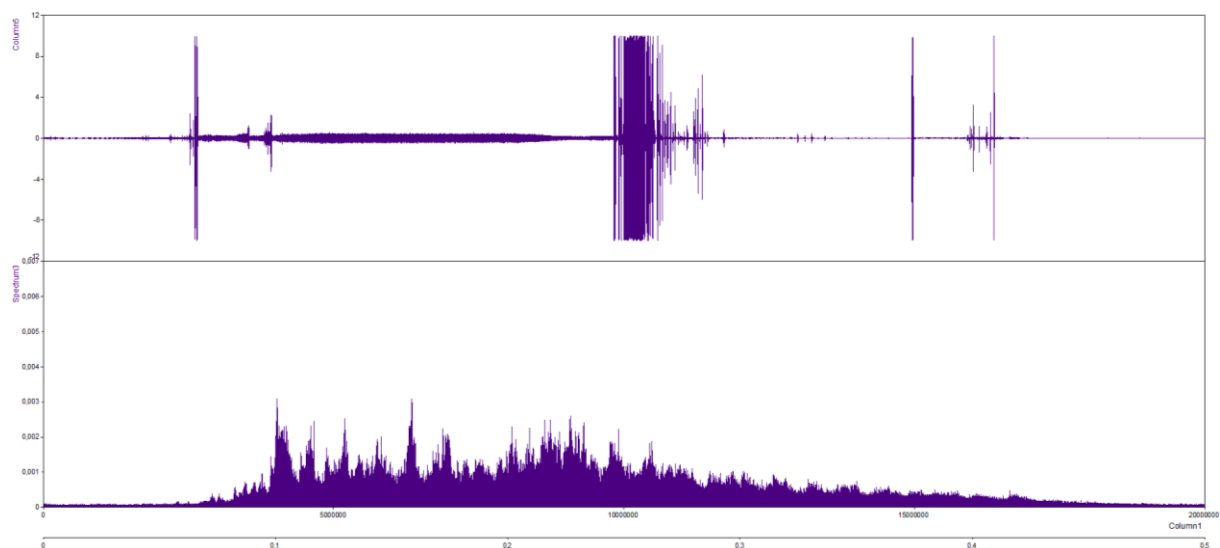


Figure 58: Wavestream curve: amplitude (V) vs time (μs) (above) and FFT curve: amplitude ($V^2\text{rms}$) vs frequency (MHz) (below) (weld nr. SW-68-R5-1.3).

Division into weld phases

Since the wavestream could be investigated in both the time domain and frequency domain, it was important to zoom into certain parts of the signal. As indicated in section 1.1.3, there are different welding phases taking place during the refill friction stir spot welding process. The signals related to the weld quality are found in the phases where the material is penetrated by the sleeve (plunge phase), during the dwell time (dwell phase) and when the pin pushes the material back into the created keyhole in order to refill the friction spot (retraction phase). When these phases are compared to the measured welding parameters, 5 phases can be distinguished. This is visible in Figure 59: the first curve is the pin position (blue), the second curve is the sleeve position (purple) and the third curve is the rotational speed (orange). They are expressed over time in ms.

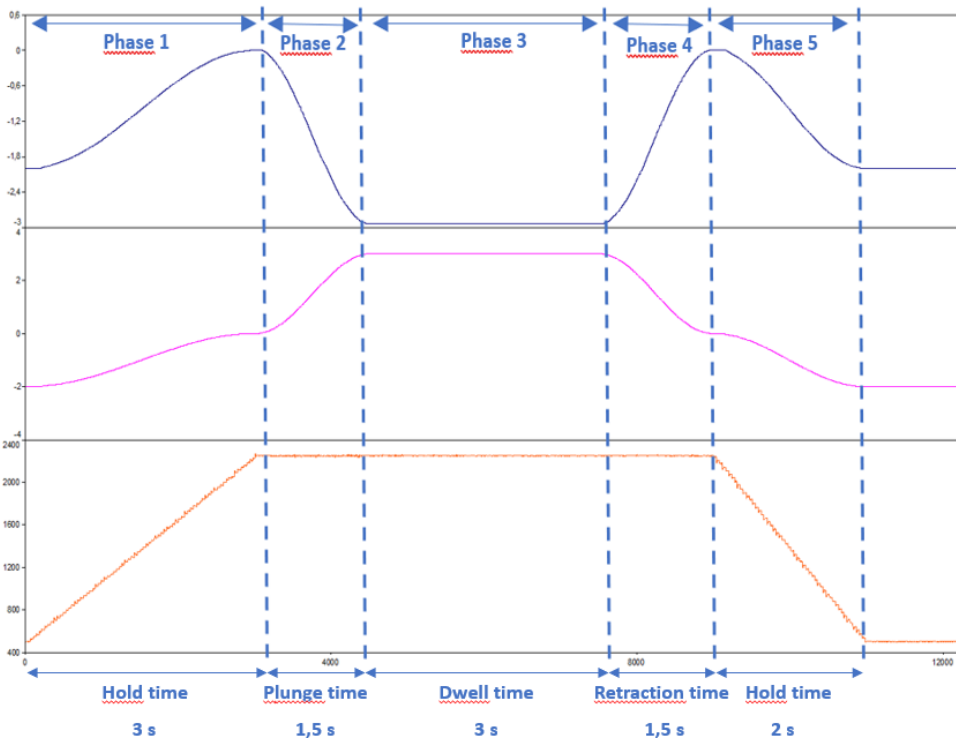


Figure 59: Division in phases based on the welding parameters (test series: SW-68-R5).

Based on the division in Figure 59, the wavestream can be divided as well. This is illustrated in Figure 60.

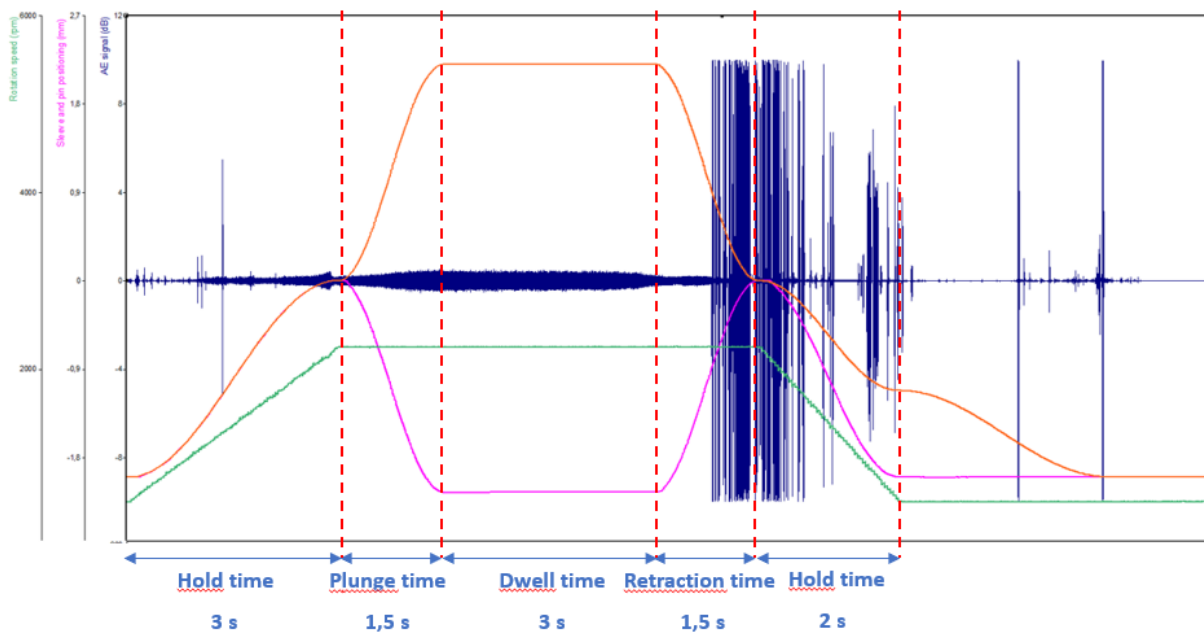


Figure 60: Division of the wavestream.

As mentioned above, it is only of an importance to investigate the phases where the signals are related to the weld quality. These are phase 2, phase 3 and phase 4, which stand for the sleeve penetration, dwell time and sleeve retraction respectively. The remaining phases 1 and 5 represent the lowering and lifting of the tool to and from the aluminium sheets, respectively. In phase 1, the tool accelerates to the selected rotational speed, while it slows down in phase 5. Selective investigation of phase 2, 3

and 4 means filtering out the signals in phase 1 and 5, which correspond to signals caused by the mechanical movement of the welding equipment.

For each investigated phase, the wavestream is plotted along with its corresponding FFT. An example for phase 2, 3 and 4 is given in Figure 61, Figure 62 and Figure 63, respectively.

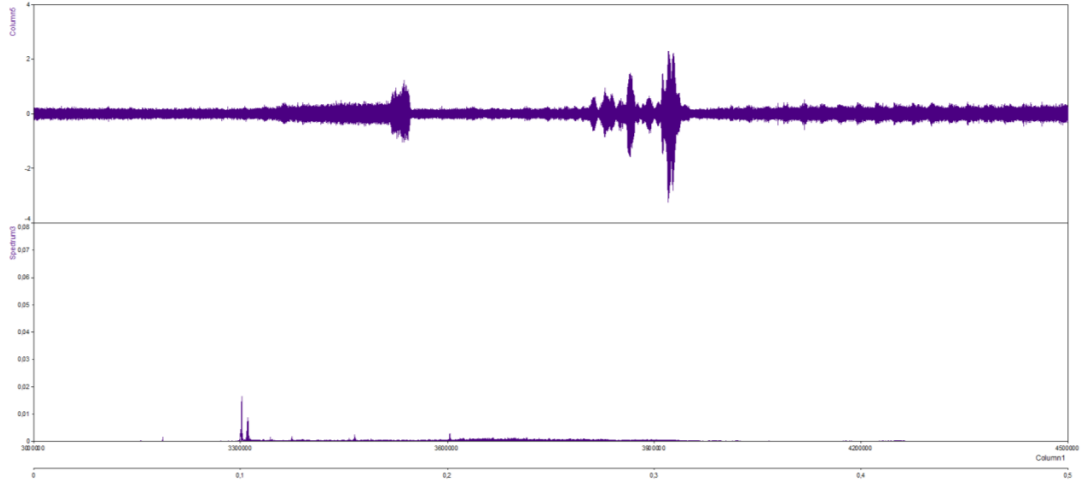


Figure 61: Wavestream of phase 2 (above) and its corresponding FFT (below) (weld nr. SW-68-R5- 1.3).

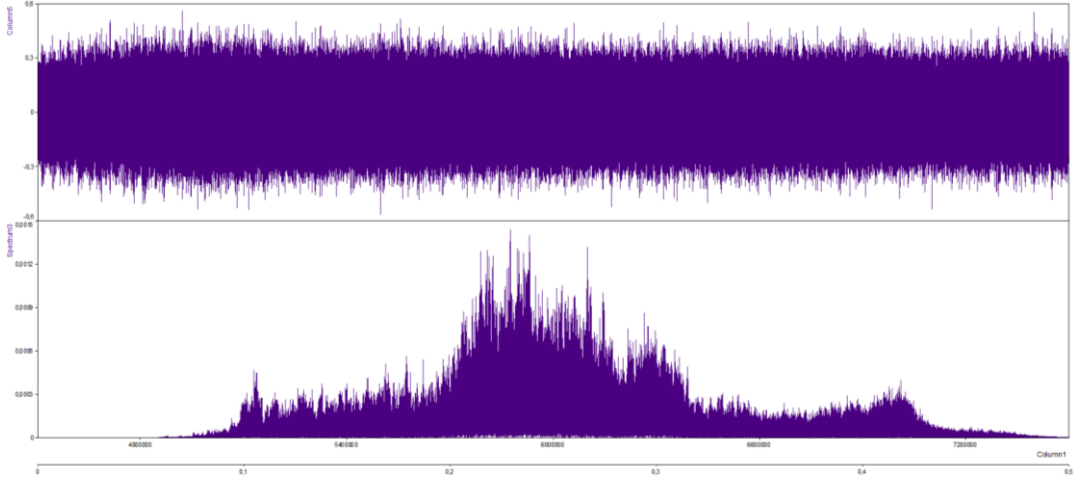


Figure 62: Wavestream of phase 3 (above) and its corresponding FFT (below) (weld nr. SW-68-R5- 1.3).

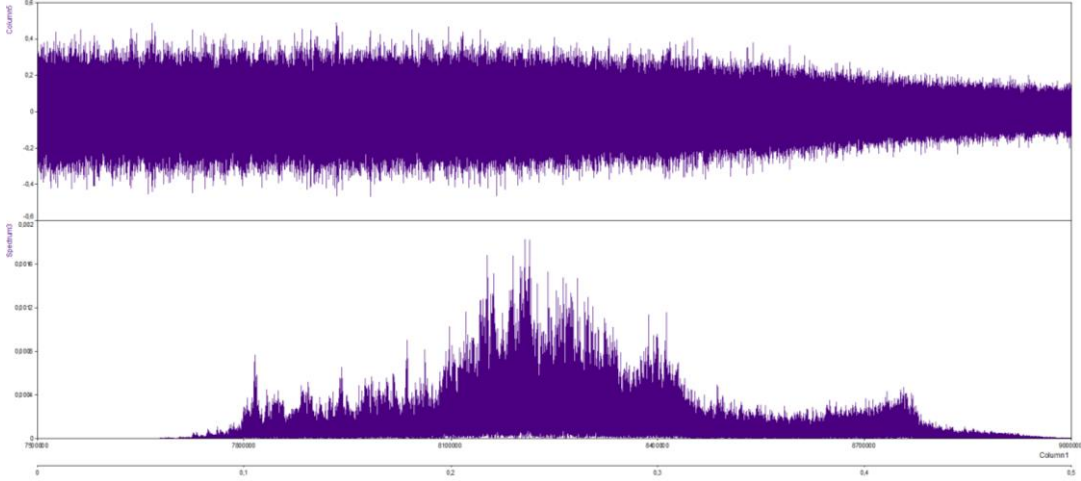


Figure 63: Wavestream of phase 4 (above) and its corresponding FFT (below) (weld nr. SW-68-R5- 1.3).

5.4.2 Hit driven data

Each time the wavestream signal exceeds the threshold, a hit is created. For each hit, different features can be extracted such as the amplitude, energy, average signal level, frequency etc. These characteristics can provide an indication of the weld quality obtained. In the following paragraphs, these different characteristics, which are processed in the Noesis program, are described in detail.

ASL/Time

Average signal leveling (ASL) in the time domain is a signal processing technique intended to increase the strength of a signal relative to noise that is obscuring it. The goal is to increase the signal-to-noise-ratio (SNR) by averaging a set of measurement values [102]. The average signal level is the logarithm of the root mean square and is a measure of the continuously varying and averaged amplitude of the wavestream signal. This way of expressing the AE signal could possibly tell more about the energy of the process and the bonding that takes place during welding. The formula for the ASL can be found below:

$$ASL = \sqrt{\frac{1}{T_{ASL}} \int_{t_0}^{t_0 + T} \left(20 \log \left(\frac{U(t)}{1\mu V} \right) - dB_{preamplifier} \right) dt}$$

Where T_{ASL} corresponds to a characteristic time, in the range of 10 to 1000 ms.

An example of the ASL/time graph for a MAG weld and refill friction stir spot weld is shown in Figure 64 and Figure 65, respectively.

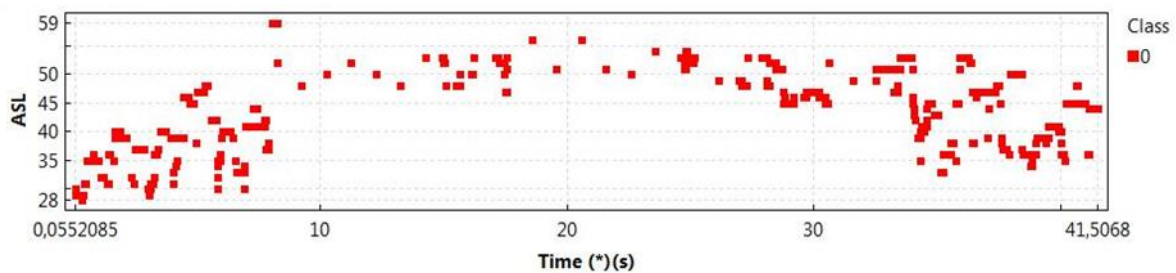


Figure 64: ASL/Time for a MAG weld (nr. SW-R22-1.5).

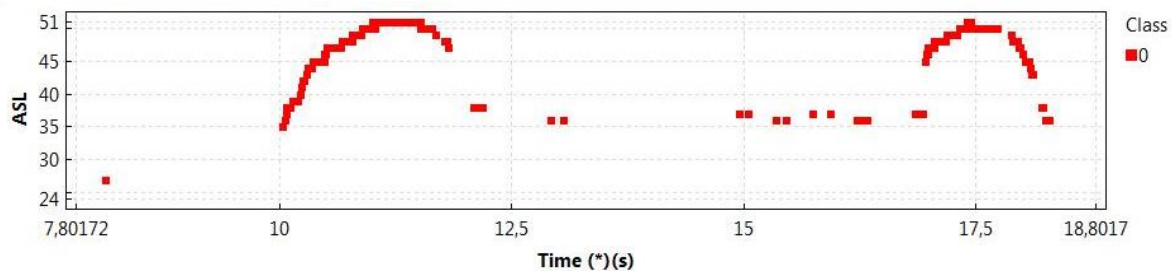


Figure 65: ASL/Time for a refill friction stir spot weld (nr. SW-68-R28-1.4).

Another format is the cumulative ASL in the time domain. In this case, the values are added consecutively. A representation of a MAG weld and refill friction stir spot weld is given in Figure 66 and Figure 67, respectively.

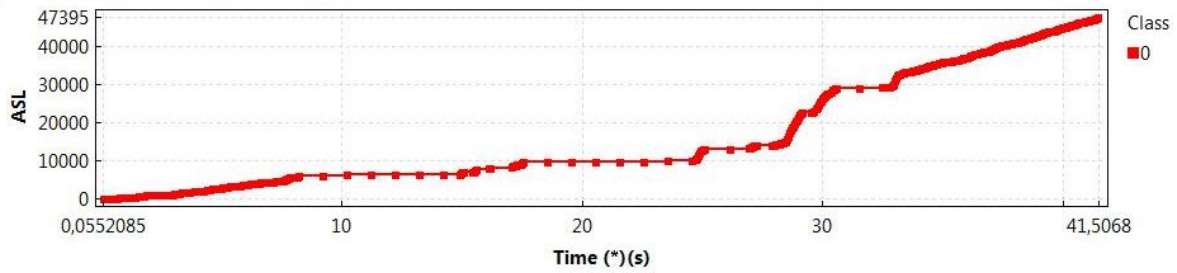


Figure 66: Cumulative ASL/Time for a MAG weld (nr. SW-R22- 1.5).

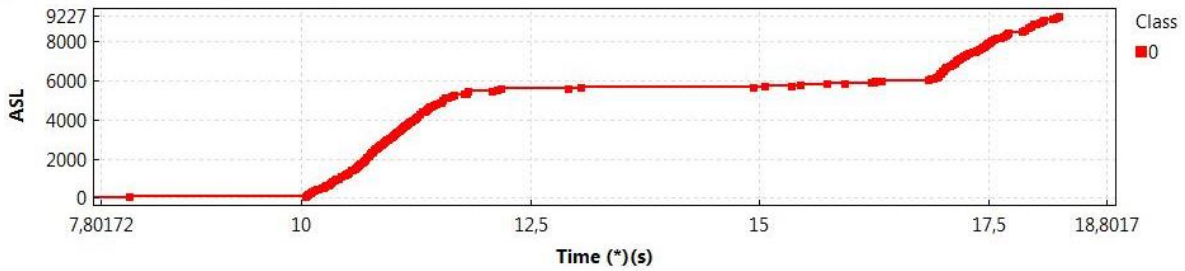


Figure 67: Cumulative ALS/Time for a refill friction stir spot weld (nr. SW-68-R28-1.4).

Duration/Amplitude

Generally, it is known that bursts created by cracks have a short duration (μs) and a high amplitude (dB). By plotting the duration on the vertical axis and the amplitude on the horizontal axis, it is possible to search for these bursts as they will be located at the right bottom corner. By using this method of representation, also deformation and electromagnetic interference (EMI) can be identified. Deformation will cause bursts with a lower amplitude, which increases slightly when the duration increases. The EMI can be found at the higher amplitudes, especially when there is a long duration. This way of examining can filter out any other irrelevant signals.

A representation of a MAG weld and a refill friction stir spot weld is visible in Figure 68 and Figure 69, respectively.

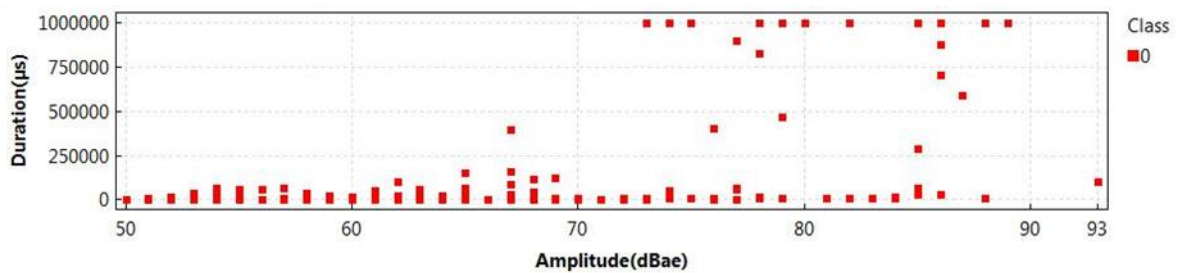


Figure 68: Duration/Amplitude for a MAG weld (nr. SW-R22- 1.5).

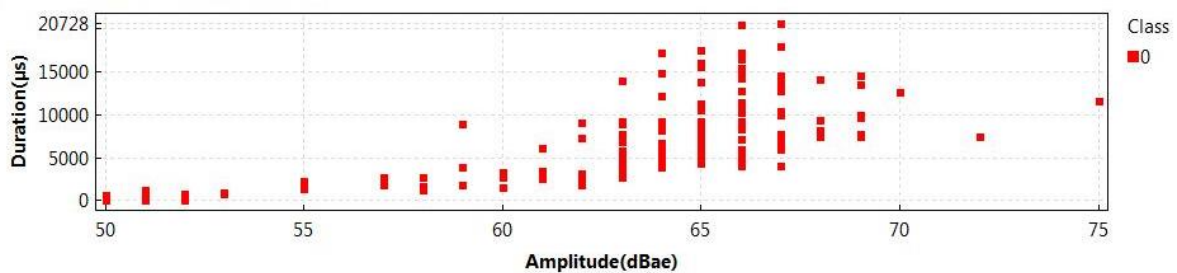


Figure 69: Duration/Amplitude for a refill friction stir spot weld (nr. SW-68-R28-1.4).

Amplitude/Time

This signal representation closely resembles the wavestream signal. The only difference is that only the points which exceed the threshold are represented. By selecting the threshold at a relevant value, it is possible to filter out the background noise, which can have a smaller amplitude. An example for the MAG weld and refill friction stir spot weld is shown in Figure 70 and Figure 71, respectively.

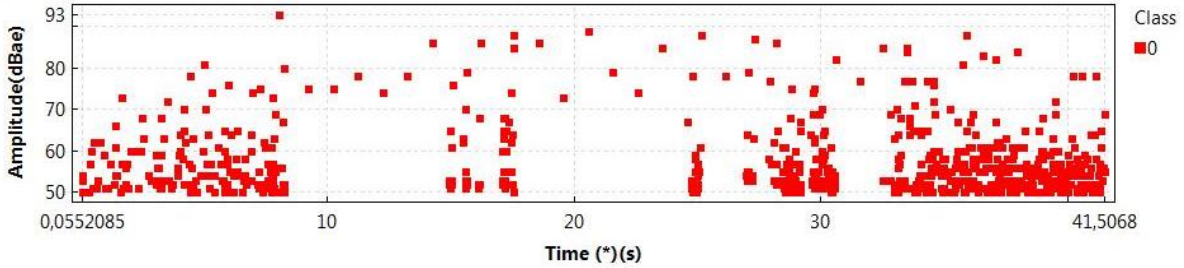


Figure 70: Amplitude/Time for a MAG weld (nr. SW-R22-1.5).

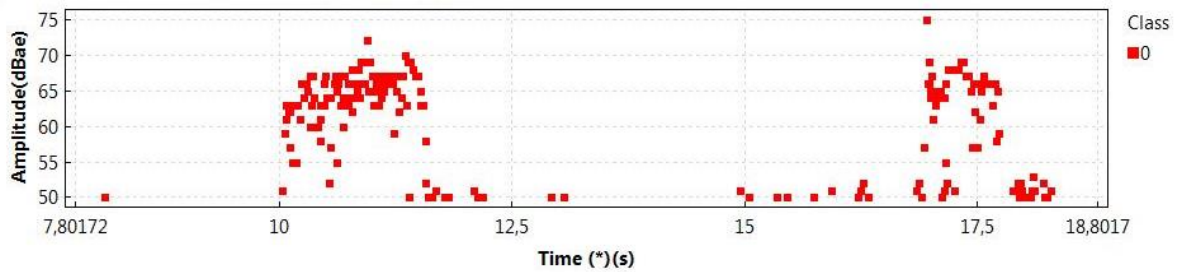


Figure 71: Amplitude/Time for a refill friction stir spot weld (nr. SW-68-R28-1.4).

Frequency centroid/Time

The frequency centroid is used to characterize the overall frequency content of an acoustic emission signal [103]. It can be considered as the “center of mass” of this frequency signal. In general, this result is not the same as the peak frequency, but it is an additional information to the characteristic average frequency [103]. Further investigation in the frequency domain is performed in the FlexPro program as a FFT curve can be calculated. The manipulating formula for obtaining a frequency centroid is shown below:

$$f_{centroid} = \frac{\int f \cdot \tilde{U}(f) df}{\int \tilde{U}(f) df}$$

An example of this representation for a MAG weld and refill friction stir spot weld is shown in Figure 72 and Figure 73, respectively.

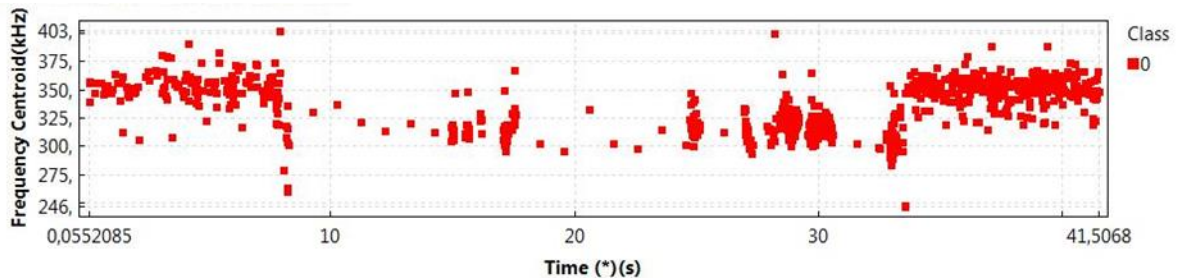


Figure 72: Frequency centroid/Time for a MAG weld (nr. SW-R22-1.5).

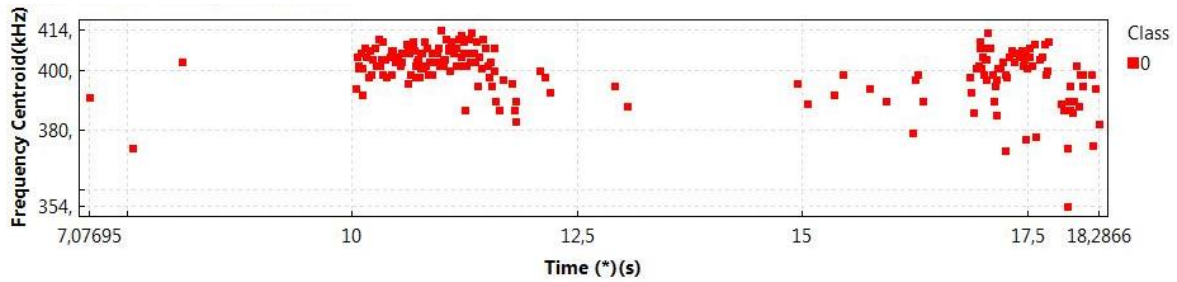


Figure 73: Frequency centroid/Time for a refill friction stir spot weld (nr. SW-68-R25-1.4).

Cumulative counts/Time

This examination method provides the number of time when the wavestream signal exceeds the threshold. When this happens, one count is added to previous value, starting at zero. This representation is very close to the absolute energy/time representation, but it is not the same. The areas where the curve has a steep slope, reveals the possibility of something going on in the material as a kind of bonding. Although this evaluation method is mostly used for identifying cold cracks (cracks that are formed once a weld is made, during cooling down), it can be useful in this setup too. An example for the MAG weld and refill friction stir spot weld is shown in Figure 74 and Figure 75, respectively.

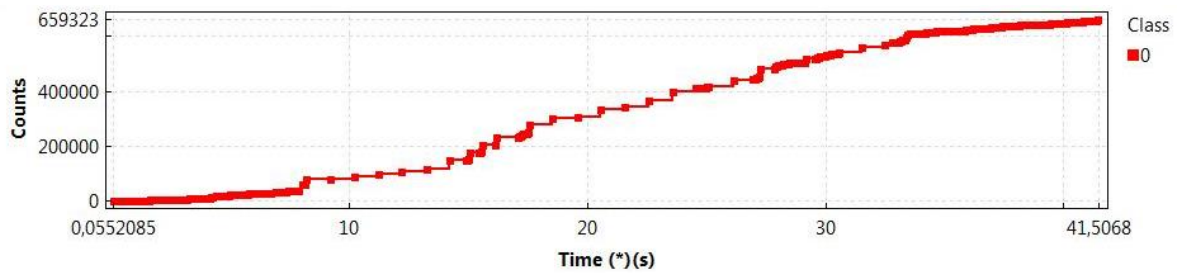


Figure 74: Counts/Time for a MAG weld (nr. SW-R22-1.5).

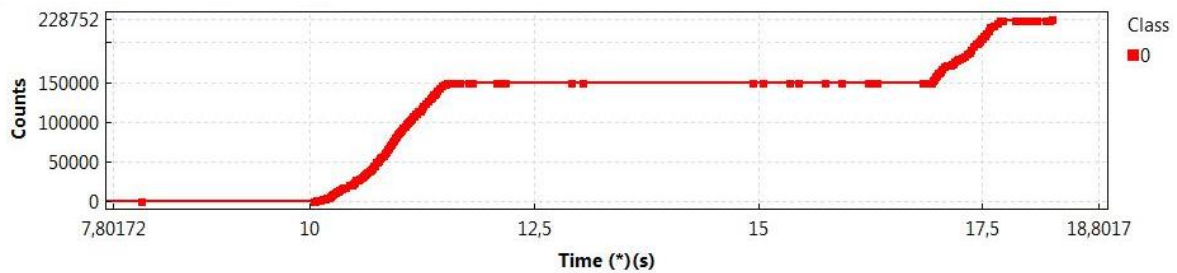


Figure 75: Counts/Time for a refill friction stir spot weld (nr. SW-68-R28-1.4).

Cumulative absolute energy/Time

The cumulative absolute energy in the time domain is an absolute measure of the electrical energy measured for an AE signal and is expressed in Atto-Joule [103]. Similar to the counts/time representation, the areas with a steep slope reveal the possibility that something is going on in the material. The formula which is used to perform this manipulation is shown below, where 'x' corresponds to the input impedance of the recording equipment.

$$W_{AE} = \int_0^{t_{AE}} \frac{(U(t))^2}{xk\Omega} dt$$

An example of this representation for a MAG weld and a refill friction stir spot weld is shown in Figure 76 and Figure 77, respectively.

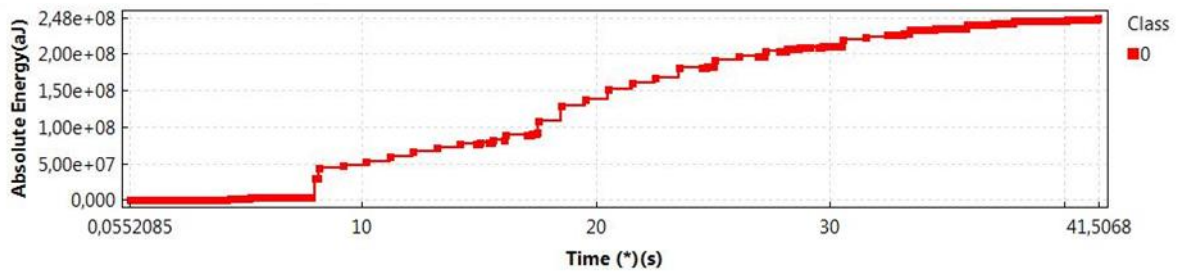


Figure 76: Absolute energy/Time for a MAG weld (nr. SW-R22- 1.5).

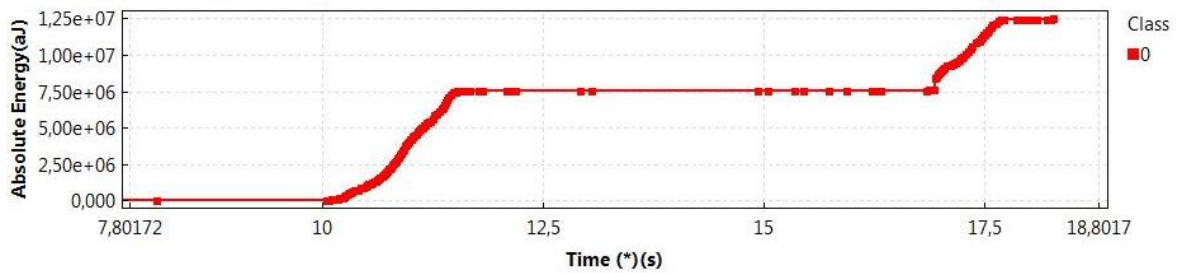


Figure 77: Absolute energy/Time for a refill friction stir spot weld (nr. SW-68-R28- 1.4).

Rise time/Time

The rise time is the time for a pulse to rise between 10% and 90% of a specified value. It is generally known that electromagnetic noises have a very small rise time. By discriminating the small rise times, it is possible to filter out the electromagnetic noises. An example of the rise time/time representation for the same MAG weld and refill friction stir spot weld is shown in Figure 78 and Figure 79, respectively.

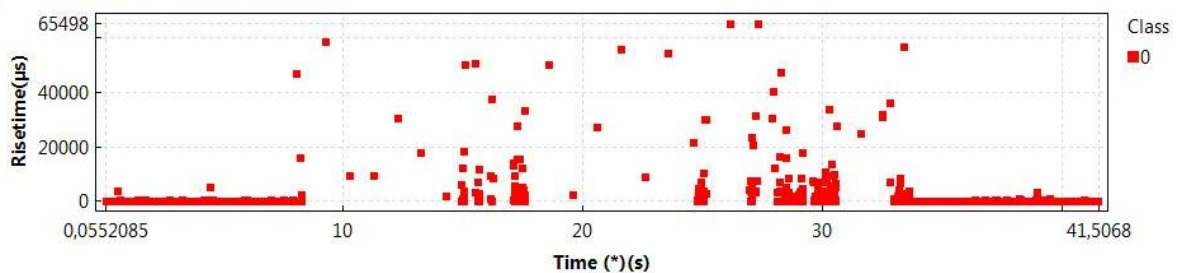


Figure 78: Risetime/Time for a MAG weld (nr. SW-R22-1.5).

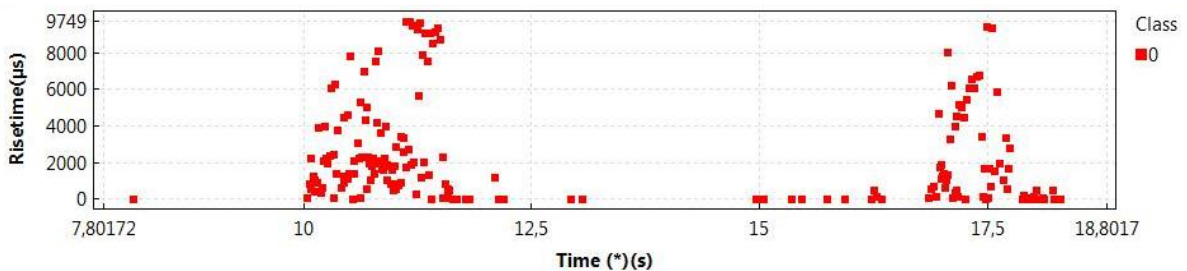


Figure 79: Risetime/Time for a refill friction stir spot weld (nr. SW-68-R28-1.4).

Energy/Counts

This representation was used for analysing the welds of the smaller MAG cobot and is an un-known method of evaluation that is investigated in the experimental research. The energy is supposed to reveal information about the fracture processes, while the counts reveal the hits where the threshold is exceeded rapidly for several times. An example of this representation for a MAG weld can be seen in Figure 80 for weld nr. SW-R21-1.3. The hits with counts higher than 15000 are encircled, in order to investigate certain parts in the signal.

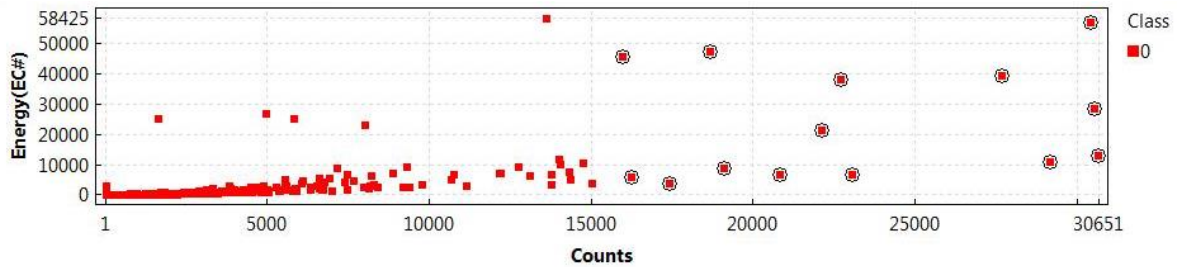


Figure 80: Energy/counts for a MAG weld (nr. SW-R21-1.3).

Absolute energy/Rise time

The expression of absolute energy expressed in terms of the rise time was also used for the analysis of the welds from the smaller MAG cobot. This method is also an unknown method of evaluation that is investigated in this experimental research. The goal was to find a link between the rise time and the absolute energy, in order to identify the noise originating from the welding equipment, which has a small rise time. An example of this examination method is given in Figure 81. The hits containing high energies and rise times were encircled in this case.

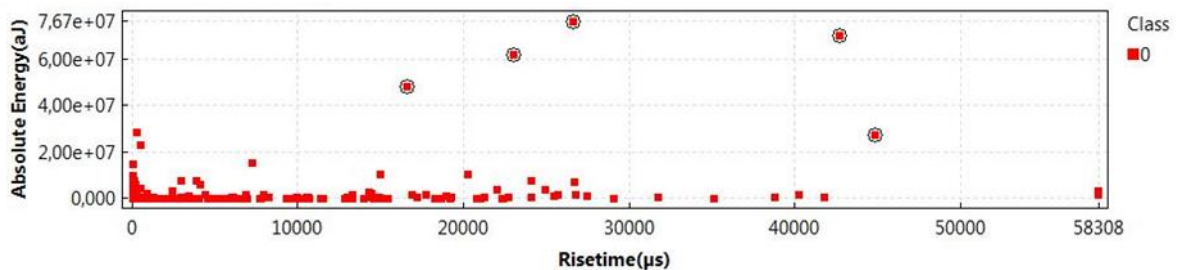


Figure 81: Absolute energy/rise time for a MAG weld (nr. SW-R21-1.3).

6 Analysis of the acoustic emission results

An overview of the results all the different test series is given in this chapter. First, the selected welding parameters are listed. These are the parameters that are varied between each test series: the plunge depth (PD), the rotational speed (RS), the plunge time (PT), the dwell time (DT), the retraction time (RT) and the hold time (HT). Also the parameters that were modified in the acoustic emission software, such as the sampling rate, the threshold and the frequency range of the digital filter, are presented. The other parameters for acoustic emission that were fixed throughout all test series are mentioned below. Moreover the cleaning frequency, the used material, the type and location of the sensor are mentioned. Next, the objective of each test series will be explained and finally, the results and conclusions are formulated, where possible problems and analysis will be discussed. The differences on the time-axis of the ASL/Time-, Frequency centroid/Time-, Absolute energy/Time- and Counts/Time-graph is due to the fact that each weld was welded at a different relative time, resulting in a different starting point. The time-graphs in this text are set at the same absolute time, resulting in the same starting point for each curve. In this way it is possible to compare the graphs. All the graphs are available in an external appendix, other important figures will be presented and described in the text. The external appendix is property of the Belgian Welding Institute.

The most important acoustic emission parameters are cited in the tables below. The fixed/variable row indicates which parameters were fixed and which were variable throughout the experimental test series.

Table 2: AE Channel Setup configuration.

AE Channel Setup						
	AE Channel	Threshold		Gain		Global waveform
		Type	dB	FTBnd	dB	
	1	FIXED	60	6	0	Enabled
Fixed / variable	Fixed	Variable				Fixed

Table 3: Preamp configuration.

Preamp				
	AE Channel	Preamp		
		Type	Gain db	Voltage
	1	2/4/6	40	28
Fixed / variable		Fixed		

Table 4: Sensors, filters and waveforms configuration.

Sensors, Filters and Waveforms									
	AE Channel	Sensor	Analog filter		Digital filter		Waveform setup		
			Lower	Upper	Lower	Upper	Sample Rate	Pre-trigger	Length
	1	WD	100 kHz	3 MHz	100 kHz	400 kHz	1 MSPS	20.000	1k
Fixed / variable	Fixed	Variable	Fixed		Variable				Fixed

Table 5: Waveform streaming configuration.

Waveform streaming							
	AE Channel	Sample Rate	Pre-trigger		Record Length		Streaming
			milliseconds	kSamples	milliseconds	kSamples	
	1	1 MSPS	20.000	25	20000	19532	Enabled
Fixed / variable	Fixed	Variable	Fixed				

Table 6: Data sets and parametric configuration.

Time Driven Channel Data								
	RMS	ASL	Absolute Energy	Counts	Duration	Amplitude	Rise Time	Time driven rate
		Disabled	Disabled	Disabled	Disabled	Disabled	Disabled	Disabled
Fixed / variable	Variable							

The time driven data representations in Table 6 were enabled since test series R5.

6.1 Test series R1 – RFSSpW

6.1.1 Selected parameters

Table 7: Welding parameters of test series R1.

PD (mm)	RS (rpm)	PT (s)	DT (s)	RT (s)	HT (s)
2	2250 - 3000	1.5	2 - 4	1.5	3

Table 8: Other parameters of test series R1.

Material (sheet thickness)	Cleaning frequency	Location of the sensor
EN AW-6082-T6 (2 mm)	After every weld	On the support arm of the welding equipment

Table 9: AE configuration of test series R1.

Sensor type	Resonance frequency (kHz)	Threshold (dB)	Frequency range of the digital filter (kHz)	Sampling rate (MSPS)	Time driven rate (s)
WD	450	60	100 - 400	1	1

6.1.2 Objective

In this test series, 16 refill friction stir spot welds are made with different welding parameters. Both the acoustic emission (AE) and welding parameters were recorded. The objective of this preliminary test series was to get acquainted with the software programs and their data processing. Different welding parameters were selected in order to investigate whether or not a change in the welding parameters resulted into a change in the waveform of the welds.

6.1.3 Results and conclusion

An example of one of the 16 welding experiments is given in Figure 82, the other curves are included in the external appendix. The most important curves are indicated, the other curves represent currents and pin and clamping forces. The waveform is expressed over time in μs , while the welding parameters

are expressed over time in ms. This is due to a difference in the sampling rate, which is the amount of samples recorded in one second.

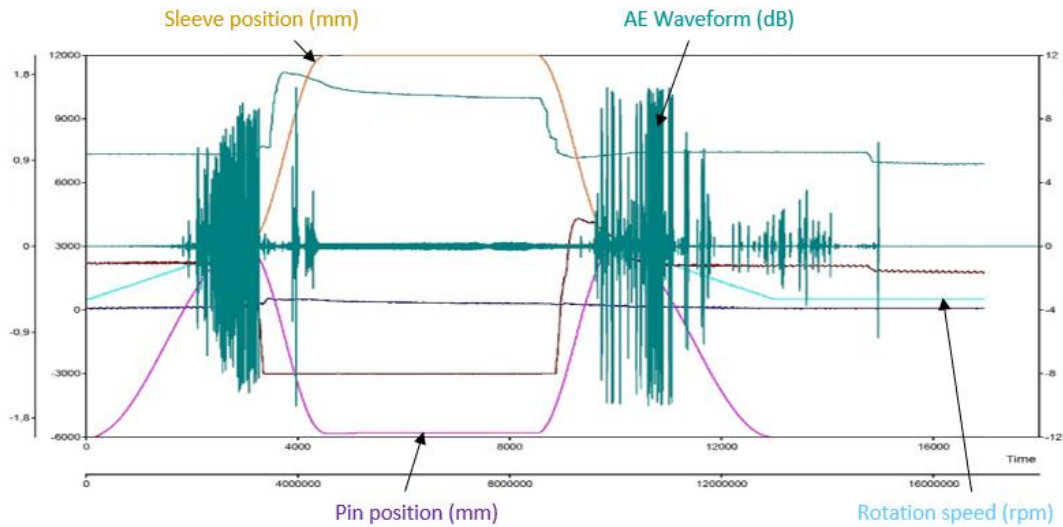


Figure 82: Waveform and evolution of the welding parameters over time (weld nr. SW-68-R1-1.2).

6.2 Test series R2 – RFSSpW

6.2.1 Selected parameters

Table 10: Welding parameters of test series R2.

PD (mm)	RS (rpm)	PT (s)	DT (s)	RT (s)	HT (s)
2.2	2250	1.5	3	1.5	2

Table 11: Other parameters of test series R2.

Material (sheet thickness)	Cleaning frequency	Location of the sensor
EN AW-6082-T6 (2 mm)	After every weld	On the support arm of the welding equipment

Table 12: AE configuration of series R2.

Sensor type	Resonance frequency (kHz)	Threshold (dB)	Frequency range of the digital filter (kHz)	Sampling rate (MSPS)	Time driven rate (s)
WD	450	60	100 - 400	1	1

6.2.2 Objective

Five friction stir spot welds were made with identical welding parameters. The waveform was recorded and divided into phases, which each represent a different time slot in the welding process. The phase distribution is visible in Figure 59 and Figure 60. The objective was to investigate the repeatability of the waveform, and therefore being able to make a standardised signal.

Phase 1 contains the hold time before plunging, phase 2 the plunge time, phase 3 the dwell time, phase 4 the retraction time and phase 5 the hold time after retracting. Based on this distribution, the waveform signal can be divided as well (see Figure 60)

Furthermore, the waveforms for each phase were transformed into the frequency domain by a fast Fourier transformation (FFT). In the frequency domain, notable peaks and similarities were identified, in order to relate them to the corresponding welding parameters.

6.2.3 Results and conclusion

An example of one of the 5 replications of the waveforms and corresponding FFT curves (weld nr. SW-68-R2-1.5) is given in Figure 83 and Figure 84, respectively. The other graphs are available in the external appendix.

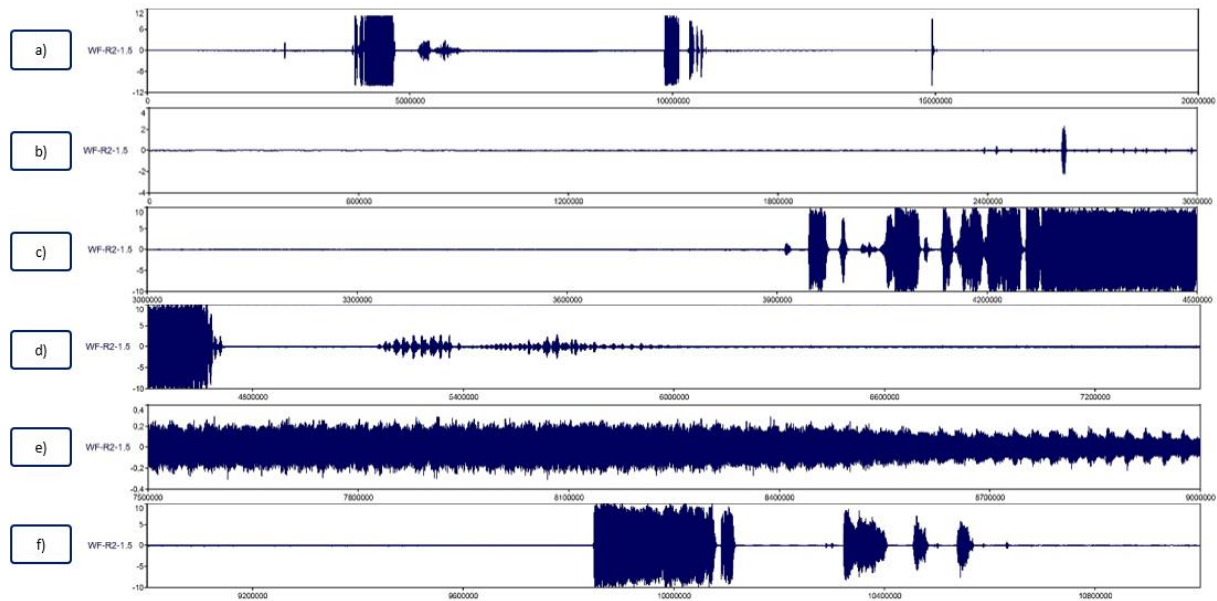


Figure 83: Amplitude (V) vs time (μs) for the complete waveform (a); waveform phase 1 (b); waveform phase 2 (c); waveform phase 3 (d); waveform phase 4 (e); waveform phase 5 (f) (weld nr. SW-68-R2-1.5).

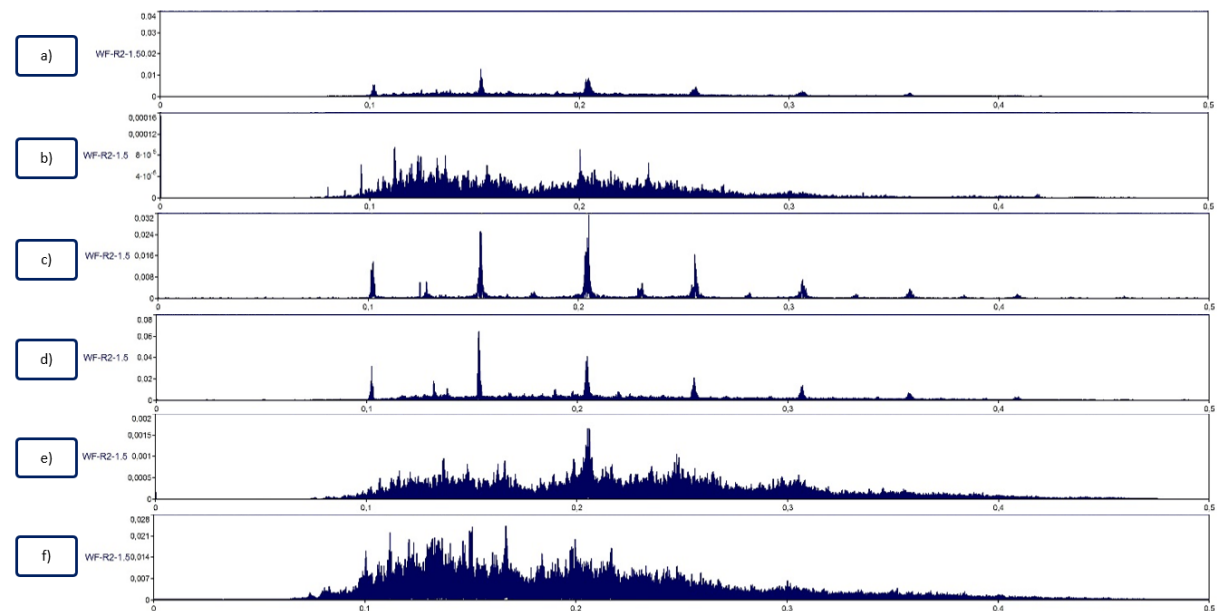


Figure 84: Amplitude (V^2_{rms}) vs frequency (MHz) of the complete FFT curve (a); FFT curve phase 1 (b); FFT curve phase 2 (c); FFT curve phase 3 (d); FFT curve phase 4 (e); FFT curve phase 5 (f) (weld nr. SW-68-R2-1.5).

By comparing the complete waveform of the weld (see Figure 83a) and the evolution of the welding parameters over time (see Figure 82), it is clear that bursts appear when the tool is lowered into the

material (during phase 2) and when it is retracted from the material (during phase 4). Although the bursts do not always have the same starting point for each replication, a possible first explanation can be the variation in thickness of the aluminium samples. In order to investigate this phenomenon, other influences were examined in further test series, such as the cleaning frequency, the temperatures achieved and the machine currents.

Comparing the other waveform results, it can be concluded that there is no repeatability of the waveform as they showed a lot of variation. Therefore, no standardised signal could be determined.

6.3 Test series R3 – RFSSpW

6.3.1 Selected parameters

Table 13: Welding parameters of test series R3.

PD (mm)	RS (rpm)	PT (s)	DT (s)	RT (s)	HT (s)
2.2	2250	1.5	3	1.5	2

Table 14: Other parameters of test series R3.

Material (sheet thickness)	Cleaning frequency	Location of the sensor
EN AW-6082-T6 (2 mm)	After every 2 welds	On the support arm of the welding equipment

Table 15: AE configuration of test series R3.

Sensor type	Resonance frequency (kHz)	Threshold (dB)	Frequency range of the digital filter (kHz)	Sampling rate (MSPS)	Time driven rate (s)
WD	450	60	100 - 400	1	1

6.3.2 Objective

In test series R3, 10 friction stir spot welds were made, with welding parameters identical to the welds in test series R2. Compared to previous test series, only the cleaning frequency was changed, in order to investigate the effect of the cleaning operation on the AE signal. The objective was to determine a standardised signal, based on the 10 AE signal results. Comparing this standardised signal to the one of series R2 would show the effect of the cleaning operation on the AE signal.

After analysing the results of series R2, no comparison could be made because no standardised signal could be determined. Therefore, the temperature influence was investigated. Three thermocouples were soldered at the clamping ring of the tool head, in order to measure the temperatures achieved during the welding process. This is discussed in detail in section 5.3.

6.3.3 Results and conclusion

The waveforms of the complete process in the time domain for welds nr. SW-68-R3-1.1 to SW-68-R3-1.5 are given in Figure 85.

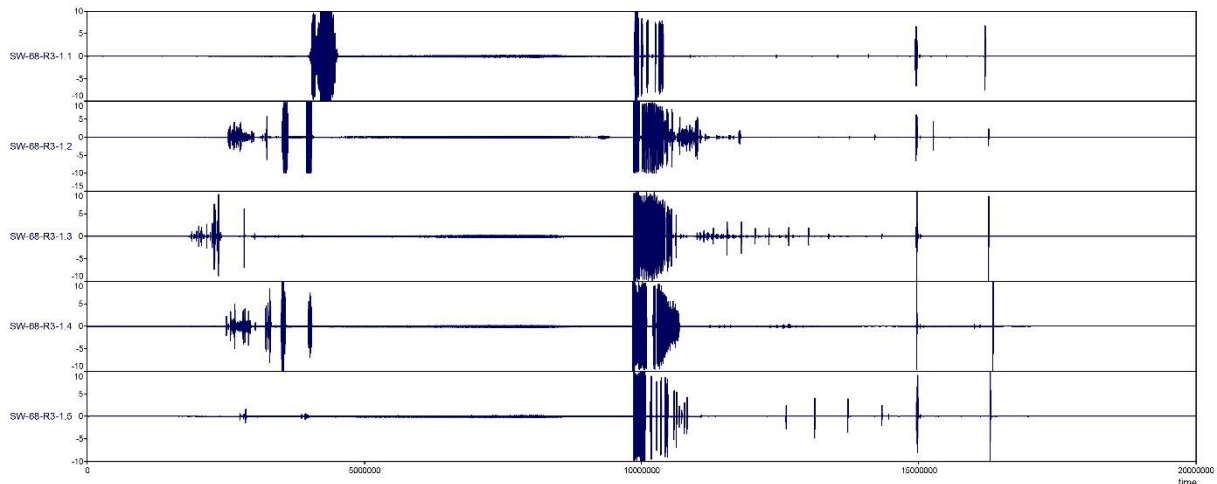


Figure 85: Waveforms of the complete process in the time domain (weld nrs. SW-68-R3-1.1 to SW-68-R3-1.5).

At the start of the test series, the tool was clean. Comparison of the 5 waveforms shows that no standardised signal could be constructed, because too much variation appeared. At the beginning of the waveform, the bursts randomly appear. However, it could be concluded that smaller bursts occur in the waveform of the 3rd and the 5th weld, since the tool has been cleaned after the 2nd and the 4th weld.

The temperatures for the first and last weld are shown in Figure 86, which showed that a difference of 32.03 °C was recorded. The temperatures of the other welds are situated in this temperature range. It can be concluded that the machine slowly heats up during the welding process. However, no correlation between the rising temperature and waveforms could be identified.

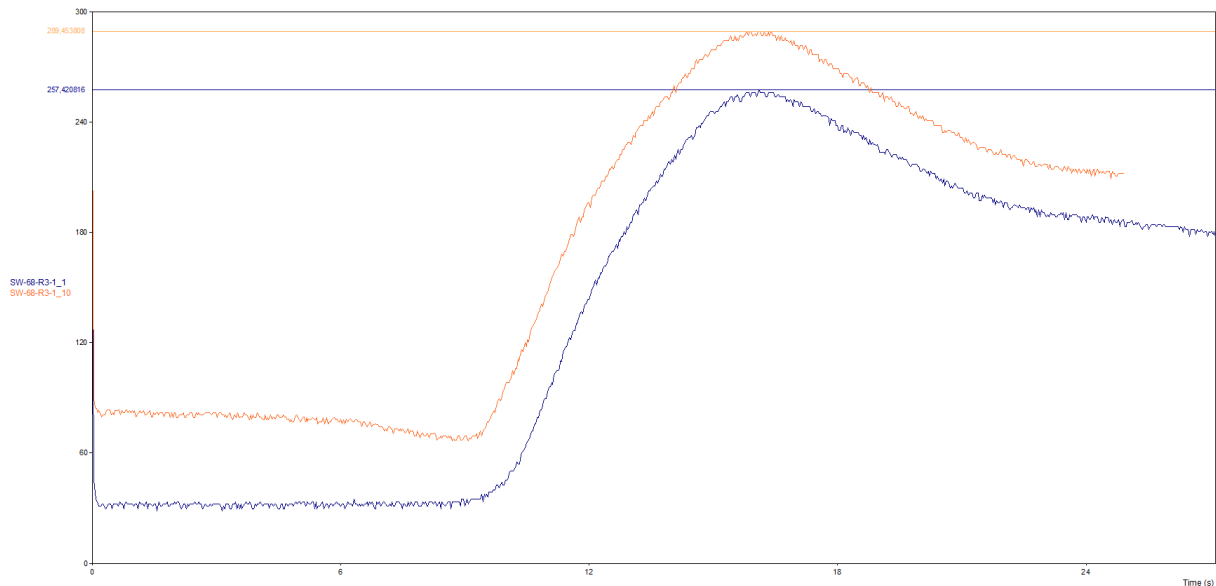


Figure 86: Temperatures for weld nrs. SW-68-R3-1.1 and SW-68-R3-1.10.

The difference between a clean tool and a polluted tool can be identified in the analysis of the pin force and the current required for the pin rotation. An example for weld nrs. SW-68-R3-1.1 to SW-68-R3-1.5 is given in Figure 87 and Figure 88, which represent the pin force and the current, respectively. In this case, weld nrs. SW-68-R3-1.2 and SW-68-R3-1.4 are welded with a polluted tool. A higher pin force and current is observed during the hold phase and the plunge phase for welds made with a polluted tool.

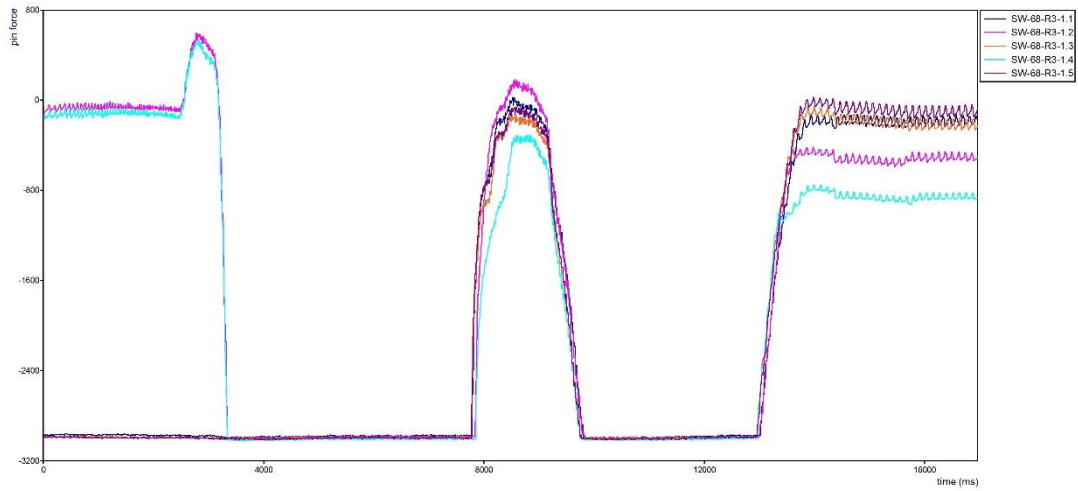


Figure 87: Pin force (N) versus time (ms) for weld nrs. SW-68-R3-1.1 to SW-68-R3-1.5.

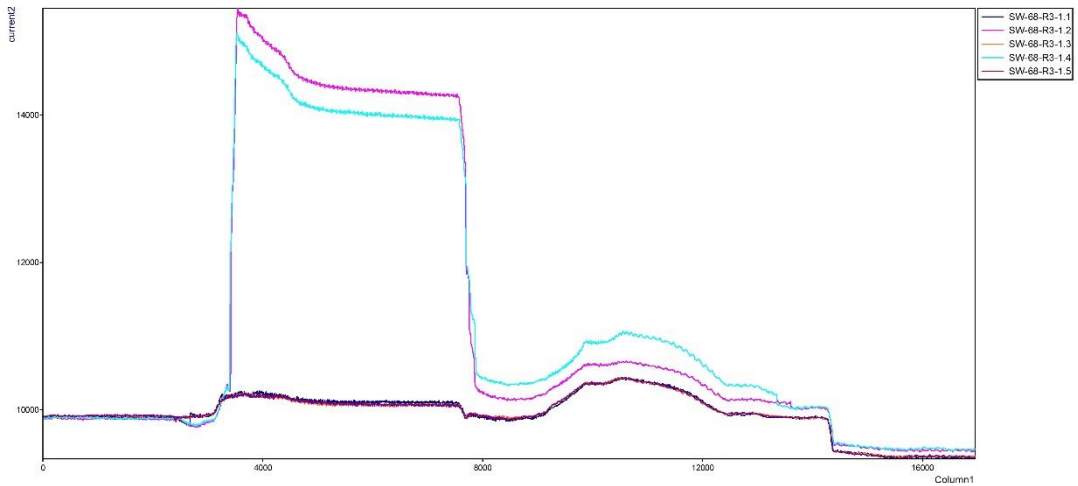


Figure 88: Current required for pin rotation (mA) vs time (ms) for weld nrs. SW-68-R3-1.1 to SW-68-R3-1.5.

6.4 Test series R4 – RFSSpW

6.4.1 Selected parameters

Table 16: Welding parameters of test series R4.

PD (mm)	RS (rpm)	PT (s)	DT (s)	RT (s)	HT (s)
3	2250	1.5	3	1.5	2

Table 17: Other parameters of test series R4.

Material (sheet thickness)	Cleaning frequency	Location of the sensor
EN AW-6082-T6 (2 mm)	After every 2 welds	On the support arm of the welding equipment

Table 18: AE configuration of test series R4.

Sensor type	Resonance frequency (kHz)	Threshold (dB)	Frequency range of the digital filter (kHz)	Sampling rate (MSPS)	Time driven rate (s)

WD	450	60	100 - 400	1	1
----	-----	----	-----------	---	---

6.4.2 Objective

The objective of this test series was to investigate the effect of the plunge depth (PD) on the waveform. The same parameters as in test series R3 were used, only the plunge depth was increased from 2.2 mm to 3 mm. Ten friction stir spot welds with the same welding parameters were made.

6.4.3 Results and conclusion

By looking at the current and temperature in relation to both the waveform in the time domain and the frequency domain, no correlation could be identified. In the time domain, the bursts in the waveforms contain too much variation in order to identify a difference between welds with a plunge depth of 2.2 mm and 3 mm. However, for welds with a larger plunge depth, the bursts during the retraction phase fade away more quickly. An explanation could be less vibrations of the tool since more material is stuck in the tolerance between the pin and the sleeve, causing a damping effect on the AE signal. An example, comparing weld nrs. SW-68-R3-1.3 and SW-68-R4-1.3, is shown in Figure 89 with the retraction phase indicated in the red rectangle.

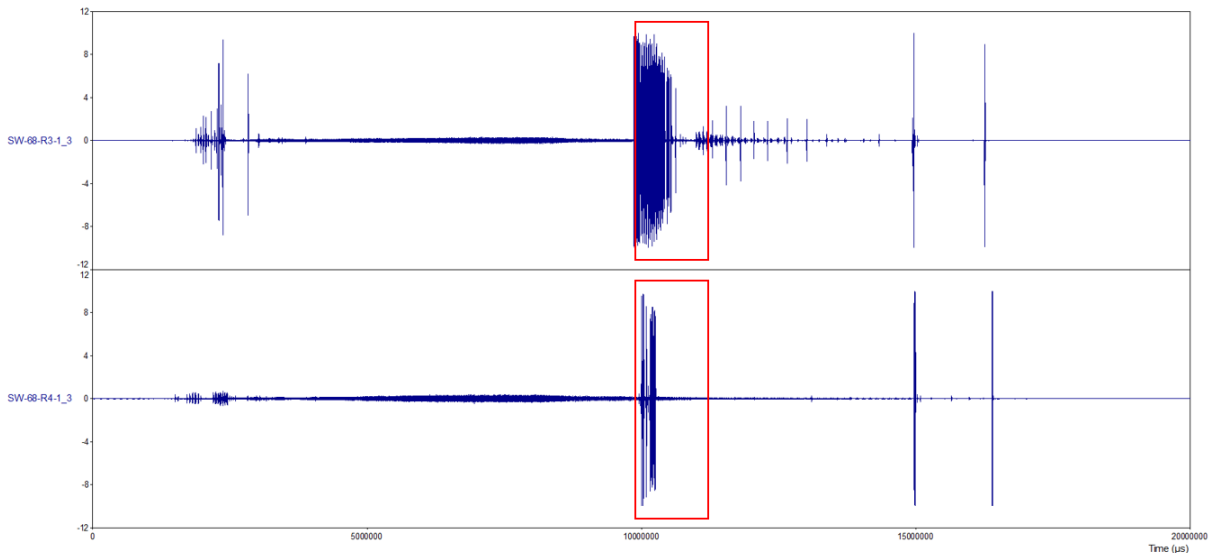


Figure 89: Waveform comparison of weld nrs. SW-68-R3-1.3 and SW-68-R4-1.3.

6.5 Test series R5 – RFSSpW

6.5.1 Selected parameters

Table 19: Welding parameters of test series R5.

PD (mm)	RS (rpm)	PT (s)	DT (s)	RT (s)	HT (s)
2.2	2250	1.5	3	1.5	2

Table 20: Other parameters of test series R5.

Material (sheet thickness)	Cleaning frequency	Location of the sensor
EN AW-6082-T6 (2 mm)	After every 2 welds	On the welding table

Table 21: AE configuration of test series R5.

Sensor type	Resonance frequency (kHz)	Threshold (dB)	Frequency range of the digital filter (kHz)	Sampling rate (MSPS)	Time driven rate (s)
WD	450	60	100 - 400	1	3

6.5.2 Objective

In test series R5, 10 friction stir spot welds were made with identical parameters. Previous test series showed that no reproducible or valid results in both the time and frequency domain were achieved, hence no correlations between the welding parameters and the waveform could be identified. Based on the recommendations of Mistras, the sensor was positioned on the welding table, the AE parameters (in particular the threshold and the time driven rate) was adjusted, and the analysis was based on both the time-driven data and the hit data set. The objective of this test series was to get acquainted with those new methods of examining. The average signal level (ASL), the frequency centroid, the cumulative counts and the cumulative energy were investigated over time for the entire process and with specific attention during the dwell time (DT). Also the Duration vs Amplitude was investigated. More information about these examination methods can be found in section 5.4. Afterwards, the lap shear strengths were determined for each weld.

6.5.3 Results and conclusion

The results for the lap shear strengths are given in Table 22.

Table 22: Lap shear strength results for test series R5.

Weld nr.	Lap shear strength (kN)
SW-68-R5-1.1	7.27
SW-68-R5-1.2	7.50
SW-68-R5-1.3	7.09
SW-68-R5-1.4	7.72
SW-68-R5-1.5	7.85
SW-68-R5-1.6	7.91
SW-68-R5-1.7	7.80
SW-68-R5-1.8	7.74
SW-68-R5-1.9	7.90
SW-68-R5-1.10	8.09

Control chart

Based on the lap shear strengths given in Table 22, a control chart (see Figure 90) was constructed in order to investigate the outliers.

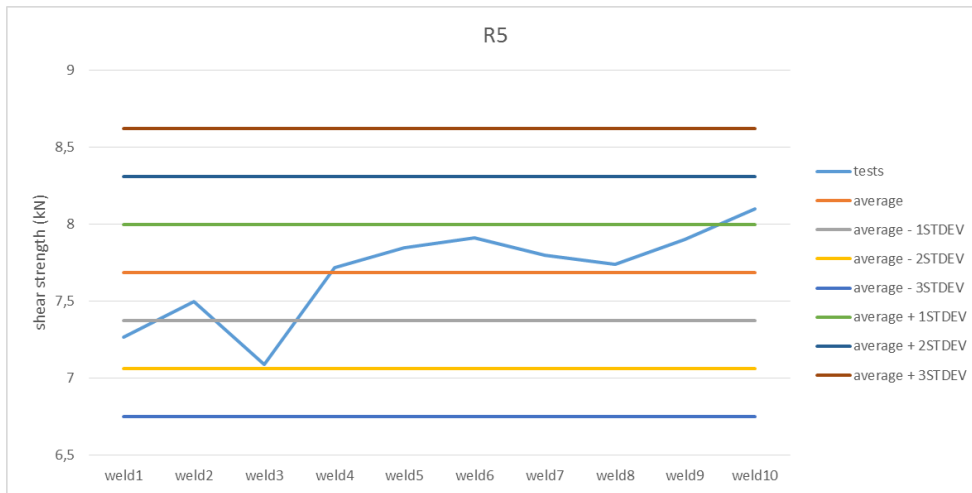


Figure 90: Control chart of the lap shear strengths in test series R5.

Waveform evaluation

Figure 90 shows that weld nrs. SW-68-R5-1.3 and SW-68-R5-1.10 are the weakest (7.09 kN) and strongest weld (8.09 kN), respectively. In order to investigate the remarkable difference of 1 kN between these two welds, the differences in the waveform are analysed. Figure 91 illustrates the waveform and fast Fourier transformed (FFT) curve of weld nr. SW-68-R5-1.3, whereas Figure 92 illustrates the waveform and FFT curve of weld nr. SW-68-R5-1.10.

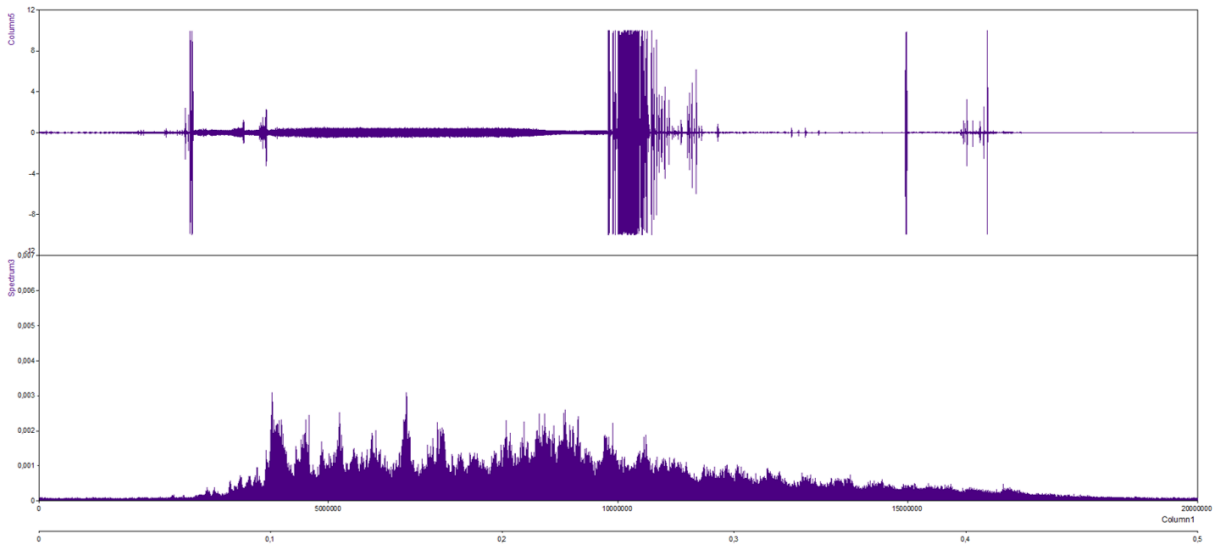


Figure 91: Waveform: amplitude (V) over time (μs) (top) and FFT curve: amplitude ($V^2\text{rms}$) over frequency (MHz) (bottom) of weld nr. SW-68-R5-1.3.

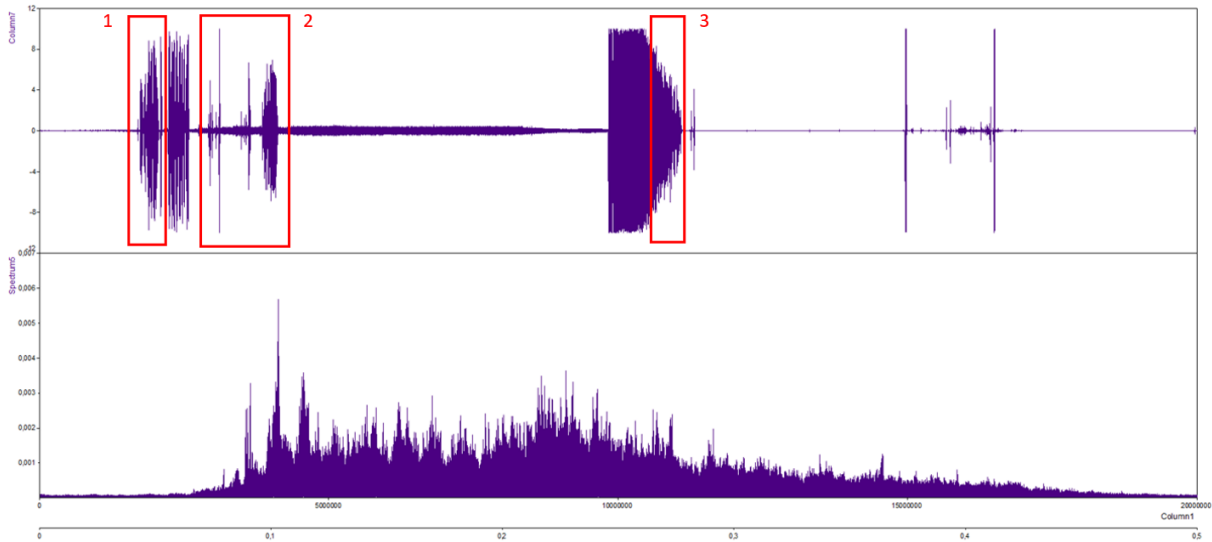


Figure 92: Waveform: amplitude (V) over time (μs) (top) and FFT curve: amplitude ($V^2\text{rms}$) over frequency (MHz) (bottom) of weld nr. SW-68-R5-1.10.

The differences between the two waveforms are indicated by red rectangles. These differences may indicate the 1 kN lap shear strength variation. However, rectangles 1 and 3 are located in the hold time phase at the start (phase 1 in Figure 59) and at the end (phase 5 in Figure 59). Due to the fact that weld errors, related to the quality, are induced in phase 2, 3 and 4, these differences do not contribute to the difference in lap shear strength.

Another difference is the surface of the FFT curve. Weld nr. SW-68-R5-1.3 has a smaller surface than weld nr. SW-68-R5-1.10. This appearance seems logical when looking at the waveform, as the waveform of weld nr. SW-68-R5-1.3 contains less bursts compared to the waveform of weld nr. SW-68-R5-1.10. However, concluding that a smaller FFT surface is associated with a lower lap shear strength is incorrect, because the FFT curves of other welds with a high lap shear strength do not conform to this pattern. An example of such a contradiction is given in Figure 93, which illustrates the waveform and FFT curve of a weld with the third highest lap shear strength (weld nr. SW-68-R5-1.8).

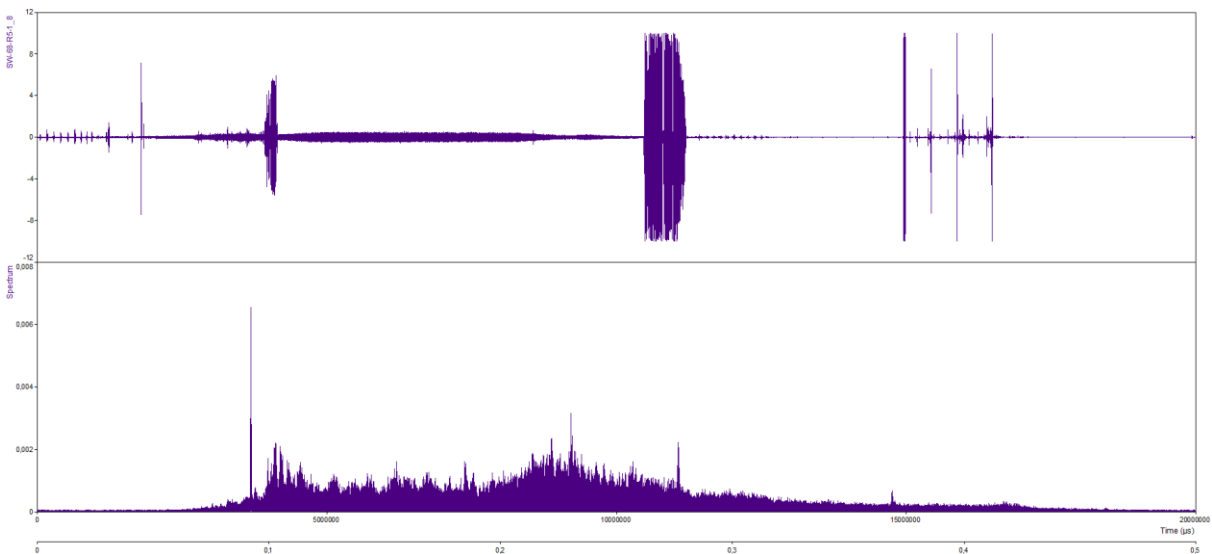


Figure 93: Waveform: amplitude (V) over time (μs) (top) and FFT curve: amplitude ($V^2\text{rms}$) over frequency (MHz) (bottom) of weld nr. SW-68-R5-1.8.

In order to investigate the differences indicated in the second rectangle the plunge time phase (phase 2 in Figure 59), is examined in more detail for both welds. Figure 94 and Figure 95 illustrate the plunge time weld nrs. SW-68-R5-1.3 and SW-68-R5-1.10, respectively.

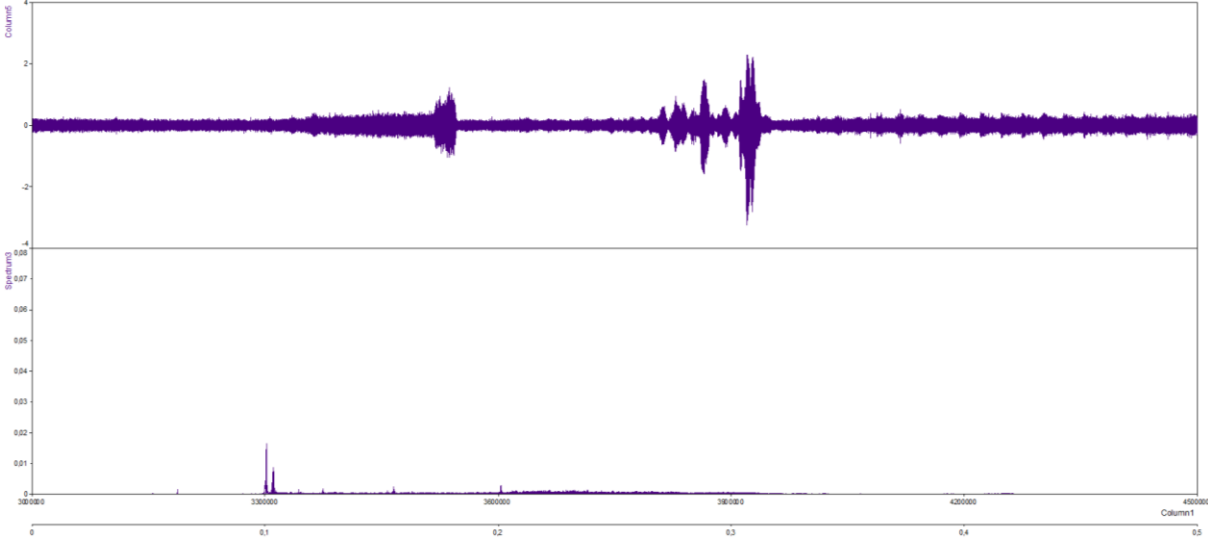


Figure 94: Plunge time phase (phase 2) of weld nr. SW-68-R5-1.3: waveform (top) and FFT curve (bottom).

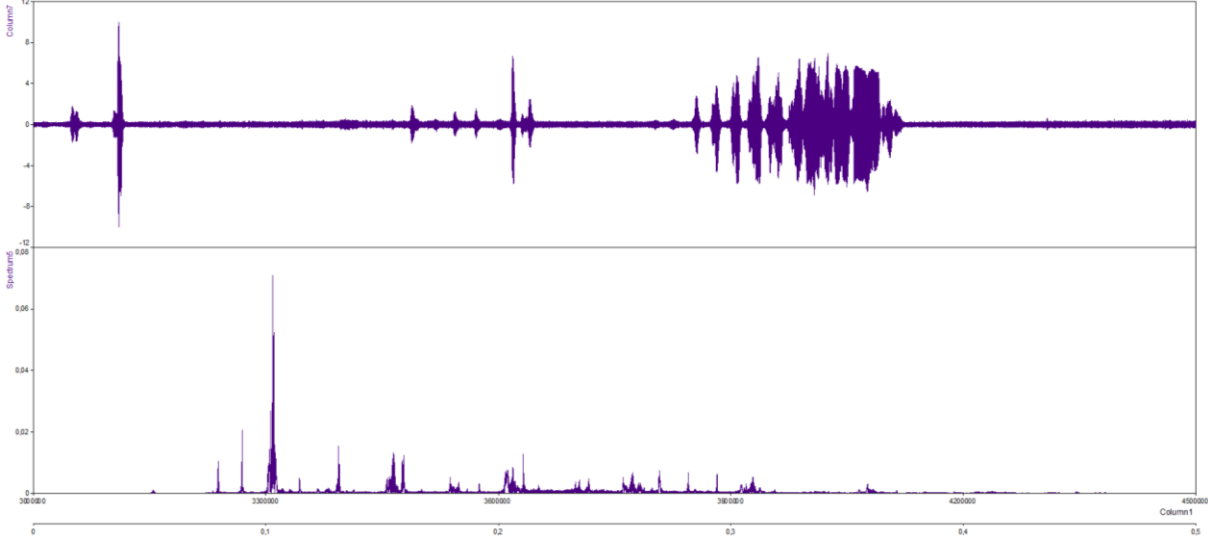


Figure 95: Plunge time phase (phase 2) of weld nr. SW-68-R5-1.10: waveform (top) and FFT curve (bottom).

By comparing the waveform and FFT, it can be concluded that the waveforms during the plunge time phase are totally different. Therefore, one can state that the differences in the lap shear strength are a result of the differences during the plunging stage. Based on the particular shape of these waveforms, it can be concluded that the presence of a large burst during the plunging stage could indicate that a higher lap shear strength is achieved.

ASL/Time

The results in the ASL/Time domain are mainly investigated in the dwell time (DT) phase. This is because during this time, together with the plunge time (PT) and the retraction time (RT), the most errors in terms of weld quality can arise. The results of weld nrs. SW-68-R5-1.1 and SW-68-R5-1.2 are given in Figure 96, where the points recorded during the DT are encircled in black. All other results are

available in the external appendix. Based on these results, it can be concluded that the same trend always appears during the DT phase, namely a horizontal straight line with values around 62 dB.

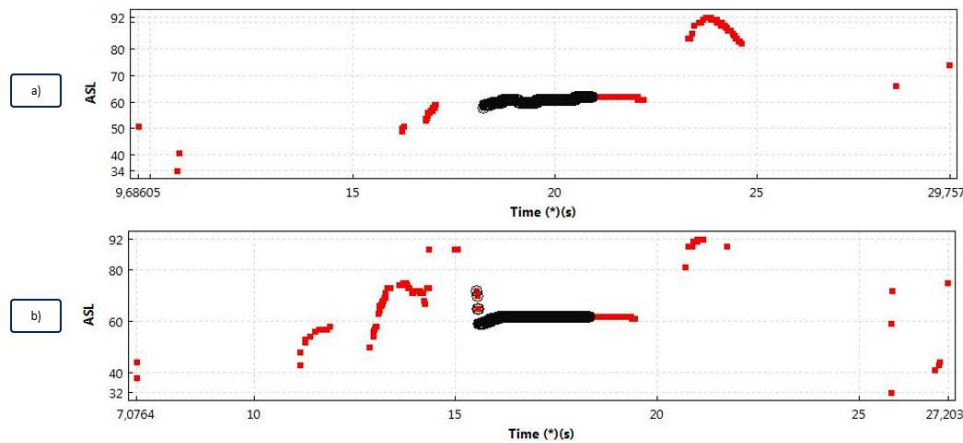


Figure 96: ASL/Time-analysis of weld nr. SW-68-R5-1.1 (a) and SW-68-R5-1.2 (b).

The only difference are the higher data points at the beginning of the DT, which already started during the PT and appear in some welds.. The appearance cannot be explained based on temperature measurements, cleaning of the tool, or lap shear strengths.

Duration/Amplitude

The duration/amplitude results are shown in Figure 97. When the signal is expressed in the Duration/Amplitude domain, the signals recorded during the DT for each weld are mostly located in the left bottom corner, which means they have both a low amplitude and a short duration (see Figure 97a and Figure 97b). Only weld nr. SW-68-R5-1.3 is an exception, as it contains several data points with a low amplitude combined with a long duration, as well as three points with a higher amplitude combined with a short duration (see Figure 97c). Comparing their lap shear strengths, it is remarkable that this weld exhibits the lowest lap shear strength. Because only one case like weld nr. SW-68-R5-1.3 was identified, it is impossible to formulate a valid conclusion relating the high amplitude to a weak weld.

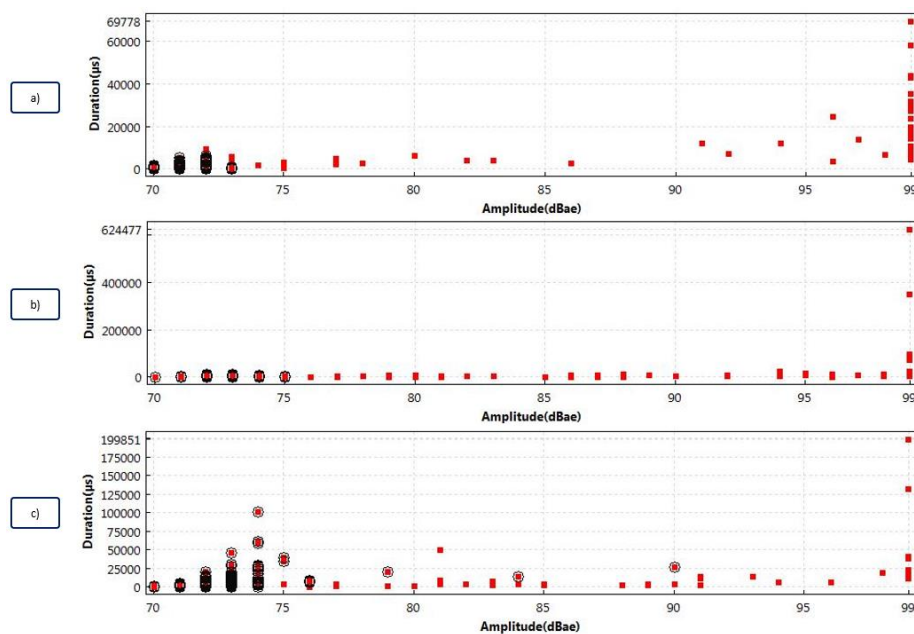


Figure 97: Duration/Amplitude-analysis of weld nrs. SW-68-R5-1.1 (a), SW-68-R5-1.2 (b), SW-68-R5-1.3 (c).

Frequency centroid/Time

The Frequency centroid/time results of weld nrs. SW-68-R5-1.1 to SW-68-R5-1.3 are given in Figure 98. In this domain, the data points during the DT phase are almost identical. Some welds contain less data points, but this is due to the fact that the amplitude did not exceed the threshold. Weld nr. SW-68-R5-1.3 is interesting, as it is the only weld with other lower frequency centroids at the beginning of the dwell time phase and exhibits the lowest lap shear strength. This weld also contains several data points with a low amplitude combined with a long duration, as well as a high amplitude combined with a short duration (as discussed in the previous paragraph). It can be concluded that at a higher temperature, the frequency centroid is slightly lower. A preliminary remark is that a lower frequency centroid is an indication of a slightly lap shear strength. However, this remark has yet to be confirmed in the next test series.

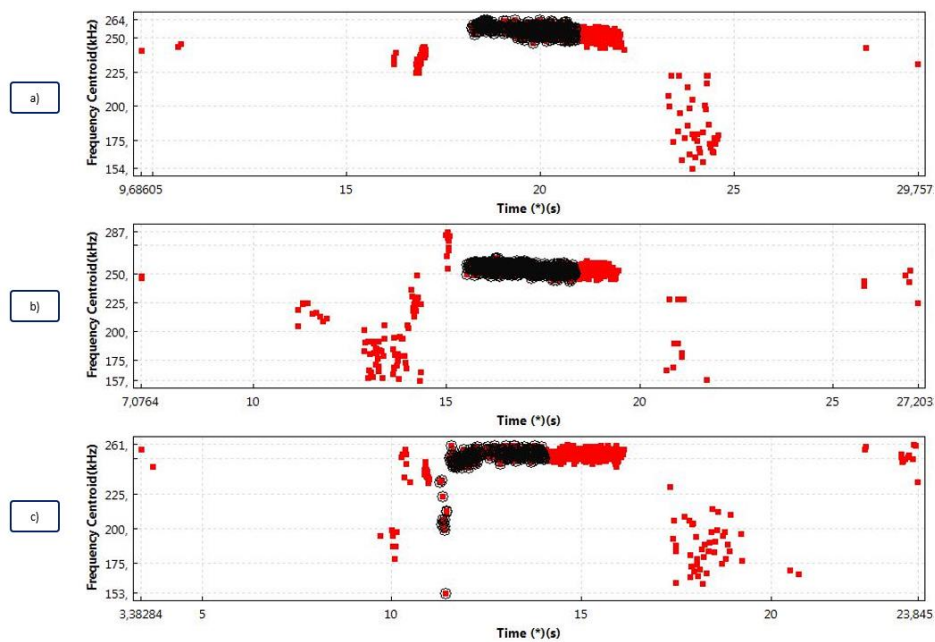


Figure 98: Frequency centroid/Time analysis for weld nrs. SW-68-R5-1.1 (263,86 °C) (a), SW-68-R5-1.2 (271,57 °C) (b), SW-68-R5-1.3 (281,81 °C) (c).

Cumulative counts/Time

The cumulative counts/time results of welds nr. SW-68-R5-1.1 to SW-68-R5-1.3 are given in Figure 99. Most counts are found before or after the DT phase, due to vibrations of the machine and tool head during the plunge time and retraction time phase. Looking at the DT phase, there are many variations in both the gradient and the size of the curve which cannot be linked to the temperature measurements, lap shear strengths or cleaning sessions. A possible conclusion based on this hit data representation is that the mechanical movements of the machine excessively overrule the AE signals, resulting in a non-representative data output.

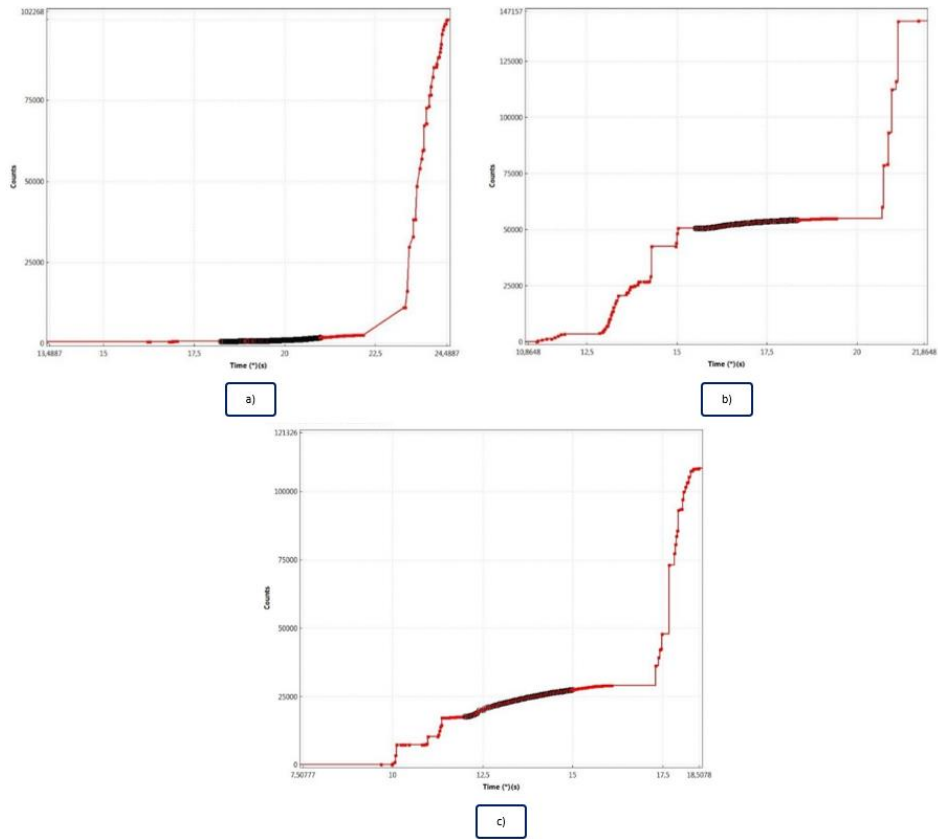


Figure 99: Cumulative counts/Time-analysis for weld nr. SW-68-R5-1.1 (a), SW-68-R5-1.2 (b), SW-68-R5-1.3 (c).

Energy/Time

The results of weld nrs. SW-68-R5-1.1, SW-68-R5-1.3 and SW-68-R5-1.5 are given in Figure 100.

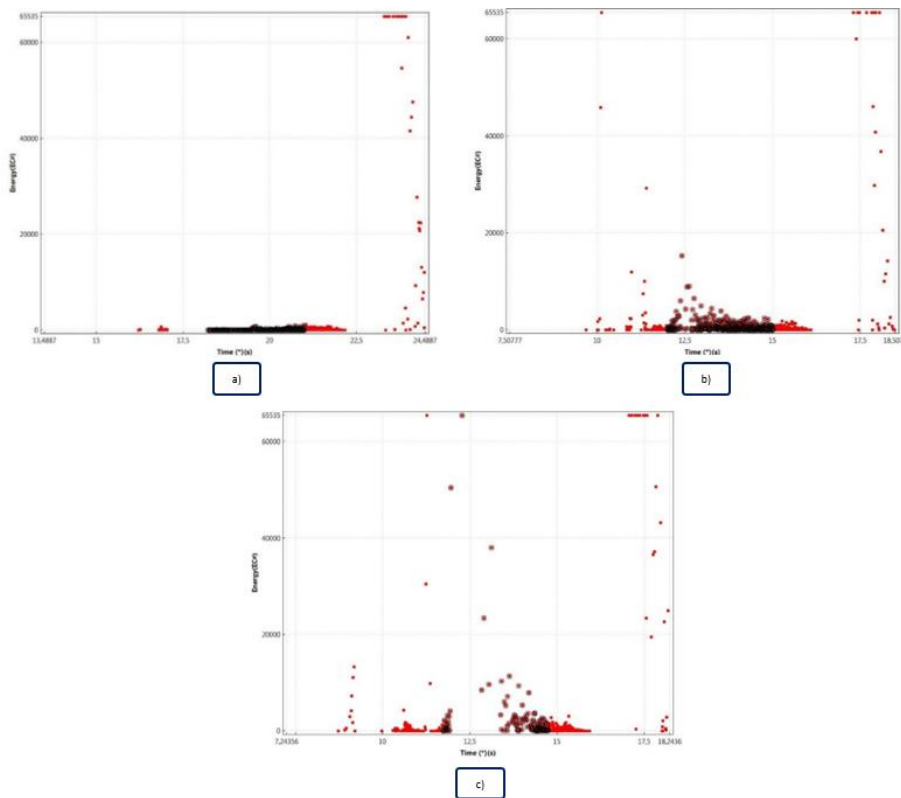


Figure 100: Energy/Time-analysis for weld nr. SW-68-R5-1.1 (a), SW-68-R5-1.3 (b), SW-68-R5-1.5 (c).

Similar to the Cumulative counts/Time-representation, the Energy/Time shows that the majority of the data points occur before and after the DT phase. When looking at more detail into the DT phase, there are many different gradients for the different tests. Therefore, based on this data representation, it is not possible to find a link between the lap shear strength and the absolute energy during the DT phase or any other phase due to the variations.

6.6 Test series R6 – RFSSpW

6.6.1 Selected parameters

Table 23: Welding parameters of test series R6.

PD (mm)	RS (rpm)	PT (s)	DT (s)	RT (s)	HT (s)
3	2250	1.5	3	1.5	2

Table 24: Other parameters of test series R6.

Material (sheet thickness)	Cleaning frequency	Location of the sensor
EN AW-6082-T6 (2 mm)	After every 2 welds	On the welding table

Table 25: AE configuration of test series R6.

Sensor type	Resonance frequency (kHz)	Threshold (dB)	Frequency range of the digital filter (kHz)	Sampling rate (MSPS)	Time driven rate (s)
WD	450	70	100 - 400	1	3

6.6.2 Objective

Test series R6 was performed in order to confirm the previous conclusions, found in test series R5. Ten friction stir spot welds were made with almost the same parameters of series R6. The difference between the two test series is a change in the PD from 2.2 mm to 3 mm. Likewise as in test series R5, the different data representations were examined. Afterwards, the lap shear strength was determined.

6.6.3 Results and conclusion

The lap shear strengths for every weld of this test series are given in Table 26.

Table 26: Lap shear strength results for test series R6.

Weld nr.	Lap shear strength (kN)
SW-68-R6-1.1	8.72
SW-68-R6-1.2	8.64
SW-68-R6-1.3	9.06
SW-68-R6-1.4	8.91
SW-68-R6-1.5	9.24
SW-68-R6-1.6	8.62
SW-68-R6-1.7	8.63
SW-68-R6-1.8	8.32
SW-68-R6-1.9	8.31
SW-68-R6-1.10	8.78

The control chart according to Table 26 is illustrated in Figure 101.

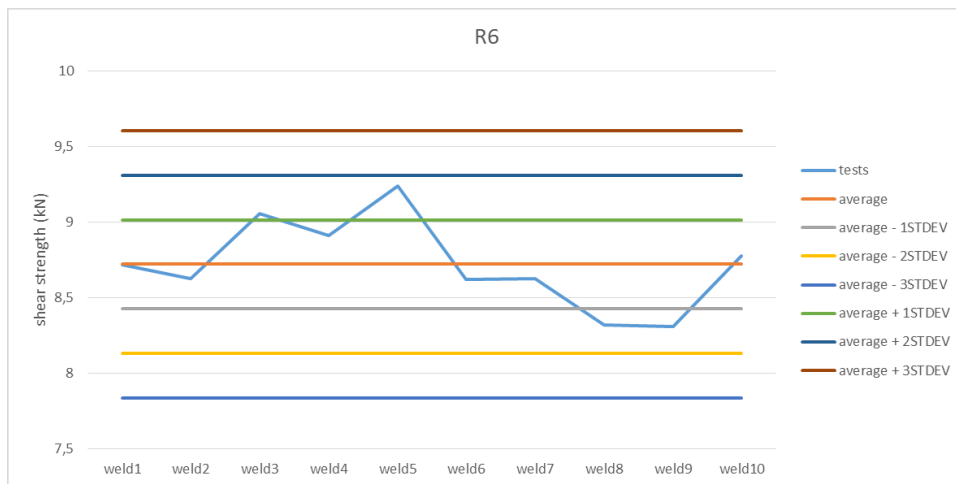


Figure 101: Control chart of the lap shear strengths in test series R6.

Waveform evaluation

Likewise as in test series R5, the strongest and weakest welds are investigated. In this case, weld nrs. SW-68-R5-1.5 and SW-68-R5-1.9 are the strongest (9.24 kN) and weakest (8.31 kN) weld, respectively. In order to investigate the remarkable difference of almost 1 kN, the differences in their waveforms are analysed. Figure 102 illustrates both the waveform and FFT curve of weld nr. SW-68-R5-1.9. Figure 103 illustrates both the waveform and FFT curve of weld nr. SW-68-R5-1.5. The differences between the two waveforms are indicated by red rectangles.

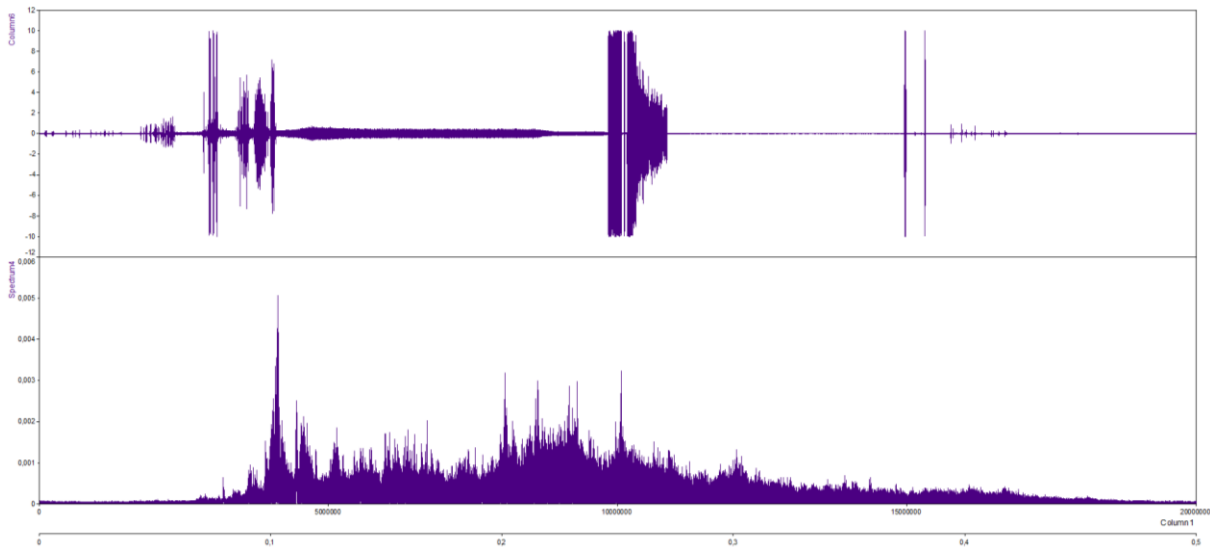


Figure 102: Waveform: amplitude (V) over time (μ s) (top) and FFT curve: amplitude (V^2rms) over frequency (MHz) (bottom) of weld nr. SW-68-R6-1.9.

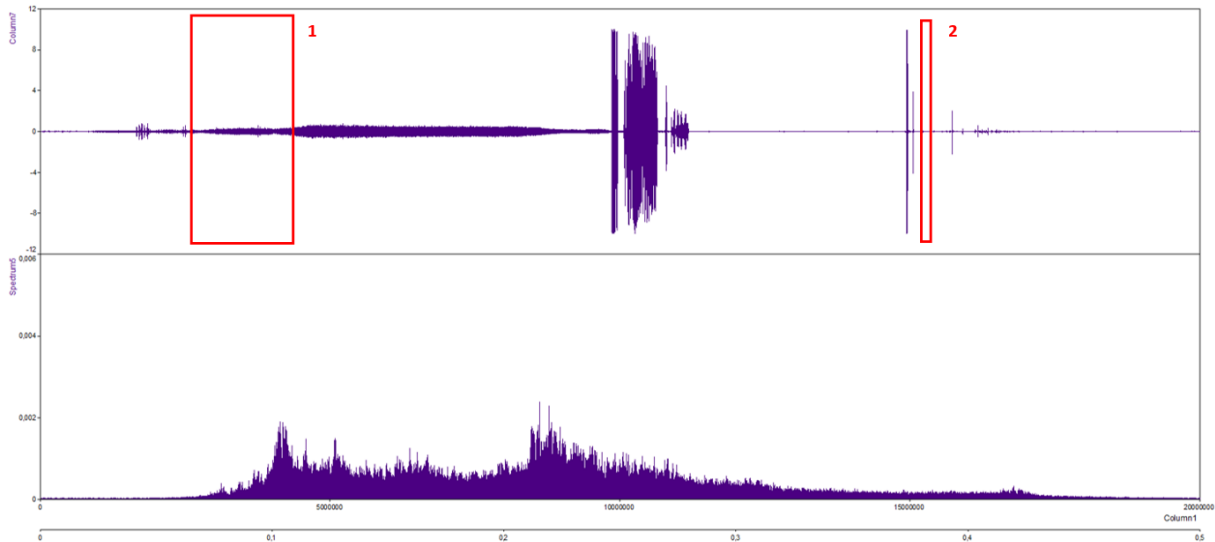


Figure 103: Waveform: amplitude (V) over time (μs) (top) and FFT curve: amplitude ($V^2\text{rms}$) over frequency (MHz) (bottom) of weld nr. SW-68-R6-1.5.

The conclusion in test series R5 cannot be confirmed in this test series, as the large burst during the plunging stage (as indicated by the first rectangle) is only present for the weakest weld but absent for the strongest weld. The relation between the bursts in the plunging stage and lap shear values is therefore incorrect. The second rectangle shows a difference after the hold time phase, and is not taken into account as this part of the welding process is not relevant anymore. The other results can be consulted in the external appendix.

ASL/Time

Examples of the ASL/time domain representation for weld nrs. SW-68-R6-1.3 and SW-68-R6-1.6 are given in Figure 104. Other results are available in the external appendix. All the results show the same trend, since the data points recorded during the dwell time phase form a straight line around 60 dB, similar as found in test series R5 in which the welds were executed with a different rotational speed.

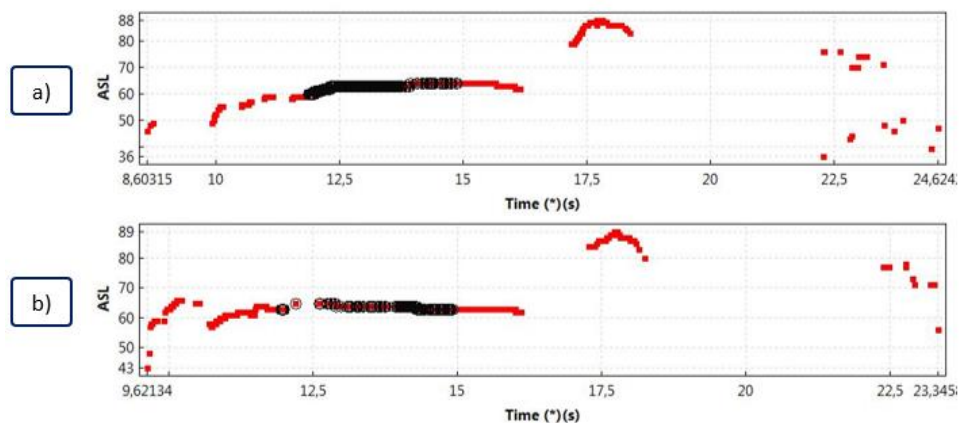


Figure 104: ASL/Time-analysis of weld nrs. SW-68-R6-1.3 (a) and SW-68-R6-1.6 (b).

Duration/Amplitude

The duration/amplitude representation for weld nrs. SW-68-R6-1.3 and SW-68-R6-1.6 are given in Figure 105. Other results are available in the external appendix.

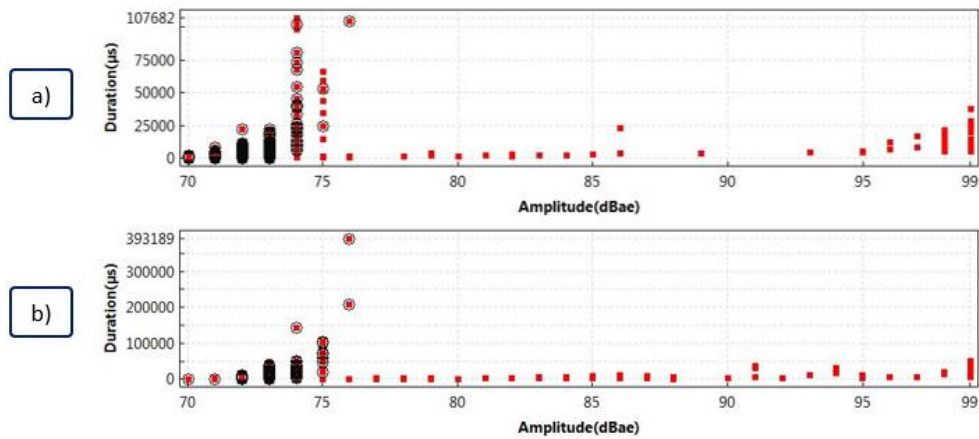


Figure 105: Duration/Amplitude-analysis of welds SW-68-R6-1.3 (a) and SW-68-R6-1.6 (b).

Even though the ASL/Time representation shows similarities among the different welds within this test series, some major differences were found. The duration of some data points of weld nr. SW-68-R6-1.6 differ with a factor of 3 compared to those of weld nr. SW-68-R6-1.3.

Frequency centroid/Time

The frequency centroid/time representation for weld nrs. SW-68-R6-1.3 and SW-68-R6-1.6 are given in Figure 106. Other results are available in the external appendix.

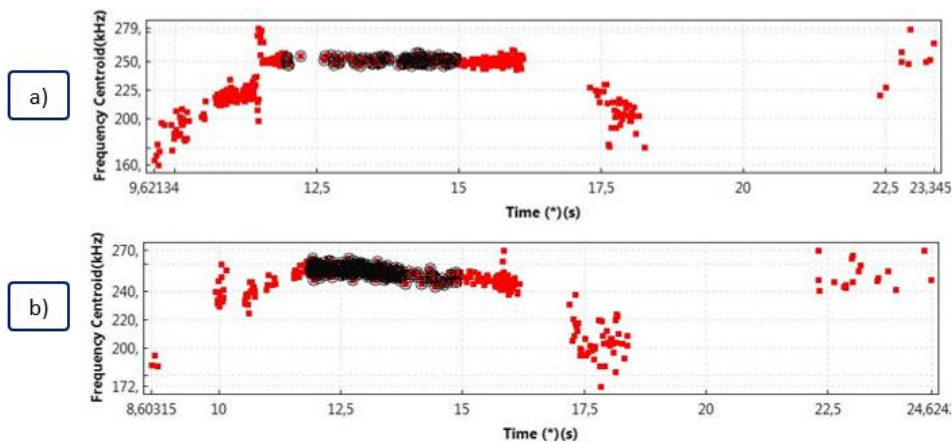


Figure 106: Frequency centroid/Time-analysis of weld nrs. SW-68-R6-1.3 (a) and SW-68-R6-1.6 (b).

The preliminary remark in test series R5 in which it was presumed that a lower frequency centroid might be an indication of a slightly higher lap shear strength, is not valid. Weld nr. SW-68-R6-1.3 shows a frequency centroid around 250 kHz, whereas the frequency centroid of weld nr. SW-68-R6-1.6 is slightly below or almost equal this value. Since Table 26 shows that weld nrs. SW-68-R6-1.3 and SW-68-R6-1.6 have a lap shear strength of 9.06 kN and 8.62 kN, respectively, it can be concluded that no correlations between the frequency centroid and the lap shear strength can be identified.

Cumulative counts/Time

The results for weld nrs. SW-68-R6-1.3 and SW-68-R6-1.6 are given in Figure 107. Other results are available in the external appendix. Both welds exhibit a difference in the gradient and amplitude of the curve, which cannot be related to the lap shear strength.

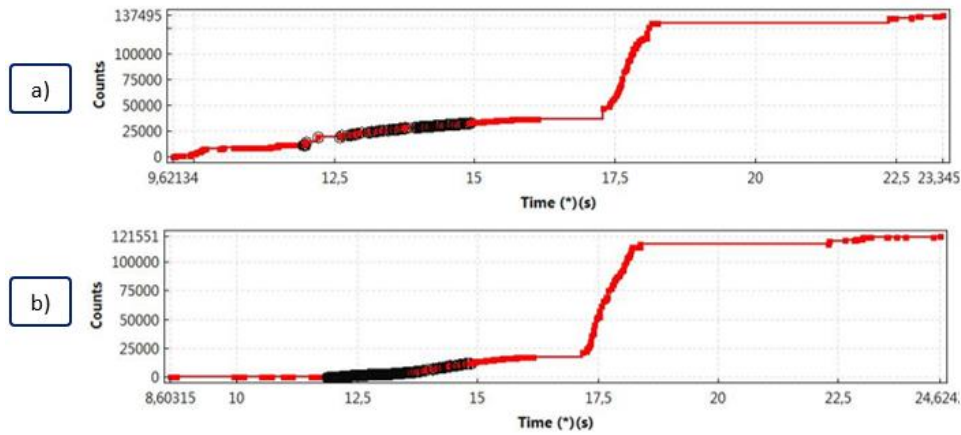


Figure 107: Cumulative counts/Time-analysis of weld nrs. SW-68-R6-1.3 (a) and SW-68-R6-1.6 (b).

Cumulative absolute energy/Time

The cumulative absolute energy/time representation for welds SW-68-R6-1.3 and SW-68-R6-1.6 are given in Figure 108. Other results are available in the external appendix.

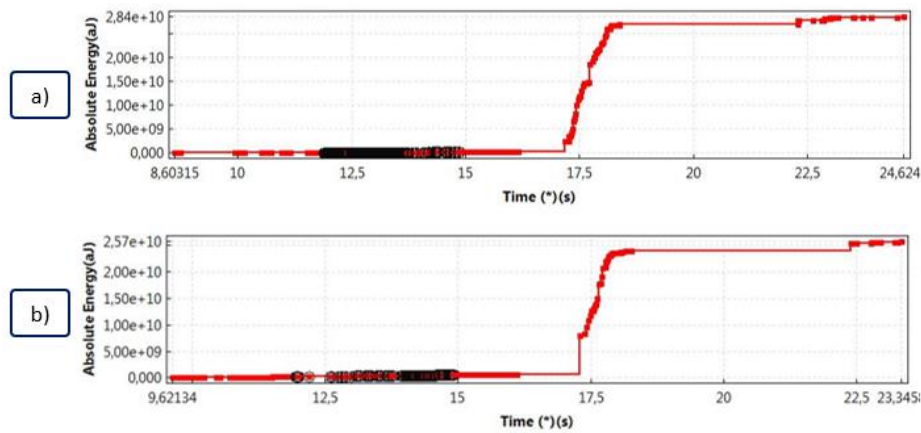


Figure 108: Cumulative absolute energy/Time-analysis of weld nr. SW-68-R6-1.3 (a) and SW-68-R6-1.6 (b).

Comparison of test series R5 and test series R6

The preliminary conclusions found in test series R5 are not confirmed in test series R6. Still too many unknown factors affect the waveform and the hit data set representation, leading to non-reproducible results for welds produced with the same welding parameters. Further research needs to be focused on identifying these unknown factors, in order to filter them out.

6.7 Test series R7 – R10 – RFSSpW

6.7.1 Selected parameters

Table 27: Welding parameters of test series R7 – R10.

Test series	PD (mm)	RS (rpm)	PT (s)	DT (s)	RT (s)	HT (s)
R7	2	3000	1.5	0	1.5	2
R8	2	1500	1.5	0	1.5	2
R9	2	1000	1.5	0	1.5	2
R10	3	1500	1.5	0	1.5	3

Table 28: Other parameters of test series R7 - R10.

Material (sheet thickness)	Cleaning frequency	Location of the sensor
EN AW-6082-T6 (2 mm)	After every 2 welds	On the welding table

Table 29: AE configuration of test series R7 - R10.

Sensor type	Resonance frequency (kHz)	Threshold (dB)	Frequency range of the digital filter (kHz)	Sampling rate (MSPS)	Time driven rate (s)
WD	450	60	100 - 400	1	3

6.7.2 Objective

The goal of these test series was to create weld defects in order to being able to relate the AE signals to this weld defect. Based on previous work [1], welding parameters were known which could induce these defects. The intention was to make a standard AE signal for this error case, which later on could be compared to other AE signals in order to predict the presence of weld defects. Both the waveform and the hit data set were examined, along with lap shear strength tests.

The induced weld defect for each test series is given in Table 30. Within each test series, the weld was replicated 4 times.

Table 30: Induced weld defects for test series R7 - R10.

Test series	Induced weld defect
R7	Incomplete refill
R8	Hooking + voids
R9	Incomplete refill
R10	Partial bonding

6.7.3 Results and conclusion

The lap shear strength results of test series R7 to R10 are given in Table 31.

Table 31: Lap shear strength results for test series R7 - R10.

Series	Weld 1.1 (kN)	Weld 1.2 (kN)	Weld 1.3 (kN)	Weld 1.4 (kN)	Avg. (kN)
R7	3.06	3.96	3.35	4.35	3.68
R8	4.80	5.24	5.53	5.60	5.29
R9	3.96	3.89	4.01	4.01	3.97
R10	5.71	6.78	6.72	6.76	6.49

Control charts based on the values in Table 31 are illustrated in Figure 109.

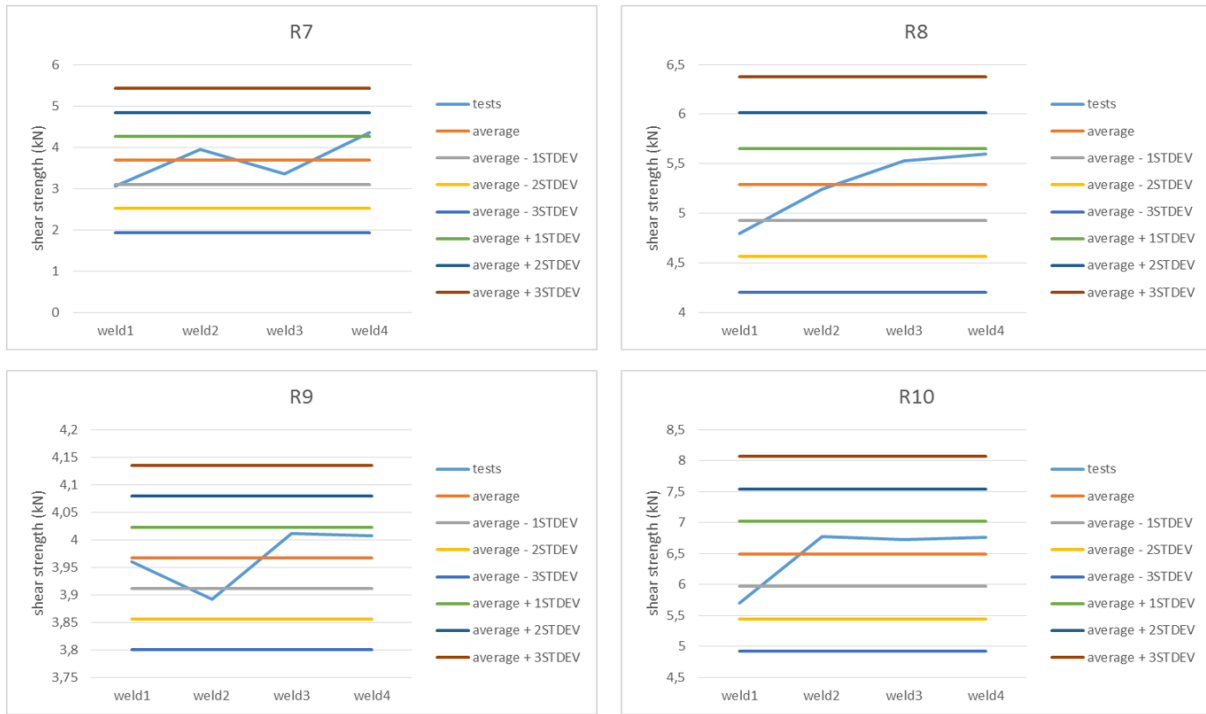


Figure 109: Control charts for series R7 - R10.

The AE results of these test series are available in the external appendix.

6.7.4 Comparison of test series R7, R8, R9 and R10

Comparing the results of test series R7 to R10 lead to no concrete conclusions. Contradictory results are observed among the different test series. It becomes clear that the background noise and mechanical movements of the welding machine overrule the AE signals, causing too much variations in the data sets. In order to further investigate the AE signals, more knowledge about the noises originating from the background and the welding equipment is needed.

6.8 Test series R11 – RFSSpW

6.8.1 Selected parameters

Table 32: Welding parameters of test series R11.

PD (mm)	RS (rpm)	PT (s)	DT (s)	RT (s)	HT (s)
-0.1 to -0.3	2250	1.5	3	1.5	2

Table 33: Other parameters of test series R11.

Material (sheet thickness)	Cleaning frequency	Location of the sensor
EN AW-6082-T6 (2 mm)	No cleaning	On the welding table

Table 34: AE configuration of test series R11.

Sensor type	Resonance frequency (kHz)	Threshold (dB)	Frequency range of the digital filter (kHz)	Sampling rate (MSPS)	Time driven rate (s)

WD	450	60	100 - 400	1	3
----	-----	----	-----------	---	---

6.8.2 Objective

In this test series, the PD was varied from -0.1 to -0.3 for the friction stir spot welds. The goal was to record the AE signals of the entire welding process, while the tool did not plunge into the material, but instead remained on the surface of the upper sheet. In this way, no friction stir spot weld was produced and only the AE signals caused by the background noise and mechanical movements of the welding machine were recorded. Identical parameters as selected in test series R5 were used in order to compare the results. The waveform and the hit data set representation were analysed.

6.8.3 Results and conclusion

Determining the ideal PD in this test series was trial and error. A value of -0.1 mm for the PD seemed inadequate as the sleeve still plunged too deeply into the material (see Figure 110). Hence, the PD was further reduced, until a value of -0.3 seemed to be sufficient. An overview of the selected PD for every weld is given in Table 35.

Table 35: Selected PD for every weld in test series R11.

Weld nr.	Plunge depth (mm)
SW-68-R11-1.1	- 0.1
SW-68-R11-1.2	- 0.2
SW-68-R11-1.3	- 0.3
SW-68-R11-1.4	- 0.3
SW-68-R11-1.5	- 0.3
SW-68-R11-1.6	- 0.3

Visual inspection

Figure 110 shows the test samples for which no welds was produced.



Figure 110: Test samples of test series R11.

Waveform evaluation

Only weld nrs. SW-68-R11-1.3 to SW-68-R11-1.6 were investigated because the PD was still too high for the previous welds. Figure 111 illustrates the waveform results which are expressed in amplitude (V) over time (μ s).

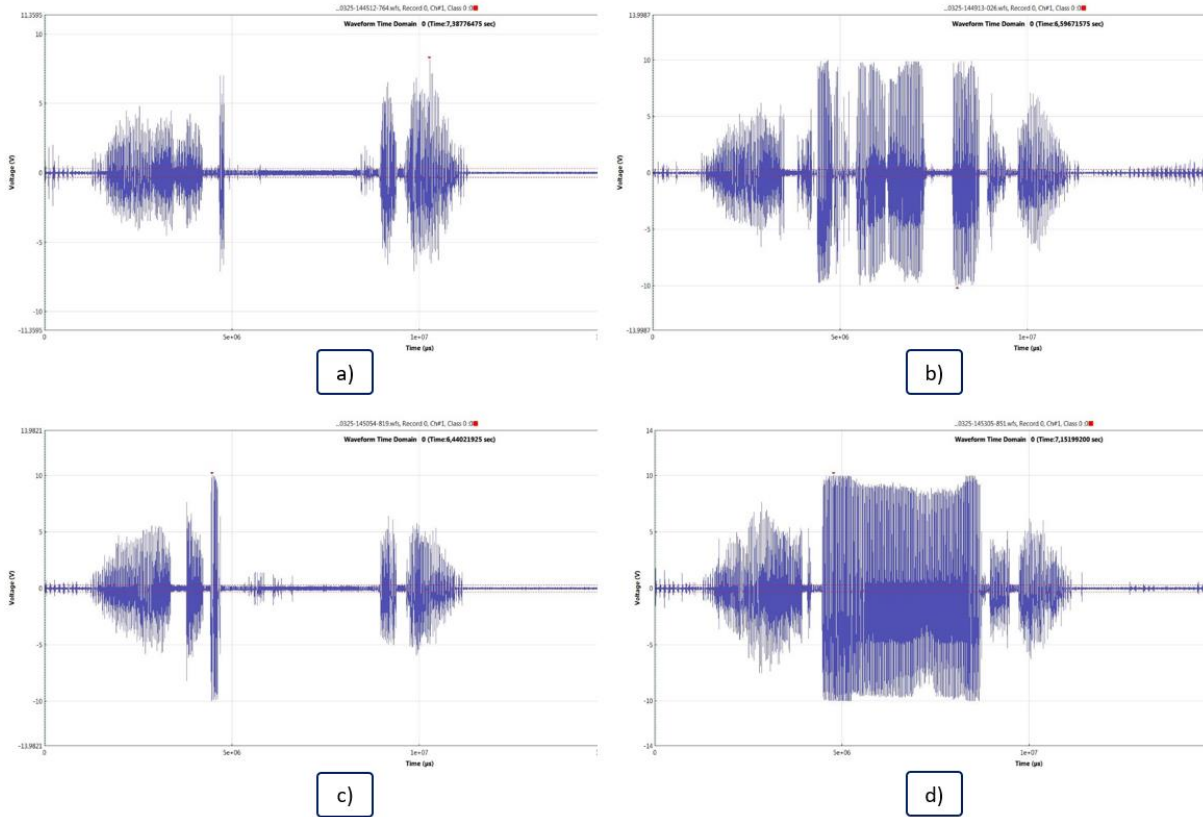


Figure 111: Waveform of weld nrs. SW-68-R11-1.3 (a), SW-68-R11-1.4 (b), SW-68-R11-1.5 (c), SW-68-R11-1.6 (d).

Based on the waveforms shown in Figure 111, very different results are obtained for the same process trials. For each process trial, the movements of the welding machine are the same, but different waveforms are produced. This phenomenon is probably the cause of the large data variations occurring in the previous test series, during which actual welding took place. Those AE signals were influenced by the signals caused by the movement of the machine, resulting in more exceedances of the threshold, named hits.

In the middle of the AE signals, shown in Figure 111b and Figure 111d, some irregular, large bursts appear. It is assumed that these bursts are caused by the sleeve vibrating against the pin, or vice versa, due to the tolerance dimensions. Since the sleeve plunges into the material during the welding process, material is located between the sleeve and pin, likely causing a damping effect on these vibrations. As a result, no large bursts such as observed in Figure 111b and Figure 111d appear in the waveforms of the previous test series. This is however an assumption, as the waveforms of weld nrs. SW-68-R11-1.3 (Figure 111a) and SW-68-1.5 (Figure 111c) do not contain these large bursts in the middle of the waveform.

ASL/Time

The signal is expressed by ASL over time (μs). The results are presented in Figure 112, with the signals recorded during the DT phase encircled in black. No reproducible results were found.

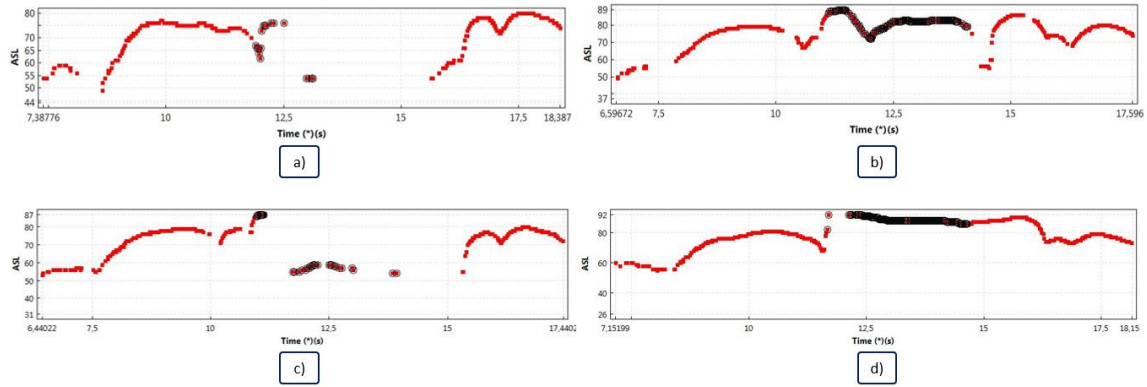


Figure 112: ASL/Time-representation of weld nrs. SW-68-R11-1.3 (a), SW-68-R11-1.4 (b), SW-68-R11-1.5 (c), SW-68-R11-1.6 (d).

Duration/Amplitude

The signal is expressed by duration (μs) over amplitude (dB). The results are shown in Figure 113, with the signals recorded during the DT phase encircled in black. No reproducible results were found.

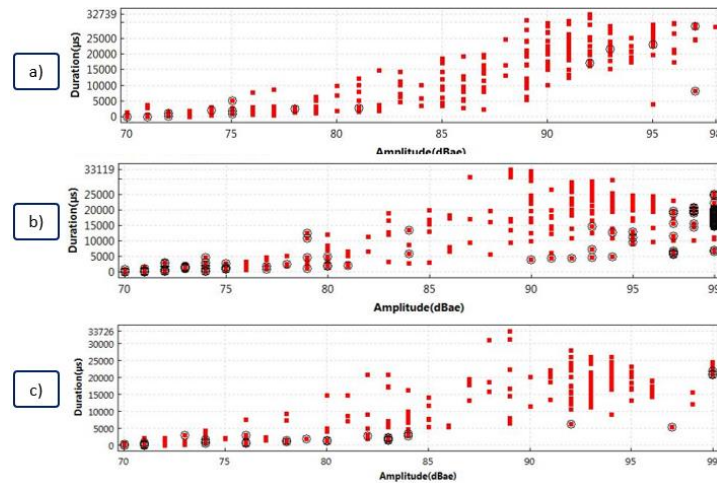


Figure 113: Duration/Amplitude-representation of weld nrs. SW-68-R11-1.3 (a), SW-68-R11-1.4 (b), SW-68-R11-1.5 (c).

The results of weld nr. SW-68-R11-1.6 are in this case not included as they are not representative.

Risetime/Time

The signal is expressed by risetime (μs) over time (μs). The results are shown in Figure 114, with the signals recorded during the DT phase encircled in black. No reproducible results were found.

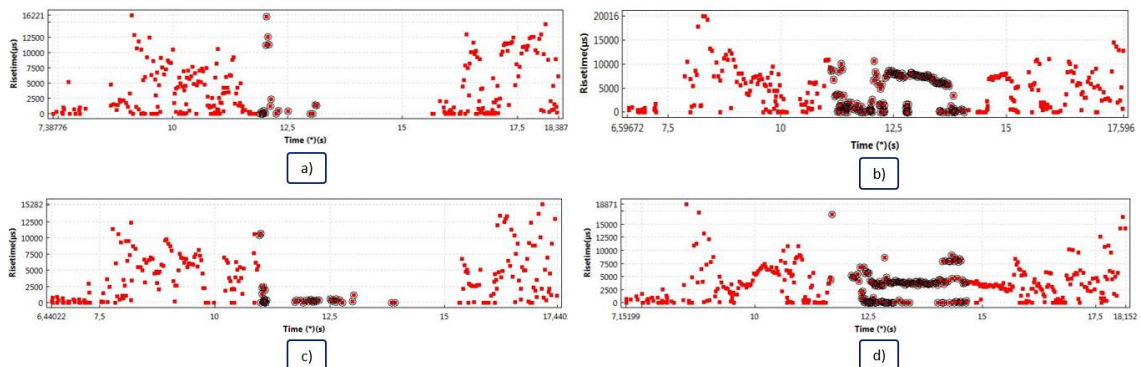


Figure 114: Risetime/Time-representation of weld nr. SW-68-R11-1.3 (a), welds SW-68-R11-1.4 (b), welds SW-68-R11-1.5 (c), welds SW-68-R11-1.6 (d).

Frequency centroid/Time

The signal is expressed by frequency centroid (kHz) over time (μ s). The results are presented in Figure 115, with the signals recorded during the DT phase encircled in black.

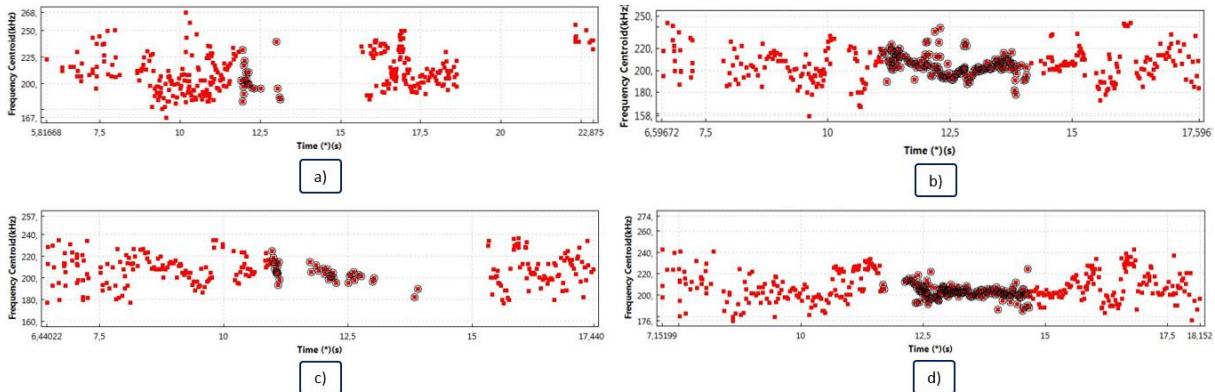


Figure 115: Frequency centroid/Time-representation of weld nrs. SW-68-R11-1.3 (a), SW-68-R11-1.4 (b), SW-68-R11-1.5 (c), SW-68-R11-1.6 (d).

General conclusion

The previous results show that the noise caused by the movements of the welding machine overrule the relevant sound originating from the welding process. Moreover, the data caused by this background noise is not reproducible. Hence, in order to be able to compare the relevant AE signals, a good AE configuration has to be found. A good configuration can be defined as one for which the AE signals are filtered from the background noise caused by mechanical movements of the welding equipment. Hence these AE signals are only derived from the welding process itself and will likely not display such variations as observed in the previous series. Since the AE signals in the previous series contained this background noise and hence showed too much varieties, their conclusions based on these results are not reliable.

6.9 Test series R12 and R13 – RFSSpW

6.9.1 Selected parameters

Table 36: Welding parameters of test series R12 and R13.

PD (mm)	RS (rpm)	PT (s)	DT (s)	RT (s)	HT (s)
3	2250	1.5	3	1.5	2

Table 37: Other parameters of test series R12 and R13.

Material (sheet thickness)	Cleaning frequency	Location of the sensor
EN AW-6082-T6 (2 mm)	After every 2 welds	On the welding table

Table 38: AE configuration of test series R12 and R13.

Test series	Sensor type	Resonance frequency (kHz)	Threshold (dB)	Frequency range of the digital filter (kHz)	Sampling rate (MSPS)	Time driven rate (s)
R12	WD	450	60	100 - 400	2	3
R13	WD	450	60	100 - 400	5	3

6.9.2 Objective

In this test series, the effect of the sampling rate and the frequency range of the digital filter was investigated, in order to construct a good AE configuration which leads to filtering out the noise originating from the equipment. The frequency range of the digital filter was therefore increased, in order to filter out the noise of the equipment, which is supposed to occur at lower frequencies. Moreover, the sampling rate was increased from 1 MSPS to 2 MSPS and 5 MSPS. The selected frequency range and the sampling rate for each test series is given in Table 38.

6.9.3 Results and conclusion

The results of these test series show that the threshold of 60 dB was too high in order to produce hits. Output representations such as ASL/Time, Duration/Amplitude, Risetime/Time, Frequency centroid/Time could not be constructed due to the fact that the AE signals did not exceed the threshold. These test series were re-produced in test series R17 and R18 with a lower threshold.

Waveform evaluation

As an example, the waveform of the welds in test series R12 are shown in Figure 116, with an indication of the threshold. Based on these results, it can be concluded that less variation appears and fewer bursts occur. Therefore the shift to a higher frequency range had a positive influence on filtering out the background noise and hence these filter settings were used in further test series.

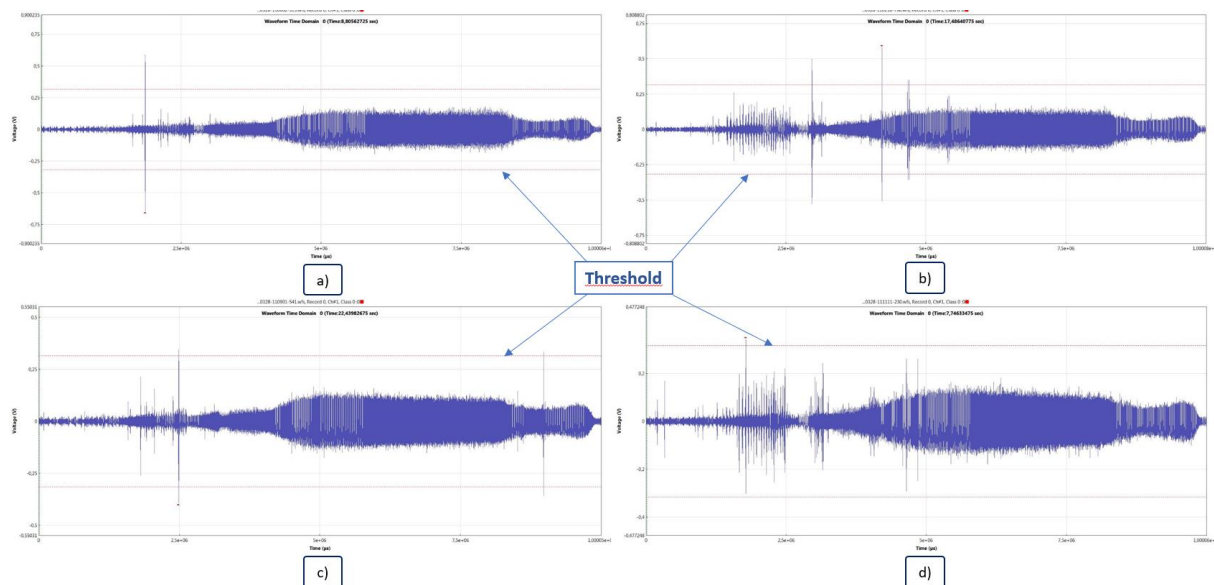


Figure 116: Waveforms of weld nrs. SW-68-R12-1.1 (a), SW-68-R12-1.2 (b), SW-68-R12-1.3 (c), SW-68-R12-1.4 (d).

All other results can be consulted in the external appendix.

6.10 Test series R14 – RFSSpW

6.10.1 Selected parameters

Table 39: Welding parameters of test series R14.

PD (mm)	RS (rpm)	PT (s)	DT (s)	RT (s)	HT (s)
3	2250	1.5	3	1.5	2

Table 40: Other parameters of test series R14.

Material (sheet thickness)	Cleaning frequency	Location of the sensor
EN AW-6082-T6 (2 mm)	After every 2 welds	On the welding table

Table 41: AE configuration of test series R14.

Sensor type	Resonance frequency (kHz)	Threshold (dB)	Frequency range of the digital filter (kHz)	Sampling rate (MSPS)	Time driven rate (s)
WD	450	60	400 - 800	2 - 5	3

6.10.2 Objective

Test series R14 can be considered as an exploratory test series in order to obtain an idea of the amount of effect of the background noise. The investigation was done by tapping the welding table, clapping hands next to the sensor and measuring the background noise.

6.10.3 Results and conclusion

Some of the results are shown in Figure 117. All other results are available in the external appendix.

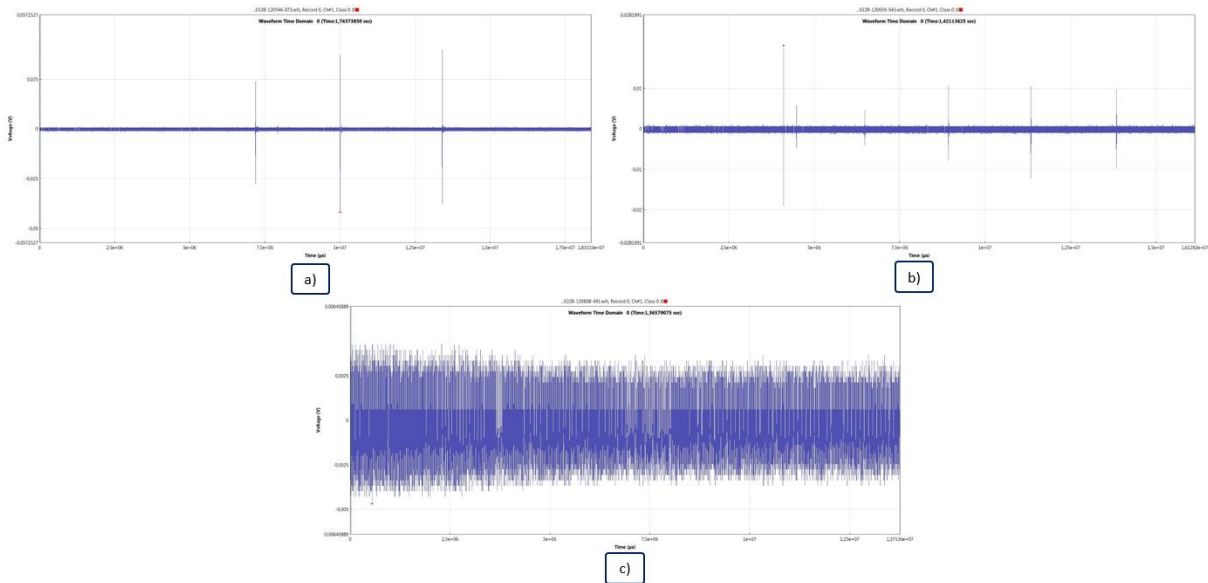


Figure 117: Results of series R14: tapping the welding table 3 times (a), clapping hands 6 times (b) and background noise (c).

Based on the results in Figure 117, it can be concluded that these disturbances have little to no effect on the AE signals while welding. Background noises such as clapping and tapping the welding table normally do not appear in the AE signals during welding. Figure 117c shows the waveform of the background noise, which is zoomed in to a large extent. Based on these results, it can be concluded with certainty that the non-reproducible AE signals are caused by from the mechanical movements of the welding machine.

6.11 Test series R15 – Arc welding

6.11.1 Selected parameters

Table 42: Arc welding parameters of test series R15.

Weld type	Current (A)	Voltage (V)	Wire feeding rate (mm/min)	Stick-out (mm)	Shield gas supply
Good welds	87	12	3	0.8	Yes
Bad welds	87	15	3	0.8	No

Table 43: Other parameters of test series R15.

Material	Cleaning frequency	Location of the sensor
Steel S235	N/A	On the sheet to be welded

Table 44: AE configuration of test series R15.

Sensor type	Resonance frequency (kHz)	Threshold (dB)	Frequency range of the digital filter (kHz)	Sampling rate (MSPS)	Time driven rate (s)
WD	450	60	400 - 800	2	3

6.11.2 Objective

Since the AE configuration used in previous test series was not accurately defined, another welding process was investigated using AE, in order to test the relevance of the use of AE. This test series consists of welds produced by MAG welding using a semi-automatic welding robot.. This was the first test series in order to get acquainted with the welding process and parameters. Six welds were made, four with a good quality and two with a bad quality. The good quality welds were produced with shielding gas, whereas the bad quality welds were made without shielding gas. The first goal of this test series is to investigate if any differences appear and to which extent these differences can be observed in the AE signals of a good quality weld and a bad quality weld. The second goal is to find a suitable threshold for this process by using a trial and error method.

6.11.3 Results and conclusion

Visual inspection

The six welds are visible in Figure 118, in which the four good welds are located at the bottom, and the two bad welds at the top.



Figure 118: Visual inspection of the welds in test series R15.

Waveform evaluation

The waveforms show a lot of variation among. For example, the waveforms of a good quality weld (SW-ROB-R15-1.1) and a bad quality weld (SW-ROB-R15-1.6) are shown in Figure 119, where the amplitude (V) is expressed over time (μs). Other results are available in the external appendix.

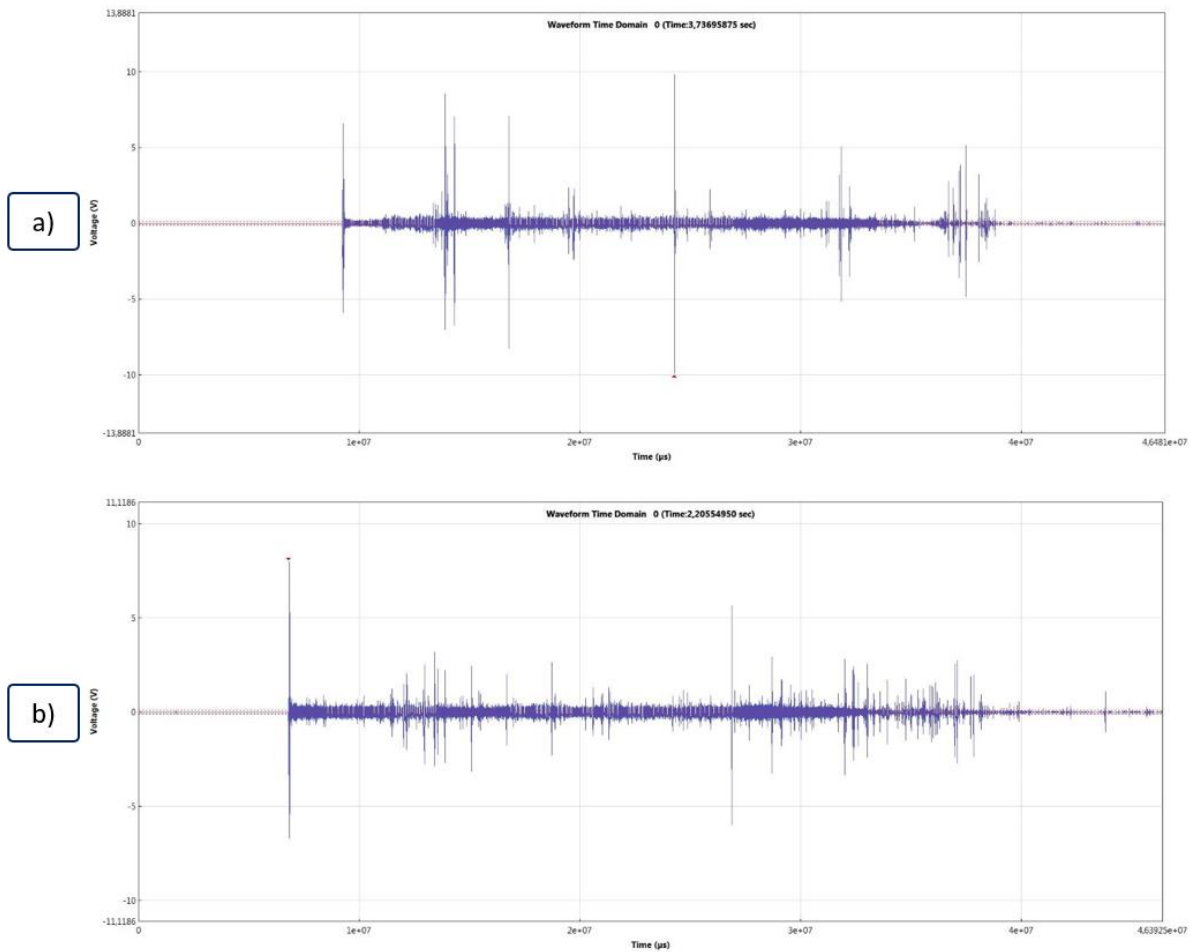


Figure 119: Waveform-analysis of weld nrs. SW-ROB-R15-1.1 (a) and SW-ROB-R15-1.6 (b).

The waveforms in Figure 119 are shifted in the time axis. This is due to the absence of an external trigger, meaning the start of the recording happened manually, causing a different starting point in time. Many random little bursts are visible, appearing at random places in time. No concrete conclusion could be drawn based on these results.

Duration/Amplitude

The duration/amplitude representation for a good quality weld (SW-ROB-R15-1.1) and a bad quality weld (SW-ROB-R15-1.6) are given in Figure 120. All other results are consultable in the external appendix.

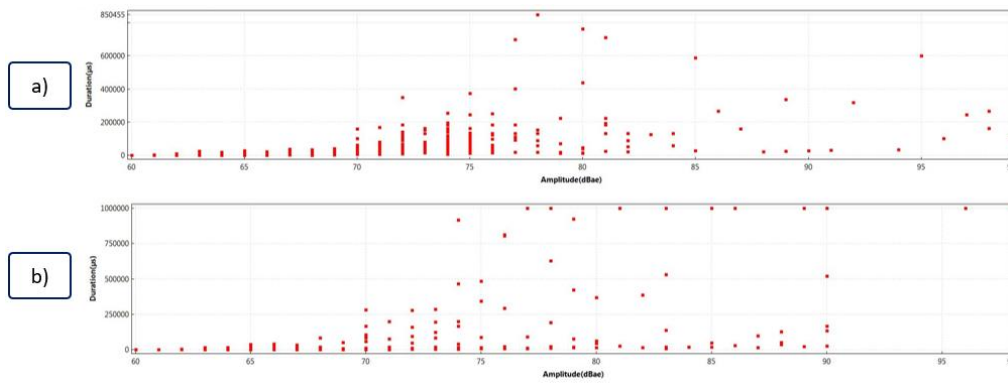


Figure 120: Duration/Time-analysis of weld nrs. SW-ROB-R15-1.1 (a) and SW-ROB-R15-1.6 (b).

Although random data points appear, it can be concluded that there are some similar data points even though there is a difference in the weld quality. Other welds on the other hand, show more variation. An example of another good quality weld (SW-ROB-R15-1.2) is given in figure Figure 121.

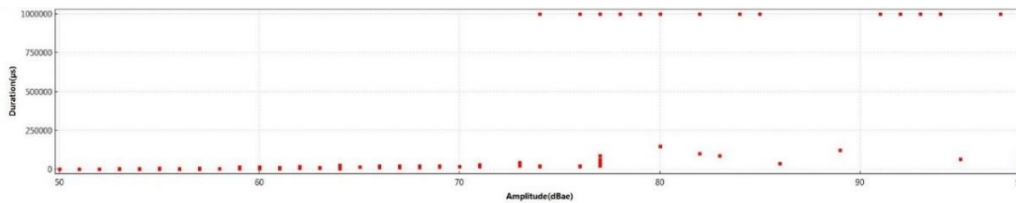


Figure 121: Duration/Amplitude-analysis of weld nr. SW-ROB-R15-1.2.

Comparing the duration/amplitude representation of two good quality welds in figure 40 and figure 39a, it is clear that there is a lot of variations among the AE signals for both good and bad quality welds. Based on these results, it is not possible to distinguish between the good and bad quality welds.

Frequency centroid/Time

In order to demonstrate the variation in the frequency centroid/time representation, the results of two good quality welds (SW-ROB-R15-1.1 and SW-ROB-R15-1.2) and one bad quality weld (SW-ROB-R15-1.6) are illustrated in Figure 122. All other results are consultable in the external appendix.

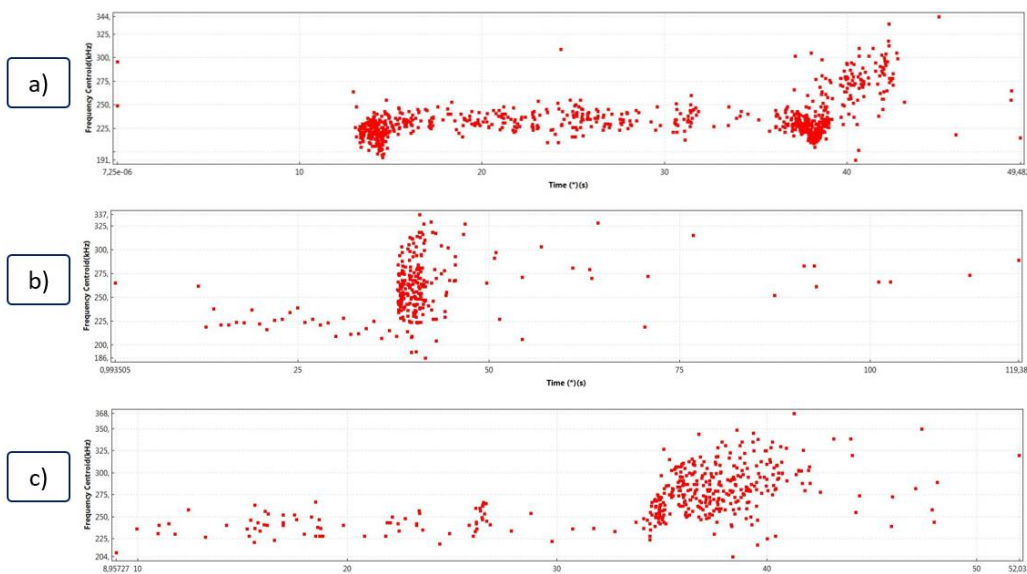


Figure 122: Frequency centroid/Time-representation of weld nrs. SW-ROB-R15-1.1 (a), SW-ROB-R15-1.2 (b) and SW-ROB-R15-1.6 (c).

ASL/Time

In order to demonstrate the variation occurring in the ASL/time representation, the results of two good quality welds (SW-ROB-R15-1.1 and SW-ROB-R15-1.2) and one bad quality weld (SW-ROB-R15-1.6) are illustrated in Figure 123. All other results are consultable in the external appendix.

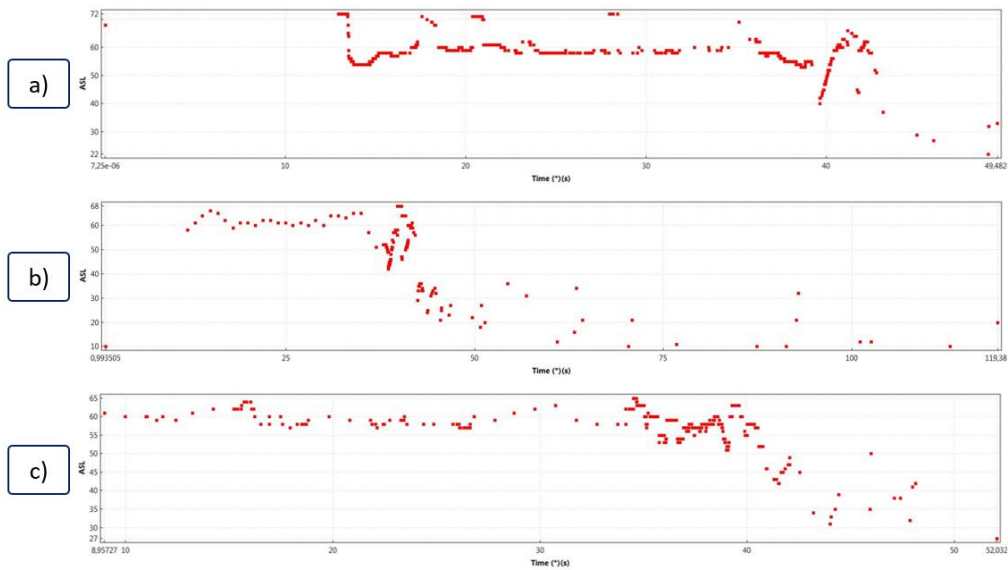


Figure 123: ASL/Time-representation of weld nrs. SW-ROB-R15-1.1 (a), SW-ROB-R15-1.2 (b) and SW-ROB-R15-1.6 (c).

Cumulative absolute energy/Time

In order to demonstrate the variation occurring in the cumulative absolute energy/time representation, the results of two good quality welds (SW-ROB-R15-1.1 and SW-ROB-R15-1.2) and one bad quality weld (SW-ROB-R15-1.6) are illustrated in Figure 124. All other results are consultable in the external appendix.

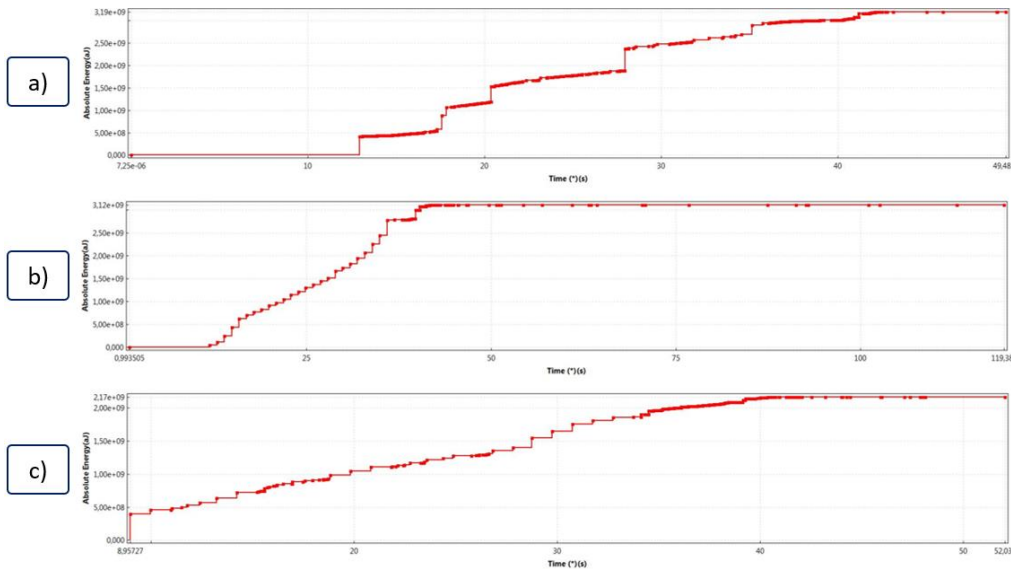


Figure 124: Cumulative absolute energy/Time-representation of weld nrs. SW-ROB-R15-1.1 (a), SW-ROB-R15-1.2 (b) and SW-ROB-R15-1.6 (c).

This data representation shows differences between a good and a bad quality weld. The good quality welds contain a cumulative absolute energy ranging from $2.8 \cdot 10^9$ to $4.6 \cdot 10^9$ aJ, whereas the bad quality welds contain a value from $1.8 \cdot 10^9$ up to $2.2 \cdot 10^9$ aJ. This phenomenon has to be further examined in order to see whether this results are repeatable and are not a coincidence.

Cumulative counts/Time

These signals are not further investigated as it showed too much variation, similar to the Duration/Amplitude, Frequency centroid/Time and ASL/Time representations. The results can be consulted in the external appendix.

Conclusion

Based on the waveform evaluation and hit data analysis, it was clear that the signals varied too much and hence are not reproducible. A possible cause could be that the gas extraction during the process produces too much noise, resulting in disturbances to the AE signals. In order to avoid these disturbances, the threshold was increased from 60 dB to 70 dB and a new test series (R16) was executed.

Although the AE signals showed much variety, the cumulative absolute energy/Time representation showed obvious differences between the good quality and the bad quality welds. Hence, in order to being able to distinguish between the good and the bad quality welds, based on this data representation, its relevance should be further investigated.

6.12 Test series R16 – Arc welding

6.12.1 Selected parameters

Table 45: Arc welding parameters of test series R16.

Weld nr.	Current (A)	Voltage (V)	Shield gas supply
SW-ROB-R16-1.1	59	10.3	Yes
SW-ROB-R16-1.2	77	12.2	Yes
SW-ROB-R16-1.3	90	12.5	Yes
SW-ROB-R16-1.4	87.2	12.7	Yes
SW-ROB-R16-1.5	87	12.5	Yes
SW-ROB-R16-1.6	87.1	12.4	Yes
SW-ROB-R16-1.7	87.5	15.4	No
SW-ROB-R16-1.8	87.5	15.4	No

Table 46: Other parameters of test series R16.

Material	Cleaning frequency	Location of the sensor
Steel S235	N/A	On the sheet to be welded

Table 47: AE configuration of test series R16.

Sensor type	Resonance frequency (kHz)	Threshold (dB)	Frequency range of the digital filter (kHz)	Sampling rate (MSPS)	Time driven rate (s)
WD	450	70	400 - 800	2	3

6.12.2 Objective

This test series consist of arc welds, produced by MAG welding, using a semi-automatic welding robot. Eight welds were produced with varying parameters, listed in Selected parameters

Table 45. The goal of this test series is to investigate the effect of the gas extraction noise on the AE signals, recorded during welding. Therefore, the threshold is increased from 60 dB to 70 dB. Possible patterns related to a change in current and voltage are also investigated.

6.12.3 Results and conclusion

Visual inspection

The eight welds are visible in Figure 125, in which the 6 good quality welds are located at the bottom, and the 2 bad quality welds at the top.



Figure 125: Visual inspection of the welds in test series R16.

Waveform evaluation

The results for a good quality weld (SW-ROB-R16-1.2) and for a bad quality weld (SW-ROB-R16-1.8) are shown in Figure 126.

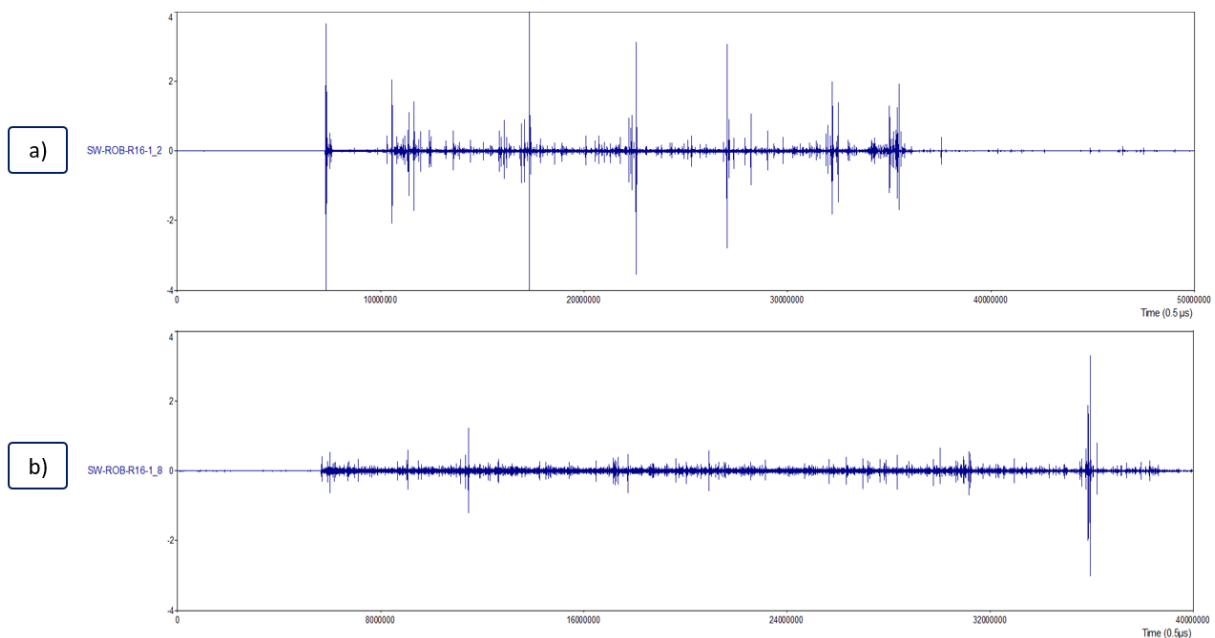


Figure 126: Waveform evaluation of weld nrs. SW-ROB-R16-1.2 (a) and SW-ROB-R16-1.8 (b).

Figure 126a shows a shorter waveform than in Figure 126b, due to a different time scale. In general, the waveforms of the good quality welds exhibit larger, thinner bursts compared to the burst found in the bad quality welds. It can however not be concluded that large, thin bursts are related to a good quality weld, since other bad quality welds in test series R15 also contain these large, thin bursts.

Metallographic evaluation

Figure 127 illustrates the cross-sections of weld nrs. SW-ROB-R16-1.1 to SW-ROB-R16-1.3.

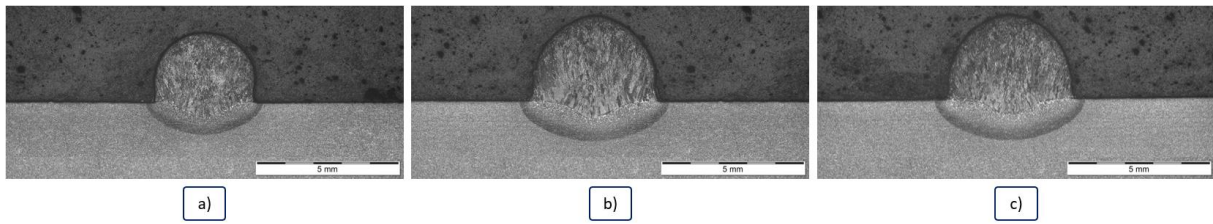


Figure 127: Cross-sections of the welds with shielding gas supply: SW-ROB-R16-1.1 (a), SW-ROB-R16-1.2 (b) and SW-ROB-R16-1.3 (c).

Since the current and the voltage for each weld from left to right increases, it can be concluded that an increase of the current and the voltage leads to an increase of the weld zone and the heat affected zone (HAZ). Using these parameters, a good diffusion between the base material and the filler material has been achieved.

Figure 128 compares the cross-sections of the welds produced with shielding gas supply to those welds produced without shielding gas supply.

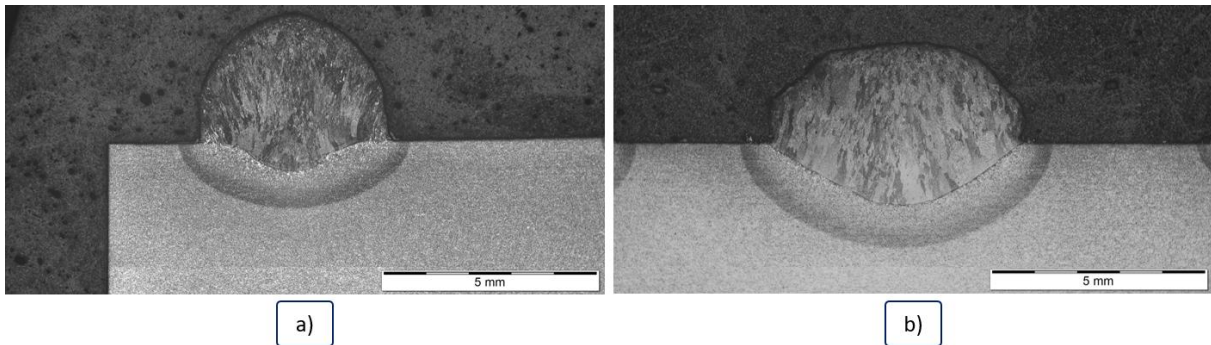


Figure 128: Cross-sections of a weld with shielding gas supply: SW-ROB-R16-1.4 (a) and without shielding gas supply: SW-ROB-R16-1.7 (b).

The comparison of Figure 128a to Figure 128b leads to the conclusion that in the welds produced without shielding gas, a welding zone is present, but little to no diffusion between the base material and the filler material has occurred..

Duration/Amplitude, Frequency centroid/Time, ASL/Time

Based on these data representations and similar to the results of test series R15, no conclusions concerning the weld quality could be made. Therefore, it is not further discussed. The results are available in the external appendix.

Cumulative absolute energy/Time

Also in this test series, there is a clear distinction in the cumulative absolute energy of a good quality weld, and a bad quality weld. The results for all the welds are illustrated in Figure 129. The brown and dark blue curve represent weld nr. SW-ROB-R16-1.7 and SW-ROB-R16-1.8, respectively, where no shielding gas was supplied. The other curves represent the good welds (SW-ROB-R16-1.1 to SW-ROB-R16-1.6).

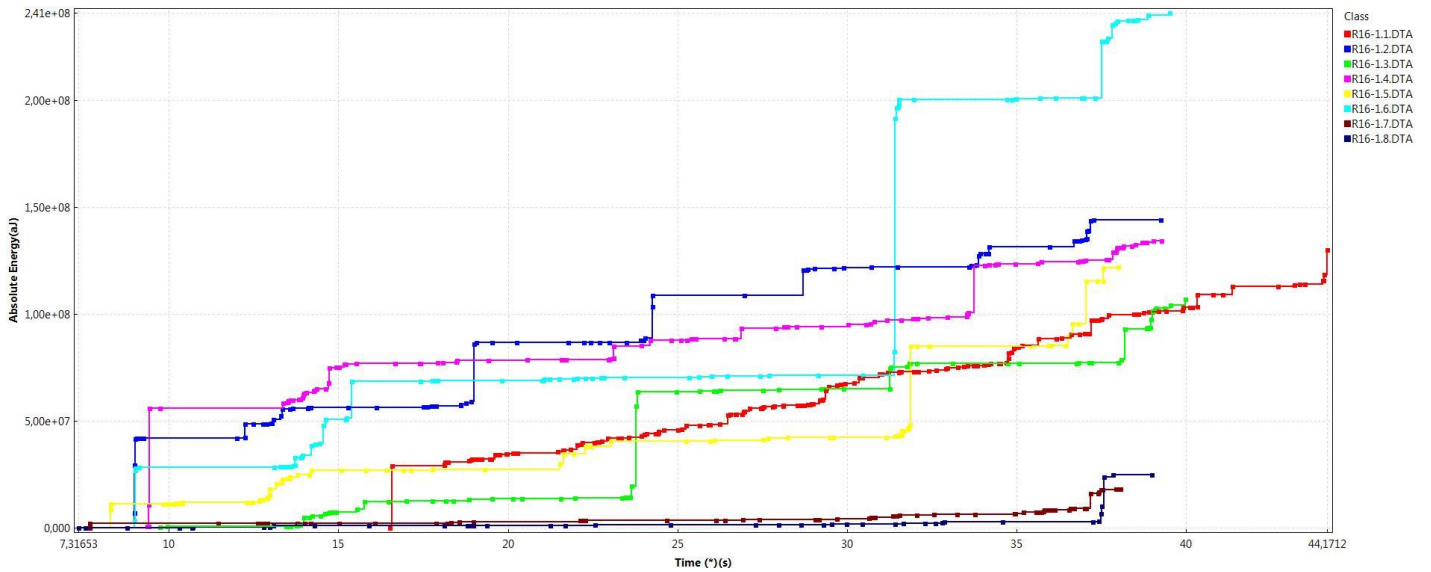


Figure 129: Cumulative absolute energy/Time of the welds in series R16.

Conclusion

Based on the cumulative absolute energy, the good quality welds can be distinguished from the bad quality welds as they contain a lower value. The absolute energy is related to the bonding, as confirmed by metallographic research. In case of the bad quality welds, there is less diffusion of the filler material into the base material.

6.13 Test series R17 and R18 – RFSSpW

6.13.1 Selected parameters

Table 48: Welding parameters of test series R17 and R18.

PD (mm)	RS (rpm)	PT (s)	DT (s)	RT (s)	HT (s)
3	2250	1.5	3	1.5	2

Table 49: Other parameters of test series R17 and R18.

Material (sheet thickness)	Cleaning frequency	Location of the sensor
EN AW-6082-T6 (2 mm)	After every 2 welds	On the welding table

Table 50: AE configuration of test series R17 and R18.

Test series	Sensor type	Resonance frequency (kHz)	Threshold (dB)	Frequency range of the digital filter (kHz)	Sampling rate (MSPS)	Time driven rate (s)
R17	WD	450	50	400 - 800	2	3
R18	WD	450	50	400 - 800	5	3

6.13.2 Objective

Test series R17 and R18 are respectively a repetition of previous test series R12 and R13, respectively, with the only difference that the threshold was lowered from 60 dB to 50 dB. For each test series, four welds were produced and the resulting waveforms and hit data representations were examined. The

goal of these test series is the same as series R12 and R13, namely to construct a good AE configuration in order to filter out the mechanical interference originating from the welding equipment.

6.13.3 Results and conclusion

Waveform evaluation

The results of these test series showed that a decrease of the threshold lead to more efficient filtering of the mechanical interferences, since smaller bursts were present in the waveforms. The results of test series R17 are given in figure 37, the results of series R18 (see external appendix) are almost exactly the same, concluding that the sampling rate does not have an effect on the filtering of mechanical interference. Therefore in further test series, a sampling rate of 2 will be used.

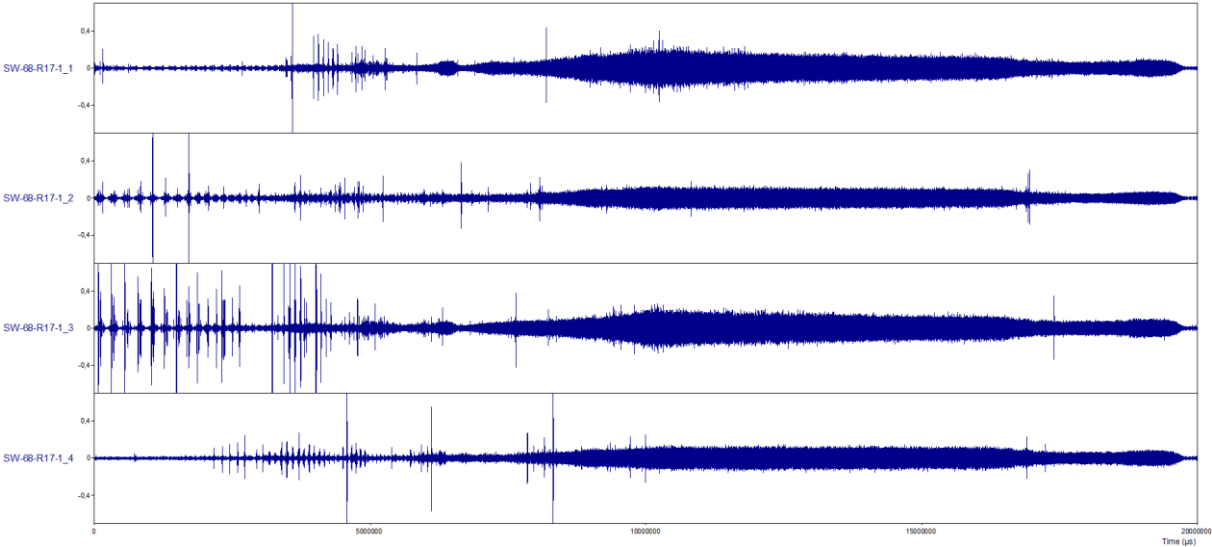


Figure 130: Waveform-analysis of test series R17.

Based on Figure 130, it is observed that weld nrs. SW-R17-1.1 and SW-68-R17-1.3 have a larger waveform compared to those of weld nr. SW-68-R17-1.2 and SW-68-R17-1.4. This could be an effect of the cleaning frequency, as the tool was cleaned after welding SW-R17-1.1 and SW-68-R17-1.3.

ASL/Time

The ASL/time representations for test series R17 are shown in Figure 131. This time, the DT phase is not encircled as the intention was to analyse the complete waveform. Other results are available in the external appendix.

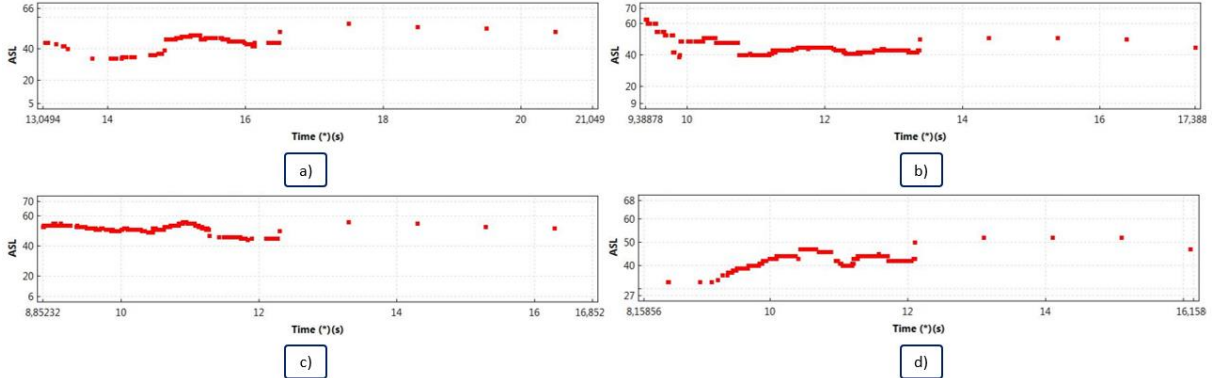


Figure 131: ASL/Time-representation of weld nrs. SW-68-R17-1.1 (a), SW-68-R17-1.2 (b), SW-68-R17-1.3 (c), SW-68-R17-1.4 (d).

Previous test series such as R5 and R6 showed that there was a straight line around 60 dB. Figure 131 shows that this straight line is lowered to a value around 40 – 50 dB, indicating that there are some differences in the waveform. Signals that were recorded in previous test series due to the mechanical movement are left out in this test series, which is a good sign.

Duration/amplitude

The results for test series R17 are shown in Figure 132. Other results are available in the external appendix.

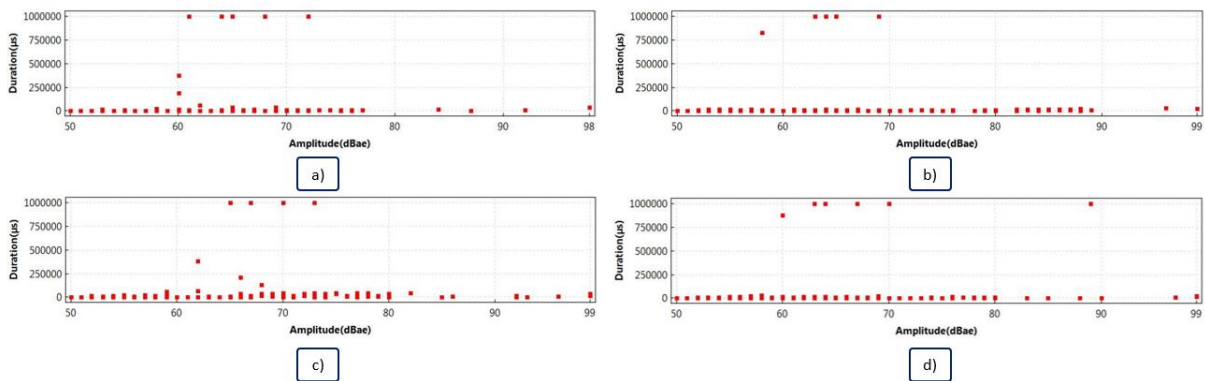


Figure 132: Duration/Amplitude-representation of weld nrs. SW-68-R17-1.1 (a), SW-68-R17-1.2 (b), SW-68-R17-1.3 (c), SW-68-R17-1.4 (d).

In general, the signals presented in Figure 132 show the same pattern, with some points located at a longer duration.

Frequency centroid/Time

The frequency centroid/time representation for test series R17 is shown in Figure 133. Other results are available in the external appendix.

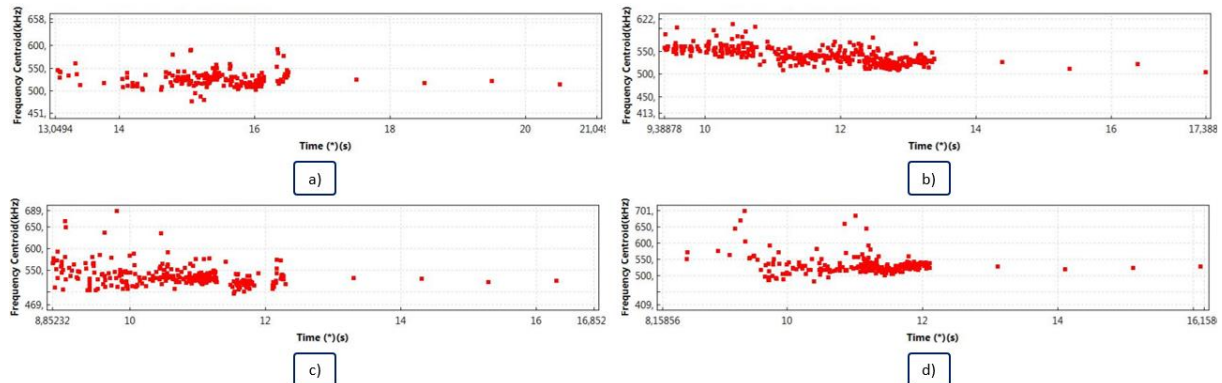


Figure 133: Frequency centroid/Time-analysis of weld nr. SW-68-R17-1.1 (a), SW-68-R17-1.2 (b), SW-68-R17-1.3 (c), SW-68-R17-1.4 (d).

Cumulative absolute energy/Time

The results for test series R17 are shown in Figure 134. Other results are available in the external appendix.

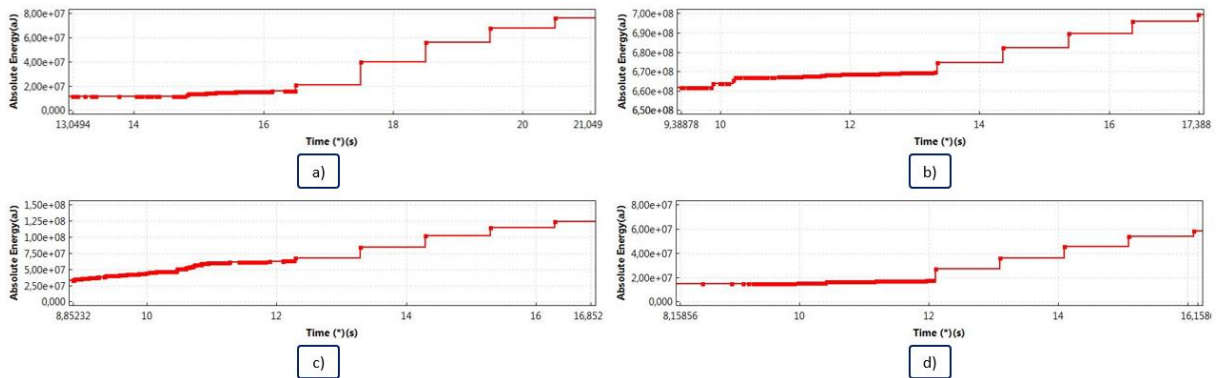


Figure 134: Cumulative absolute energy/Time-analysis of welds SW-68-R17-1.1 (a), SW-68-R17-1.2 (b), SW-68-R17-1.3 (c), SW-68-R17-1.4 (d).

The Absolute energy/Time-representation is very important since the absolute energy is related to the bonding of the friction stir spot weld. In each of the four welds, the same course can be observed, but there are still some differences in the magnitude of the absolute energy.

Cumulative counts/Time

The results for test series R17 are shown in Figure 135. Other results are available in the external appendix.

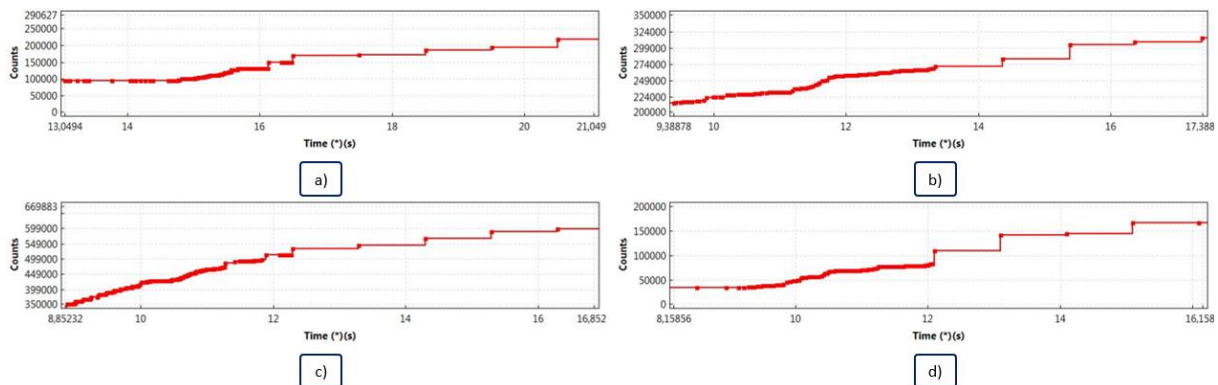


Figure 135: Cumulative counts/Time-analysis of welds SW-68-R17-1.1 (a), SW-68-R17-1.2 (b), SW-68-R17-1.3 (c), SW-68-R17-1.4 (d).

These signals still show some varieties based on the magnitude of the counts.

6.13.4 Comparison of test series R17 and R18

The comparison between test series R17 and R18 shows that the sampling rate had little to no influence on the AE signals. Therefore, the sampling rate is fixed at 2 MSPS in the further test series. In general, the AE signals in these test series show more similarities than those in previous ones, meaning that most of the mechanical interference is filtered out. This is due to the combination of a change in the digital filters and threshold lowering. However, there are still some varieties in the signal (in particular in the magnitudes of the absolute energy and the number counts) which should be avoided.

6.14 Test series R19 and R20 – RFSSpW

6.14.1 Selected parameters

Table 51: Welding parameters of test series R19 and R20.

PD (mm)	RS (rpm)	PT (s)	DT (s)	RT (s)	HT (s)
3	2250	1.5	3	1.5	2

Table 52: Other parameters of test series R19 and R20.

Test series	Material (sheet thickness)	Cleaning frequency	Location of the sensor
R19	EN AW-6082-T6 (2 mm)	After every 2 welds	On the welding table
R20	EN AW-6082-T6 (2mm)	After every 2 welds	On the aluminium sheet

Table 53: AE configuration of test series R19 and R20.

Sensor type	Resonance frequency (kHz)	Threshold (dB)	Frequency range of the digital filter (kHz)	Sampling rate (MSPS)	Time driven rate (s)
R50D	500	50	400 - 800	2	3

6.14.2 Objective

The effect of the sensor type is investigated in these test series. In previous test series, the WD-type sensor was used, whereas in these test series, the R50D sensor is used. The difference between the two sensors is the resonance frequency. More properties of these sensors can be found in the appendix. The same welding parameters as in the previous test series R17 and R18 are applied. The difference between test series R19 and R20 is that in series R20 the sensor was located on the aluminium sheet in order to investigate the effect of the distance between the sensor and the welding tool. Generally, it is known that a smaller number of high frequent signals are lost when this distance is smaller. The waveform and hit data set representation were investigated, as well as metallographic research.

6.14.3 Results and conclusion

Waveform evaluation

The waveforms of test series R19 and R20 are given in Figure 136 and Figure 137, respectively. The scale of the amplitude axis in Figure 136 is [-0.25; 0.25], whereas the scale of the amplitude axis in Figure 137 is three times larger: [-0.75; 0.75]. Therefore, it can be concluded that the signals in test series R20 are larger. This is due to the fact that less signals are lost along the way. The waveforms of test series R19 show a good, almost clean result with almost no varieties. The waveforms of test series R20 contain more little bursts which could be related to the weld quality.

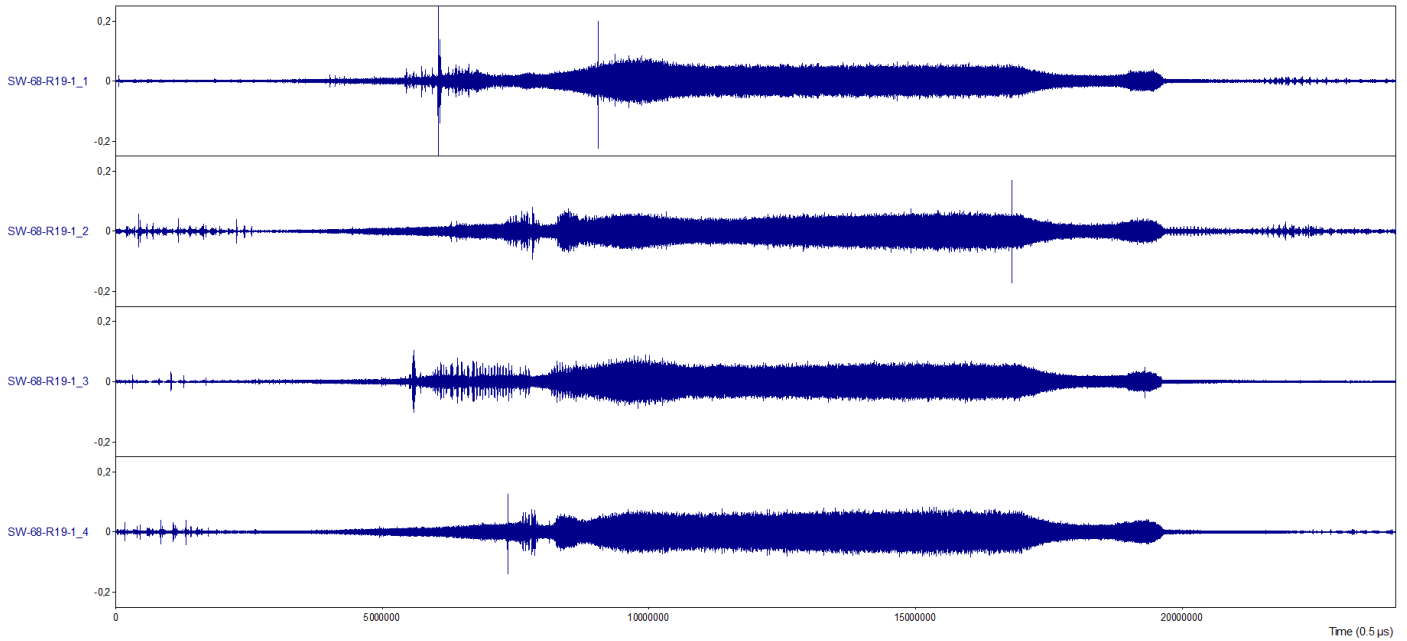


Figure 136: Waveform-analysis of test series R19.

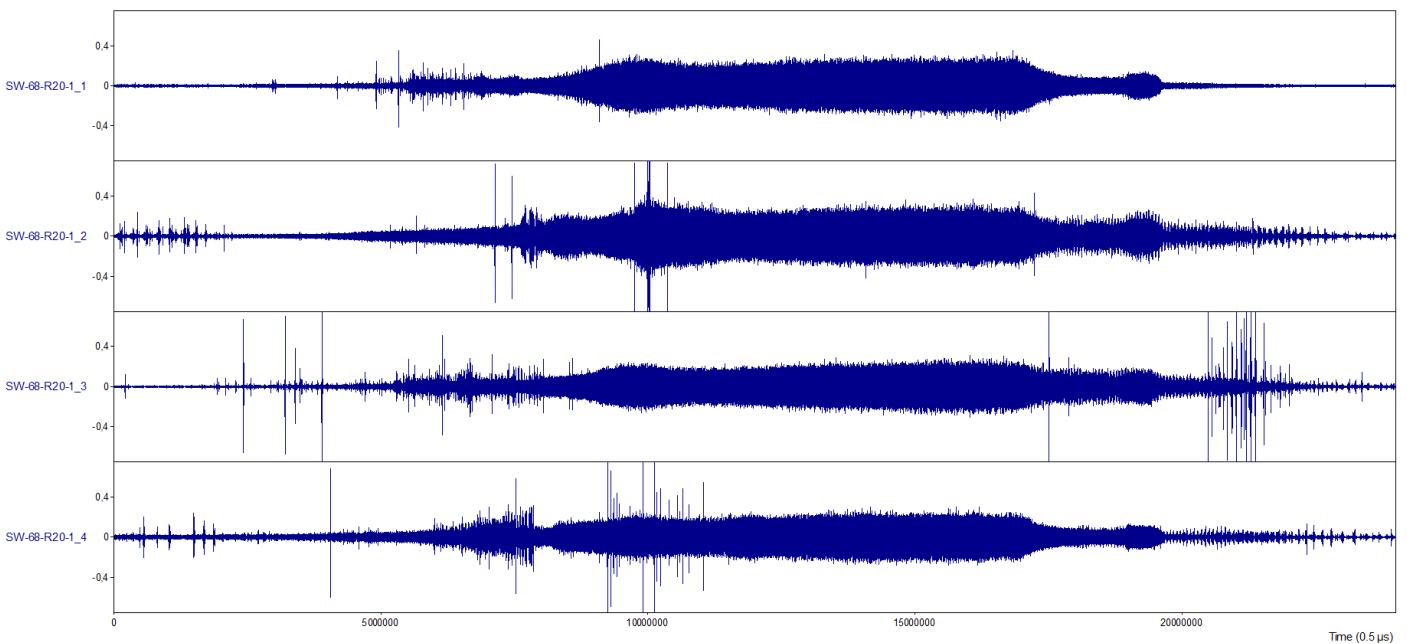


Figure 137: Waveform-analysis of test series R20.

Metallographic evaluation

Metallographic research is executed in order to examine the relevance of the AE configuration. Based on the waveform analysis, the cross-sections of the four welds should be very similar as their waveforms are also very similar. Figure 138 illustrates the cross-section of the four welds of series R19. The bonding length is measured and indicated in red, possible defects are indicated by blue circles.

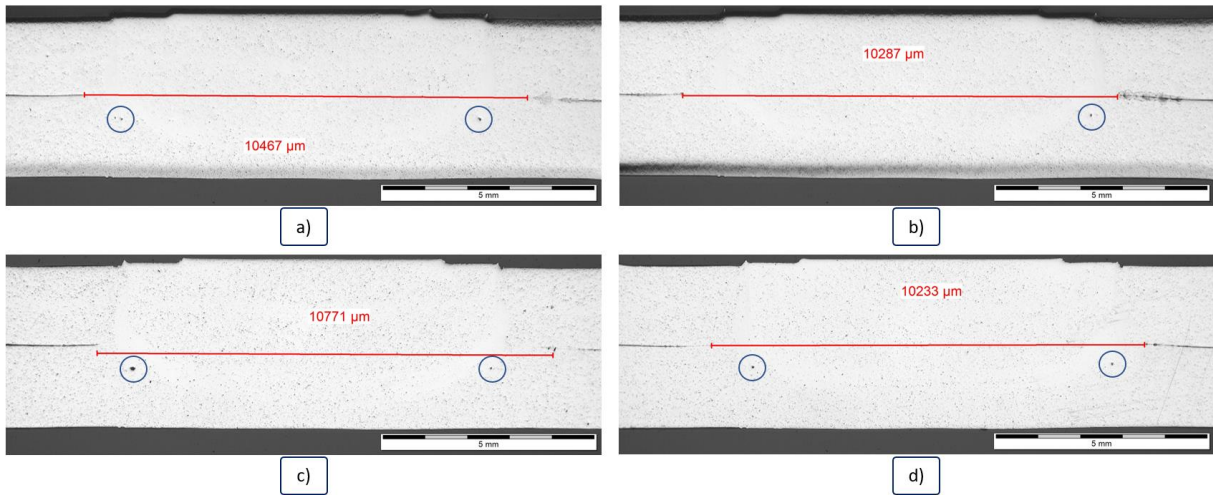


Figure 138: Metallographic research of weld nrs. SW-68-R19-1.1 (a), SW-68-R19-1.2 (b), SW-68-R19-1.3 (c), SW-68-R19-1.4 (d).

The metallographic results of test series R19 are very similar as no weld defects other than the small voids in the corner of the welds appear. The variations in the bonding length can be attributed to the location of the cut required for examining the cross-sections. Since the weld nugget is a cylinder, it is difficult to cut it perfectly through the centre. Based on these results, it can be concluded that the AE configuration is relevant and can be used in further investigations.

Figure 139 contains the metallographic results of series R20. Because the same welding parameters were used, the same minor voids in the corners appeared.

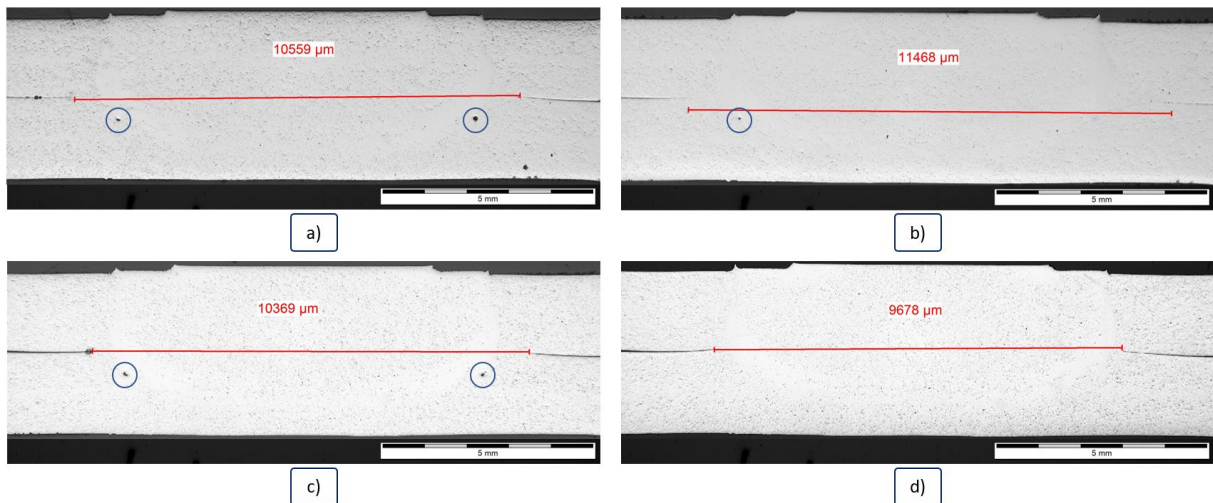


Figure 139: Metallographic research of weld nrs. SW-68-R20-1.1 (a), SW-68-R20-1.2 (b), SW-68-R20-1.3 (c), SW-68-R20-1.4 (d).

Also in this case, the variations in the bonding length can be attributed to imperfect cutting of the welds.

ASL/Time

Since the four welds of each test series are almost identical and show very little varieties in terms of their waveforms and their metallographic cross-section, two welds of test series R19 will be compared to two welds of test series R20 in Figure 140. The result for the other welds are consultable in the external appendix.

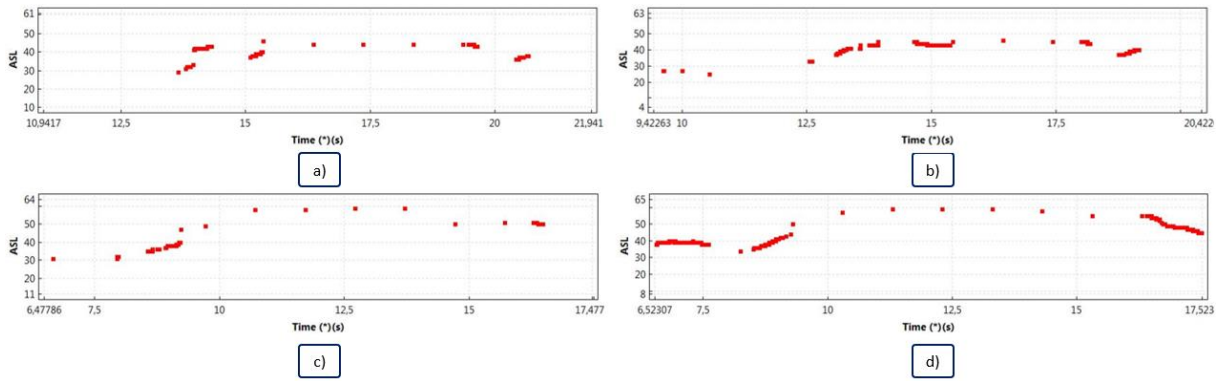


Figure 140: ASL/Time-analysis of weld nrs. SW-68-R19-1.1 (a), SW-68-R19-1.2 (b), SW-68-R20-1.1 (c), SW-68-R20-1.2 (d).

The signals show much similarities for both test series. The only difference however is the magnitude of the ASL, which is larger in test series R20 than in test series R19.

Duration/amplitude

The results of weld nrs. SW-68-R19-1.1, SW-68-R19-1.2 SW-68-R20-1.1 and SW-68-R20-1.2 are illustrated in Figure 141.

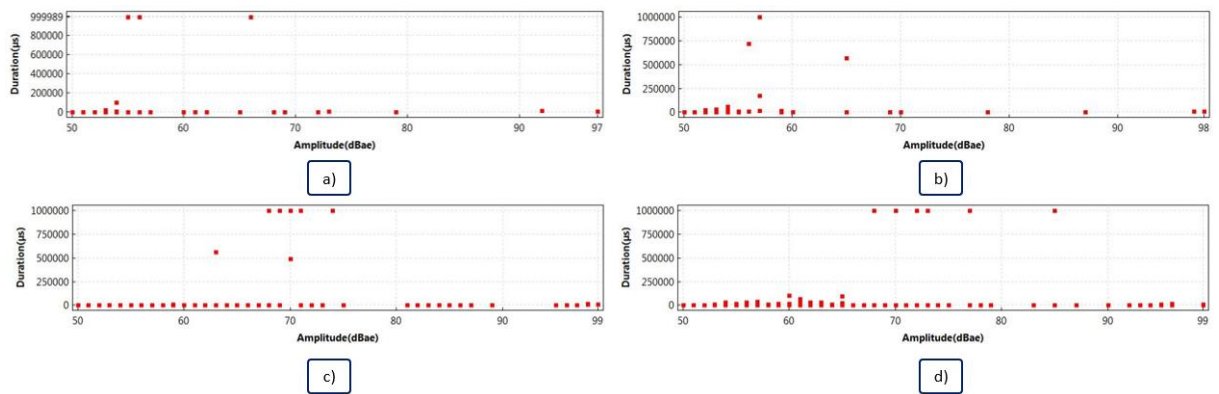


Figure 141: Duration/Amplitude-analysis of weld nrs. SW-68-R19-1.1 (a), SW-68-R19-1.2 (b), SW-68-R20-1.1 (c), SW-68-R20-1.2 (d).

Frequency centroid/Time

The results of weld nrs. SW-68-R19-1.1, SW-68-R19-1.2 SW-68-R20-1.1 and SW-68-R20-1.2 are illustrated in Figure 142.

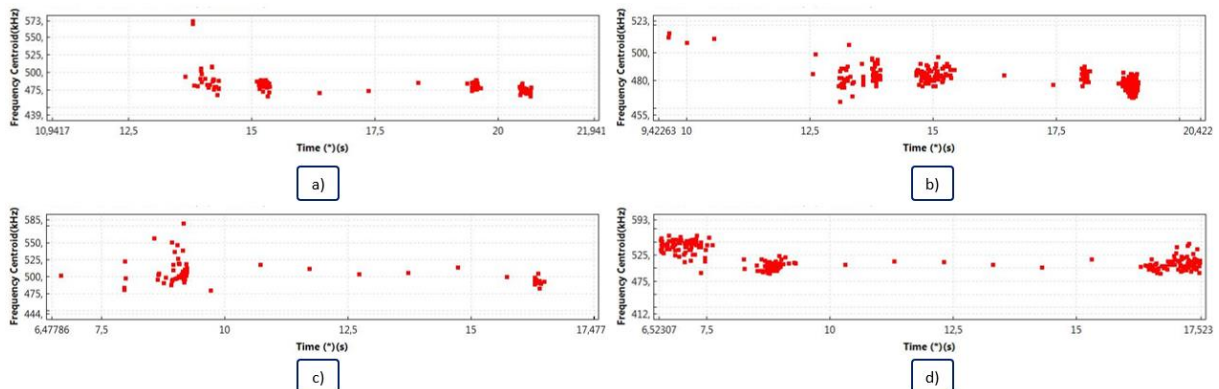


Figure 142: Frequency centroid/Time-analysis of welds SW-68-R19-1.1 (a), SW-68-R19-1.2 (b), SW-68-R20-1.1 (c), SW-68-R20-1.2 (d).

These signals show some minor differences, but these are mainly located around 480 kHz and 500 kHz for test series R19 and R20 respectively.

Cumulative absolute energy/Time

The results of weld nrs. SW-68-R19-1.1, SW-68-R19-1.2 SW-68-R20-1.1 and SW-68-R20-1.2 are illustrated in Figure 143.

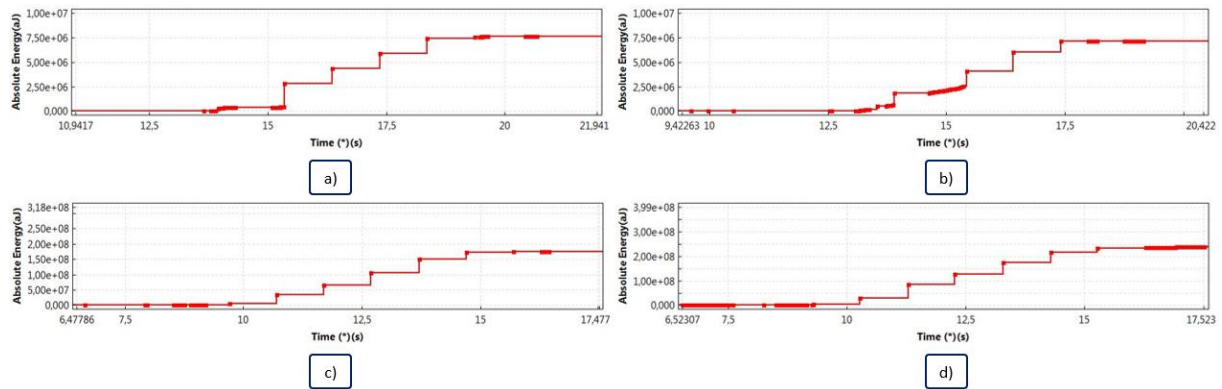


Figure 143: Cumulative absolute energy/Time-analysis of weld nrs. SW-68-R19-1.1 (a), SW-68-R19-1.2 (b), SW-68-R20-1.1 (c), SW-68-R20-1.2 (d).

The signals show the same course and the magnitude of the absolute energy hardly differs between the signals of each test series. The cumulative absolute energy values are $7.5 \cdot 10^6$ and $2 \cdot 10^8$ for test series R19 and R20, respectively.

Cumulative counts/Time

The results of weld nrs. SW-68-R19-1.1, SW-68-R19-1.2 SW-68-R20-1.1 and SW-68-R20-1.2 are illustrated in Figure 144.

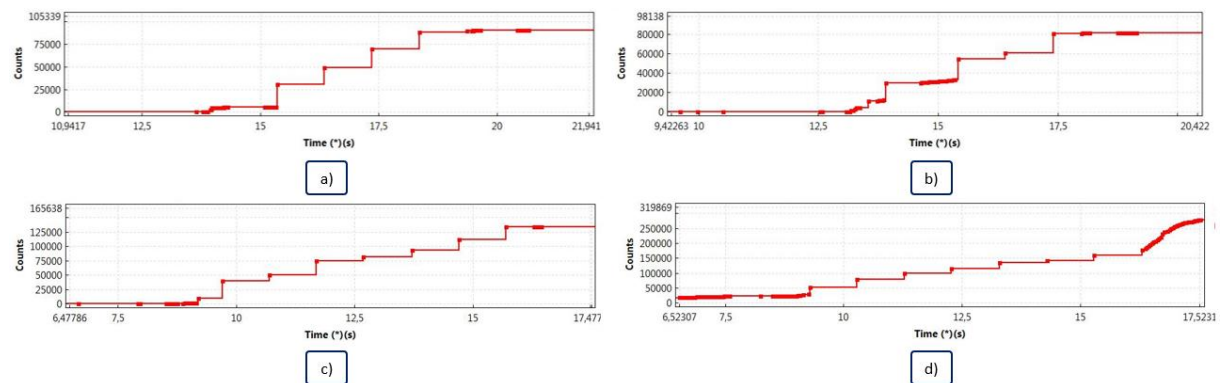


Figure 144: Cumulative counts/Time-analysis of weld nr. SW-68-R19-1.1 (a), SW-68-R19-1.2 (b), SW-68-R20-1.1 (c), SW-68-R20-1.2 (d).

The signals of the welds in test series R19 show almost the same number of counts, namely around 80000, whereas there is some variation in test series R20. As the weld quality conclusions are not based on this hit data set representation, the variation is acceptable. Although in further investigation, these variations should be examined.

6.14.4 Comparison of test series R19 and R20

When looking at the overall results, almost no variations between the AE signals appear as they did in test series R17 and R18. Therefore, the switch from a WD sensor to a R50D sensor with a slightly higher

resonance frequency resulted into an AE configuration that is appropriate to use in further investigations concerning the weld quality. Also the location of the sensor is very important. For future test series, the sensor is preferably placed on the aluminium sheets in order to reduce the signal loss.

6.15 Test series R21– Arc welding

6.15.1 Selected parameters

Table 54: Arc welding parameters of test series R21.

Zones	Current (A)	Voltage (V)	Wire feeding rate (mm/min)	Stick-out (mm)	Shield gas supply
Zone 1: good quality	233	31.4	10.7	9	Yes
Zone 2: bad quality	40	14.5	1.2	0.5	Yes
Zone 3: bad quality	30	19	1.5	0.9	Yes
Zone 4: good quality	233	31.4	10.7	9	Yes

Table 55: Other parameters of test series R21.

Material	Cleaning frequency	Location of the sensor
Steel S235	N/A	On sheet to be welded

Table 56: AE configuration of test series R21.

Sensor type	Resonance frequency (kHz)	Threshold (dB)	Frequency range of the digital filter (kHz)	Sampling rate (MSPS)	Time driven rate (s)
R50D	500	50	400 - 800	1	3

6.15.2 Objective

This test series consists of four arc welds, produced by MAG welding, using a semi-automated cobot. The welds were divided into four zones, in which different parameters were used for each zone. The parameters for these zones are listed in Selected parameters

Table 54. The goal of this test series is to be able to distinguish the zones of the welds, based on the AE signal and compare these with previous results of test series R15 and R16, which contained welds produced by MAG welding using a semi-automated robot.

For recording the AE signals, the same AE configuration as with the friction spot welding machine in test series R20 is used, because these settings showed promising results in terms of filtering the mechanical interferences.

6.15.3 Results and conclusion

Visual inspection

Figure 145 contains the four arc welds, produced in test series R21. Two good quality weld zones (zone 1 starting from the right and zone 4 ending on the left) and two bad quality weld zones (zone 2 and zone 3 in between) are produced for each weld.

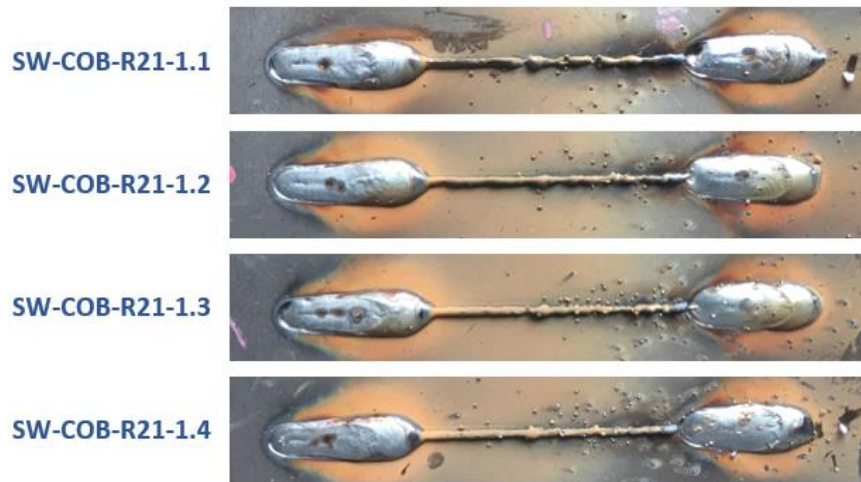


Figure 145: Visual inspection of the arc welds in series R21.

Waveform evaluation

Figure 146 illustrates the waveforms of weld nrs. SW-COB-R21-1.3 and SW-ROB-R21-1.4. Other results are consultable in the external appendix.

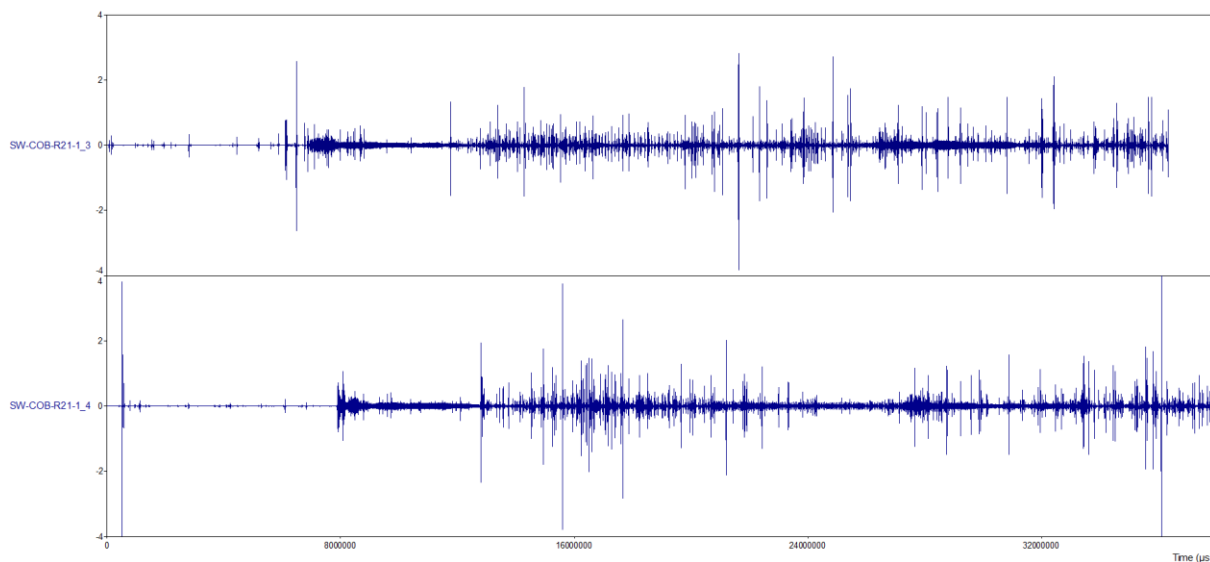


Figure 146: Waveform evaluation of the welds in test series R21 (weld nrs. SW-COB-R21-1.3 and SW-COB-R21-1.4).

Based on the waveforms shown in Figure 146, zone 1 is clearly visible as it shows a relative clean signal. It is remarkable that in zone 4, this signal does not appear even though the same welding parameters were used. No explanation for this can be found.

Furthermore, distinguishing the other zones based on time is difficult because the recording was triggered manually, meaning that the signals have a different starting point and therefore are shifted along the time-axis.

Metallographic evaluation

Metallographic research leads to very similar results for each of the arc welds, made in this test series. Figure 147 illustrates the cross-sections of weld nrs. SW-COB-R21-1.3 and SW-COB-R21-1.4 for each zone. All other metallographic results are available in the external appendix.

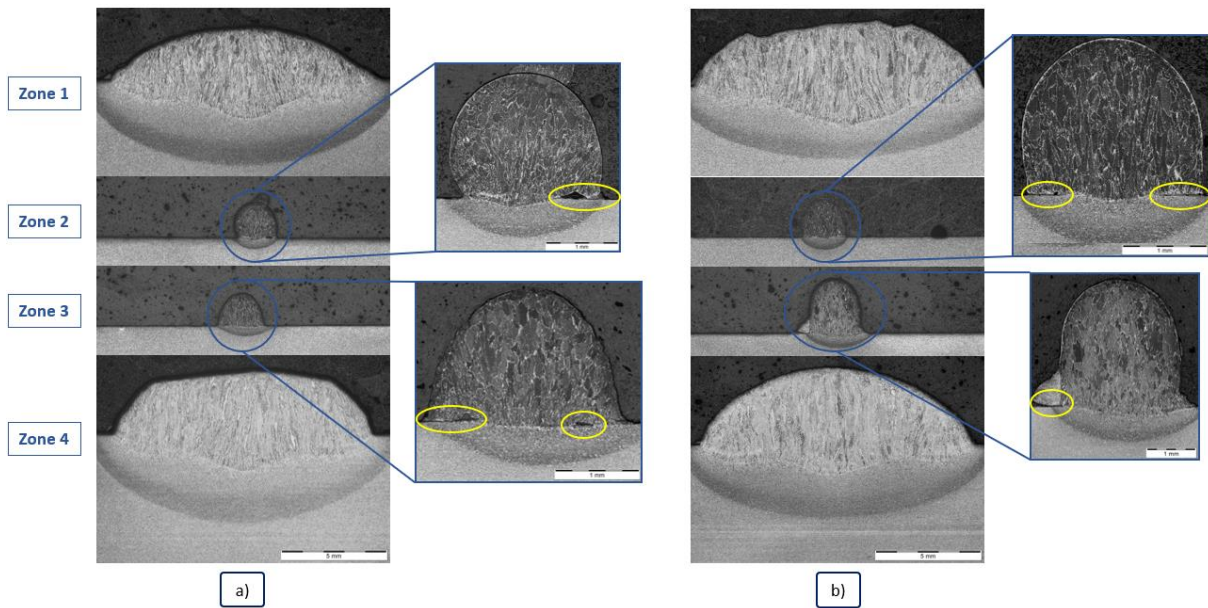


Figure 147: Metallographic evaluation of weld nrs SW-COB-R21-1.3 (a) and SW-COB-R21-1.4 (b).

When looking at the detailed view of the bad arc weld zone, it is clear that there is little diffusion from the filler material to the base material, and also small voids appear, encircled in yellow.

Duration/Amplitude

No concrete conclusions can be drawn based on these results. Therefore, they are not further discussed in arc welding test series. However, these results are available in the external appendix.

Frequency centroid/Time

Figure 148 illustrates the results of weld nrs. SW-COB-R21-1.3 and SW-COB-R21-1.4.

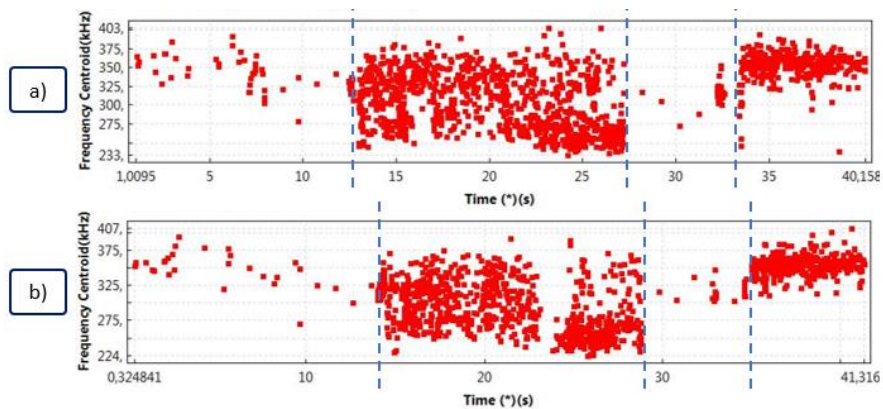


Figure 148: Frequency centroid/Time-analysis of weld nrs. SW-COB-R21-1.3 (a) and SW-COB-R21-1.4 (b).

The four different welding zones can be distinguished. However, the first good weld quality zone (left) does not contain as much data points as the last good weld quality zone (right), even though they were produced with the same welding parameters. This is similar to the difference observed in the waveform signal in Figure 146, for which a relatively small signal in zone 1 was observed, whereas a signal with a large amplitude was found in zone 4.

ASL/Time

The ASL/Time results can be consulted in the external appendix. It is hard to recognize the different parts of the welds, based on this signal representation. Therefore, the cumulative ASL is set out over time in Figure 149. The signals of weld nrs. SW-COB-R21-1.3 and SW-COB-R21-1.4 show the different parts which can be distinguished based on the gradient of the curve. However, weld nrs. SW-COB-R21-1.1 and SW-COB-R21-1.2 show fewer transitions. The blue lines indicate the zones, based on the time values of the blue lines in Figure 148.

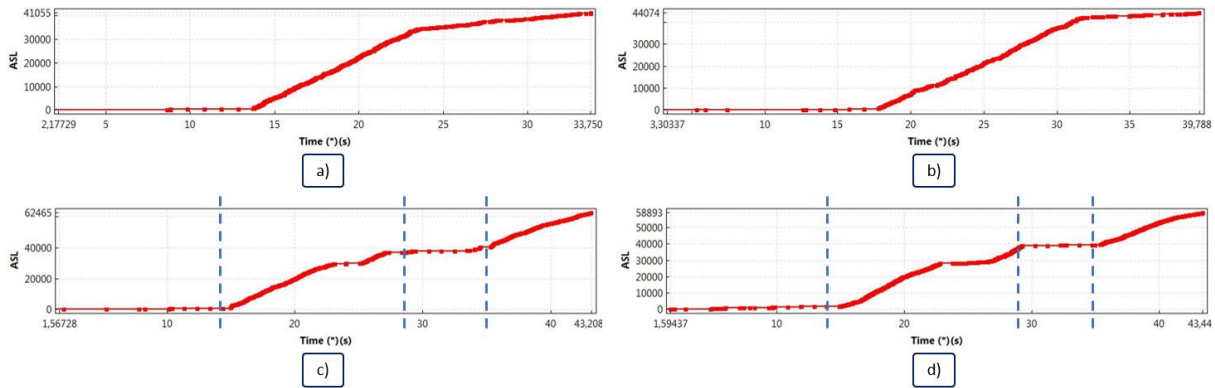


Figure 149: Cumulative ASL/Time-analysis of weld nrs. SW-COB-R21-1.1 (a), SW-COB-R21-1.2 (b), SW-COB-R21-1.3 (c), SW-COB-R21-1.4 (d).

Cumulative absolute energy/Time

The results of weld nrs. SW-COB-R21-1.3 and SW-COB-R21-1.4 are illustrated in Figure 150.

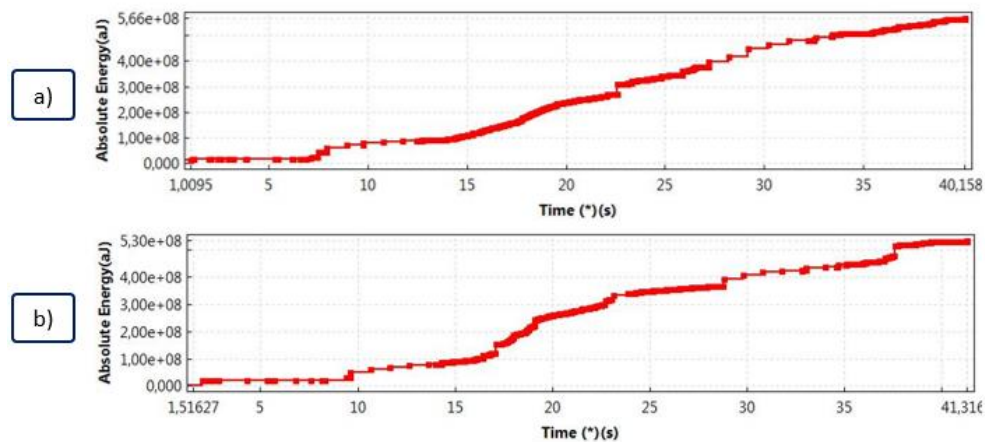


Figure 150: Cumulative absolute energy/Time of welds SW-COB-R21-1.3 (a) and SW-COB-R21-1.4 (b).

Based on this data representation, no concrete conclusions can be drawn as the different zones cannot be distinguished.

Conclusion

In the frequency centroid/time representation, reproducible results were achieved as four welding zones could be distinguished. Although the results of the cumulative ASL/Time representation showed promising results, no explanation could be found for the differences in gradient between the first two welds, and the last two ones.

6.16 Test series R22 and R23 – Arc welding

6.16.1 Selected parameters

Table 57: Arc welding parameters of test series R22 and R23.

Test series	Current (A)	Voltage (V)	Wire feeding rate (mm/min)	Stick-out (mm)	Shielding gas supply
R22	233	31.4	10.7	9	Yes
R23	40	14.5	1.2	0.5	Yes

Table 58: Other parameters of test series R22 and R23.

Material	Cleaning frequency	Location of the sensor
Steel S235	N/A	On the sheet to be welded

Table 59: AE configuration of test series R22 and R23.

Sensor type	Resonance frequency (kHz)	Threshold (dB)	Frequency range of the digital filter (kHz)	Sampling rate (MSPS)	Time driven rate (s)
R50D	500	50	400 - 800	1	3

6.16.2 Objective

Test series R22 contains four good quality welds, produced by MAG welding using a semi-automated cobot. The same welding parameters of the zone 1 in test series R21 was applied in order to compare the results.

Test series R23 contains three bad quality welds, also produced by MAG welding using the semi-automated cobot. Here, the same parameters as zone 2 of test series R21 were applied. The intention is to compare the results of test series R22 and R23 to R21, in order to being able to distinguish the different zones.

6.16.3 Results and conclusion

Visual inspection

The four good quality arc welds and the three bad quality arc welds are illustrated in Figure 151 and Figure 152, respectively. Keep in mind that they are not in order.



Figure 151: Visual inspection of the good quality arc welds in test series R22.

In Figure 151, some spatters can be observed, which are actually a welding defect. More information concerning the spatters is discussed in section 2.2.1.



Figure 152: Visual inspection of the bad quality arc welds in test series R23.

Waveform evaluation

Figure 153 shows the waveforms of weld nrs. SW-COB-R22-1.1, SW-COB-R22-1.2, SW-COB-R23-1.1 and SW-COB-R23-1.2. Based on these results, no concrete conclusions can be drawn.

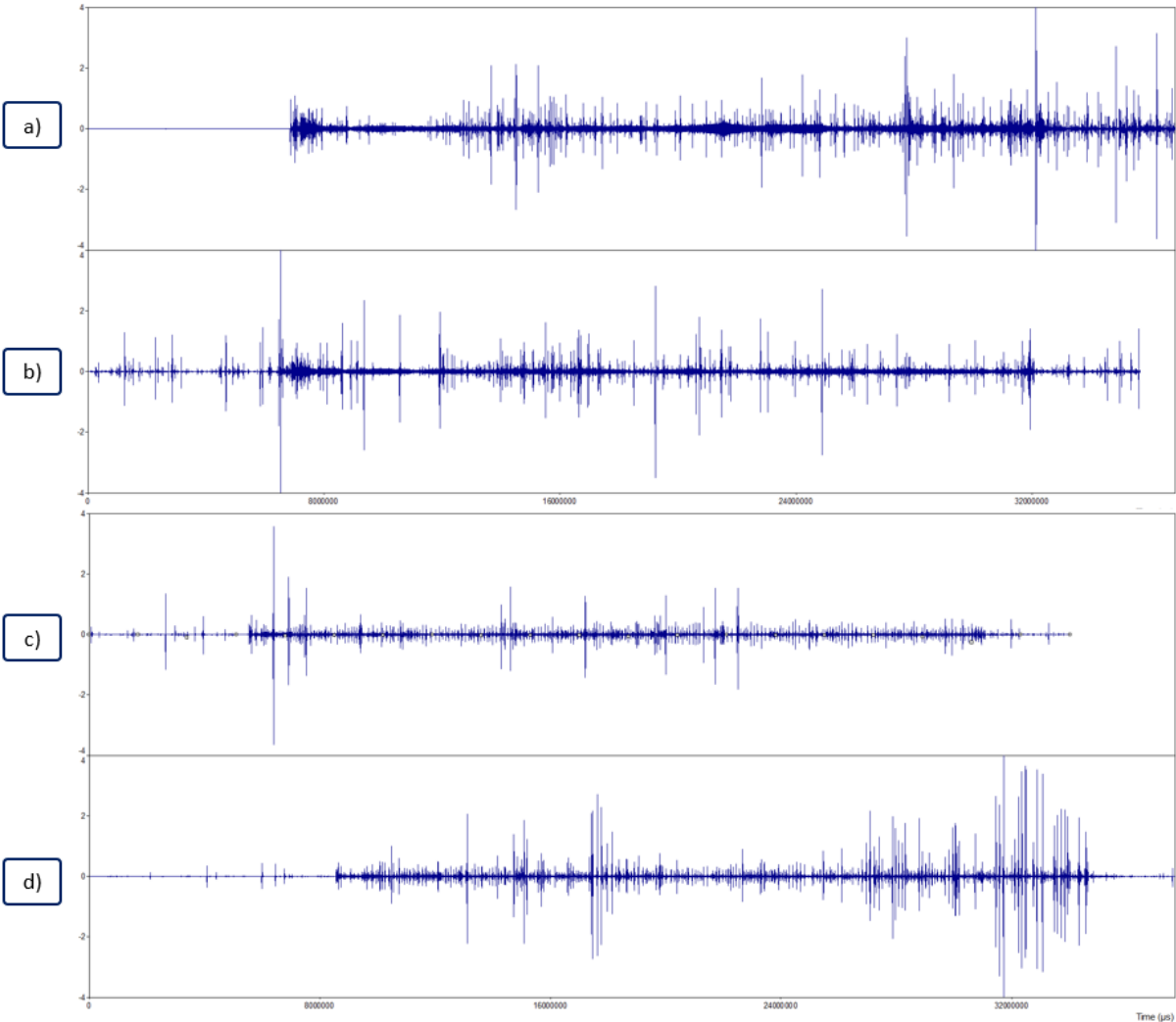


Figure 153: Waveform evaluation of weld nrs. SW-COB-R22-1.1 (a) and SW-COB-R22-1.2 (b), SW-COB-R23-1.1 (c) and SW-COB-R23-1.2 (d).

Metallographic evaluation

The metallographic cross-sections of test series R22 are similar to zone 1 and 4 of the welds discussed in test series R21 (see Figure 147a and Figure 147b), since the same welding parameters were used. They also showed a good diffusion between the filler material and the base material, which can be found in the external appendix.

Also the metallographic cross-sections of test series R23 are similar to zone 2 of the welds discussed in series R21 (see Figure 147a and Figure 147b), since the same welding parameters were used. There are zones with little diffusion between the filler material and the base material, but also the voids appear. The results can be consulted in the external appendix.

Cumulative ASL/Time

The results of weld nr. SW-COB-R22-1.1 (good quality weld) and SW-COB-R23-1.1 (bad quality weld) are shown in Figure 154. All other results of these test series show the same trend.

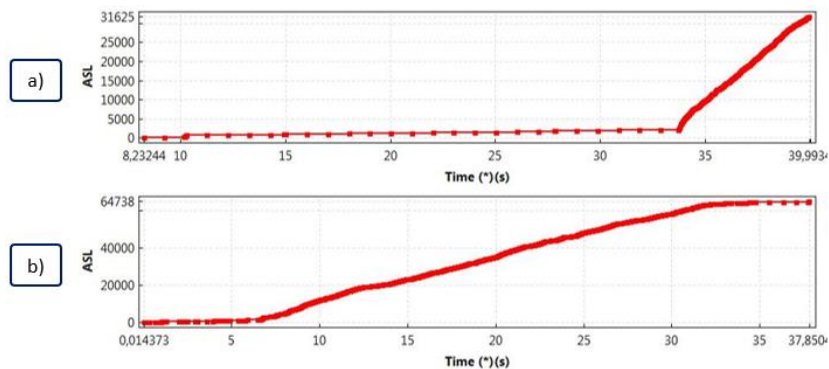


Figure 154: Cumulative ASL/Time-analysis of welds SW-COB-R22-1.1 (a) and SW-COB-R23-1.1 (b).

Comparing these results, it is remarkable that the bad quality welds of series R23 show a steep gradient, indicating that the AE signal has exceeded the threshold to a larger extent, whereas the good quality welds of test series R22 contain a flat gradient. This phenomenon is in contradiction to the results achieved in test series R21, where the good quality welds exhibited a steep gradient, and the bad welds a flat gradient.

Frequency centroid/Time

The results of welds SW-COB-R22-1.1 and SW-COB-R23-1.1 are illustrated in Figure 155.

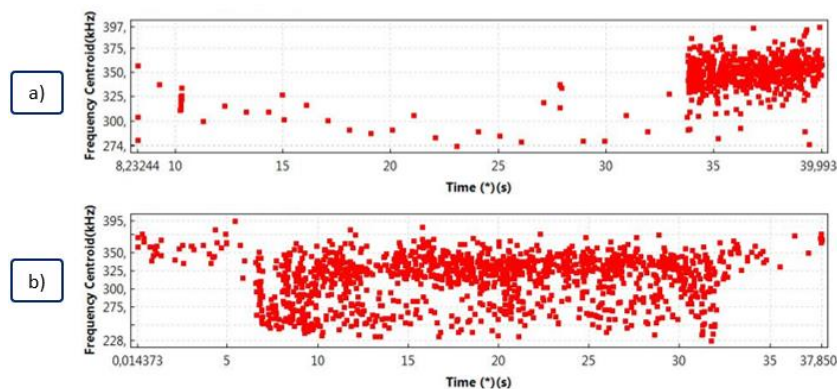


Figure 155: Frequency centroid/Time-analysis of weld nrs. SW-COB-R22-1.1 (a) and SW-COB-R23-1.1 (b).

These results confirm the results achieved in test series R21, where likewise the bad quality welding zone exhibited many frequency centroid points (see Figure 148).

Cumulative absolute energy/Time

Figure 156 shows the cumulative absolute energy versus time for every weld in test series R22 and R23, except welds nr. SW-COB-R22-1.1 and SW-COB-R23-1.3 which were exceptions that contained irrelevant information.

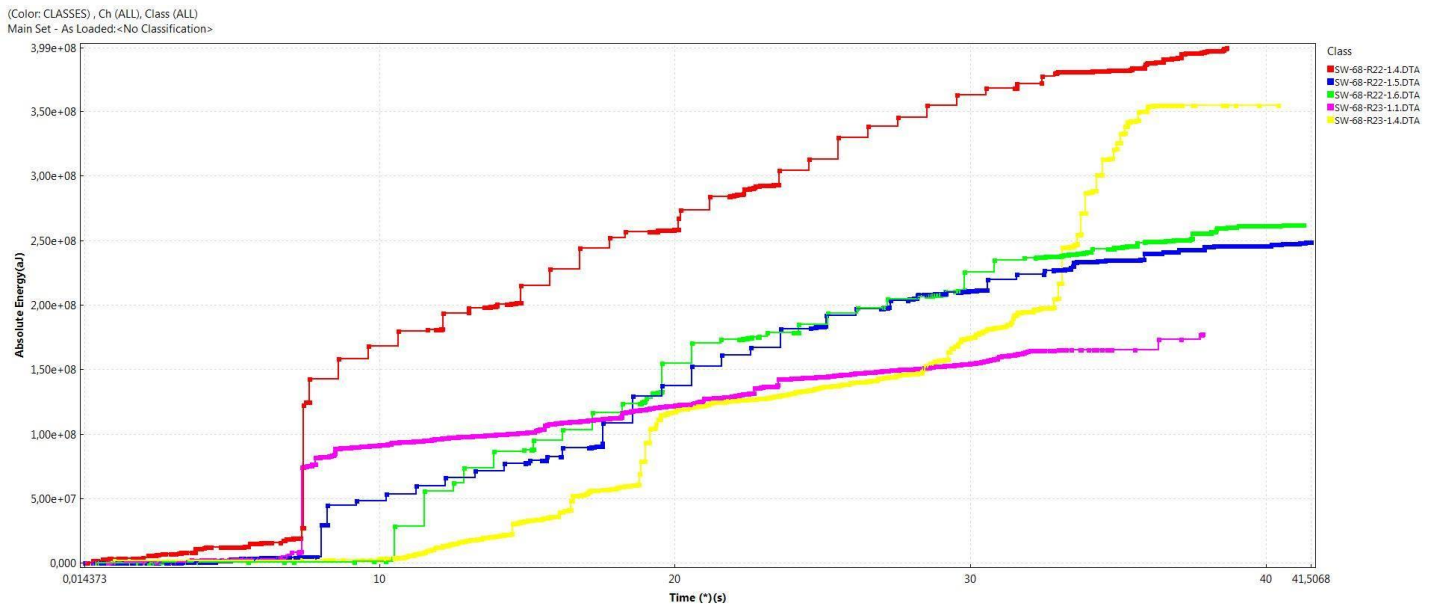


Figure 156: Cumulative absolute energy-analysis of the welds in test series R22 and R23.

Based on these results, and similar to the results achieved in test series R21, no distinction between the good quality and the bad quality welds can be made.

6.16.4 Comparison of test series R22 and R23

Based on these results, the differences in the frequency centroid/time data representation showed promising results as this data could be correlated to the weld quality. However, the other hit data set representation show some uncertainties which require more investigation.

6.17 Test series R24, R25 and R26 – Arc welding

6.17.1 Selected parameters

Table 60: Arc welding parameters of test series R24, R26 and R26.

Test series	Weld type	Current (A)	Voltage (V)	Wire feeding rate (mm/min)	Stick-out (mm)	Shielding gas supply
R24	Good quality welds	87	12	3	0.8	Yes
R25	Bad quality welds	87	15	3	0.8	No
R26	Alternating good and bad quality welds	87	12 - 15	3	0.8	Yes - No

Table 61: Other parameters of test series R24, R25 and R26.

Material	Cleaning frequency	Location of the sensor
Steel S235	N/A	On the sheet to be welded

Table 62: AE configuration of test series R24, R25 and R26.

Sensor type	Resonance frequency (kHz)	Threshold (dB)	Frequency range of the digital filter (kHz)	Sampling rate (MSPS)	Time driven rate (s)
R50D	500	50	400 - 800	1	3

6.17.2 Objective

Test series R24 and R25 are a re-production of test series R15. In test series R24, the good quality welds were reproduced and in test series R25, the bad quality welds. In order to investigate the effect of the sensor type, the WD sensor was replaced by a R50D sensor. Since the R50D sensor type had positive results in terms of filtering the mechanical interferences originating from the refill friction stir spot welding equipment, it was also investigated for the arc welding processes. For each test series, three arc welds were produced with MAG welding, using a KUKA welding robot.

Test series 26 is a special test series, during which the welding parameters of test series R24 are used. During the process, the welding parameters are switched to the values of the welding parameters in test series R25, in order to investigate the transition. Practically this is done by turning off the shielding gas supply after a few seconds during the welding process.

6.17.3 Results and conclusion

Visual inspection

Since the welds are the same as in test series R15, it is referred to section 6.11.3.

Waveform evaluation

Due to similar results within each test series, only one weld for each test series is shown in Figure 157. Other results are available in the external appendix.

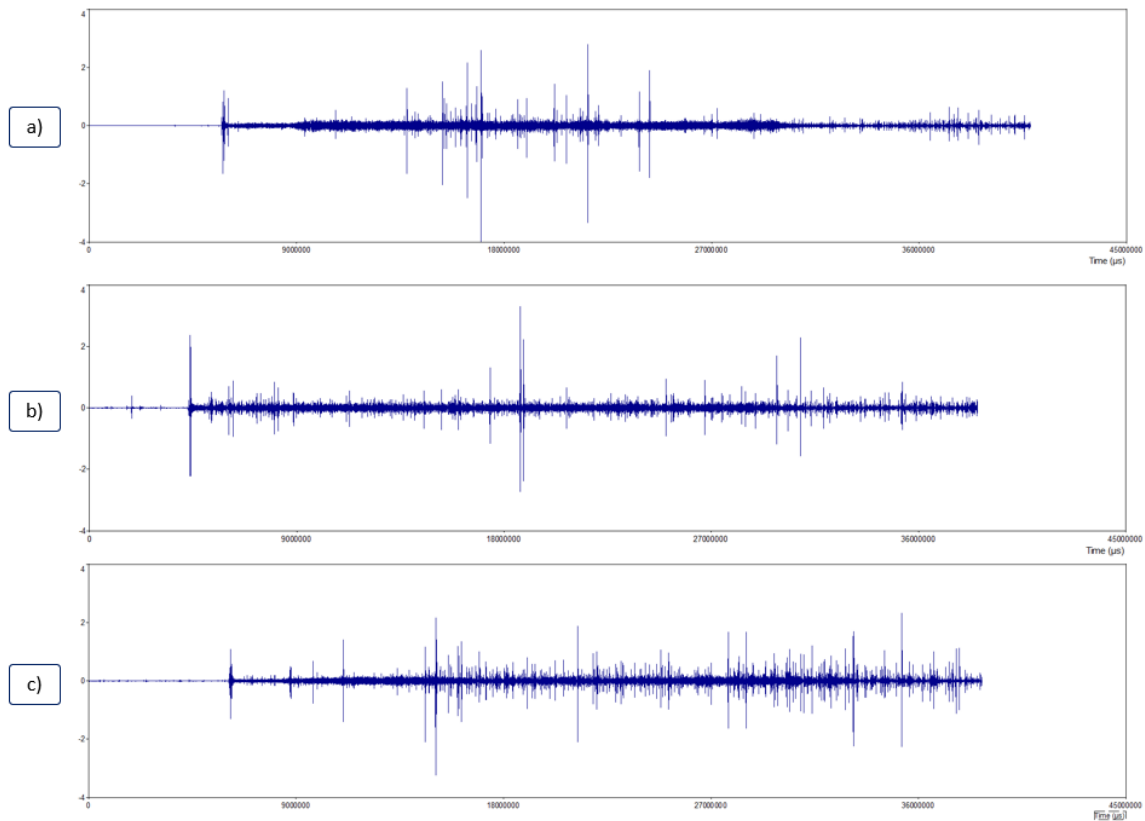


Figure 157: Waveform evaluation of weld nrs. SW-ROB-R24-1.2 (a), SW-ROB-R25-1.2 (b) and SW-ROB-R26-1.2 (c).

Duration/Amplitude, Frequency centroid/Time, ASL/Time

Based on these hit data representations and similar to the results achieved in test series R15 and R16, no concrete conclusions concerning the weld quality could be made. Therefore, it is not further discussed. The results are available in the external appendix.

Cumulative absolute energy/Time

Figure 158 shows the cumulative absolute energy over time for each weld in test series R24, R25 and R26.

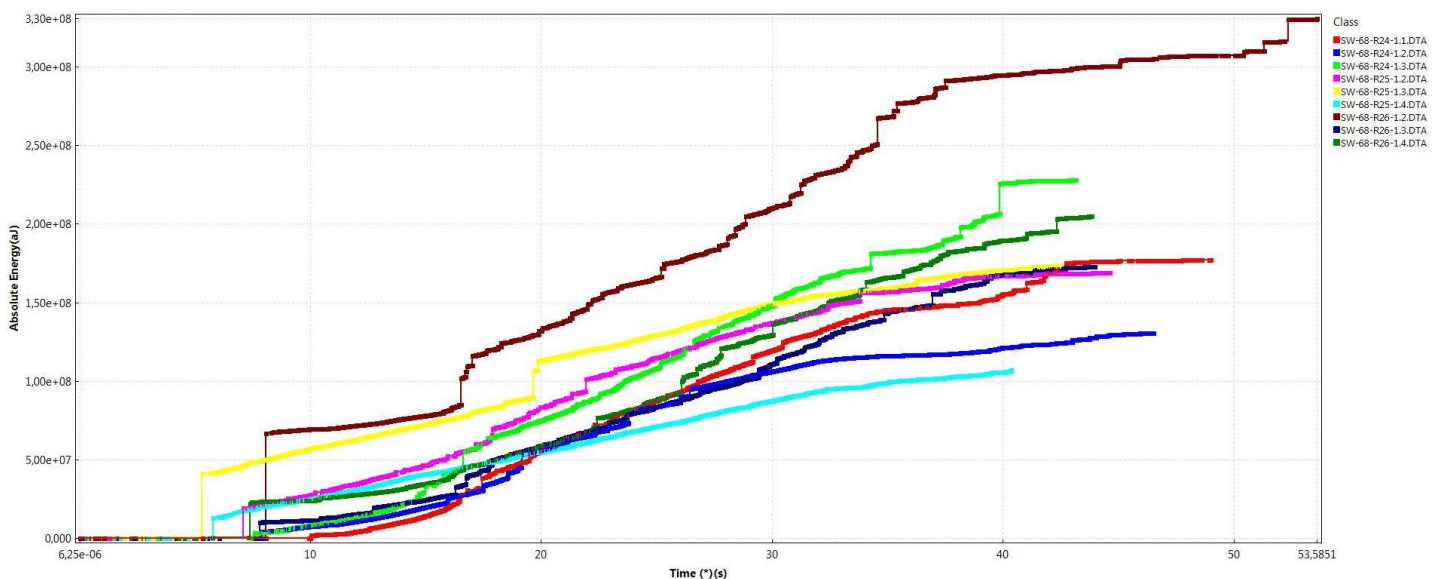


Figure 158: Cumulative absolute energy of the welds in test series R24, R25 and R26.

Figure 158 shows that no distinction between the good quality and bad quality welds can be made, as opposed to the results achieved in similar to test series R15 and R16 (see Figure 124 and Figure 129). When analysing the results of test series R26, no transition between welding with shielding gas and welding without shielding gas can be identified within the hit data representation. The only outlier based on the absolute energy values is weld nr. SW-ROB-R26-1.1, however no conclusions can be drawn based on this.

6.17.4 Comparison of test series R24, R25 and R26 to test series R15 and R16

Based on the cumulative absolute energy versus time data representation, it can be stated that the R50D sensor type is not suitable for recording the AE signals during the arc welding process. While the WD sensor type showed good results, by distinguishing between the good and bad quality welds, this sensor is not capable of detecting the weld quality. This conclusion can also explain why in test series R21, R22 and R23 no transitions were visible in the cumulative absolute energy/time data representation. It is recommended to use the WD sensor type in further arc welding experiments with the welding robot.

6.18 Test series R27 – Arc welding

Test series R27 consists of one weld which was produced to do an experiment in the software. Since only one weld was made, and cannot be compared to another welds, the results are not discussed. They are available in the external appendix.

6.19 Test series R28 – RFSSpW

6.19.1 Selected parameters

Table 63: Welding parameters of test series R28.

PD (mm)	RS (rpm)	PT (s)	DT (s)	RT (s)	HT (s)
-0.3	2250	1.5	3	1.5	2

Table 64: Other parameters of test series R28.

Material (sheet thickness)	Cleaning frequency	Location of the sensor
EN AW-6082-T6 (2 mm)	After every 2 welds	On the welding table

Table 65: AE configuration of test series R28.

Sensor type	Resonance frequency (kHz)	Threshold (dB)	Frequency range of the digital filter (kHz)	Sampling rate (MSPS)	Time driven rate (s)
R50D	500	50	400 - 800	1	3

6.19.2 Objective

In order to test the relevance of this new AE configuration, which was constructed based on several test series), a test series was executed during which only the AE signals, caused by the mechanical movements of the welding equipment were recorded. This is similar to the test series R11, which was executed with another AE configuration. The only differences between test series R28 and R11 are the sensor type, the threshold and the frequency range of the digital filter. If the recorded signals show little to no large bursts during the plunging, dwell and retraction phase, no AE signals due to the

mechanical movements of the welding machine are recorded. This way, this AE configuration can be used for the further analysis of the AE of welds, inducing weld defects. Four tests were performed without plunging. The waveforms and hit data set representations were analysed.

6.19.3 Results and conclusion

The waveforms of the four tests are presented in Figure 159.

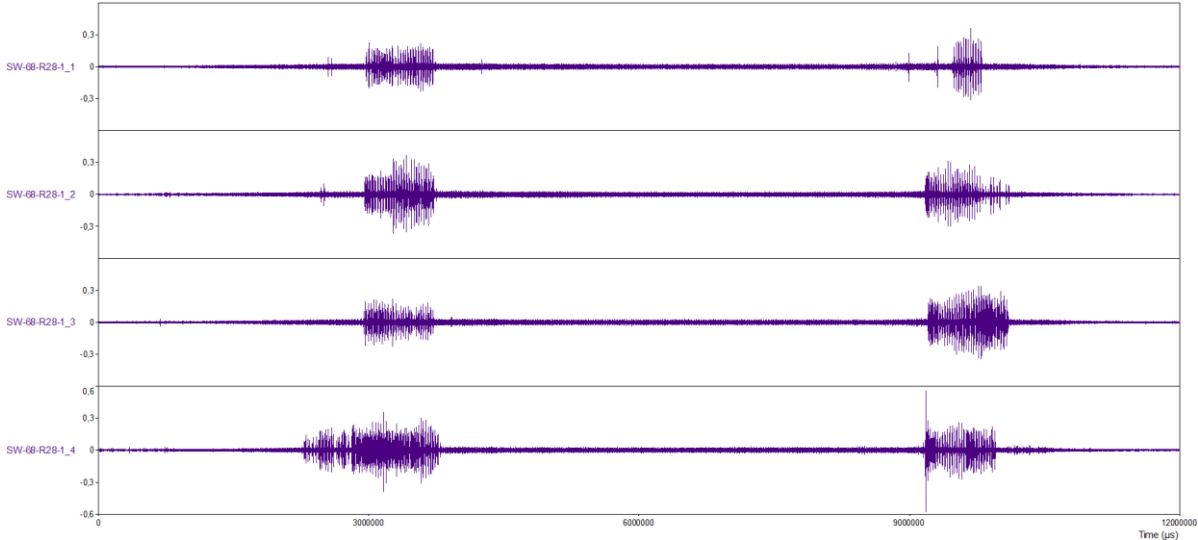


Figure 159: Waveform-analysis of test series R28.

The waveform signals in Figure 159 are zoomed in to a large extent because these small signals would otherwise not be visible on the scale which was used for the waveforms in the previous test series. No large bursts nor random signals appear as found in test series R11. This means that the mechanical movements of the machine are completely filtered out from the AE signal, and that the signals obtained in test series R19 and R20 only contain information related to the welding process. If any weld defect appears and emits an acoustic signal, it will exceed the threshold and the signal related to the defect can be analysed. The question is whether or not the AE signal originating from the weld defect would exceed the threshold. This has to be investigated in further research.

6.20 General conclusion

A set-up is found to filter out the background noise during the AE measurement of refill friction stir spot welding FSSW. With this set-up further research on welding errors can be started up. Until now no links between AE results and welding errors can be found but there is proved that the technique is promising. Few remarkable trends on FSSW AE results are found, these have to be confirmed by further research. Different methods of evaluating the AE results are suggested.

No good AE configuration for the arc welding is found, but a few trends on the AE results are found. It is shown that the AE setup is different for other welding techniques and that the sensor type has an important role. The absolute energy/time representation showed the most promising results to analyse arc welding, other less promising evaluation techniques are also given.

The results in the frequency domain were not further examined, as it showed no unambiguous result. A specific investigation of the frequency domain can be useful but there has to be watched out for aliasing. The temperature measurements were also not further examined as it had no effect on the lap shear strengths. Placing the thermocouples on the plates can possibly give a better result, this has to be examined in further research.

Summarizing this chapter, a recap of all the relevant configurations and data outputs for each welding process are given in Table 66.

Table 66: Recap of all relevant configurations and data outputs according to each welding process.

		RFSSpW	Arc welding - robot	Arc welding - cobot
AE configuration	Sensor type	R50D sensor	WD	WD
	Resonance frequency (kHz)	500	450	450
	Location of the sensor	On the aluminium sheets	On the sheet to be welded	On the sheet to be welded
	Threshold (dB)	50	70	70
	Frequency range of the digital filter (kHz)	400 - 800	400 - 800	400 – 800
	Sampling rate (MSPS)	2	2	2
	Time driven rate (s)	3	3	3
Relevant data output		Cumulative absolute energy/time + Duration/amplitude	Cumulative absolute energy/time	Cumulative absolute energy/time + Frequency centroid/time

7 Further investigation

Although this work was very interesting, it shows that the AE monitoring of a welding process is a very complex task. It was difficult to deduce concrete conclusions about the weld quality for friction spot welding or arc welding. Possible further investigations of both these processes are discussed in the following paragraphs.

7.1 RFSSpW

The main problem with AE monitoring of RFSSpW is the noise caused by the movements of the welding machine or surrounding other equipment. During the research, the random occurrence of the noise prevented that the important information about the welding process or weld quality, could not be extracted from the acoustic measurements. At a last investigations of the master dissertation, a standard configuration which filters out the noise shows promising results. Nevertheless, this configuration still has to be investigated further, in order to examine the detection capabilities for all the possible weld defects.

Once a good configuration is found to filter out the noise, future work building further on this dissertation can consist of inducing defects in the welds and measure the AE during the weld cycles. If the signals created by these defects exceed the proposed threshold during the DT, these signals can be analysed without the interference of noise.

A list with the AE results of these defects could be composed with the use of NOESIS, in order to recognise a pattern and determine a standardised signal for each kind of defect. When a weld is made, the AE measured during the weld cycle could be compared with the standardised signals of the different weld defects. When the AE of the weld is not comparable to these standardised signals, it can be concluded that no weld defects are present.

It might be possible that the signals of the induced defects won't exceed the threshold during the welding process when using the proposed setup. When this situation occurs, the threshold could be lowered. However, when the threshold is lowered, this could lead to the recording of unwanted noise in the AE signals. Since this is a sensitive investigation, it is suggested to examine new frequency and time ranges. This investigation is trial and error which means that the new configuration may also contain noise.

A second solution is to investigate other types of sensors, with different properties (resonance frequency), although it was stated by the supplier that the currently-used sensor has the best properties for this application.

When it turns out that the noise still overwhelms the important information in the measured signals, the locating technique can be used. This technique works with different sensors and measures the difference in arrival time of the signals between the different sensors. If the location of the sensors is well-known, the source location of this signal can be determined. Once the sources are known, a lot of the noises of the machine can be filtered out, although a 100% filtering of noise is not possible.

Another solution might be filtering out the noise mechanically by making the machine hermetically sealed. In this way, the cause of the noise is avoided and therefore not recorded.

Concluding, the AE monitoring of RFSSpW is a promising technique, but yet a lot of research has to be done before it can be used in industry.

7.2 MIG/MAG robot welding

A lot more is reported in literature about AE monitoring of MIG/MAG welding, although measuring was more difficult. Due to the limited time spent for this technique, a good suitable setup was not yet found. In future work, more research could be done concerning the ideal frequency range, sensors and the development of an external trigger for the process. Afterwards, the proposed analysing techniques could be followed with special attention for the cumulative counts/time, cumulative absolute energy/time, energy/rise time and energy/counts representations.

Also in this case, a database with induced defects and their AE results could be composed to develop automated pattern recognition to automate detection of weld defects.

Furthermore, there are also other non-destructive testing methods possible which are also applicable. They are shortly discussed below.

Radiographic inspection or X-ray: it is one of the most important, versatile and widely accepted non-destructive examination method. It works with the ability of X-rays to go through a metal and produce photographic records of the transmitted radiant energy. All materials will absorb a known amount of this energy, depending on their structure. The absorbed amount of energy then indicates discontinuities and inclusions within an opaque material [104].

Magnetic particle inspection (MPI): a method which locates and defines discontinuities in magnetic materials. It's mostly used for detecting surface defects in welds which are too small to be seen with the naked eye and those who lie slightly in the subsurface [104].

Ultrasonic inspection: a method of detecting discontinuities by sending a high-frequency sound beam through a material or weld on a predictable path. Some of the sounds reflect back when the sound beam's path collides on an interruption. This sound is collected by an instrument, amplified and displayed as a vertical trace on a video screen, indicating is there are any weld defects or not [104].

8 Conclusion

This master dissertation investigated the use of acoustic emission (AE) on different welding processes: refill friction stir spot welding (RFSSpW) and arc welding. Chapter 1 introduced these processes by discussing the principles, processes, tools and parameters. The intention of this work was to determine the weld quality based on the AE results. The weld quality depends of the presence of certain weld defects, which were discussed in Chapter 2. Furthermore in Chapter 3, more information concerning the AE process could be found. In order to execute the test series, described in Chapter 6, a setup in all these welding processes was needed. This setup was discussed in Chapter 4, while Chapter 5 focused on the different evaluation methods, used in Chapter 6.

Although this work was very interesting, it shows that the AE monitoring of a welding process is a very complex task. It was difficult to deduce concrete conclusions about the weld quality for friction spot welding or arc welding. For each welding process, a promising AE configuration was found which could be used in further research. These AE configurations are given in Table 66 and require further examination.

Previous chapter recommended future research options, while this section will list the most important conclusions, made in this investigation.

1. Refill friction stir spot welding

- The results in the frequency domain showed no unambiguous result.
- Temperature is not directly related to the lap shear strengths.
- Only phase 2, 3 and 4 (see Figure 60) have an influence on the weld quality and lap shear strength.
- With the usage of the R50D sensor, a threshold of 50 dB and the digital filter range set on 400 – 800 kHz, a good AE configuration is found to filter out the background noise during the AE measurement.
- Relevant data outputs are the cumulative absolute energy/time- and duration/amplitude representation.

2. Arc welding

- With the usage of the WD sensor, a threshold of 70 dB and the digital filter range set on 400 – 800 kHz, a good AE configuration is found to distinguish good and bad welds based on the shielding gas supply.
- Relevant data outputs are the cumulative absolute energy/time- and frequency centroid/time representation.

Concluding, the AE monitoring of welding processes is a promising technique, but yet a lot of research has to be done before it can be used in industry.

References

- [1] T. Kolba, "Experimental investigation of the weldability of aluminium alloys using friction spot welding," 2016.
- [2] P. V. R. K.Faes, "KWALITEITSCONTROLE VAN LASSEN DOOR AKOESTISCHE EMISSIE." [Online]. Available: https://www.bil-ibs.be/sites/default/files/publicaties/metallerie/201702_kwaliteitscontrole_van_lassen_door_akoestische_emissie.pdf.
- [3] J. Vercauteren, "aluminium alloys using friction spot welding Experimental investigation of the weldability of high strength," 2017.
- [4] D. A. Hartman, T. J. Lienert, W. L. Stellwag, M. J. Cola, V. R. Davé, and I. E. Brazil, "Acoustic Monitoring of Inertia Friction Welded Austenitic Stainless Steels: Initial Studies," *FABTECH Int. AWS Weld. Show*, pp. 1–4, 2007.
- [5] P. A. F. de Barros, L. C. Campanelli, N. G. Alcântara, and J. F. Dos Santos, "An investigation on friction spot welding of AA2198-T8 thin sheets," *Fatigue Fract. Eng. Mater. Struct.*, vol. 40, no. 4, pp. 535–542, 2017.
- [6] J. Meschut, G.; Rethmeier, M.; Janzen, V.; Frei, "Einfluss von Punktdurchmesser, Fehlstellen und Imperfektionen auf das Festigkeitsverhalten von Aluminiumpunktschweißverbindungen," 2016.
- [7] L. Appel, "Reibpunktschweißen und Reibelementsweißen - alternative Sonderverfahren für Überlappverbindungen," 2014.
- [8] M. K. Kulekci, "Effects of Process Parameters on Tensile Shear Strength of Friction Stir Spot Welded Aluminium Alloy (EN AW 5005)," *Arch. Metall. Mater.*, vol. 59, no. 1, pp. 221–224, 2014.
- [9] and R. M. T. Montag, J.-P. Wulfsberg, H. Hameister, "Influence of Tool Wear on Quality Criteria for Refill Friction Stir Spot Welding (RFSSW) Process," 2014.
- [10] and K. F. W. Elegeert, F. Vos, "The friction spot welding of high-strength Al alloys', master dissertation at KU Leuven," 2015.
- [11] J. M. Antonini, *Comprehensive Materials Processing*. 2014.
- [12] unknown, "Arc Welding," 2019. [Online]. Available: https://en.wikipedia.org/wiki/Arc_welding.
- [13] Unknown, "Gas metal arc welding," 2019. [Online]. Available: https://en.wikipedia.org/wiki/Gas_metal_arc_welding.
- [14] Unknown, "Mig Mag welding." [Online]. Available: <https://www.telwin.com/en/telwin-academy/saldatura/mig-mag-welding/>.
- [15] Unknown, "AN INTRODUCTION TO MIG WELDING." [Online]. Available: https://www.weldability-sif.com/media/docs/Intro_MIG_Welding.pdf.
- [16] unknown, "Welding Consumables," 2015. [Online]. Available: https://www.weldersuniverse.com/filler_rods_consumeables.html.
- [17] "GMAW circuit." [Online]. Available: https://en.wikipedia.org/wiki/Gas_metal_arc_welding#/media/File:GMAW_Circuit.svg.

- [18] B. Parra, V. T. Saccon, N. G. de Alcântara, T. Rosendo, and J. F. dos Santos, "an Investigation on Friction Spot Welding in Aa6181-T4 Alloy," *Tecnol. em Metal. e Mater.*, vol. 8, no. 3, pp. 184–190, 2011.
- [19] H.M.RaoJ.B.JordonaM.E.BarkeyY.B.GuoaXumingSuchH.Badarinarayand, "Influence of structural integrity on fatigue behavior of friction stir spot welded AZ31 Mg alloy," 2012.
- [20] Koen Faes, "Friction spot welding," 2019. [Online]. Available: <https://www.bil-ibs.be/en/friction-spot-welding>.
- [21] Z. Shen, X. Yang, S. Yang, Z. Zhang, and Y. Yin, "Microstructure and mechanical properties of friction spot welded 6061-T4 aluminum alloy," *Mater. Des.*, vol. 54, no. October, pp. 766–778, 2014.
- [22] M. M. M. M. B. A. Imadb, "Parametric studies of the process of friction spot stir welding of aluminium 6060-T5 alloys," 2009.
- [23] J. Y. Cao, M. Wang, L. Kong, and L. J. Guo, "Hook formation and mechanical properties of friction spot welding in alloy 6061-T6," *J. Mater. Process. Technol.*, vol. 230, pp. 254–262, 2016.
- [24] H. Badarinarayan, Y. Shi, X. Li, and K. Okamoto, "Effect of tool geometry on hook formation and static strength of friction stir spot welded aluminum 5754-O sheets," *Int. J. Mach. Tools Manuf.*, vol. 49, no. 11, pp. 814–823, 2009.
- [25] T. Rosendo, M. Tier, J. Mazzaferro, C. Mazzaferro, T. R. Strohaecker, and J. F. Dos Santos, "Mechanical performance of AA6181 refill friction spot welds under Lap shear tensile loading," *Fatigue Fract. Eng. Mater. Struct.*, vol. 38, no. 12, pp. 1443–1455, 2015.
- [26] M. D. Tier *et al.*, "The influence of refill FSSW parameters on the microstructure and shear strength of 5042 aluminium welds," *J. Mater. Process. Technol.*, vol. 213, no. 6, pp. 997–1005, 2013.
- [27] C. Paper *et al.*, "A Study About the Mechanical Properties of Alclad AA2024 Connections Processed by Friction Spot Welding 1," no. July 2015, 2009.
- [28] A. P. Camilo *et al.*, "7th International EWI / TWI Seminar on Joining Aerospace Materials A Review on Microstructure and Properties of Friction Stir Spot Welds (Refill) in Aircraft Aluminium Alloys," pp. 17–19, 2014.
- [29] J. A. E. Mazzaferro *et al.*, "Preliminary study on the mechanical behavior of friction spot welds," *Soldag. Inspeção*, vol. 14, no. 3, pp. 238–247, 2010.
- [30] S. T. Amancio-Filho, A. P. C. Camillo, L. Bergmann, J. F. dos Santos, S. E. Kury, and N. G. A. Machado, "Preliminary Investigation of the Microstructure and Mechanical Behaviour of 2024 Aluminium Alloy Friction Spot Welds," *Mater. Trans.*, vol. 52, no. 5, pp. 985–991, 2011.
- [31] K. Faes and K. Deplus, "Friction spot joining of high strength aluminium alloys," 2015.
- [32] C. C. de Castro, A. H. Plaine, G. P. Dias, N. G. de Alcântara, and J. F. dos Santos, "Investigation of geometrical features on mechanical properties of AA2198 refill friction stir spot welds," *J. Manuf. Process.*, vol. 36, no. October, pp. 330–339, 2018.
- [33] R. C. Brzostek, U. Suhuddin, and J. F. dos Santos, "Fatigue assessment of refill friction stir spot weld in AA 2024-T3 similar joints," *Fatigue and Fracture of Engineering Materials and Structures*, vol. 41, no. 5, pp. 1208–1223, 2018.
- [34] Z. Li, S. Gao, S. Ji, Y. Yue, and P. Chai, "Effect of Rotational Speed on Microstructure and

- Mechanical Properties of Refill Friction Stir Spot Welded 2024 Al Alloy," *J. Mater. Eng. Perform.*, vol. 25, no. 4, pp. 1673–1682, 2016.
- [35] S. Ji, Y. Wang, J. Zhang, and Z. Li, "Influence of rotating speed on microstructure and peel strength of friction spot welded 2024-T4 aluminum alloy," *Int. J. Adv. Manuf. Technol.*, vol. 90, no. 1–4, pp. 717–723, 2017.
- [36] Z. Li, S. Ji, Y. Ma, P. Chai, Y. Yue, and S. Gao, "Fracture mechanism of refill friction stir spot-welded 2024-T4 aluminum alloy," *Int. J. Adv. Manuf. Technol.*, vol. 86, no. 5–8, pp. 1925–1932, 2016.
- [37] S. M. O. Tavares, "Design and advanced manufacturing of aircraft structures using friction stir welding," no. July, 2011.
- [38] Y. Yue, Y. Shi, S. Ji, Y. Wang, and Z. Li, "Effect of Sleeve Plunge Depth on Microstructure and Mechanical Properties of Refill Friction Stir Spot Welding of 2198 Aluminum Alloy," *J. Mater. Eng. Perform.*, vol. 26, no. 10, pp. 5064–5071, 2017.
- [39] S. B. M. Lage *et al.*, "A study of the parameters influencing mechanical properties and the fatigue performance of refill friction stir spot welded AlMgSc alloy," *Int. J. Adv. Manuf. Technol.*, vol. 100, no. 1–4, pp. 101–110, 2019.
- [40] and J. F. dos S. U. Suhuddin, L. Campanelli, M. Bissolatti, H. Wang, R. Verastegui, "A review on microstructural and mechanical properties of friction spot welds in Al-based similar and dissimilar joints.," 2013.
- [41] L. Zhou, L. Y. Luo, T. P. Zhang, W. X. He, Y. X. Huang, and J. C. Feng, "Effect of rotation speed on microstructure and mechanical properties of refill friction stir spot welded 6061-T6 aluminum alloy," *Int. J. Adv. Manuf. Technol.*, vol. 92, no. 9–12, pp. 3425–3433, 2017.
- [42] J. Y. Cao, M. Wang, L. Kong, H. X. Zhao, and P. Chai, "Microstructure, texture and mechanical properties during refill friction stir spot welding of 6061-T6 alloy," *Mater. Charact.*, vol. 128, pp. 54–62, 2017.
- [43] Y. Q. Zhao, H. J. Liu, S. X. Chen, Z. Lin, and J. C. Hou, "Effects of sleeve plunge depth on microstructures and mechanical properties of friction spot welded alclad 7B04-T74 aluminum alloy," *Mater. Des.*, vol. 62, pp. 40–46, 2014.
- [44] Z. Shen, Y. Chen, J. S. C. Hou, X. Yang, and A. P. Gerlich, "Influence of processing parameters on microstructure and mechanical performance of refill friction stir spot welded 7075-T6 aluminium alloy," *Sci. Technol. Weld. Join.*, vol. 20, no. 1, pp. 48–57, 2015.
- [45] A. Kubit, R. Kluz, and D. Wydrzyński, "Analysis of Structure and Shear/Peel Strength of Refill Friction Stir Spot Welded 7075-T6 Aluminium Alloy Joints," *Adv. Sci. Technol. Res. J.*, vol. 11, no. 3, pp. 297–303, 2017.
- [46] A. Kubit, M. Bucior, D. Wydrzyński, and Ł. Bąk, "Experimental investigation of the degree of weakening in structural notch area of 7075-T6 aluminum alloy sheet welded with the RFSSW method," *ITM Web Conf.*, vol. 15, no. January, p. 04006, 2017.
- [47] A. Kubit, M. Bucior, D. Wydrzyński, T. Trzepieciński, and M. Pytel, "Failure mechanisms of refill friction stir spot welded 7075-T6 aluminium alloy single-lap joints," *Int. J. Adv. Manuf. Technol.*, vol. 94, no. 9–12, pp. 4479–4491, 2018.
- [48] Z. Shen, X. Yang, Z. Zhang, L. Cui, and T. Li, "Microstructure and failure mechanisms of refill friction stir spot welded 7075-T6 aluminum alloy joints," *Mater. Des.*, vol. 44, no. October 2017, pp. 476–486, 2013.

- [49] J. Hou, "Comparison of Resistance Spot Welding and Refill Friction Stir Welding of Al 7075 Sheets Friction Stir Welding (FSW) Background :"
- [50] P. S. Effertz, V. Infante, L. Quintino, U. Suhuddin, S. Hanke, and J. F. Dos Santos, "Fatigue life assessment of friction spot welded 7050-T76 aluminium alloy using Weibull distribution," *Int. J. Fatigue*, vol. 87, pp. 381–390, 2016.
- [51] H. Okada, K. Kamimuki, and M. Fujimoto, "Application Study of Refill FSSW on Aerospace Industry," no. 1.
- [52] Y. Song, X. Yang, L. Cui, X. Hou, Z. Shen, and Y. Xu, "Defect features and mechanical properties of friction stir lap welded dissimilar AA2024-AA7075 aluminum alloy sheets," *Mater. Des.*, vol. 55, pp. 9–18, 2014.
- [53] Z. Shen, Y. Ding, O. Gopkalo, B. Diak, and A. P. Gerlich, "Effects of tool design on the microstructure and mechanical properties of refill friction stir spot welding of dissimilar Al alloys," *J. Mater. Process. Technol.*, vol. 252, no. November, pp. 751–759, 2018.
- [54] Z. Li, Z. Xu, L. Zhang, and Z. Yan, "Friction spot welding of dissimilar 6063/5083 aluminium alloys," *Mater. Sci. Technol. (United Kingdom)*, vol. 33, no. 14, pp. 1626–1634, 2017.
- [55] P. Evans, "22 possible causes of weld metal porosity," 2019. [Online]. Available: <https://www.thefabricator.com/article/arcwelding/22-possible-causes-of-weld-metal-porosity>.
- [56] T. Huissen, "Mig/Mag welding problems." [Online]. Available: <http://www.ceweld.com/en/content/migmag-welding-problems>.
- [57] G. Strong, "8 ways to avoid weld porosity," 2015. [Online]. Available: <https://makemoneywelding.com/8-ways-to-avoid-weld-porosity/>.
- [58] Unknown, "DEFECTS/IMPERFECTIONS IN WELDS - SLAG INCLUSIONS," 2019. [Online]. Available: <https://www.twi-global.com/technical-knowledge/job-knowledge/defects-imperfections-in-welds-slag-inclusions-043>.
- [59] Unknown, "Slag (welding)," 2019. [Online]. Available: [https://en.wikipedia.org/wiki/Slag_\(welding\)](https://en.wikipedia.org/wiki/Slag_(welding)).
- [60] Unknown, "What is Welding Defects – Types, Causes and Remedies?," 2017. [Online]. Available: <https://www.theweldingmaster.com/welding-defects/>.
- [61] Unknown, "Welding faults," 2019. [Online]. Available: <https://fitsatlas.com/fitz-atlas-of-coating-defects/welding-faults>.
- [62] "BNWL-SA-2727 THE USE OF ACOUSTIC EMISSION AS A WELD QUALITY MONITOR By W . D . Jolly September 1969 Research Supported By United States Atomic Energy Commission Under Contract Number AT (45-1) -1830 Battelle Memorial Institute Pacific Northwest Lab," 1969.
- [63] W. J. P. Vink, "Niet-destructief onderzoek (edition 2)," 2000.
- [64] H. J. Schoorlemmer, "akoestische emissie analyse tijdens lassen," 1983.
- [65] E. For, "N Ovel a Coustic E Mission S Ignal P Rocessing," vol. 1, no. May, 2008.
- [66] Monte Roberto, "AE Testing of spherical vessels," 2018. [Online]. Available: <https://www.tuvaustriaitalia.com/en/services/acoustic-emission/ae-testing-of-spherical-vessels>. [Accessed: 28-Apr-2019].

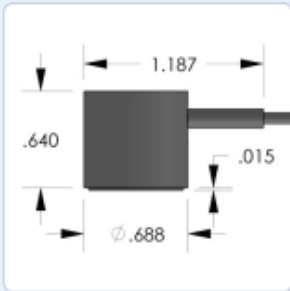
- [67] S. G. Plc, "AE Leak Detection Explained," 2019. [Online]. Available: <http://midasvalvediagnostics.com/acoustic-emissions/ae-leak-detection-explained.php>.
- [68] P. A. Fleming, "monitoring and control in friction stir welding," 2009.
- [69] Unknown, "Nondestructive Testing Encyclopedia - Acoustic Emission -." [Online]. Available: <https://www.ndt.net/article/az/ae/marse.htm>.
- [70] S. Senthilkumar, M. Boopathi, A. Srivani, and G. Mannayee, "A review on application of acoustic emission analysis in friction stir welding," *J. Chem. Pharm. Sci.*, vol. 10, no. 1, pp. 715–723, 2017.
- [71] MISTRAS, "NOESIS™ - ADVANCED DATA ANALYSIS PATTERN RECOGNITION SOFTWARE." [Online]. Available: <https://www.physicalacoustics.com/by-product/noesis/>.
- [72] S. Xu, "Discrete Fourier Transform - Simple Step by Step," 2015. [Online]. Available: https://www.youtube.com/watch?v=mkGsMWi_j4Q.
- [73] Unknown, "What Makes a Fourier Transform Fast?," 2019. .
- [74] B. Van Veen, "The Fast Fourier Transform Algorithm," 2012. [Online]. Available: https://www.youtube.com/watch?v=EsJGul7e_ZQ.
- [75] R. Tolimieri, M. An, and C. Lu, "Cooley-Tukey FFT Algorithms," pp. 72–93, 2013.
- [76] Unknown, "Cooley–Tukey FFT algorithm," 2019. [Online]. Available: https://en.wikipedia.org/wiki/Cooley–Tukey_FFT_algorithm.
- [77] V. TECHNOLOGIES, "The FFT: An Efficient Class of Algorithms," 2019. [Online]. Available: <https://www.vocal.com/noise-reduction/fft-algorithms/>.
- [78] V. Soundararajan, H. Atharifar, and R. Kovacevic, "Monitoring and processing the acoustic emission signals from the friction-stir-welding process," vol. 220, pp. 1673–1686, 2016.
- [79] C. Chen, R. Kovacevic, and D. Jandgric, "friction stir welding of 6061 aluminum," vol. 43, pp. 1383–1390, 2003.
- [80] Unknown, "Spectral density," 2019. [Online]. Available: https://en.wikipedia.org/wiki/Spectral_density.
- [81] Unknown, "Pattern recognition," 2019. [Online]. Available: https://en.wikipedia.org/wiki/Pattern_recognition.
- [82] unknown, "Dislocation," 2019. [Online]. Available: <https://en.wikipedia.org/wiki/Dislocation>.
- [83] P. Geertsma, "Welke insluitels kunnen in lasfouten aanwezig zijn?," 2014. [Online]. Available: <http://www.technischwerken.nl/kennisbank/techniek-kennis/welke-insluitels-kunnen-in-lasfouten-aanwezig-zijn/>.
- [84] Unknown, "Theory - Acoustic Waves." [Online]. Available: https://www.nde-ed.org/EducationResources/CommunityCollege/Other Methods/AE/AE_Theory-Wave.php.
- [85] M. J. G. N. Boon, D. S. Zarouchas, M. Martinez, D. Gagar, R. Benedictus, and P. Foote, "Temperature and load effects on acoustic emission signals for structural health monitoring applications," *7th EWSHM*, pp. 1171–1178, 2014.
- [86] Unknown, "FFT Fundamentals (Sound and Vibration Measurement Suite)," 2008. [Online]. Available: http://zone.ni.com/reference/en-XX/help/372416B-01/svtconcepts/fft_funda/.
- [87] Z. Elman, "Acoustic Emission Apparatus and Data Acquisition." [Online]. Available:

- <https://www.slideshare.net/mboria/acoustic-emission-sensors-equipment>.
- [88] “connector.” [Online]. Available: https://www.google.com/url?sa=i&source=images&cd=&cad=rja&uact=8&ved=2ahUKEwj5hNyzu9fhAhWSLIAKHUjOAUwQjRx6BAgBEAU&url=https%3A%2F%2Fen.wikipedia.org%2Fwiki%2FBNC_connector&psig=AOvVaw1KWtz_v1DKTIkMd0Md302q&ust=1555602056223729.
- [89] “cable.” [Online]. Available: https://www.google.com/url?sa=i&source=images&cd=&cad=rja&uact=8&ved=2ahUKEwi-9arYu9fhAhXBjIAKHxneAhUQjRx6BAgBEAU&url=https%3A%2F%2Fmy.rs-online.com%2Fweb%2Fp%2Fcoaxial-cable%2F0822901%2F&psig=AOvVaw3nMbYA2YM9SHJSYL2DP_Q-&ust=1555602114319858.
- [90] R. B. M. and S. U. Suresha C N, “APPLICABILITY OF ACOUSTIC EMISSION IN THE ANALYSIS OF FRICTION STIR WELDED JOINTS,” 2009.
- [91] Y. Lee, A. M. Hossain, S. Hong, Y. Yum, and K. Park, “Characterization of Friction Stir Spot Welding of Aluminum Alloys using Acoustic Emissions,” *Isape*, vol. 8, pp. 527–529, 2011.
- [92] M. Loman, C. K. E. Nizwan, and N. M. Yusof, “Defect Detection on Welding Joint using Acoustic Emission Technology,” 2013.
- [93] A. Sala, F. Tonolini, G. Villa, and G. Nardoni, “Monitoring of acoustic emission during the welding process,” *Weld. Int.*, vol. 1, no. 7, pp. 655–658, 1987.
- [94] E. Nefedyev, V. Gomera, and A. Sudakov, “Application of Acoustic Emission Method for Control of Manual Arc Welding , Submerged Arc Welding,” *31st Conf. Eur. Work. Gr. Acoust. Emiss. – We.4.A.2*, pp. 1–9, 2014.
- [95] Unknown, “KUKA,” 2019. [Online]. Available: <https://www.kuka.com/nl-be/over-kuka>.
- [96] Unknown, “2/4/6 - SWITCH SELECTABLE GAIN SINGLE ENDED AND DIFFERENTIAL PREAMPLIFIER.” [Online]. Available: <https://www.physicalacoustics.com/by-product/2-4-6/>.
- [97] Z. Z. X. Y. J. Z. G. Z. X. X. B. Zou, “Effect of welding parameters on microstructure and mechanical properties of friction stir spot welded 5052 aluminium alloys.” [Online]. Available: <https://www.sciencedirect.com/science/article/pii/S0261306911002330>.
- [98] Unknown, “Thermokoppel,” 2019. [Online]. Available: <https://nl.wikipedia.org/wiki/Thermokoppel>.
- [99] Unknown, “Seebeck-effect,” 2019. [Online]. Available: <https://nl.wikipedia.org/wiki/Seebeck-effect>.
- [100] Unknown, “AEWIN™ - REAL-TIME DATA ACQUISITION AND REPLAY SOFTWARE.” [Online]. Available: <https://www.physicalacoustics.com/by-product/aewin/>.
- [101] weisang, “FlexPro, the analysis software for fast and easy data analysis & presentation.” [Online]. Available: <https://www.weisang.com/en/flexpro/at-a-glance/>.
- [102] Unknown, “signal averaging,” 2019. [Online]. Available: https://en.wikipedia.org/wiki/Signal_averaging.
- [103] Unknown, “Appendix A: Acoustic Emission—Parameters of Influence.”
- [104] Unknown, “The ABC’s of Nondestructive Weld Examination,” 2019. [Online]. Available: <https://www.lincolnelectric.com/en-us/support/process-and-theory/Pages/nondestructive-weld-detail.aspx>.

Appendix A: Datasheet WD sensor

PRODUCT DATA SHEET

WD Sensor Wideband Differential Sensor

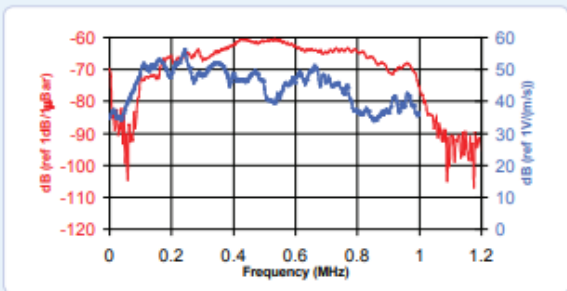


DESCRIPTION AND FEATURES

WD is a true differential wideband sensor with a very high sensitivity and bandwidth. It has a very good frequency response over the range of 100 – 900 kHz. Differential sensors differ from their general purpose counterparts by employing two sensing elements with opposite polarization directions. The two signal leads feed into a differential pre-amplifier which eliminates common-mode noise resulting in a lower noise output from the pre-amplifier. Noise improvements to the tune of 2 dB can be achieved using differential sensors over a single ended sensor. This sensor features a rugged steel construction with an integrated twin axial cable exiting on the side.

APPLICATIONS

This sensor is well suited for structural health monitoring of large structures like storage tanks, pipelines etc. This sensor is an ideal candidate for applications requiring high bandwidth for frequency analysis of the AE signals for noise discrimination and source identification. Wideband sensors are particularly well suited for research applications where a high fidelity AE response is required. It can be easily mounted using epoxy.



OPERATING SPECIFICATIONS

Dynamic

Peak Sensitivity, Ref V/(m/s).....	56 dB
Peak Sensitivity, Ref V/μbar.....	-61 dB
Operating Frequency Range.....	125-1000 kHz
Resonant Frequency, Ref V/(m/s).....	125 kHz
Resonant Frequency, Ref V/μbar.....	450 kHz
Directionality.....	+/-1.5 dB

Environmental

Temperature Range.....	-65 to 177°C
Shock Limit.....	500 g
Completely enclosed crystal for RFI/EMI immunity	

Physical

Dimensions.....	0.7"OD X 0.65"H
	17.8 mm OD X 16.5 mm H
Weight.....	20 grams
Case Material.....	Stainless Steel
Face Material.....	Ceramic
Connector.....	BNC
Connector Locations.....	Side

ORDERING INFORMATION AND ACCESSORIES

WD.....	WD
Cable (specify length in '-XX' m at end of PN).....	1 m
Magnetic Hold-Down.....	MHSTD
Pre-Amplifier.....	0/2/4, 2/4/6
Preamp to System Cable (specify length in 'm').....	1234-X
Amplifier Subsystems.....	AE2A or AE5A

Sensors include

NIST Calibration Certificate & Warranty



WORLDWIDE HEADQUARTERS:
195 Clarksville Rd •
Princeton Jct, NJ 08550 • USA
T: +1.609.716.4000 • F: +1.609.716.0706
E-MAIL: sales.systems@mistrasgroup.com

CANADA T: +1.403.556.1350
CHINA T: +86.10.5877.3831
FRANCE T: +331.498.26040
GERMANY T: +49.040.2000.4025
GREECE T: +30.210.2846.801-4

HOLLAND T: +31.010.245.0325
INDIA T: +91.22.2586.2444
JAPAN T: +81.33.498.3570
MALAYSIA T: +60.9.517.3788
MIDDLE EAST T: +973.17.729.356

RUSSIA T: +7495.789.4549
SCANDINAVIA T: +46(0)31.252040
S. AMERICA T: +55.11.3082.5111
UK T: +44(0)1954.231.612

Appendix B: Datasheet R50D sensor



MISTRAS
A World of NDT Solutions

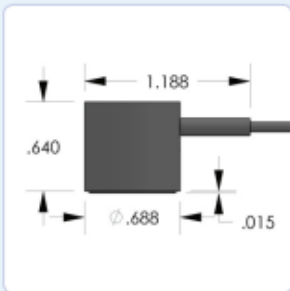
Products & Systems
Division



PRODUCT DATA SHEET

R50D Sensor

General Purpose Differential Sensor

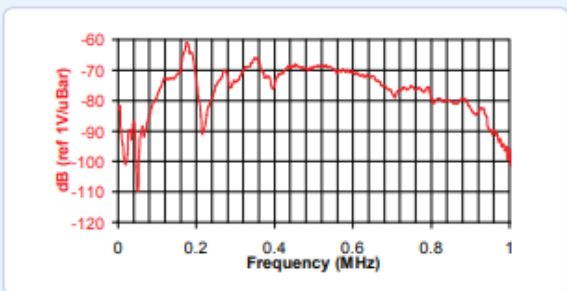


DESCRIPTION AND FEATURES

R50D is a differential sensor designed to isolate the sensing terminals electrically from the cavity. This electrical isolation makes the sensor particularly useful for applications where high background electrical noise is a major concern. It has a very good sensitivity and frequency response over the range of 100 – 700 kHz. The two signal leads from the sensing element feed into a differential pre-amplifier which eliminates common-mode noise resulting in a lower noise output from the pre-amplifier. This sensor features a rugged steel construction and a dual BNC connector with an integrated twin axial cable exiting on the side.

APPLICATIONS

The sensor can be used in applications that require very good EMI shielding, high sensitivity. Typical applications for the sensor include monitoring big power transformers, large steel and concrete structures.



OPERATING SPECIFICATIONS

Dynamic

Peak Sensitivity, Ref V/(m/s).....	62 dB
Peak Sensitivity, Ref V/μbar.....	-62 dB
Operating Frequency Range.....	100-700 kHz
Resonant Frequency, Ref V/(m/s).....	100 kHz
Resonant Frequency, Ref V/μbar.....	500 kHz

Environmental

Temperature Range.....	-65 to 177°C
Shock Limit.....	500 g
Completely enclosed crystal for RFI/EMI immunity	

Physical

Dimensions.....	0.7"OD X 0.65"H
	18 mm OD X 17 mm H
Weight.....	
Case Material.....	Stainless steel
Face Material.....	Ceramic
Connector.....	Dual BNC
Connector Locations.....	Side
Grounding.....	Internal (isolated from casing)

ORDERING INFORMATION AND ACCESSORIES

R50D.....	R50D
Cable (specify cable length '-XX' m at end of PN).....	1 m
Preamp to System Cable (specify length in 'm').....	1234-X
Magnetic Hold-Down.....	MHSTD
Pre-amplifier.....	0/2/4, 2/4/6
Amplifier subsystems ... AE2A, AE5A or standard AE systems	

Sensors include

NIST Calibration Certificate & Warranty



WORLDWIDE HEADQUARTERS:
195 Clarksville Rd •
Princeton Jct, NJ 08550 • USA
T: +1.609.716.4000 • F: +1.609.716.0706
E-MAIL: sales.systems@mistrasgroup.com

CANADA T: +1.403.558.1350
CHINA T: +86.10.5877.3831
FRANCE T: +331.498.26040
GERMANY T: +49.040.2000.4025
GREECE T: +30.210.2846.801-4

HOLLAND T: +31.010.245.0325
INDIA T: +91.22.2586.2444
JAPAN T: +81.33.498.3570
MALAYSIA T: +60.9.517.3788
MIDDLE EAST T: +973.17.729.356

RUSSIA T: +7495.789.4549
SCANDINAVIA T: +46(0)31.252040
S. AMERICA T: +55.11.3062.5111
UK T: +44(0)1954.231.612

Appendix C: Datasheet 2/4/6 preamplifier



MISTRAS
A World of NDT Solutions

Products & Systems
Division

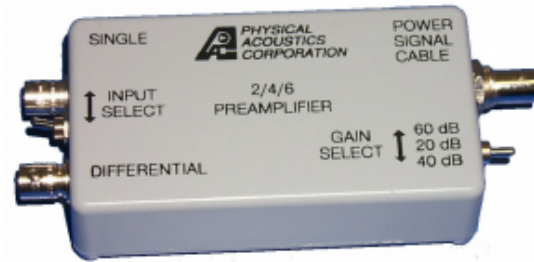
2/4/6 Preamplifier

Description:

The 2/4/6 preamplifier was designed to be used with all available AE systems that have power supplied via the output signal BNC. It is supplied with 20/40/60 dB gain (switch selectable) and operates with either a single ended or differential sensor. Plug in filters provide the user with flexibility to optimize sensor selectivity and noise rejection. These filters are provided in the Low Pass (LP), High Pass (HP), and Band Pass (BP) configurations, and offers constant insertion loss for easy filter swapping without the need for recalibration. Automatic Sensor Test (AST) is standard. This option provides the sensor with the ability to characterize its own condition as well as send out a simulated acoustic emission wave that other sensors can detect.

Features:

- 20/40/60 Selectable Gain
- Wide Dynamic Range > 90dB Standard
- Low Noise < 2=V (With Standard* Filter & Input Shorted)
- Large Output Signal 20Vpp into 50 Ω
- Single Power/Signal BNC or Optional Separate Power/Signal BNC
- Plug-in Filters (Utilizes the same filter as the SPARTAN 2000)
- High Input Impedance
- Standard Auto Sensor Test
- Input Protection



Electrical Specifications:

- Gain Selectable: 20/40/60 dB + 0.5% dB
- Input Impedance: 10K Ω // 15pF
- Power Required: 18-28V DC
- Operating Current: 30mA (With AST Installed)
- 28mA (Without AST Installed)
- Dynamic Range: 80dB (Utilizing an R15 Sensor)
- 90dB (50 Ω Input)

Environmental Specifications:

- Temperature: -40 C to +65 C

Gain Selection	20dB	40dB	60dB
• Bandwidth (-3dB):	10kHz-2.5MHz	10kHz-2.0MHz	10kHz-900kHz
• Output Voltage (50 Ω Load):	6Vpp	20Vpp	20Vpp
• CMRR (500kHz):	42dB	42dB	42dB
• Noise (RMS rti):			

Filter Frequency Response Hz	20dB With R15 Sensor	40dB With R15 Sensor	60dB With R15 Sensor	20dB Input Shorted	40dB Input Shorted	60dB Input Shorted
135k-185k	3 μ V	1.4 μ V	1.5 μ V	2.0 μ V	0.6 μ V	0.42 μ V
100k-300k*	3 μ V	1.8 μ V	1.8 μ V	2.3 μ V	1 μ V	0.8 μ V
10k-2.0M	5 μ V	4 μ V	3 μ V	4 μ V	3 μ V	2.5 μ V

*Standard filter

195 Clarksville Road, Princeton Junction, NJ 08550 USA
Phone: (609) 716-4000 • Fax: (609) 716-0706
Email: sales.systems@mistrasgroup.com • www.mistrasgroup.com

Appendix D: Datasheet AE2A/AE5A wide bandwidth amplifier

AE2A & AE5A: Low Noise, High-Performance and Wide Bandwidth Amplifier Systems for Acoustic Emission Preamplifiers and Sensors



PAC's **AE2A/AE5A** second generation series of AE Amplifiers are small, high-performance Acoustic Emission (AE) systems that amplify and filter an incoming AE signal either directly from an AE sensor or from an external preamplifier. The resulting high-frequency AE analog signal output can be connected to a variety of external monitoring and data acquisition instruments. The AE output is most commonly connected to an analog or digital oscilloscope in order to view a cause and response relationship. The model AE2A covers the entire **traditional** AE bandwidth up to 2 MHz, while the model AE5A covers the **extended** AE frequency up to 5 MHz.

Featuring variable gain, **low noise** and an optional variety of high pass, low pass and band pass filters, this device has a plug-in filter to optimize sensor selectivity and noise rejection. An optional internal preamplifier is available for situations where the sensor cable is short (<2m), to eliminate the need for external preamplifiers. Also available is an RMS output option. This option provides an additional

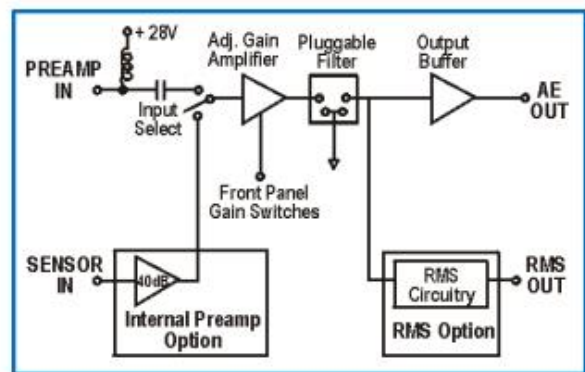
analog AE output signal, which is converted to an RMS representation, with selectable **time constants** of 50ms and 500ms, and is user selectable. In cases where an external preamplifier is needed, the AE2A and AE5A are fully compatible with PAC's line of preamplifiers such as the 1220A, PAC 2/4/6, 0/2/4, 4/6, ILXXS, ILXXD, as well as PAC's line of integral preamplifier AE sensors such as R6I, R15I, R30I, R50I and WDI.

AE2A/AE5A Features:

- Pluggable filter modules with the capability of using high pass, bandpass or low pass filter to vary the bandwidth of the detected AE signal. PAC stocks many types of filters and also has the capability of supplying custom user-requested filters with fast turnaround
- Capability of interfacing and powering PAC 1220A series preamplifiers, 2/4/6, 0/2/4, 4/6, In-Line series preamplifiers (e.g. IL-40D, IL-40S) and integral preamplifier sensors) through a single coax cable
- AE output is can drive an analog signal source of 50 ohms

Options:

- Options include an internal 40 dB preamplifier
- RMS analog signal processing option with 50 and 500 millisecond time constants



AE Signal Processing Specifications:

Specification Description	AE2A	AE5A
• Dynamic Range	93 dB standard	
• Bandwidth	3 kHz - 2 MHz	10 kHz - 5 MHz
• Noise	4 μ Vrms RTI max	6 μ Vrms RTI max
• AE Input (standard for preamplifier (100 ma current limit))	50 W AE input with integral 28 VDC power	
• AE Signal Output	17 Vp-p into 50W load (20 Vp-p burst)	
• Internal Filtering	Via PAC 1220 Series plug-in filters; User specified	
• Internal Gain	0 - 61 dB (3 dB steps)	0 - 41 dB (3 dB steps)
Options		
• RMS Output (with 2 selectable time constants, 50 & 500 milliseconds via front panel switch)	0 - 7 Volts	
• Optional Internal Preamplifier	40 dB gain (Bandwidth same as above for specific unit AE2A or AE5A)	
• Optional Switched Sensor Input (comes with preamplifier option)	10 kW/20 pf load to optional internal preamplifier	

Electrical Specifications:

- Power: 110 or 220 VAC 50/60Hz (field selectable)
- Operating Current: <1 amp AC (at 110 VAC)
<0.5 amp AC (at 240 VAC)
- Fuse Requirements: Uses standard 5 x 20 mm fuses
Uses 0.5 amp (for 220 - 250 VAC operation)
Uses 1.0 amp (for 100 - 120 VAC operation)

Environmental Specifications:

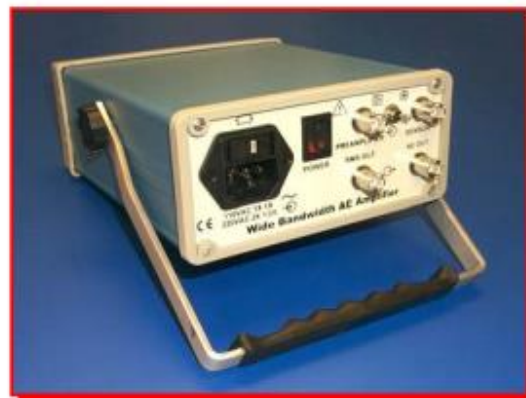
- Temperature: - 0 °C to + 50 °C (+32 °F to 122 °F)

Physical Specifications:

- Dimensions: 6" (L) x 5½" (W) x 2½" (H)
15.24cm x 13.97cm x 6.35cm
- Weight: 2.7 lbs. (1.2 kg)

CE Mark Compliance:

- Electrical Safety Stds: Meets EN60950 (IEC-950)
- EMC Emission Stds: Meets EN55011, EN55022
- EMC Immunity Stds: Meets EN50082, IEC-1000-4-2, IEC-1000-4-3, IEC-1000-4-4



For more information about the
AE2A/AE5A Amplifier Systems
 Call (609) 716-4000 or e-mail us at sales@pacndt.com

For information on PAC products and services,
 visit our web site at: www.pacndt.com



HQTS: 195 Clarksville Road • Princeton Junction, NJ 08550 • Phone: (609) 716-4000 • Fax: (609) 716-0706
 • email: sales@pacndt.com • Internet: www.pacndt.com **Subsidiaries:** • Cambridge (44) 1954-231612
 • Paris (33) (1) 4982-6040 • Tokyo (81) (3) 3498-3570 • São Paulo (55) (11) 3082-5111 • Athens (30) (210) 284-6801
 • Moscow (7095) 789-45-49 • Beijing (86) (10) 8497-3570 • Buenos Aires (54) (11) 4345-0400 • Wolfegg
 (49) (75) 272312 • Rotterdam (31) (10) 245 0325 **Representatives:** Worldwide.

Sound Technology for Safety & the Environment

Acoustic emission as on-line tool for non-destructive inspection of welding

Dries De Ruyck, Hannes Polijn
Student numbers: 01500150, 01508860

Supervisors: Prof. dr. ir. Wim De Waele, Dr. ir. Koen Faes (BIL)
Counsellor: Ir. Irene Kwee (Belgisch Instituut voor Lastechniek)

Master's dissertation submitted in order to obtain the academic degree of
Master of Science in de industriële wetenschappen: elektromechanica

Academic year 2018-2019